

Spring 2011

# Wireless Sensor Integrated Tool for Characterization of Machining Dynamics in Milling

Christopher Adam Suprock  
*University of New Hampshire, Durham*

Follow this and additional works at: <https://scholars.unh.edu/dissertation>

---

## Recommended Citation

Suprock, Christopher Adam, "Wireless Sensor Integrated Tool for Characterization of Machining Dynamics in Milling" (2011).  
*Doctoral Dissertations*. 575.  
<https://scholars.unh.edu/dissertation/575>

This Dissertation is brought to you for free and open access by the Student Scholarship at University of New Hampshire Scholars' Repository. It has been accepted for inclusion in Doctoral Dissertations by an authorized administrator of University of New Hampshire Scholars' Repository. For more information, please contact [nicole.hentz@unh.edu](mailto:nicole.hentz@unh.edu).

Wireless Sensor Integrated Tool for Characterization of Machining Dynamics in Milling

BY

CHRISTOPHER ADAM SUPROCK  
B.S., Pennsylvania State University, 2007

DISSERTATION

Submitted to the University of New Hampshire  
in Partial Fulfillment of  
the Requirements for the Degree of

Doctoral Degree  
in  
Systems Design Engineering

May, 2011

UMI Number: 3467369

All rights reserved

INFORMATION TO ALL USERS

The quality of this reproduction is dependent upon the quality of the copy submitted.

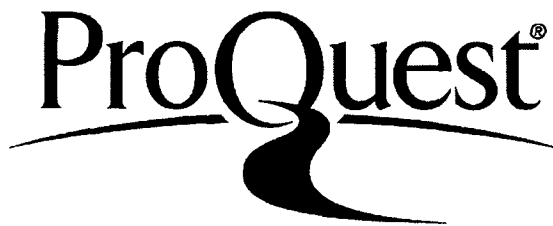
In the unlikely event that the author did not send a complete manuscript and there are missing pages, these will be noted. Also, if material had to be removed, a note will indicate the deletion.



UMI 3467369

Copyright 2011 by ProQuest LLC.

All rights reserved. This edition of the work is protected against unauthorized copying under Title 17, United States Code.

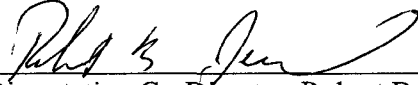


ProQuest LLC  
789 East Eisenhower Parkway  
P.O. Box 1346  
Ann Arbor, MI 48106-1346

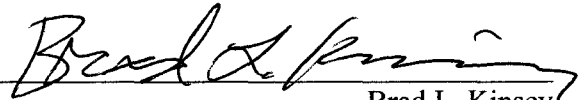
This dissertation has been examined and approved.



Dissertation Director, Barry K. Fussell  
Professor of Mechanical Engineering



Dissertation Co-Director, Robert B. Jerard  
Professor of Mechanical Engineering



Brad L. Kinsey  
Associate Professor of Mechanical Engineering



Kent A. Chamberlin  
Professor of Electrical and Computer Engineering



Wayne J. Smith  
Lecturer of Electrical and Computer Engineering

Date May 10, 2011



Dedication

*To my father, You have inspired me to earn this degree.*

## ACKNOWLEDGMENTS

I would like to acknowledge the assistance of Jeff Nichols, who was instrumental in developing a serial transmitter version of the smart tool holder.

I would like to acknowledge the members of my committee, in particular Prof. Fussell and Prof. Jerard.

## Table of Contents

Acknowledgments.....	iv
List of Figures.....	vii
List of Tables.....	x
Abstract.....	xi
Chapter 1: Introduction.....	1
1.1 Sensor Application for Characterization of Tool Chatter.....	8
1.2 Research Goals.....	12
1.3 Contributions of the Dissertation.....	13
Chapter 2: Sensor Exploration and Preliminary Development.....	15
2.1 Choosing Sensor Technologies for Characterizing Machining Dynamics.....	15
2.2 Tool Tip Accelerometer.....	17
2.3 Validating Bandwidth from Electret Accelerometer Prototypes.....	26
2.4 Wire Strain Gauges.....	29
2.5 Tool Torque Measurement with an AC Coupled Wire Strain Gage.....	37
2.6 Conclusions About the Wired Strain Gauge.....	41
2.7 Semiconductor Strain Gauges .....	42
2.8 Approximate Calibration from Cutting Data.....	45
2.9 Test Setup for Evaluating Bending Cross Talk.....	47
2.10 Validation of Strain Gage Location Considering Tool Dynamics .....	49
2.11 Chapter Summary.....	56
Chapter 3: Experimental Applications For Observation of Milling Phenomenon.....	58
3.1 Electret Accelerometer Based Tool Tip Acceleration Measurements.....	58
3.2 Observing Chatter with Electret Accelerometer Based Tool Holder.....	64
3.3 Chatter Prediction Using the Electret Sensor Integrated Tool.....	65
3.4 Chatter Frequency Using The Sensor Integrated Tool.....	74
3.5 Frequency Based Observations and Experimental Stability Lobe Diagrams.....	76
3.6 Tool Torque Measurement.....	85
3.7 Chapter Summary.....	88
Chapter 4: In situ Chatter Frequency Prediction Using Torque Data.....	90
4.1 Linear Predictive Coding and Formant Frequency Tracking.....	91
4.2 Impulse Response Testing.....	94
4.3 Application of LPC Methods to Estimate Chatter Frequencies.....	96
4.4 Time Varying Effects on LPC Frequencies and Predicting Stable Cutting Speeds .....	102
4.5 Validating the LPC Frequencies by Inducing Chatter.....	103
4.6 Changes in the LPC Frequencies as a Function of Spindle Speed.....	104
4.7 Estimating Chatter Frequency with LPC during Partial Engagement Cutting.....	107

4.8 Chapter Summary.....	108
Chapter 5: Predicting Chatter Frequency With Coupled Workpiece and Tool Holder Dynamics.....	111
5.1 Using the LPC Model as an Adaptive Filter.....	115
5.2 Closed Loop Pole Magnitude and Bifurcation of the Chatter Frequency.....	121
5.3 Chapter Summary.....	123
Chapter 6: Time Domain Modeling of Tool Chatter to Capture System Behavior.....	124
6.1 Time Domain Cutting Tool 2DOF Model.....	124
6.2 Conclusions about the Time Domain Cutting Tool 2DOF Model.....	135
6.3 Time Domain Coupled Cutting Tool & Work Piece 4DOF Model.....	135
6.4 Replicating the Cantilever Cutting Test with the 4DOF Model.....	142
6.5 Chapter Summary.....	143
Chapter 7: Conclusions.....	146
7.1 Conclusions and Outcomes.....	146
Chapter 8: Future Work.....	150
8.1 Suggested Directions and Topics for Future Work.....	150
8.2 Mathematical Method for Estimating Stability Lobes from LPC Model.....	151
8.3 Variation in the Stability Lobes Throughout Cutting.....	156
8.4 Including Stochastic Noise Effects to Time Domain Models.....	157
List of References.....	158

## LIST OF FIGURES

Figure 1.1: Embodiment of a Sensor Integrated Tool.....	8
Figure 1.2: The role of phase shift in regenerative chatter.....	9
Figure 1.3: Feedback loop with time delay .....	10
Figure 1.4: Stability Lobe Diagram for Axial Depth versus RPM.....	10
Figure 2.1: Sensor Classification Tree.....	16
Figure 2.2: Desired Placement of Tool Tip Accelerometer.....	18
Figure 2.3: Accelerometer Integrated Indexable End Mill.....	18
Figure 2.4: Bluetooth Test Interface.....	21
Figure 2.5: Response Spectra for Piezoelectric and Wireless Electret Accelerometers...	22
Figure 2.6: Face Mill .....	24
Figure 2.7: Face Mill Accelerometer Orientation.....	24
Figure 2.8: Face Mill Accelerometer Leads.....	25
Figure 2.9: Electret Sensor Prototype 2 Fixtured in Tool Holder.....	26
Figure 2.10: Electret Accelerometer/Wireless Transmitter Frequency Response.....	27
Figure 2.11: Electret Accelerometer Frequency Accuracy.....	28
Figure 2.12: Wire Strain Gage Installation and Orientation, Prototype 3.....	30
Figure 2.13: Torque Sensor Integrated Tool and Transmitter, Prototype 3.....	31
Figure 2.14: Wired Strain Gauge Calibration Curve.....	32
Figure 2.15: Dual Strain Bridge and Amplifier Circuit.....	33
Figure 2.16: A2DP Transmitter Response Transfer Function (transmitter voltage input / receiver voltage output) 0 to 20 kHz.....	35
Figure 2.17: A2DP Transmitter Response Transfer Function (transmitter voltage input / receiver voltage output) 0 to 2 kHz.....	36
Figure 2.18: A2DP Transmitter Noise Response.....	36
Figure 2.19: AC Coupled Wire Torque Gage Experimental Plot.....	37
Figure 2.20: AC Coupled Torque Plot from Ideal Force Model.....	38
Figure 2.21: Calibrated AC Coupled Wire Torque Gage Cutting Test.....	39
Figure 2.22: AC Coupled Torque (top) compared to Resolved Bed Force(bottom).....	40
Figure 2.23: Spindle Power compared to AC Coupled Torque.....	41
Figure 2.24: Location of Semiconductor Gauges on Tool Holder Body, Prototype 4.....	42
Figure 2.25: Location of Semiconductor Gauges on Tool Holder Body, Prototype 4.....	43
Figure 2.26: Semiconductor Gage Peak Value Calibration (Prototype 4).....	46
Figure 2.27: Semiconductor Smart Tool Testing Jig.....	48
Figure 2.28: Long Overhang Torsional Dynamics.....	54
Figure 2.29: Short Overhang Torsional Dynamics.....	54
Figure 2.30: Short Overhang Bending Dynamics.....	55
Figure 3.1: Time Signal From the Face Mill Acceleration Sensors.....	59
Figure 3.2: Detailed Time Signal From the Face Mill Acceleration Sensors.....	60
Figure 3.3: Single Tooth Pass Time Response.....	61
Figure 3.4: Half Immersion Upmill and Downmill Cuts.....	63

Figure 3.5: Slot Cut Acceleration at Three Feed Rates.....	63
Figure 3.6: Observing Tool Chatter with Electret Accelerometer.....	64
Figure 3.7: Observation of Chatter Buildup Referenced to Workpiece Photo.....	65
Figure 3.8: Waterfall Plot of Chatter Development.....	66
Figure 3.9: A Typical Stability Lobe Diagram.....	68
Figure 3.10: Directional Chatter for Increasing Spindle Speed at 8.89mm Axial Depth. .	70
Figure 3.11: Directional Chatter for Decreasing Spindle Speed, AD=8.89mm.....	71
Figure 3.12: Superimposed Absolute Vibration Magnitudes from the Frequency Sweep Tests.....	73
Figure 3.13: Phase Angle Tangent Magnitude vs Spindle Speed.....	76
Figure 3.14: Identifying Chatter Frequencies.....	77
Figure 3.15: Bandpass Isolation of the Chatter Frequency.....	80
Figure 3.16: Theoretical vs Actual Spindle Speed.....	83
Figure 3.17: Experimental Stability Lobes.....	84
Figure 3.18: Torque Signal Showing Insert Run Out.....	86
Figure 3.19: Torque Signal Showing Entrance Effects and Regenerative Tool Chatter...	87
Figure 4.1: Baseline X Direction Tap Test.....	95
Figure 4.2: Baseline Y Direction Tap Test.....	95
Figure 4.3: XY Slot Cutting Experimental Orientation.....	97
Figure 4.4: Torque Plot from the XY Slot Cut.....	97
Figure 4.5: Dominant Formant Frequencies of the XY Slot Cut.....	98
Figure 4.6: Multiple Chatter Frequencies (Schmitz/Smith [48] pp 205).....	99
Figure 4.7: 10th Order Model Frequency Response From Cutting Torque Data.....	100
Figure 4.8: 64th Order Model Frequency Response From Cutting Torque Data.....	101
Figure 4.9: PSD of Stable (no chatter) Raw Torque Data.....	102
Figure 4.10: Drifting System Poles During Steady State Cutting.....	103
Figure 4.11: PSD of Raw Torque Data Under Induced Chatter .....	104
Figure 4.12: Multi-Depth Slot Cutting Experimental Orientation.....	105
Figure 4.13: Chatter Frequencies vs. RPM.....	107
Figure 4.14: Quarter Radial Immersion Experimental Orientation.....	107
Figure 4.15: 64th Order Model Frequency Response From Quarter Radial Immersion Cutting Torque Data.....	108
Figure 5.1: Cantilever Workpiece and Tool Holder.....	112
Figure 5.2: Cantilever with Tap Test Accelerometer.....	113
Figure 5.3: 85.85mm Cantilever Tap Test.....	114
Figure 5.4: 108.70mm Cantilever Tap Test.....	115
Figure 5.5: LPC Predicted System Frequencies Throughout Cut (Cantilever 108.7mm) .....	118
Figure 5.6: LPC Predicted System Frequencies Throughout Cut (Cantilever 85.85mm) .....	119
Figure 5.7: Statistical Variation of Stiffness Estimated from Chatter Frequency .....	121
Figure 5.8: Transition between tool and workpiece chatter during cantilever cutting experiments.....	123
Figure 6.1: Spindle+Tool Stiffness X Direction.....	125

Figure 6.2: Spindle+Tool Stiffness Y Direction.....	126
Figure 6.3: Impulse response of the tool and spindle.....	126
Figure 6.4: Geometry of Cutting Forces, Entrance, and Exit Angles.....	128
Figure 6.5: Simulated radial displacement observed for increasing spindle speed.....	131
Figure 6.6: Simulated radial displacement observed for decreasing spindle speed. ....	131
Figure 6.7: Instabilities for simulated data.....	133
Figure 6.8: Resolved Instabilities .....	133
Figure 6.9: Instabilities for experimental data.....	133
Figure 6.10: Simulated chip thickness.....	134
Figure 6.11: 4DOF System Model.....	136
Figure 6.12: 4DOF Model Frequency PSD.....	139
Figure 6.13: 4DOF Model Spindle Speed Sweep.....	139
Figure 6.14: 4 DOF Model with Infinitely Stiff Workpiece.....	141
Figure 6.15: 2DOF Model for Comparison to 4DOF Model.....	141
Figure 6.16: 4 DOF Model With Workpiece Compliance.....	142
Figure 6.17: 4DOF Model Changing Cantilever Length .....	143
Figure 8.1: Stability Lobe Diagram Generated From LPC Coefficients.....	156
Figure 8.2: Stability Lobe Distribution.....	157

## LIST OF TABLES

Table 1.1: Sensor Integrated Tooling System Criteria.....	7
Table 2.1: Smart Tool Prototype Names and Descriptions .....	17
Table 2.2: Influence of Cross Talk on Semiconductor Torque Data.....	49
Table 3.1: Electret Accelerometer Prototype Cutting Test Geometries.....	61
Table 3.2: Electret Accelerometer Prototype Cutting Test Feed Rates.....	62
Table 3.3: Electret Accelerometer Prototype Cutting Test Vibration Magnitudes.....	63
Table 3.4: Selected Stable and Unstable Spindle Speeds from Figure 3.12.....	73
Table 3.5: Calculated Unstable Speeds.....	75
Table 3.6: Stable Speeds Predicted by the Phase Shift Tangent.....	76
Table 3.7: Chatter Frequency Dependency on Cutting Direction.....	78
Table 4.1: Predicted and Actual Chatter Frequencies as a Function of Spindle Speed for Slot Cuts.....	106
Table 5.1: Cantilever Workpiece Lengths.....	113



## ABSTRACT

Wireless Sensor Integrated Tool for Characterization of Machining Dynamics in Milling

by

Christopher Adam Suprock

University of New Hampshire, May, 2011

Degree Adviser: Barry Fussell

A first step towards practical sensing in the machining environment is the development and use of low cost, reliable sensors. Historically, the ability to record in-process data at an end mill tool tip has been limited by the sensor location. Often, these sensors are mounted on the material workpiece or the machine spindle at significant physical distance from the cutting process. Of specific interest are the problems of tool chatter which causes limitations to productivity and part quality. Although tool chatter is a substantial issue in machining, it remains an open research topic. In this research, a sensor integrated cutting tool holder is developed to specifically analyze the problems related to tool chatter.

With the sensor integrated cutting tool holder, the signal to noise ratio is higher than traditional sensing methods. Because of the higher sensitivity, new data analysis methods can be explored. Specifically, the sensor is used in conjunction with a data dependent linear predictive coding algorithm to demonstrate effective prediction of chatter frequencies from stable cutting.

## CHAPTER 1

### Introduction

In order for a condition monitoring system to be widely accepted by industry the deployment onto shop floor machinery must be low cost, noninvasive, and cause no reduction of the machining envelope. A monitoring system typically requires data collection sensors to be located on the machine. In the case of a dynamics monitoring system, the sensors must be sampled at high speed and with a high signal to noise ratio. Unfortunately, many sensor types are high in cost, size, or are difficult to deploy. As a result, it is desirable for a machining dynamics monitoring system to take advantage of existing hardware infrastructure while using inexpensive sensors that have a low profile within the machine.

One instance of a non-invasive sensor is a power monitor located on a spindle drive motor [1]. In this work, an example of combining mechanistic and geometric models with a spindle drive power monitor was discussed for end milling. Although non-invasive and cost effective, data sources such as power monitoring do not provide sufficient bandwidth to capture many important details of the machining process.

During operations such as end milling, it is necessary to capture a broad range of frequencies for analysis purposes. Currently, this can be achieved with a variety of sensor types including force dynamometers, accelerometers, acoustic emissions sensors, or contact microphones. A recent example can be seen in work by Byrne et al. [2] for

drilling and Parl [3] for end milling. In these studies, piezoelectric force sensors are integrated into the machine spindle. Although such devices are effective, machine tool manufacturers have yet to add sensor components to their products.

From an industrial perspective, this is understandable. First, one can note the wide variety of sensor and signal processing combinations available [4]. Each technique is often coupled with a specific sensor type and is designed to solve a particular condition monitoring problem. Second, many condition monitoring techniques require sensors such as bed-type dynamometers which are largely impractical [5]. From a research perspective, these sensor types are necessary for the development and validation of robust system models. However, in application, the sensing approach should accommodate cost, ease of setup, and performance.

Many modern numerical control (NC) machine systems are operated from a software interface located on a PC based platform. Due to the primitive level of NC control development, the majority of these systems rely on a variation of RS-274, the most common form of which is known as G-code. Because of the low overhead involved with running an NC machine, the PC platform has almost all of its system resources available for use. As a result, there is significant flexibility for on board data acquisition (DAQ), novel software, and emerging hardware applications. One such example can be seen in work by Jerard [6] where a PC based testbed is host to both data acquisition and software based model calibration. This vision for an expandable machining test bed has provided the foundation for the current work described herein.

A first step towards practical sensing in the machining environment is the

development and use of low cost, yet reliable sensors. It is important to explore the use of a low cost accelerometers, novel strain sensing technologies, and the processes of embedding them in cutting tool hardware.

Coupled with sensing technologies, wireless data transmission is starting to be widely used in industrial process control. For example, Callaway [12] discusses the application of wireless sensor networks for shop floor deployment. Wireless process control has numerous benefits including a low profile, ease of deployment, and the ability to monitor from a central location. Similarly, Sudararajan et al. [13] describe the potential of wireless monitoring specifically for machine tools.

Historically, the ability to record in-process data at an end mill tool tip has been limited by the sensor location. Often, these sensors are mounted on the material workpiece or the machine spindle at significant physical distance from the cutting process. Recently, Wright et al. [14] took advantage of wireless transmission for measuring cutting tool temperature. In this work, resistive temperature detectors (RTDs) were placed on the backside of end-mill inserts. A primary goal of this research was to demonstrate the possibility for small form-factor wireless systems applied to tool condition monitoring. The success of this project is a promising exhibit of wireless applicability to end mill tool condition monitoring.

Of specific interest are the problems of tool chatter. Although tool chatter is a substantial issue in machining, it remains an open research topic. Tool chatter presents limitations to productivity and part quality. The physical mechanisms of tool chatter are complex and influenced by a myriad of variables which make the controlled study of this

phenomenon difficult with traditional sensing technologies. Traditional sensors have problems with location and dynamics associated with distant measurement from the workpiece-tool interface. Another difficulty is the bandwidth and frequency response of data acquisition.

End mill data contains a broad spectrum of useful information but requires significantly higher bandwidth than from a spindle motor power sensor. In an example by Dini et al. [15], close proximity wireless acquisition of cutting torque signals was conducted using a commercial rotating dynamometer. In this case, the dynamometer is directly placed between the spindle and tool. This method is excellent for capturing a torque signal, however, commercial dynamometers are high in cost and increase the spindle compliance.

Vibration measured by spindle mounted sensors suffers from attenuation and noise introduced by spindle bearings, tool holder, and collet interfaces. Accurate measurement of in-process tool tip response is vital to the development of tool dynamic models. Cheng et al. [16], used receptance coupling substructure analysis (RCSA) to indirectly characterize tool tip dynamics during spindle rotation. Receptance coupling is the process of using an artifact (baseline tool assembly or blank) to characterize the spindle side response. The spindle response can be analyzed in series with different tools placed into the assembly so that the tool response can be considered in series 'coupled' with the response of the spindle. Although informative, these techniques require precision tool holding setups to mitigate clamping repeatability and tight coupling between the spindle and tool. Like any indirect estimation method, RCSA is not as effective as

measuring the signal at its source.

A commercial product called the Harmonizer [53] relies on recording acoustic emissions from the cutting process and analyzing the frequency content to make manual adjustment to the cutting parameters. While this works to avoid chatter for steady state cutting and instances where compliance of the tool holder does not change, the method requires test cuts and manual setup of spindle speed parameters.

By employing wireless techniques and embedded sensors, the tool-workpiece interactions can be more clearly observed. It should be possible to monitor the stability of the cut during changing cutting conditions and therefore improve cutting efficiency by avoiding chatter or forced vibrations **during** the cutting process. The sensor may also be useful for detecting undesirable tool eccentricity, i.e., runout. Moreover, it is possible to monitor these items on multiple machines from a control location without interfering with shop floor activity.

Recent advances in wireless sensor technology have explored the use of single-sensor integrated tooling for sampling tool tip conditions for vibration and temperature [13, 14, 26, 27]. Various sensor configurations can be used to collect information from the cutting process. Several sensing technologies are appropriate for dynamic sensing of frequency information to determine system state during the cutting process. Tool tip vibration data has been particularly useful for studying tool runout, chatter, and wear. The vibration amplitude is relative to the spindle speed and cutting geometry [26]. While vibration information is useful, it does not directly measure cutting forces or torque. In many cases, force or torque is not required (to at least partially characterize machine

dynamics). Cutting torque provides the actual magnitude of the tangential cutting force. A sensor technology must be chosen with the application in mind. Environmental variables also play a role in the selection of sensor technologies. For instance, vibration sensors using sealed electret condensers are susceptible to drift at elevated temperatures [28], and therefore can only be applied in cutting operations involving coolant or in locations where the temperature gradient is low.

With multiple sensor options available for studying end milling cutting dynamics, it is desirable to standardize a transmitter design to sample a variety of sensors from a single receptacle located in the tool holder. In particular, the ability to simultaneously sample multiple sensors can improve resolution on the end milling system [29]. Therefore, a wireless data transmission method might be generalized to accept and simultaneously sample multiple sensors from within sensor integrated tooling. There have been no solutions that satisfy this need to this point.

Commercial rotating sensor systems require slip rings or receivers in close contact proximity to the signal source [30]. This limits practical applications on the shop floor due to harsh environments, chip control, and fluid use. Slip rings are also an expensive addition to a sensor system. This method is excellent for capturing a torque signal in laboratory settings, however, in commercial settings dynamometers are rarely used due to high cost and an increase in the spindle compliance. In a practical application, the spindle stiffness must be maintained in order to hold surface tolerances and prevent conditions that may lead to tool chatter. In addition to increased compliance, the workspace envelope is reduced by placement of the commercial dynamometer between

the spindle and tool holder. Since the cutting energy provided by torque is of primary interest to end milling process modeling and control, it is important to develop more robust sensor methods.

Due to the cost and limitations of current commercial sensor systems, machine tool manufacturers have been hesitant to accept sensor integration techniques. Although work such as Suprock [31] explores inexpensive machine tool sensor solutions, there are numerous factors beyond sensor cost and performance. For machine tool manufacturers, the scalability of sensor systems is a major concern. Since machine tools have a long operational lifespan, the sensor system must be reconfigurable and non-invasive to the machine tool platform. Simply, it must be fast and easy to upgrade when new sensing techniques become available or if the sensor system becomes damaged. For a wireless sensor integrated tooling system to be accepted by industry, the criteria listed in Table 1.1 must be met.

*Table 1.1: Sensor Integrated Tooling System Criteria*

Does not increase the compliance of the cutting system
Compatible with existing tool types
Interchangeable sensor types
Significant range and bandwidth while avoiding interference
Inexpensive
Easy to install, replace, and reconfigure
Open for custom software development and controller integration



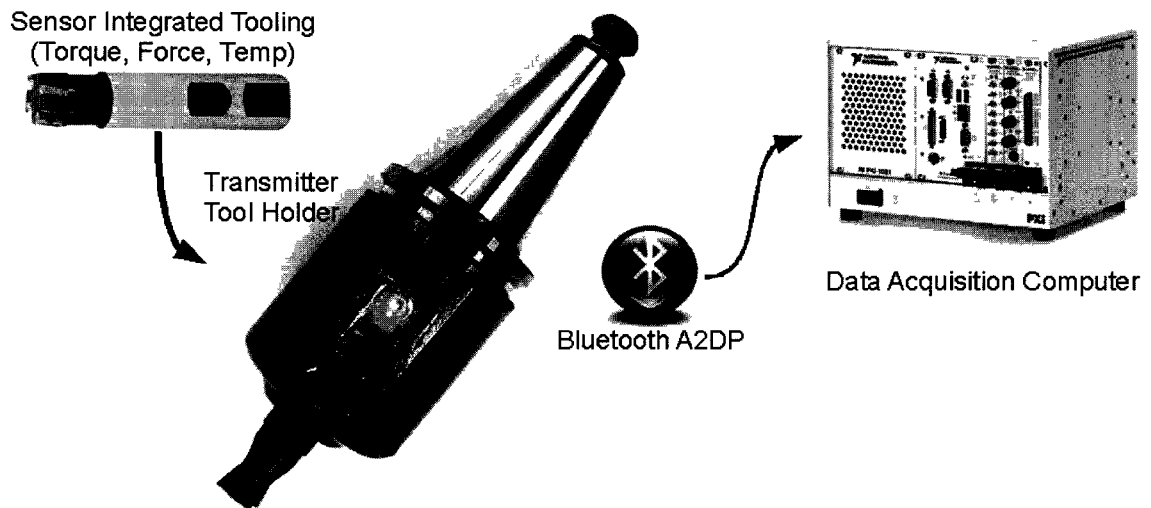


*Figure 1.1: Embodiment of a Sensor Integrated Tool*

A system that meets these criteria can contribute to the evolution of NC machine tool control, cutting process monitoring, and accurate modeling of the cutting system. Figure 1.1 illustrates one embodiment to meet these criterion.

### **1.1 Sensor Application for Characterization of Tool Chatter**

Regenerative chatter is a major limitation to the productivity and quality of machining operations due to the excessive rate of tool wear and scrap parts produced with poor surface quality. Tool chatter can be compared to a phonograph record that replays the surface finish on the previously cut workpiece material. Unlike a phonograph, the playback surface is being rewritten as it is being replayed. The surface waviness follows the dynamic deflection in the machining structure. When the peak deflections in the machine tool structure are out of phase with the previously cut surface waviness, the effect is considered regenerative since deflections compound over consecutive cycles. In

this scenario, peak deflection intersects with peak thickness in the surface causing high instantaneous forces. The surface profile is a feedback mechanism for instability when the surface profile and deflection are “regenerative”. This leads to greater forces and greater deflections. Dynamic chip thickness and peak forces are affected leading to poor surface finish and possible machine tool damage.

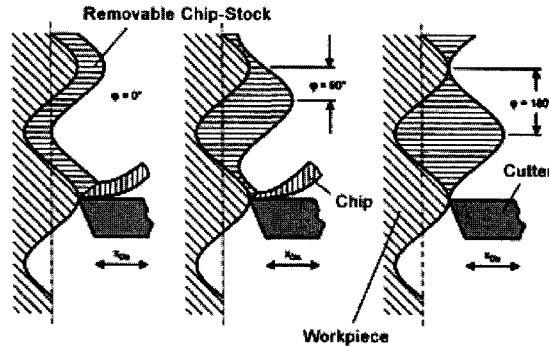


Figure 1.2: The role of phase shift in regenerative chatter

Typical machining chatter analysis techniques examine the stability of a closed-loop model (force process and machine tool-part structure) of the machining operation to determine the stable process parameter space. Almost all chatter analysis techniques assume a linear force process and are based on the concept of stability lobe diagrams [33]. Figure 1.3 shows the cutting system feedback loop from a controls perspective. The variables driving the system are the feed per tooth,  $h_0$ , the cutting force model,  $F(s)$ , (relating chip thickness to output force), and the system compliance model is  $G(s)$ . The time delay is related to the period,  $T$ , of tooth passing. As shown in Figure 1.2, this the worst case is a phase shift causing the surface waviness to be intersected by deflections in the cutter. The worst case for regenerative instability occurs when the phase shift is around  $270^\circ$  ( $-90^\circ$ ).

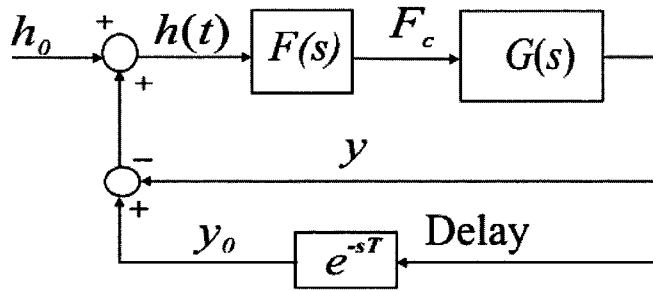


Figure 1.3: Feedback loop with time delay

Stability lobe diagrams, as shown in Figure 1.4, are plots revealing the acceptable axial depth of cut vs spindle speed (typically in RPM). The plots identify the axial cutting depth ( $b_{lim}$ ) at which instability occurs given the forcing frequency applied to the system. For interrupted cutting, such as end milling, the forcing frequency is the tooth passing frequency of the cutting, which is the product of the tooth count and spindle speed.

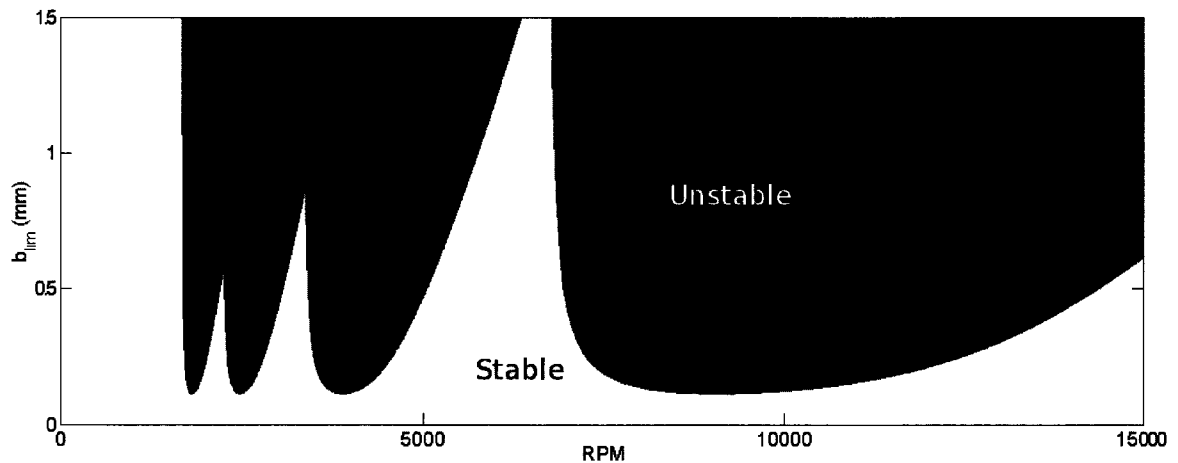


Figure 1.4: Stability Lobe Diagram for Axial Depth versus RPM

Clearly, it is desirable to operate the cutting process in an area of high material removal rate that occurs within the stable zone. Theory and experimental verification have shown that the limiting stable axial depth of cut (for a given radial immersion, feed, and workpiece material) is highly dependent on the selected spindle speed and frequency response of the tool-spindle-workpiece system [34, 35]. The prediction of stable cutting

regions is a critical requirement for high-speed milling operations. However, significant changes in system dynamics occur during high-speed rotation. Such changes include thermal expansion, changing stiffness of elastohydrodynamic boundary layers in the bearings, and rotational inertia. These changes and others such as workpiece stiffness and machine stiffness make the chatter prediction process more difficult, since these variables affect the overall stiffness and damping of the dynamic system [34].

Although several analytical methods to predict stability lobes have been presented in recent literature [35, 36, 37], these models lack the ability to predict the changes in tool frequency response and chatter if cutting conditions or machine dynamics change. To account for these parameter variations, techniques such as the 'multifrequency solution' consider the harmonics of the tooth passing frequency and deviation in system response from the open loop transfer function of the tool/spindle at harmonics of the tooth passing frequencies [37]. Time domain simulations have also been investigated to account for nonlinear effects that are difficult to model analytically [38]. These new techniques give an accurate description of the problem for steady state cutting but still lack the ability to predict chatter if cutting conditions or machine dynamics are changing.

Traditionally, stability lobes are calculated from the Frequency Response Function (FRF) of the end mill spindle [25]. The FRF, in the standard terminology of control engineering, is the transfer function of the system plant. Classical stability analysis treats the FRF as a linear time-invariant plant. One of the findings of the research described in this dissertation is the extent to which the FRF is not constant. For example, most methods used to generate the FRF do not include the effects of workpiece dynamics and

are deficient for short overhang stiff tools, where the spindle dynamics have a significant role in the chatter mode. Spindle dynamics are influenced by changes in the bearings during rotation and temperature effects. Since these effects are highly variable or difficult to directly measure, a method is designed in this research for in-cut stability estimation using a sensor integrated tool. Moreover, the tools used throughout this work have a short overhang from the tool holder. This means that the spindle dynamics have a higher influence on the chatter condition than with a slender tool.

The methods developed in this research are capable of generating an experimental stability lobe diagram. In this way, it is possible to have a more accurate characterization of the milling system and how it changes as a function of cutting conditions. Additionally, the method can be used to find conditions for higher material removal rates.

## **1.2 Research Goals**

The first research goal is consistently focused around developing embedded sensor instrumentation for cutting tools. This includes invention of sensors, evaluation of sensing technologies, and transmission methods. The hypothesis is that these instruments are useful research tools and industrial feedback for the study of machine dynamics, specifically tool chatter. The applications discussed in this dissertation focus on the use of sensor integrated tool holders to observe, quantify, and predict tool chatter.

The second research goal is to use a sensor integrated tool holder for data dependent dynamic modeling of the machine tool system. This is done through the exploration of autoregressive model-based system identification techniques. The hypothesis is that chatter frequencies can be estimated in-process.

The third goal in this research is to understand the underlying physics of phenomenon observed with the sensor integrated tools. This is done through the application of mechanistic modeling in the form of a time domain model.

The development and application sections have subdivisions based on the various sensing technologies explored while the mechanistic modeling sections are focused solely on the subject of tool chatter. The data dependent modeling combines application of a sensor integrated tool with model based prediction.

The organization of this dissertation follows the paths and topics covered, why they are covered, and what contribution they serve to the field.

### **1.3 Contributions of the Dissertation**

This work has resulted in several novel contributions to metal cutting research.

- The sensor development has created a smart tool holder capable of recording information from the live cutting process. There is a substantial improvement over the traditional methods of using external sensors or force sensing based on bed dynamometer. Many problems with external sensing are circumvented by a smart tool holder and measurements are more direct.
- Cutting dynamics have been observed from the tool holder. High signal-to-noise ratio enable clear observation of frequency content and how the cutting signal behaves throughout cutting.
- Drift in the frequency content during cutting provides an explanation for the difficulty predicting stable cutting speeds from traditional methods (i.e. tap tests) and suggests that the system FRF may be changing during the cutting process.

- Chatter frequencies are observed in stable cuts before the onset of chatter. The closed loop frequency content of the system is of great importance to the optimization of cutting processes in real time. This is a significant advance to the state of the art, since it was previously very difficult to observe tool frequencies during live cutting.
- The introduction of time domain models to replicate spindle speed sweep tests and capture the behavior observed during speeds sweeping experiments. Both 2 degree of freedom and 4 degree of freedom models are explored.

## CHAPTER 2

### Sensor Exploration and Preliminary Development

#### **2.1 Choosing Sensor Technologies for Characterizing Machining Dynamics**

Thoughtful selection of the proper sensing technology for a sensor integrated tool requires addressing the criteria outlined in the Introduction (see Table 1.1). Further considerations may include practical commercial availability of the sensing technology and its survivability in the machining environment. The tool holder is subjected to a wide and hostile range of environmental conditions.

Therefore, significant effort has been given towards developing and evaluating a number of sensor options. The types of sensor explored are accelerometer, strain, and temperature. All of these sensors relate physically to the machining process and their specific applications will be discussed. Figure 2.1 gives a high level overview of these three sensing technologies and their applicability from the standpoint of a successful sensing product. It is critical to realize that each sensor type is categorized by its advantages and disadvantages and that it is not implied that one sensor type is superior or inferior to the others. Figure 2.1 approaches the subject from an objective of application based (laboratory or industrial) use. For controlled laboratory use, all of the sensors are applicable and can be effectively applied.



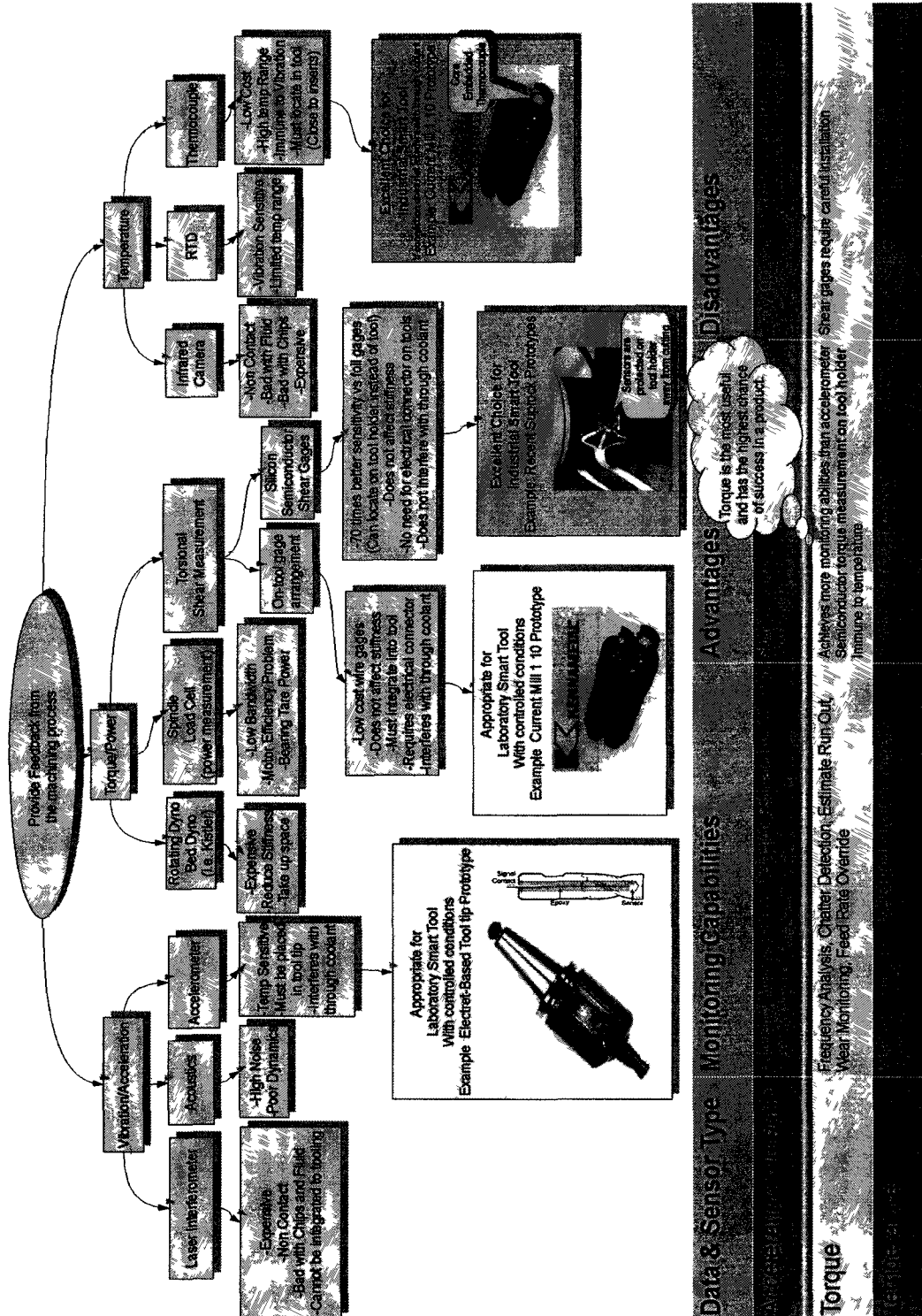


Figure 2.1: Sensor Classification Tree

There are four prototype smart tools discussed in this dissertation. Prototype 1 is an electret accelerometer based face mill with the sensors oriented tangentially. Prototype 2 is an electret accelerometer based indexable end mill with a single axially oriented sensor. Prototype 3 is a torque sensing tool holder based on wire strain gages. Prototype 4 is a torque sensing tool holder based on semiconductor strain gages. For clarification and reference, Table 2.1 gives a list of the different tools and their features.

*Table 2.1: Smart Tool Prototype Names and Descriptions*

Tool Name	Sensor Type	Description
Prototype 1	Electret Accelerometer	Orientation for torsional vibration
Prototype 2	Electret Accelerometer	Axial Orientation
Prototype 3	Wire Strain Gauge	Torsional Strain on Tool Holder
Prototype 4	Semiconductor Strain Gauge	Torsional Strain on Tool Holder

## **2.2 Tool Tip Accelerometer**

Acceleration data is useful for frequency analysis of cutting data in an end milling system. It is desirable to place an accelerometer at the tip of an end milling tool to avoid dynamics introduced between the tool tip and alternative sensing locations. Placing the sensor directly at the signal source also increases signal to noise ratio. In a traditional application, stationary accelerometers are located on the machine tool spindle. Unfortunately, it is difficult to estimate tool tip motion from a spindle mount sensor, as the estimation methods are fraught with error introduced by assumptions about the tool holder dynamics, spindle interface (clamping) behavior, and spindle dynamics. Although elegant mathematical solutions to this problem have been introduced [32], they are not widely adopted due to difficult setup and/or calibration. This placement of an

accelerometer bypasses the need for methods such as receptance coupling substructure analysis (RCSA) [32] and directly samples the frequency information from the source. This dissertation explores a different approach where the sensors are embedded into the cutting tools themselves. Figures 2.2 and 2.3 show an accelerometer integrated concept (Prototype 2). Appendix A documents the full development and calibration of the electret accelerometer technology. While promising for certain applications, as explained in Appendix A, the sensors described in the rest of this chapter were deemed more appropriate for the specific research goals of this dissertation.

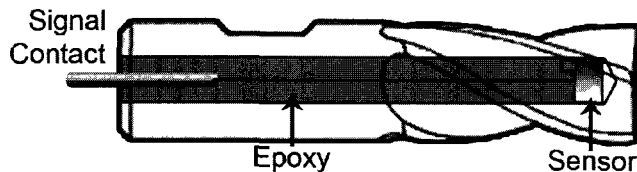


*Figure 2.2: Desired Placement of Tool Tip Accelerometer*

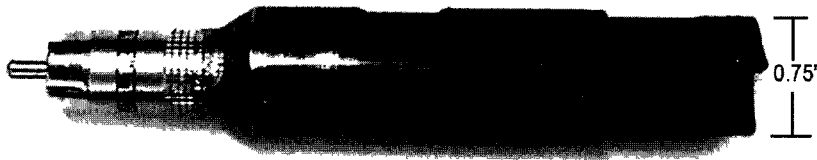


*Figure 2.3: Accelerometer Integrated Indexable End Mill*

### **2.2.1 Feasibility of Wireless Sampling for the Electret Accelerometer**

The next step towards developing an end milling condition monitoring system involves installing these sensors within the tool holder. Given that the electret was shown to provide a repeatable and mappable signal (see Appendix A), it was the first sensor to be explored with a wireless interface. These sensors will directly record the tool response without the need for signal transfer through the spindle or workpiece. The sensors are embedded into the tool holder in close proximity to the cutting tool, and thus requires a

means of data transmission that does not rely on a physical connection to the sensor.

Although a wireless data transmission method solves the physical problems involved with the integration of a sensor within the tool holder, the end milling environment presents additional challenges from the perspective of electromagnetic interference. Electric motors operate the machine spindle as well as the x, y, and z translation of the bed. The proximity of these motors to the wireless transmitter presents a problem due to the wide spectrum of electromagnetic interference generated during the cutting process. Moreover, these motors do not remain at a constant speed during cutting, resulting in the interference spectrum continually changing throughout the cutting process.

An additional issue with using a wireless connection is that the bandwidth of the wireless interface must be able to capture a large frequency range from the electret accelerometer. As previously mentioned, the end milling system produces a wide spectrum of useful information and it must be captured with substantial resolution for analysis purposes.

Upon investigation of existing commercial methods of wireless data transmission, it becomes evident that the majority of existing commercial methods have significant drawbacks relating to the challenges expressed above. For instance, an FM or AM interface is immediately eliminated by the expected high level of radio frequency noise. Other methods such as the 802.XX standards require a substantial power source and are not commercially offered in a form that is small enough to practically position within a typical end milling tool holder.

Although most existing wireless protocols are not ideal, the Bluetooth protocol was

found to answer the demands of tool holder placement, bandwidth, and motor interference. The Bluetooth wireless standard has been designed for implementation in devices such as wireless headsets, cellular telephones, and data transmission over Personal Area Networks. As a result, Bluetooth transmitters and receivers have been designed with physical size as a primary constraint, often being smaller than several centimeters in size. Since Bluetooth was developed for data transmission, the 2.0 version of the protocol reaches transmission rates of 2.1 Mbps, which is sufficient bandwidth to capture high resolution end milling data. Additionally, the upcoming version 3.0 is anticipated to reach transmission rates of 480Mbps. Manufacturers identify transmission range between 10 to 30 meters depending on interference, which is adequate for transmission out of the end mill (~2 meters).

The Bluetooth standard was developed using spread-spectrum techniques [11] considering that the devices would be used in environments with a high level of electromagnetic interference across a broad spectrum. The standard uses the license-free ISM band at 2.4-2.4835 Ghz and is divided into 79 channels. These channels can be changed at up to 1600 times per second to actively avoid interference. As a result, the quality and continuity of transmission is high, even in noisy radio environments.

The wireless response testing performed in this work was conducted on a shaker table with an electromagnetic motor. The field generated by this motor swept the test spectrum and did not appear to cause interruption of the Bluetooth transmitter.

### **2.2.2 Bluetooth and the Electret Accelerometer**

Similar to the electret characterization work described in Appendix A, the Bluetooth

accelerometer interface was assessed by contrasting its frequency response with that of the piezoelectric accelerometer sampled through a traditional DAQ system. Figure 2.4 details the shaker table and attached sensors.

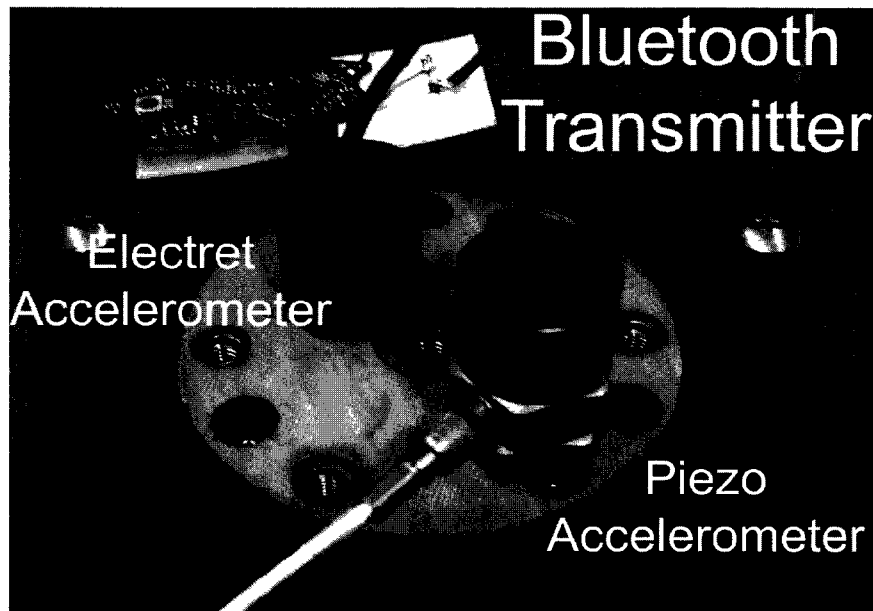


*Figure 2.4: Bluetooth Test Interface*

A sinusoidal vibration input is generated using a shaker table. A single-axis PCB piezoelectric accelerometer (Model 320 C33, serial number 5901) is fixed to the table at the same reference point as the electret sensor. The output sensitivity of this piezoelectric accelerometer is 100mV/g with a maximum range of 50g's. This piezoelectric accelerometer is amplified through a PCB charge amplifier. The corresponding voltage signal is monitored through a traditional DAQ system. The electret sensor is sampled by the Bluetooth transmitter and sent as a 16 bit digital signal to the PC's Bluetooth wireless receiver. Both the piezoelectric accelerometer and the Bluetooth electret accelerometer signals are sampled at 20 kHz. Figure 2.5 shows the response curves for the electret accelerometer sampled via the Bluetooth interface and the baseline piezoelectric

accelerometer.

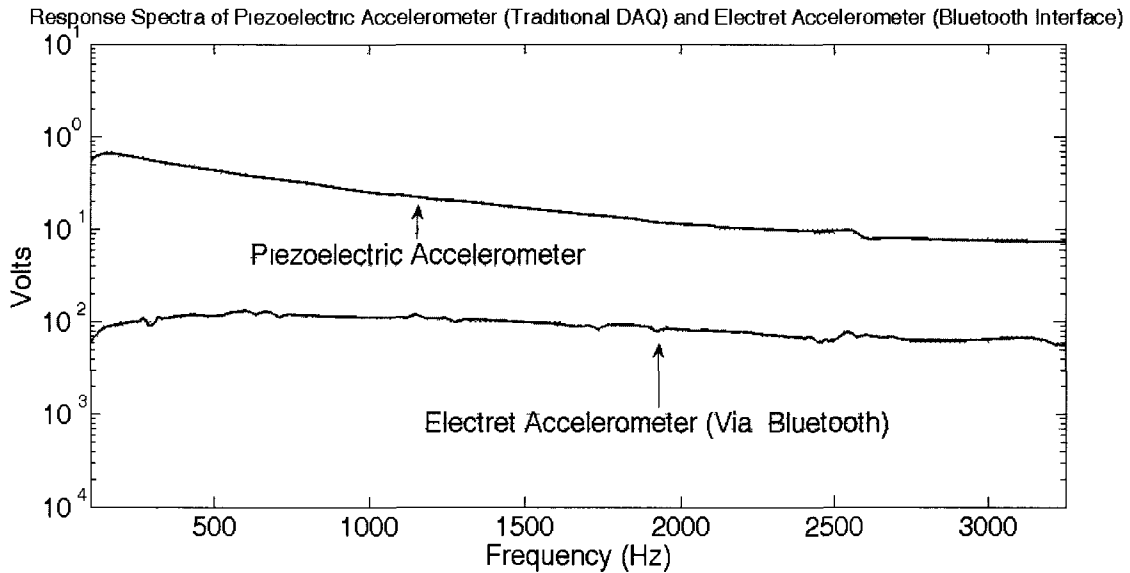


*Figure 2.5: Response Spectra for Piezoelectric and Wireless Electret Accelerometers*

This calibration procedure is described in detail in Appendix A. The Bluetooth wireless interface produced a stable response between 100 and 3500 Hz.

The results observed from the testing of the Bluetooth Wireless interface are promising and identify that the method is acceptable for transmitting high bandwidth acceleration data from the electret sensor. Due to the acceptable bandwidth, it is feasible to use the Bluetooth interface for application in a smart tool holder.

### **2.2.3 Electret Accelerometer Prototypes**

Two prototypes were designed, built and tested based on the electret accelerometer described in Appendix A. Prototype 1 consists of a 76.2 mm (3") OD four insert facemilling tool holder. This platform was chosen for a first prototype since it provides sufficient room for sensor and transmitter placement without interfering with the cutting process. Figure 2.6 details the location of the tool holder within the mill. Placement of the

electret sensor is within 8 millimeters of the tool-workpiece interface. The sensor system has been integrated in a fatigue notch located behind/below the insert set bolt so that it does not impact the structural integrity of the tool holder. As a result, only a slight modification is required for sensor embedding.

Placement of a sensor behind each insert cutter provides input from each individual tooth as it enters and exits the workpiece. Recalling that the sensors used in this device are linear impedance changing, the sensors are wired in series. Because the sensors are wired in series, the sensor system will be more sensitive to vibrations in the tangential direction (see figure 2.7) and should be relatively insensitive to vibrations in the X and Y direction. Specifically, the transistors inside the electret accelerometers are operating in the linear region and increase and decrease their resistance according to the voltage applied by the electret element. Since the configuration is in series, if an acceleration is applied in the XY plane, one accelerometer will increase resistance while the other will decrease by the same amount. This behavior negates inputs in the XY plane while enhancing tangential accelerations that cause all four accelerometers to change resistance in the same way. The only acceleration that causes all four accelerometers to respond similarly is torsional. Figures 2.6-2.8 detail the orientation and location of the accelerometers.

Placement of the transmitter circuit and sensor wiring is facilitated by a shroud designed to mount onto the tool holder body. This shroud is fabricated from ABS plastic on a rapid prototyping machine. The shroud provides wire routes for the sensors in addition to protection from chips and cutting fluid. The transmitter is powered by a



rechargeable 3.7V lithium ion battery, also mounted within the protective shroud. For a video of fabricating the smart tool holder described in this section, refer to [41].

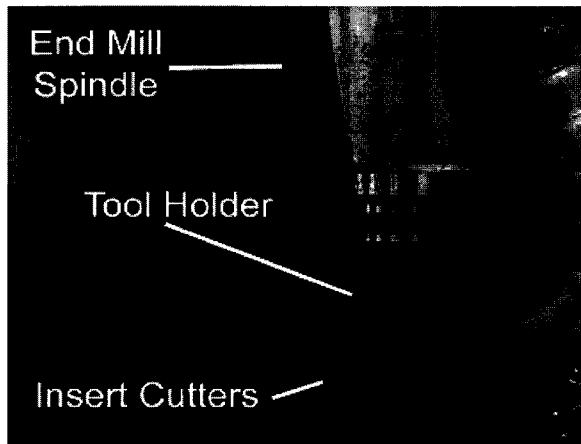


*Figure 2.6: Face Mill*

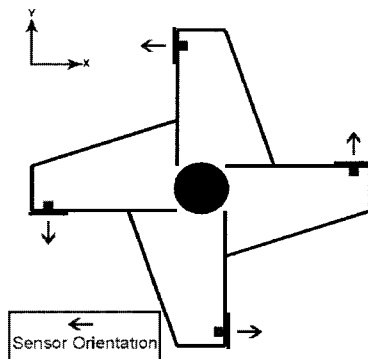


*Figure 2.7: Face Mill Accelerometer Orientation*

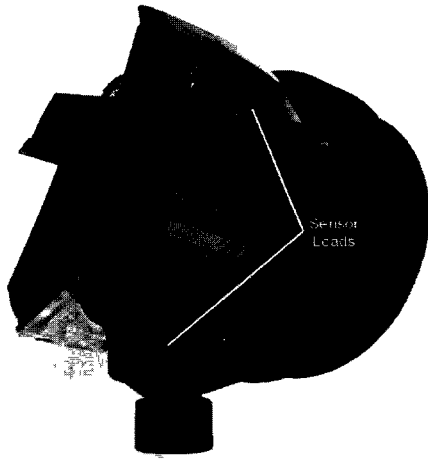


*Figure 2.8: Face Mill Accelerometer Leads*

For the electret accelerometer Prototype 2, a Sandvik 19.05 mm diameter helical two insert tool (RA390-019M19-11L Coromill 390) was selected. A helical insert tool was chosen since it is possible to embed the sensor and reuse the sensor integrated tool indefinitely, replacing failed inserts. The tool was modified with a 6mm axial hole for sensor placement and the sensor was embedded 5mm from the carbide cutting inserts. As shown in Figures 2.2 and 2.3, the sensor is oriented in the axial direction. The sensor is now oriented so that the cutting forces (in the XY plane) are perpendicular to the orientation of the sensor. Figure 2.3 presents a photograph of the sensor integrated tool with carbide cutters and sensor signal contact. An RCA type terminal contact was selected because it is axisymmetric and can easily mate with a counterpart terminal located in the tool holder. Figure 2.9 is representative of the second electret prototype tool body.

Although a 19.05 mm (0.75") insert tool was selected for this study, this design can

accommodate any sensor integrated tool with a 19.05 mm shank. Designing the tool and tool holder as complimentary devices provides a system that is more resource-efficient and scalable. The ability to reconfigure the tool holder with any variety of sensor integrated tools increases convenience for both research and potential production purposes.

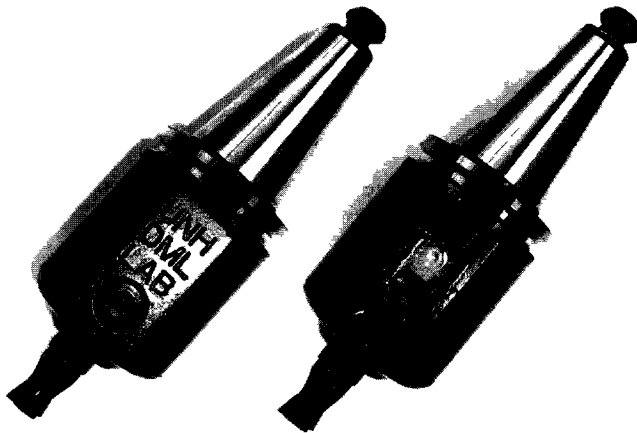


*Figure 2.9: Electret Sensor Prototype 2 Fixtured in Tool Holder*

### **2.3 Validating Bandwidth from Electret Accelerometer Prototypes**

It is important to understand the bandwidth and response of the Bluetooth Headset protocol used to transmit from the electret accelerometers. The first step in this process is evaluation of the sensor and transmitter from a shaker testbed. By doing so, the wireless transmitter system is compared to a known sensor on a wired system and conventional analog to digital converter.

Two points are important in this test; First, the sensor/transmitter system should have a relatively flat response, as to not skew the magnitudes or cause poor coherence at frequencies of interest. The second is to evaluate frequency accuracy of the measurements, to determine the system's frequency resolution and correctness. Similar to

the shaker testing of the wired electret accelerometer described in Appendix A, the wireless transmitter is used as the interface during a set of frequency response tests. The results of these tests show that the transmitter correctly relays the sensor signal. This response can be compared to the wired electret corrected response in Appendix A. Figure 2.10 shows the results of the wireless transmitter tests.

An interesting observation is a reduced frequency bandwidth in the wireless transmission, due to an anti-aliasing filter before the ADC on the Bluetooth unit.

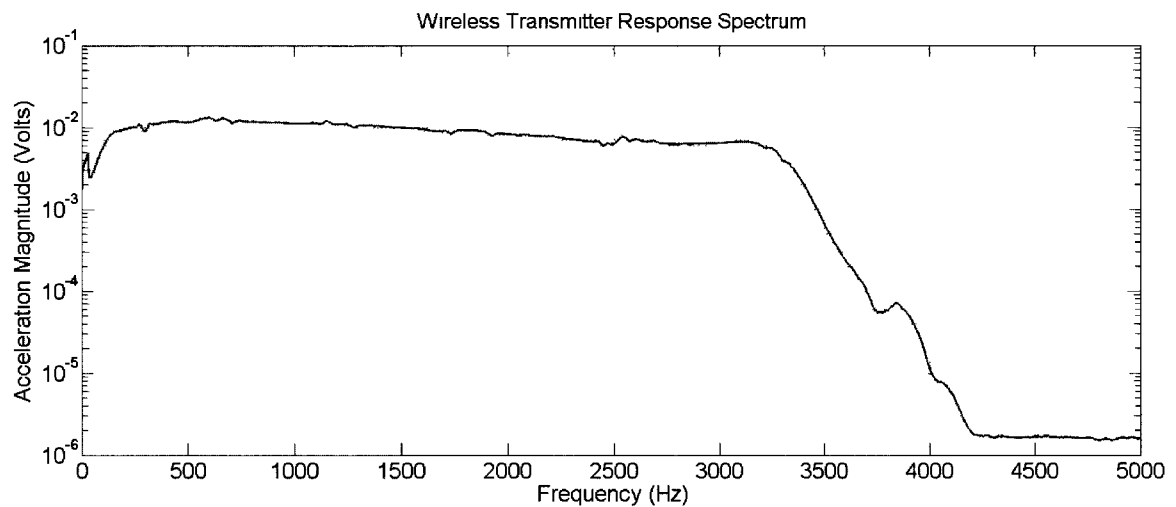


*Figure 2.10: Electret Accelerometer/Wireless Transmitter Frequency Response*

Appendix A discusses calibration and response of the electret sensor in detail. The electret accelerometer is a new sensor and it is important to understand that the frequencies measured are correct, and not artifacts, of the measurement system. Frequency accuracy is evaluated most easily from cutting data bench marked against a bed dynamometer. Since the cutting signal is interrupted, there are harmonics that extend throughout the frequency domain from the tooth passing frequency. This gives multiple points of comparison between the known sensor and the electret accelerometer system. A merit to this approach is that the frequency accuracy is determined using the actual signal

source (cutting). It would be time consuming to test multiple discrete frequencies using a shaker table. Furthermore, the shaker table cannot produce an interrupted or non sinusoidal input which is an important difference in the frequency content of the shaker input as opposed to a cutting acceleration signal.

One drawback to comparing the smart tool to the bed dynamometer is the bandwidth of the bed dynamometer is limited by ringing at frequencies close to the resonant frequency of the dynamometer. The resonant frequency of the dynamometer can be between 700-1000Hz depending on the mass of the workpiece. However, low frequencies such as tooth passing and subsequent harmonics can be observed with good precision.

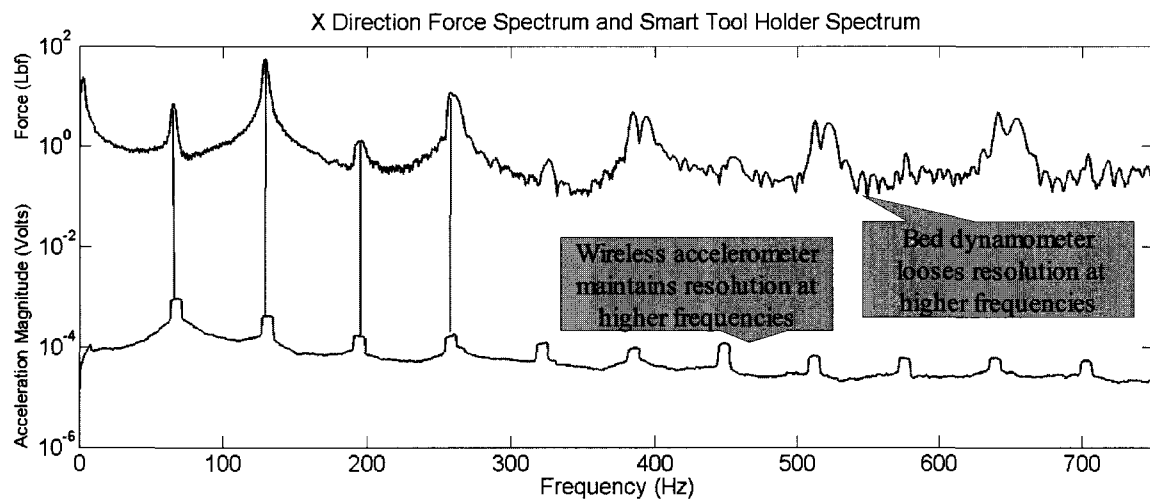


Figure 2.11: Electret Accelerometer Frequency Accuracy

In Figure 2.11, it is shown that the frequency content of the electret accelerometer system is aligned well with the force dynamometer. It is notable that there is little ringing on the acceleration signal, whereas the dynamometer frequency content becomes more affected with increasing frequency.

Although the location of the harmonics is correct, the magnitude variations are different than shown on the force dynamometer. Also, it can be seen that the precision of

the frequencies is slightly less on the acceleration system (i.e. peak width). It is believed that the precision is an artifact of clock jitter on the transceiver device, but cannot be verified because the transceiver for these electret accelerometer prototypes is a commercially available Bluetooth headset module. The bluetooth module does not have a crystal.

As shown, the magnitude information was not consistent, but the frequency content has a higher bandwidth and similar accuracy to the force dynamometer. Thus, frequency based analysis using the electret accelerometer shows promise.

## **2.4 Wire Strain Gauges**

Force measurement is also desirable for determining the force magnitude, hence tool deflection, at specific frequencies. Prototype 3 uses wire strain gages to estimate force. The wire strain gauge is a well understood technology and does not require extensive testing to verify repeatable linear response characteristics. The wired strain gauge has a number of technical challenges associated with installation on a tool holder body. Unlike the tool tip accelerometer shown in Figures 2.2 and 2.3, the wired strain gauge must reside on the surface of the metal holder body, furthest away from the neutral axis of the tool holder body. The neutral axis of the tool is shown in Figure 2.12 below with the  $C_L$  notation. Wire strain gauges have a typical gauge factor of between 2 and 3.

The bridge circuit is located on the outer radius of the end mill cutting tool. This tool, Prototype 3, is used in chatter build up tests shown in Chapter 3. An indexable insert cutter, ISCAR HELI2000, was chosen. The HELI2000 is very similar to the Sandvik tool modified with the electret accelerometer. This cutter represents a 'worst case' scenario for

the measurement of strain. It is a short overhang tool with a 19.05 mm shank. However, it was estimated that wire gauges would provide sufficient sensitivity for a torsion measuring bridge. The relationship for sensitivity can be given as:

$$\frac{V_o}{V} = \frac{\eta T D_o}{2 I_o E} \quad (2.1)$$

where  $V_o$  is the bridge output voltage,  $V$  is the excitation voltage,  $\eta$  is the gauge factor,  $E$  is the material modulus,  $D_o$  is the tool diameter,  $I_o$  is the area moment of inertia, and  $T$  is the applied torque. At a 3 volt excitation voltage, the sensitivity is expected to be approximately  $4.3 \cdot 10^{-5}$  V/(N\*m). With a 100x amplifier gain and a 10x software gain, the recorded voltage will reach  $\pm 1$  volt when 23.2 N\*m is applied to the tool. Figure 2.12 shows the location of the wire gauges.

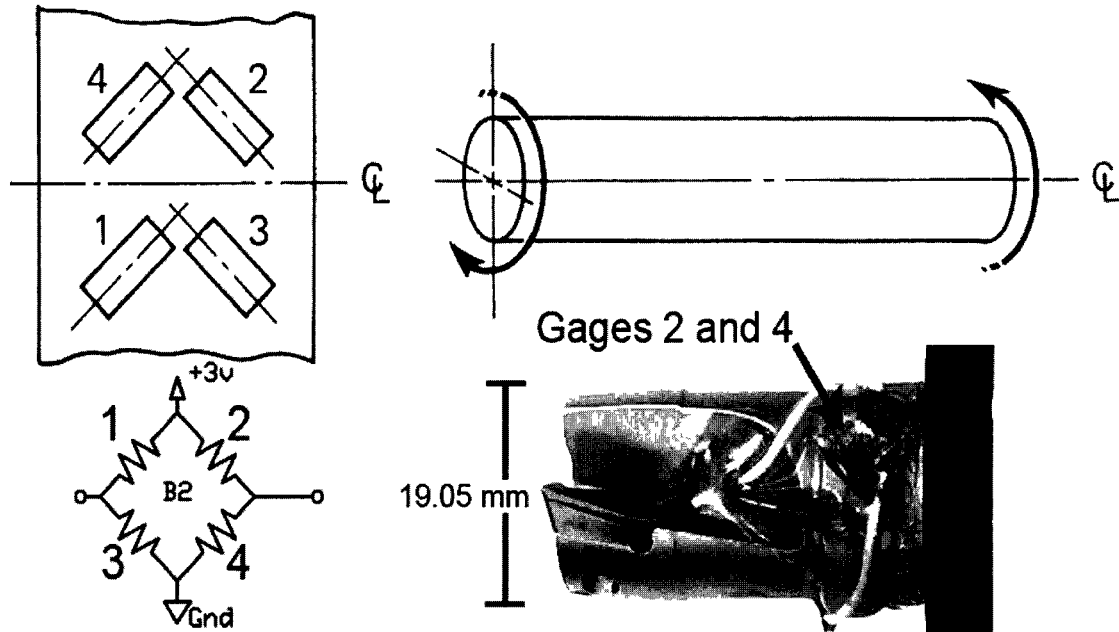
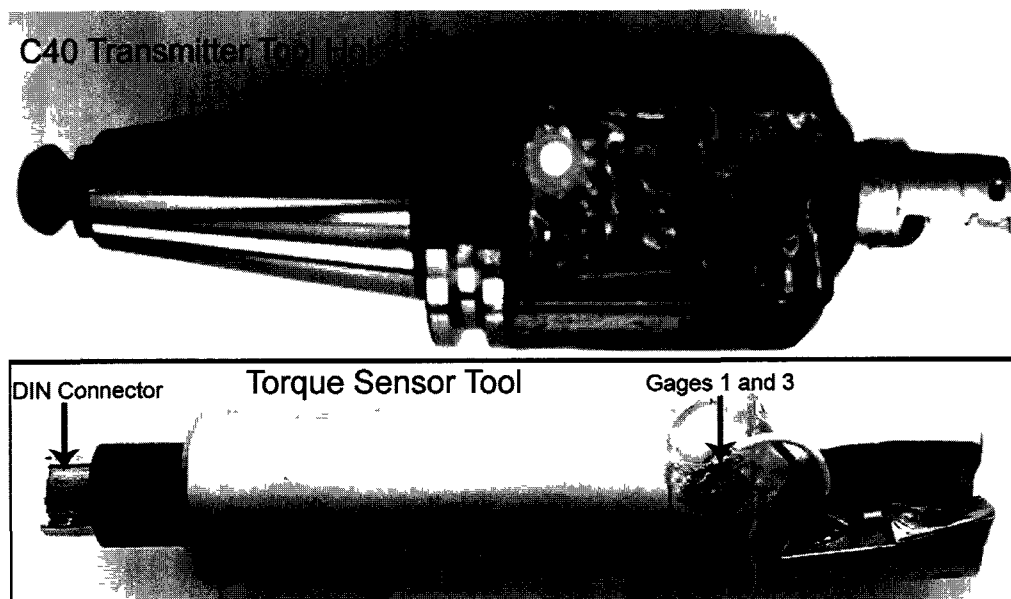


Figure 2.12: Wire Strain Gage Installation and Orientation, Prototype 3

The tool used is a through-coolant design. The coolant channel provided a convenient route for the sensor signal wires without interrupting the cutting process or altering the

physical geometry of the tool holder. Figure 2.13 details the position of the mini DIN connector and strain gauge rosettes. Because of the prototype nature of this tool, the gauges and signal wires were protected by epoxy and not fully encased by a protective cover. The wire torque gauge is linear and can be understood by applying a static moment of different known values. The torque sensor is a full bridge shear arrangement to minimize temperature and shaft bending effects. The torque resolution is 16 bits sampled at 10 kHz. Figure 2.14 shows the calibration points of the torque sensor and linear data regression. The tool holder was calibrated with a constant torque wrench with a selectable torque limit. The error of the torque wrench is unknown, e.g. cross talk from bending, however it is assumed that the torque wrench calibration is sufficient for demonstrating that the tool had a linear relationship between applied torque and output.



*Figure 2.13: Torque Sensor Integrated Tool and Transmitter, Prototype 3*



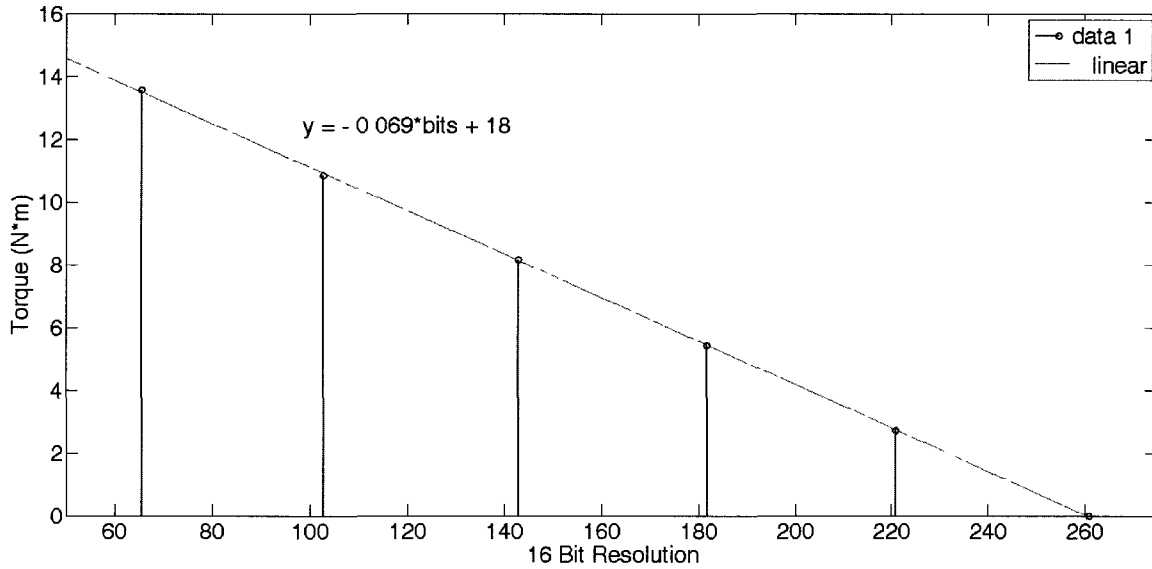


*Figure 2.14: Wired Strain Gauge Calibration Curve*

Following a similar design scheme to the vibration sensor-integrated tooling systems described in [26], this high bandwidth stereo transmitter includes a printed circuit amplifier board, symmetric geometry for low eccentricity, and reduced wire routing for an improved signal to noise ratio. Prototype 3 is also waterproof for experimental testing with cutting fluid. Figure 2.13 shows a profile of the transmitter tool holder design featuring the amplifier circuit face.

#### **2.4.1 Signal Conditioning for the Wired Strain Gage**

The signal conditioning system is designed to support sensor integrated tooling on a 3 volt supply. The tooling interface is made through a 6 contact male mini DIN connector on the top of the tooling unit. A counterpart mini DIN connector is located inside of the tool holder. Analog Devices 623 instrumentation amplifier chips were selected as gain multipliers. The gain was set to 100 to increase the signal from low level sensor output to the  $\pm 1$  volt range required by the Bluetooth transmitter.

Since this sensor system is designed to observe a dynamic process, capacitors were

included in series with the sensor signal leads to create a high pass filter that eliminates the low frequency components and DC under a corner of 10 Hz. The capacitors eliminate any temperature effects in the lead wires as well as reducing the power consumption of the sensors.

To power both the signal conditioning system and the Bluetooth transmitter, current is supplied from a 3.7 volt lithium ion battery. The voltage to the signal conditioning circuit is regulated by an AN77L03 3 volt regulator. This component is critical to prevent gain drift in the amplifier circuit as the battery discharges. The battery power supply and charging circuit are located on the A2DP Bluetooth transmitter. Figure 2.15 details the signal conditioning circuit (located in the tool holder) and strain gauge bridges located (on the sensor integrated tool). The sensor integrated tooling designed to work with this amplifier-transmitter tool holder is not limited to strain bridge circuits. However, to test this prototype, a torque bridge was constructed.

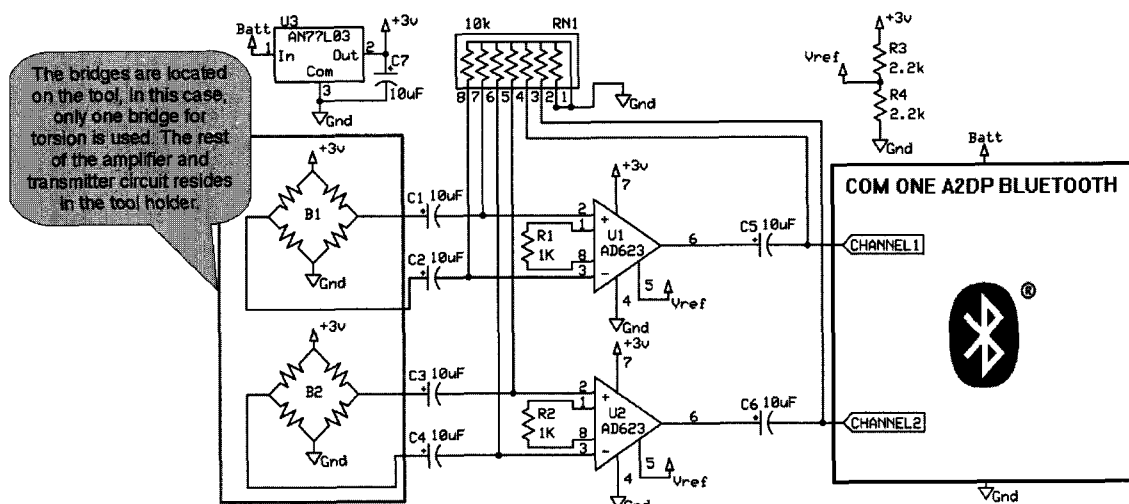


Figure 2.15: Dual Strain Bridge and Amplifier Circuit

The frequency response of the AD623 instrumentation amplifier is affected by

varying the gain resistor load. With a gain resistor of 1 k $\Omega$ , the specified frequency response of this amplifier is 0 to approximately 10 kHz. Although the specified amplifier response is to 10 kHz, the observed response attenuates at approximately 17 kHz. With a frequency response of 0 to 10 kHz, this amplifier circuit is sufficient for conditioning signals of all end milling phenomenon. At 10 kHz, observation of the milling tooth passing frequency is possible up to a theoretical 300,000 RPM with a two flute tool.

#### **2.4.2 Bluetooth and The Wired Strain Gage**

As with the electret accelerometer, the data must be broadcast from the tool to a receiving location outside of the cutting process. This is again done with a Bluetooth transmitter, but a different type of transmitter is evaluated. The transmitter circuit is modified from a Com One A2DP stereo audio transmitter (retail cost approximately \$40). This transmitter contains the necessary transceiver hardware and A/D circuit to transmit stereo voltage signals of  $\pm 1$  volt. The A2DP transmitter conforms to the published specifications in [11] and is capable of sending a stereo audio signal to the Bluetooth receiver at 48.0 kHz. The analog signal conditioning circuit on this particular transmitter has a high frequency roll-off with a corner frequency of 20 kHz. This is observed in preliminary testing of the device and exists to prevent aliasing in the A/D. Tests are conducted on the device to verify expected specifications. The effective frequency bandwidth of this transmitter is approximately 10 Hz to 20 kHz. Figure 2.16 details the frequency response of the transmitting unit. The frequency response is shown as a transfer function between the input and transmitter responses. The input to generate this transfer function is a sine chirp from 0 to 20 kHz of input voltage conducted over a one

minute interval. This bandwidth is sufficient for observing high speed milling phenomena. For high clarity in common machining frequencies, the 0 to 2000 Hz band of the response has been characterized separately with a one minute 0 to 2 kHz chirp and is shown in Figure 2.17. Note: The response figures should not be confused with noise characteristics, which are shown separately. The response is input voltage/output voltage and should be close to a value of  $\sim 1$ . Note that low frequency error is associated with data compression present in the A2DC standard. For this reason later prototypes (Prototype 4) used loss-less data transmission over a serial data link. The noise response is shown in a separate figure as a spectrum of the output data with no signal.

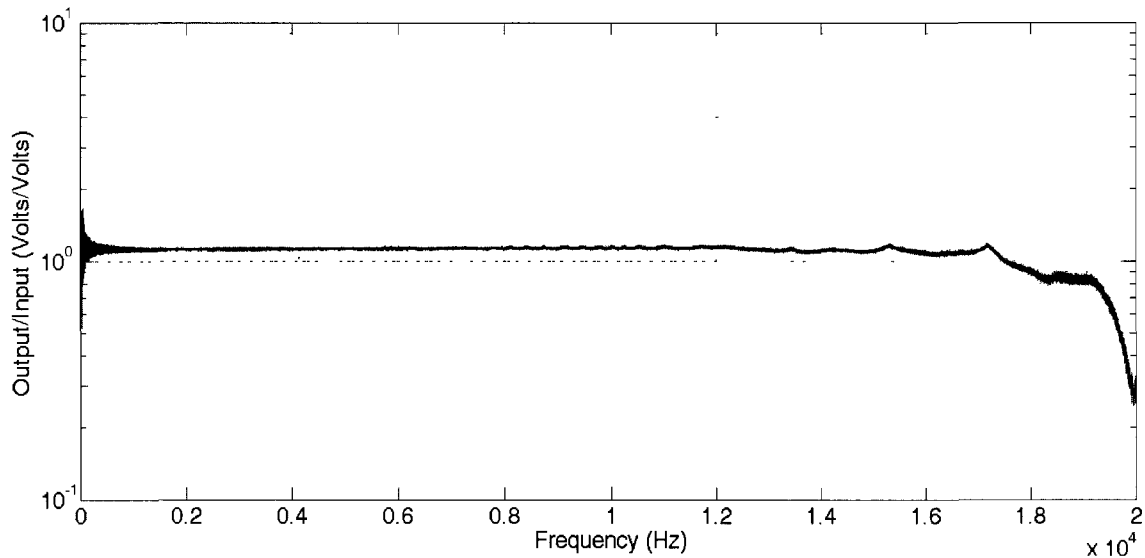


*Figure 2.16: A2DP Transmitter Response Transfer Function (transmitter voltage input / receiver voltage output) 0 to 20 kHz*

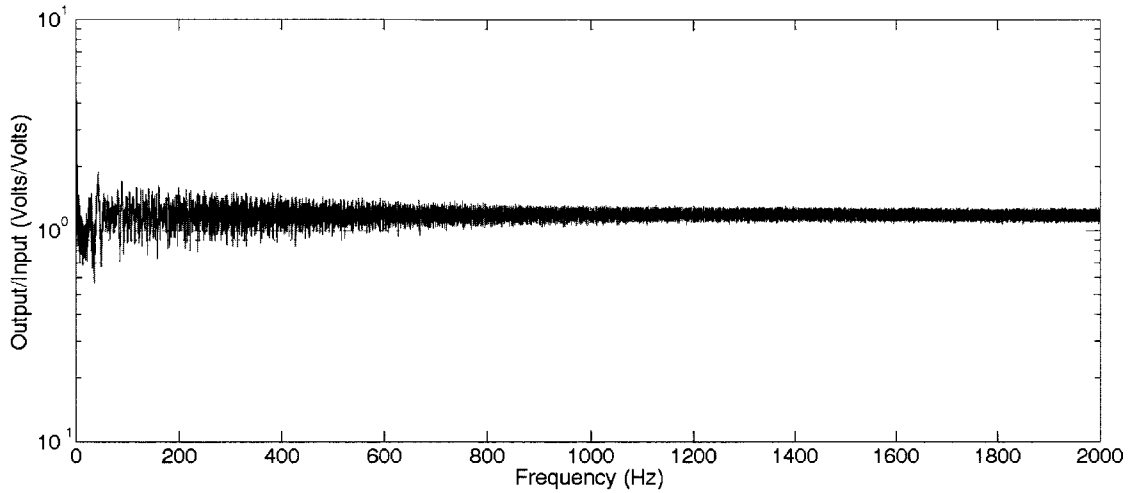


*Figure 2.17: A2DP Transmitter Response Transfer Function (transmitter voltage input / receiver voltage output) 0 to 2 kHz*

The noise floor of the A2DP transmitter is also evaluated to understand the lower limits of transmission resolution and the input amplitudes required for sending high quality data signals through the system. Figure 2.18 shows the noise response spectrum of the transmitter. The noise introduced by the transmitter is found to be negligible and is on the order of  $10^{-7}$  volts.

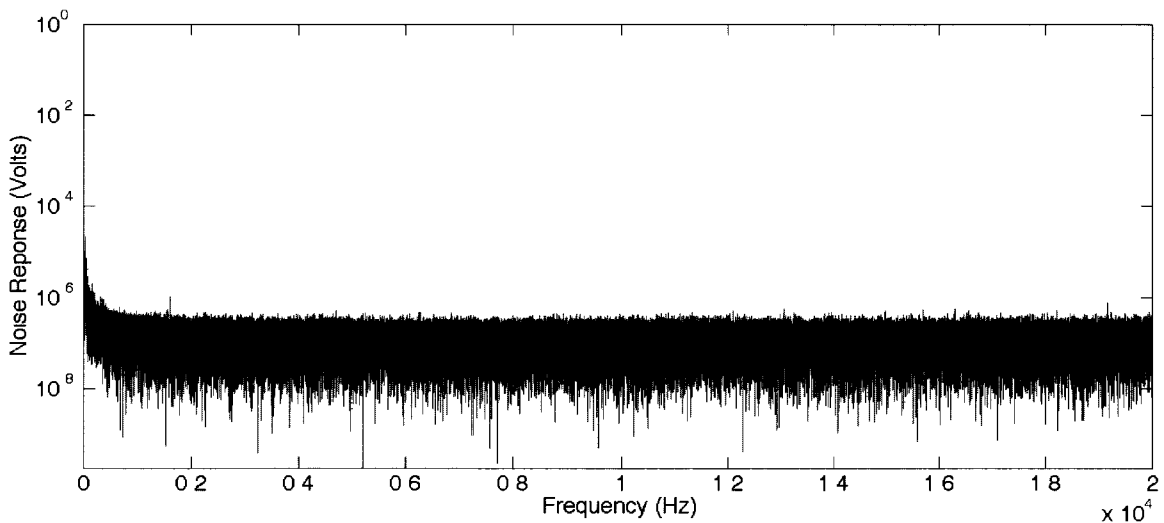


*Figure 2.18: A2DP Transmitter Noise Response*

### **2.5 Tool Torque Measurement with an AC Coupled Wire Strain Gage**

Experiments were conducted with AC coupling a wire strain gauge system. Although the slope of the DC calibration from the wired gauge tool still applies, the intercept value of the calibration curve is changed and centers around zero.

To estimate the integrity of the torque signal acquired by the AC coupled sensor integrated tooling, the signal shape can be compared to the output of an analytical cutting force model discussed in [20]. Although contrasting the experimental torque to the output from an “ideal” model does not provide magnitude information, the signal shape of the experimental signal agrees well with the model signal characteristics. Figures 2.19 and 2.20 show both the model and experimental torque plots.

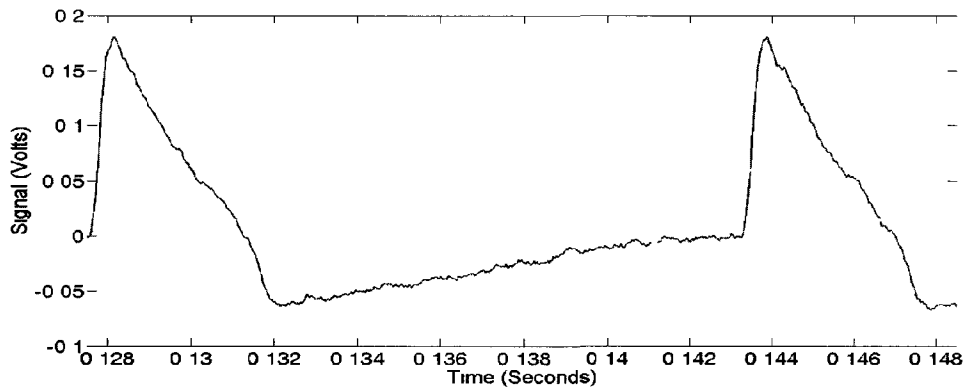


*Figure 2.19: AC Coupled Wire Torque Gage Experimental Plot*

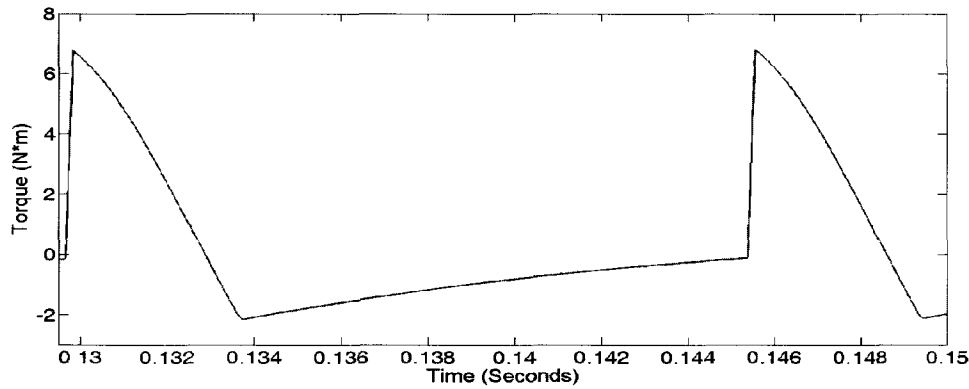


*Figure 2.20: AC Coupled Torque Plot from Ideal Force Model*

The cutting parameters for this test are down milling, 3/4" cutter diameter, 1/8 inch axial engagement, 0.375" radial engagement, tooth passing speed of 3819 RPM, with an average chip thickness of 0.004" in 6061 Aluminum. The cutting force model used to help generate the simulated results is a validated mechanistic model detailed in [20].

It may be noted that the experimental and model plots have 'negative' torque values. Recalling that the amplifier and transmitter circuitry is designed to pass a dynamic signal, the DC value is attenuated and high pass information remains. The same effect is recreated in the model output by passing a 4th order high pass Butterworth filter over the simulated torque data. As with the experimental signal, the model FIR filter was given a corner frequency of 10 Hz. In this way, the dynamic torque signal is found to be nearly identical in all features (with the exception of magnitude) to the simulated data set.

To further evaluate the transmitter, tests are conducted with parameters similar to the model validation experiment. However, these tests were conducted with a bed mount dynamometer. Using the torque sensor integrated tool, a measured comparison can be made between the output of the transmitter and the force output of the bed dynamometer sampled at 20 kHz. Although the bed dynamometer does not provide a direct

measurement of torque, the force in X or Y directions can be used to calculate the moment supplied by the tool. This is done in a half-immersion cut where the tool completely exits the material and reengages the material with the cutting edge tangent in the X direction. The moment is then estimated by knowing the impact force in the X direction at the tool radius of 0.009525 m (0.375"). The impact torque from the integrated sensor system is measured as a voltage signal. By a ratio of this peak voltage signal to the peak estimated torque, the voltage signal can be scaled. Figure 2.21 shows the voltage signal from the sensor integrated tool after being scaled by this technique. This suggests that output from the wireless tool holder is reasonable and useful for observing the magnitude of dynamic torque. This agreement also supports the effectiveness of the bed dynamometer sensitivity analysis for approximating torque supplied by the tool.

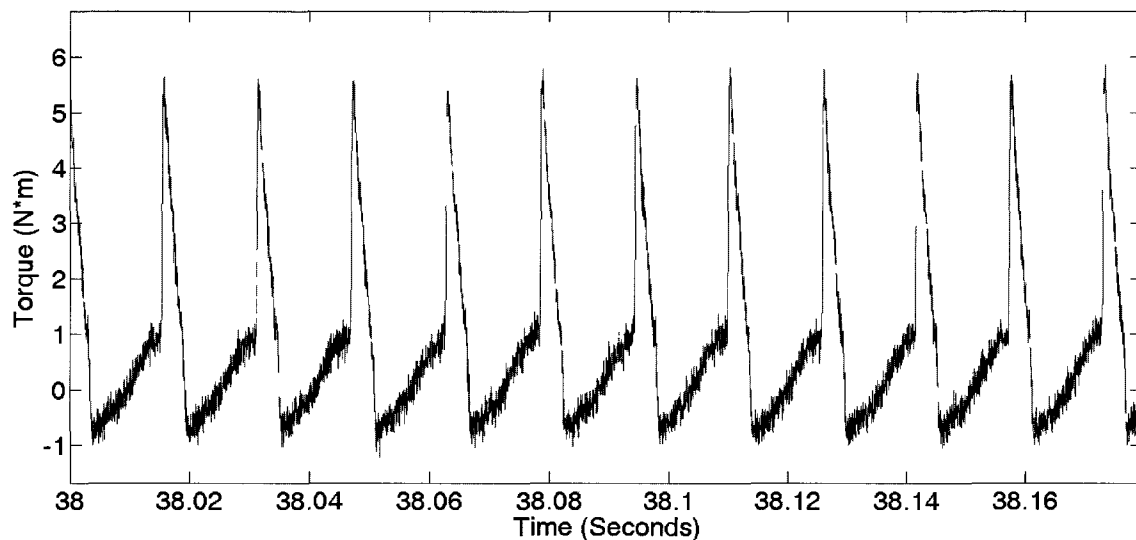


*Figure 2.21: Calibrated AC Coupled Wire Torque Gage Cutting Test*

Furthermore, a comparison can be made between the resolved XY bed force and the torque. This contrast confirms that the duration of engagement with the workpiece is correctly determined by the torque signal. Figure 2.22 illustrates the resolved bed force



and dynamic torque. Since the natural frequency of the bed dynamometer is approximately 1000 Hz, frequency content above 400 Hz has been attenuated in the signals shown in Figure 2.22.

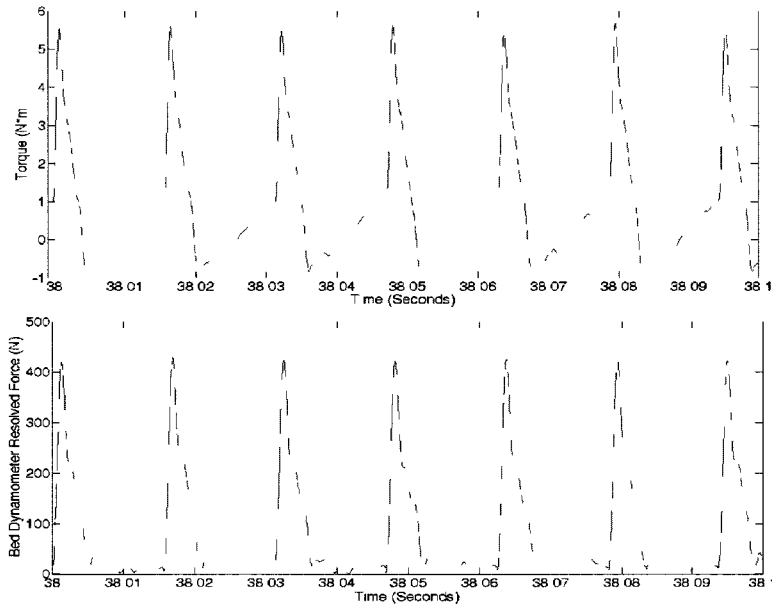


*Figure 2.22: AC Coupled Torque (top) compared to Resolved Bed Force(bottom)*

In addition to collecting force values from the bed dynamometer, spindle power data was also collected at 20 kHz. Figure 2.23 shows output from both the wireless torque sensor and the spindle load cell.

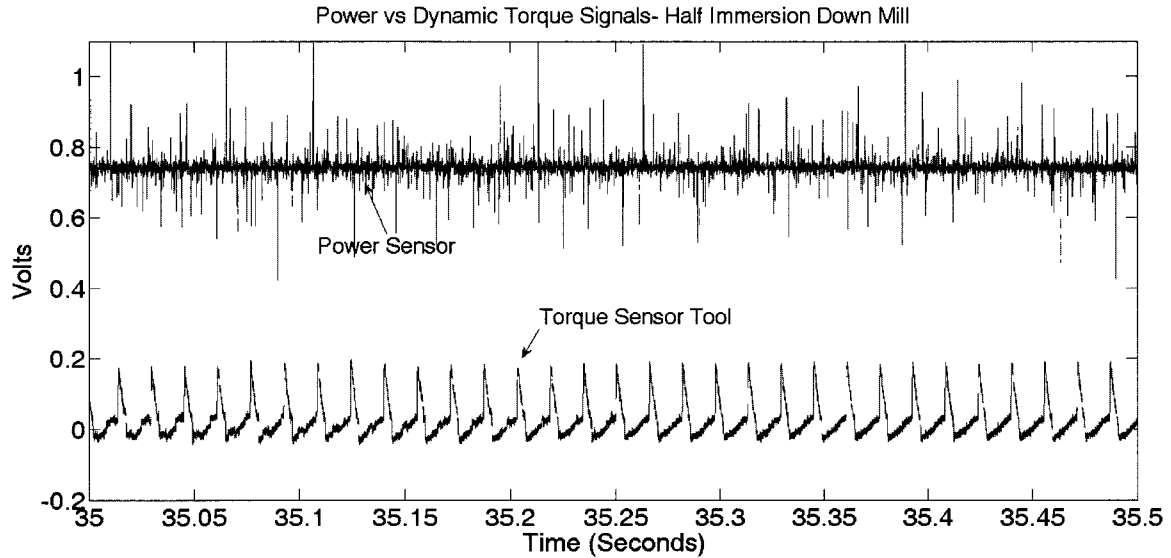


*Figure 2.23: Spindle Power compared to AC Coupled Torque*

It is immediately obvious that the power sensor has a lower dynamic bandwidth than the wireless torque sensor tool. The power sensor was over sampled to expose the large amount of high frequency noise present in the power signal. The superiority of the wireless torque signal to the power sensor is apparent in both resolution and signal to noise ratio. However, the power sensor specializes in sampling frequency content below the 10 Hz cut off of the dynamic torque signal, specifically, the DC component.

## **2.6 Conclusions About the Wired Strain Gauge**

The methods of wireless transmission and feasibility of using the A2DP transmitter to send a signal from a sensor integrated tool was demonstrated. The results are encouraging and show that it is possible to record a torque signal with good signal to noise ratio. The Bluetooth A2DP audio profile is acceptable for transmitting end milling sensor data up to 8.5kHz. The system has shown excellent response and bandwidth capabilities to 17 kHz, which exceeds the requirements for typical end milling sensor data.

## 2.7 Semiconductor Strain Gauges

After discussions with engineers from industry, it was apparent that location of the strain gauge sensor on the tooling body was risky due to the abuse that the tools experience in the field. The presence of chip buildup and the need to use high pressure through coolant dictated the technical necessity for a relocation of the gauging. A resulting solution was to use to a semiconductor gauge technology with a gauge factor of 150 instead of the gauge factor of 2 common to wire gauges. The gauges are located on the shank of the tool holder itself, where it is protected from the cutting process. Figures 2.24 and 2.25 shows the location of semiconductor gauges on the tool holder for Prototype 4.

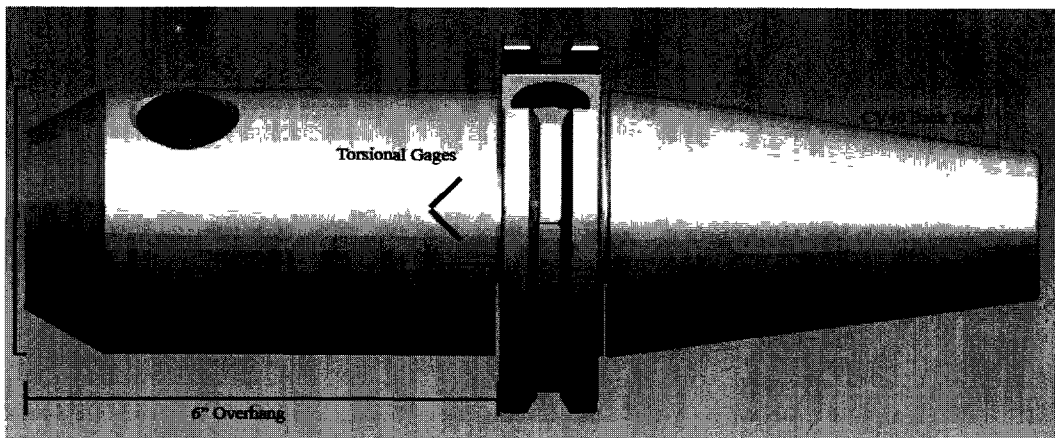


*Figure 2.24: Location of Semiconductor Gauges on Tool Holder Body, Prototype 4*

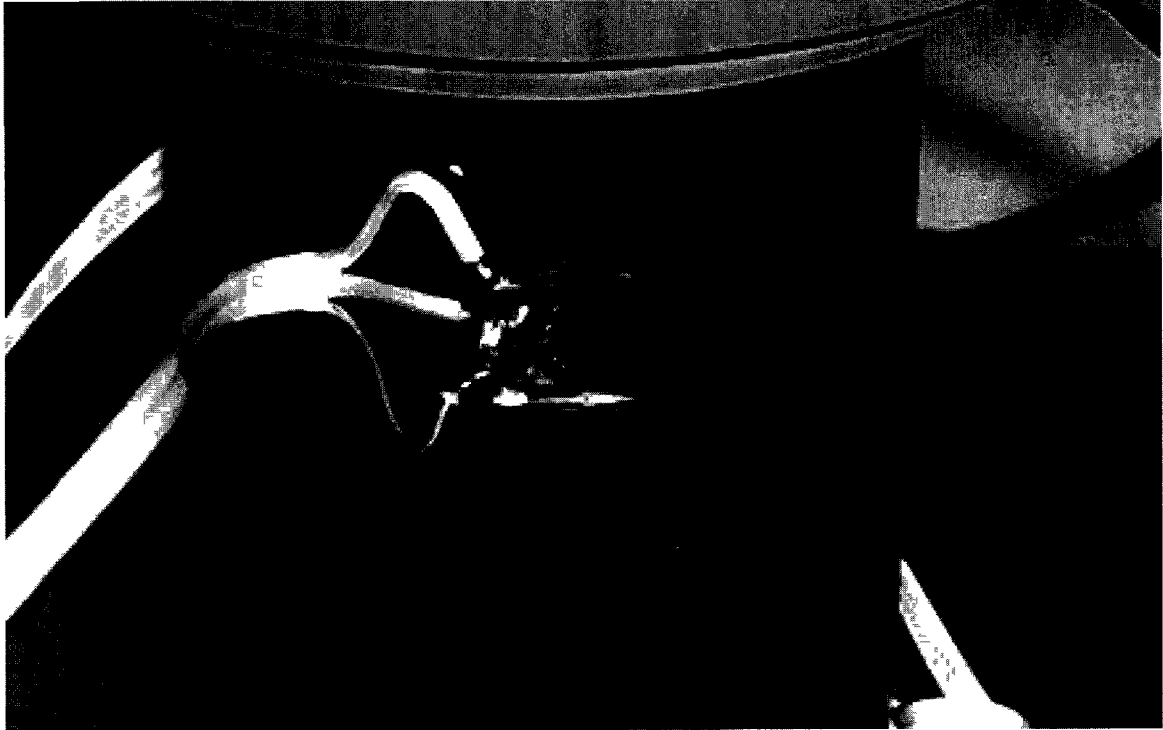


*Figure 2.25: Location of Semiconductor Gauges on Tool Holder Body, Prototype 4*

The  $V_o$  of the semiconductor gauges is calculated by the same method as the wire gauges on the tool body. The diameter and gauge factor are different, but otherwise Equation 2.1 applies. Measurement and instrumentation of the semiconductor strain gauges is similar to the methods applied to the wire gauges. A similar instrumentation amplifier and analog front end were used to AC couple the semiconductor gages. A different digital transmitter was used since the A2DP transmitter was replaced by a Bluetooth Serial transmitter implemented by Jeff Nichols, an ECE grad student [10]. The digital transmitter has no effect on the data once it has been sampled by the ADC and acts as an intermediary to the PC side.

It was discovered that the semiconductor gauges are sensitive to light and temperature. Thus, it was necessary to shield the gauge installation from light exposure,

especially in the infrared spectrum. Limited testing was done with LEDs of various wavelengths and it was found that the infrared spectrum caused the most disturbance. Light emission below 300  $\mu\text{m}$  was found to be most disturbing. The situation was easily corrected by the introduction of opaque epoxy to cover the gauge installation. Temperature drift is an issue only in an unmatched semiconductor gauge set. The installations done on the smart tools are AC coupled to mitigate this problem because it manifests at low frequencies and DC. Temperature changes are observed to occur over several seconds. Because temperature drift does not affect the linearity of the strain gages, it does not have an effect on the higher frequency data of interest. For acquiring DC information, Kyowa gauges with a temperature resistance coefficient matched to the thermal expansion coefficient of the steel substrate were evaluated, and is an area for future research beyond the scope of this thesis. A tool holder was constructed with these gauges but was not used for the dissertation work.

Since the semiconductor gauges used were AC coupled to eliminate the temperature DC resistance change, calibration was more challenging than static loading. The performance characteristics that are needed for this tool are accurate frequency content from 10Hz to 4kHz. For the purpose of chatter frequency detection, gain information and cross talk are not critical features. However, it is important to understand what information the data contains and how it manifests in the signal. Since the equipment to do AC coupled cross talk and sensitivity tests is not typical, testing methods consist of cutting experiments and a test jig fabricated to apply dynamic bending loads from a materials testing machine.

## **2.8 Approximate Calibration from Cutting Data**

A preliminary calibration effort was made by running experimental cuts on the bed dynamometer and extracting forces from the impact of the tooth in a specific axis. A 2<sup>nd</sup> order 50Hz Butterworth low pass filter was applied to the dynamometer data to attenuate ringing around the dynamometer natural frequency of 1kHz. This cutoff is valid for comparison because it is applied to both the dynamometer and smart tool data. A half immersion cut was performed so that the tooth entered fully engaged in the X direction. The impact force multiplied by the tool radius gave an approximation for the torque value. Time aligning the peaks of the smart tool data with the X direction dynamometer data allows a curve to be plotted for different feed rates (input force values).

There are several sources of error in this calibration method. First the peak force must be determined from the load cell, which has an underdamped response. Second, cross talk effects on the tool holder body are not separated from the tool holder signal. Third, alignment of the cut must be precise half-immersion so that the cutting tool impacts in a vector tangential to its rotation.

The first source of error when calibrating from cutting tests can be addressed by applying a low pass filter to both the load cell and tool holder data. The filter attenuates frequencies above the tooth passing frequency. This does an acceptable job eliminating ringing in the load cell, which is the primary cause of overshoot error when the tool impacts the workpiece. For instance, if the tooth passing frequency is 40Hz and the second order filter is set to -3dB of 50Hz, -40dB occurs before 500Hz and the ringing of the load cell can be controlled. The same filter must be applied to both the load cell and

tool holder data.

The cross talk cannot be known from the data without extensive computations and knowledge of the rotational angle of the tool from which forces and their vector can be calculated. This work has been touched on, but is beyond the scope of this dissertation.

The third source of error is the most minor, and is negligible due to the CNC movement of the bed after a cleaning cut is performed on the workpiece. A precise half-immersion cut can be performed within the tolerance of the bed movement.

To generate the calibration curve, a cut is repeated at different feed rates with a constant spindle speed. This creates different chip thickness and subsequently different forces from which a trend can be determined. Figure 2.26 shows an example of a torque versus the sensor output in bits. The force recorded on the load cell is multiplied by the cutting tool radius (in this case 0.375") to convert to a torque value.

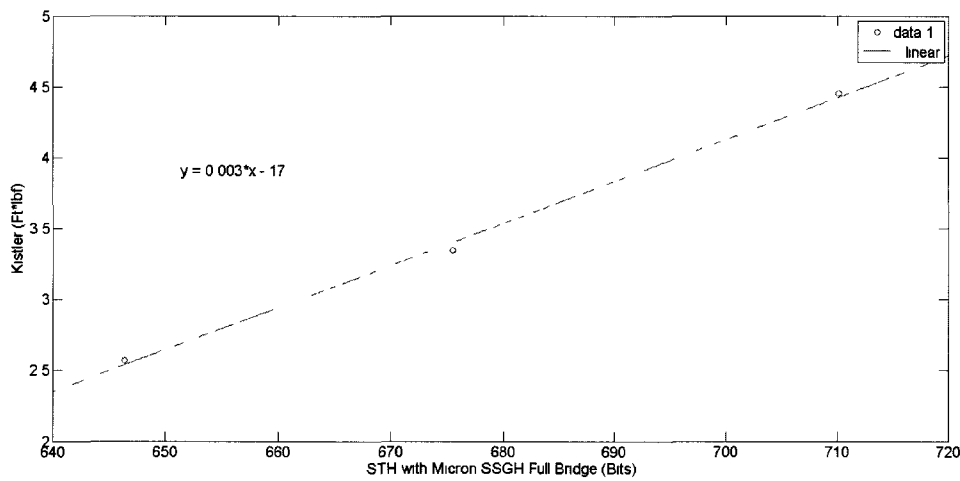


*Figure 2.26: Semiconductor Gage Peak Value Calibration (Prototype 4)*

## **2.9 Test Setup for Evaluating Bending Cross Talk**

While the results of the cutting calibration were promising, there was no evaluation of potential cross talk present in the system. This addresses the weakness in the cutting test calibration (i.e. the inability to distinguish bending cross talk from cutting data). In this application, cross talk refers to the interference of bending strain with the proper detection of torsional strain in the tool holder body.

For evaluating cross talk in the smart tool system, a special jig was constructed to mount onto a materials testing machine, see Figure 2.27. The Instron materials testing machine is capable of applying a position controlled oscillating input with a frequency up to 60 Hz.

The test jig used for these experiments consisted of a fabricated aluminum C channel with a high bending stiffness. Steel bolts were used to affix the walls of the C channel to the base. The channel was anchored onto the Instron bottom platen with a 1.25” threaded steel rod. The tool holder under test mounts into a pair of support clamps that compliment the CV40 taper geometry and render the tool in a bending configuration. Steel U bolts are used to retain the tool in the support clamps. Bending force is applied by the Instron upper platen through a load cell.



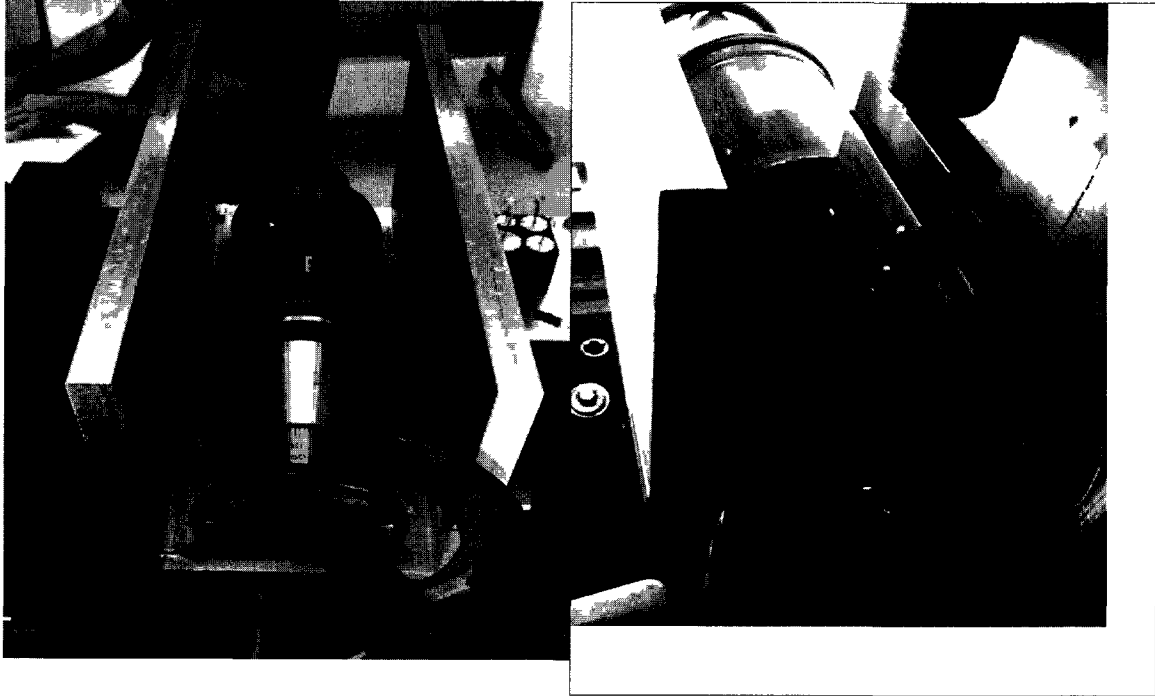


*Figure 2.27: Semiconductor Smart Tool Testing Jig*

The tool and jig are preloaded to a static force value of 100lbf, to eliminate slack in the linkages and clamping. After this preload is set, the oscillating force is applied. To obtain information on different input vectors, the tool is rotated using a reference line and 360 degree protractor attached to the retaining bolt of the smart tool. This setup was accurate within a few degrees and was sufficient for evaluating the effect of cross talk at various rotation orientations. It is important to observe these effects at different rotations in order to accurately replicate the rotating radial force experienced in cutting.

The bending cross talk is characterized by applying the curve fit from Figure 2.26 so that the influence on the torsion data can be evaluated. These tests were conducted at a peak of ~20 lbf on an Instron materials testing machine. The influence of bending on torque data is approximated by applying the gage sensitivity (V/bit) to the RMS cross talk

bits recorded for each applied bending load. This gives the equivalent bending cross talk in units of Ft\*lb. The influence of this cross talk is calculated by assuming the peak bending load was applied at the tool radius (in this case 0.375”) and dividing the cross talk torque value by the actual torque value created at the applied force.

Table 2.2: Influence of Cross Talk on Semiconductor Torque Data

Angle (Degrees)	Peak Bending Load (lbf) ~20lbf	RMS Cross Talk (Bits)	RMS Cross Talk Equivalent Ft*lb	Influence on Torque Data (0.375” radius) Ft*lb (cross talk)/ Ft*lb
0	19.8700	18.3557	0.0551	$0.0551/(19.87/\sqrt{2})*0.375/12)= 12.5\%$
20	19.8300	16.5122	0.0495	11.30%
40	20.0900	11.8388	0.0355	7.99%
60	19.8700	9.8798	0.0296	6.74%
80	20.3000	6.5299	0.0196	4.37%
100	20.7400	6.9360	0.0208	4.59%
120	20.5200	7.3297	0.0220	4.85%
140	19.7900	7.8930	0.0237	5.42%
160	20.2000	10.4044	0.0312	6.98%
180	20.3000	6.3266	0.0190	4.24%

The results indicate that significant cross talk does exist, but that does not render the data unusable for frequency analysis, particularly if the magnitude information is not essential. The objective is to acquire accurate system frequencies and not to calibrate cutting force models. For calibrating cutting force models, more precision is needed which could be obtained by creating a dynamic torsional testing jig, which is beyond the scope of this dissertation. Also, the need to AC calibrate may be obsolete by the introduction of DC capable semiconductor strain sensing.

## **2.10 Validation of Strain Gage Location Considering Tool Dynamics**

Confidence in the measurements acquired by a sensor integrated tool requires a

fundamental understanding of how the instrument responds to physical stimulus under a variety of conditions. For an AC coupled sensor integrated tool, the DC effects of temperature and adhesive creep are mitigated by a first order high pass filter realized in the analog measurement system. The remaining concerns in this AC instrument are the cross talk and frequency response of the physical system.

It is desirable to monitor torque during cutting since the torque signal is axis symmetric and can be related to instantaneous chip thickness without the need to resolve direction vectors from radial force. This reduces the sampling hardware complexity as well as computational burden. To measure torque, the sensor integrated tool obtains input from a strain gauge bridge oriented for sensitivity to torsional strain. A torsional configuration was implemented under the assumption that the torsional dynamics occur at much higher frequency than those experienced in the bending axes. However, it is necessary to confirm theoretically and with modeling techniques that the torsional dynamics can be neglected. Figure 2.24 shows the tool and location of the gages.

Mechanics of materials and vibration theory offer a useful approach to modeling the frequency response. Since the tool holder is accurately approximated as an axisymmetric cylinder, the frequency response is modeled for two degrees of freedom (DOF), for radial and torsion (rotational) deflections. The first is the torsional DOF. Computing the natural frequency of the torsional DOF is similar to computing a linear spring constant such that:

$$F = kx \text{ is analogous to } T = \kappa \phi \quad (2.1)$$

Where  $T$  is torque in N/m,  $\kappa$  is the torsional spring constant, and  $\phi$  is the angular displacement in radians. The torsion relationship for a circular cross section is

given as:

$$\frac{T}{J} = \frac{G\phi}{l} \quad (2.2)$$

For the case of the cylindrical tool holder body,  $J$  is equal to the polar moment of inertia:

$$J = \frac{\pi D^4}{32} \quad (2.3)$$

where  $D$  is the cylindrical diameter of the holder body. The length of the tool holder,  $l$ , is measured from the nose to the v-flange. From Equations 2.1 and 2.2,  $\kappa$  can be defined in terms of  $\phi$  and  $T$  as:

$$\kappa = \frac{GJ}{l} \quad (2.4)$$

Evaluating Equation 2.4 for the tested tool length of 6" (0.1524 m), cylindrical diameter of 1.75" (0.04445 m), and the shear modulus of steel 79.3 GPa,  $\kappa = 199447 \frac{N/m}{rad}$ .

In order to compute the torsional natural frequency, another analogy can be made to linear natural frequency such that:

$$\omega_n = \sqrt{\left(\frac{k}{m}\right)} \text{ is analogous to } \omega_\phi = \sqrt{\left(\frac{\kappa}{J_o}\right)} \quad (2.5)$$

where  $J_o$  is the polar mass moment of inertia. The polar mass moment of inertia is computed by:

$$J_o = c \frac{\rho l \pi D^4}{32} \quad (2.6)$$

The inertial constant  $c$  relates the bulk mass of the cylindrical holder body,  $m$ , to

the inertial mass equivalent of the system. This inertial constant ranges between 1 for a solid cylinder and <0.5 for a thin walled cylinder. The density of steel,  $\rho$ , is approximately 8100 kg/m<sup>3</sup>.

Evaluating equation 2.5 with the computed values of  $J_o = 4.73 \times 10^{-4} \text{ kg m}^2$  and

$$\kappa = 199447 \frac{\text{N/m}}{\text{rad}}, \text{ the torsional natural frequency of the system } \omega_\phi = 20532 \text{ rad/s}$$

or 3268 Hz.

These results are promising since several conservative assumptions were made including an overestimation of the density, assumption of a solid cylinder, and neglect of the chamfer between the holder body and v-flange. A solid cylinder was assumed to compute the polar mass moment of inertia since the tool is located within the holder and fills a large portion of the inner volume of the overhang. In order to confirm these hand calculations with a more accurate representation of the physical system, finite element analysis is conducted using ANSYS to predict the fundamental torsional mode of the holder body.

The Finite Element Analysis (FEA) model was configured using a solid model of a cutting tool body designed to house a future generation sensor-integrated tooling system. This cutting tool body is based on a Kennametal shrink fit geometry front-end, with very similar geometry to the assumptions made in the previous hand analysis of torsional vibration. The tapers, chamfers, and shank taper make this a more realistic representation of the actual system. FEA is the most accurate method by which to predict vibrational modes in complex elastic geometries.

Constraints for this model were a fixed boundary condition on the taper face, and axis-symmetric frictionless constraints to prevent bending deflection of the holder body. The torsional DOF was uninhibited and the model was run with a rotational displacement initial condition to simulate a torsional impulse from the cutting tool.

This analysis was conducted for both a long-overhang tool (worst case scenario, Figure 2.28) and a short overhang tool (Figure 2.29). The results were similar in magnitude (different in value) to the hand calculation, but are more accurate since the geometry is not simplified and the materials properties are correctly modeled. This model demonstrates that the long overhang tool has a torsional fundamental mode of approximately 7000 Hz and the short overhang tool is approximately 13000 Hz. These results indicate that the hand analysis was 2 to 3 times lower, as a result of the assumptions. This is likely due to the use of a point mass assumption versus a distribution of mass used in the FEA.

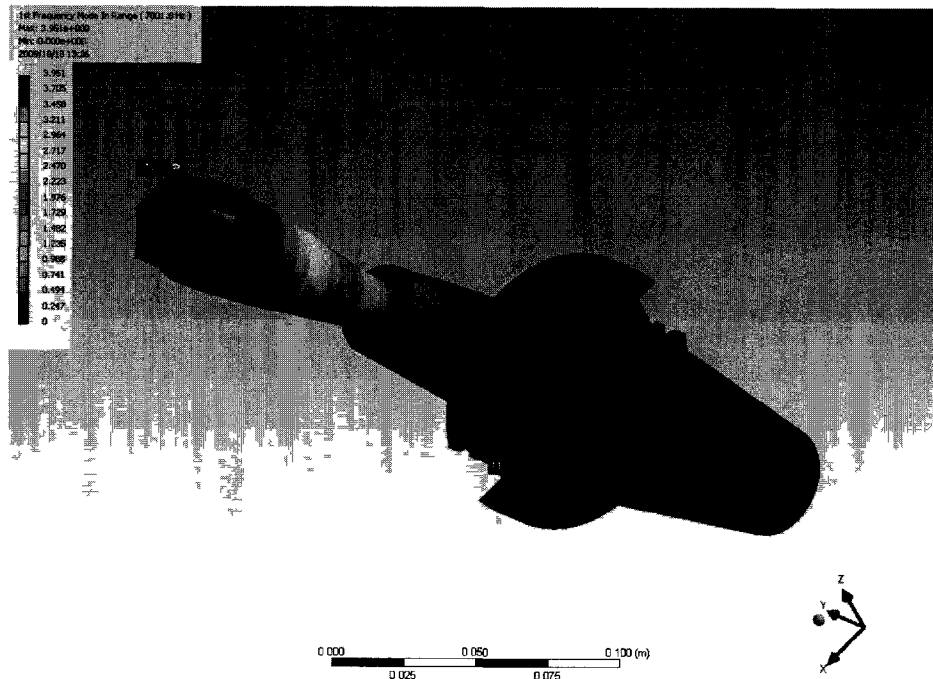


Figure 2.28: Long Overhang Torsional Dynamics

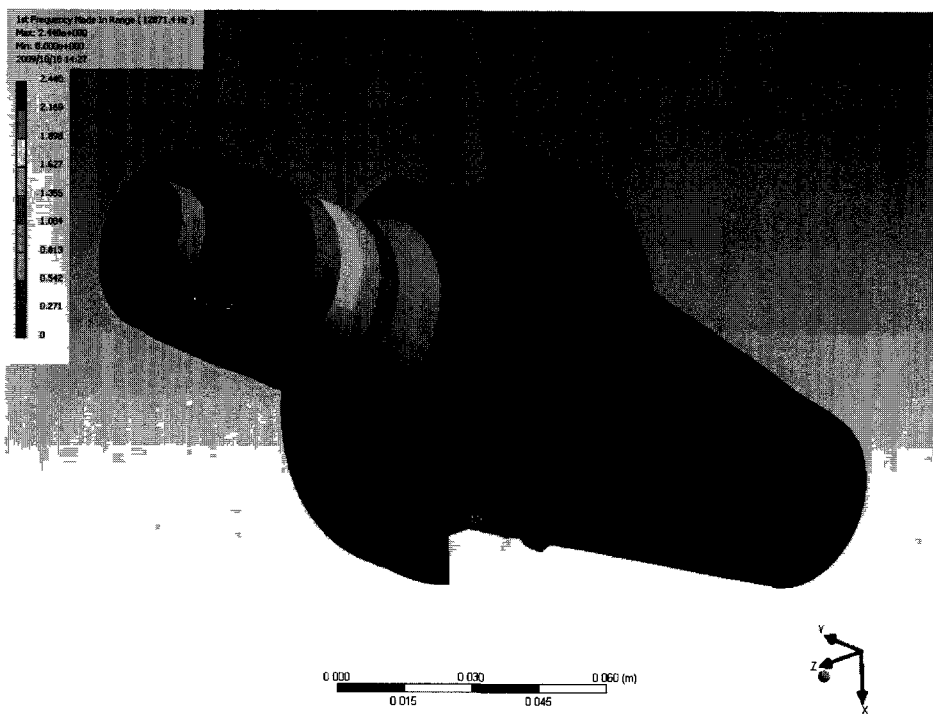
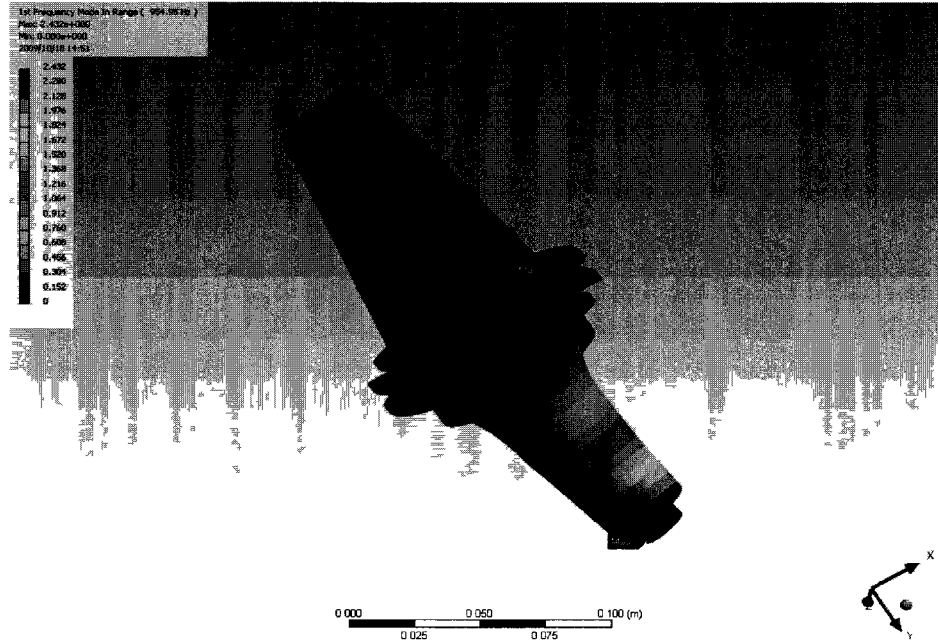


Figure 2.29: Short Overhang Torsional Dynamics



*Figure 2.30: Short Overhang Bending Dynamics*

The bending fundamental mode was also estimated using the FEA model. This was found to be significantly lower than the torsional modes, at around 950 Hz for the short overhang tool (Figure 2.30). This was anticipated based on the results of experimental tests. In experiments, the chatter frequency has been observed between 700 and 1000 Hz, depending on the tooling geometry. This means that the torsional natural frequency is around 13 times greater than the bending natural frequency for the short tool and 10 times greater for the long overhang tool. This is promising for the use of torque to monitor chip thickness during cutting.

With a high natural frequency in the torsional DOF (with respect to bending dynamics), the dynamics introduced by torsional vibration can be neglected in a chatter model incorporating the smart tool instrument. Recalling that the instrument has a sampling bandwidth up to 10.24 kHz, the torsional dynamics are entirely attenuated by



the anti-aliasing filter (4.5kHz) on the analog subsystem. Confirming that torsional natural frequency is substantially higher than bending validates methods of frequency analysis that assume the torsional strain relates to the bending strain, coupled through cutting chip thickness, i.e. without considering the torsional dynamics.

## **2.11 Chapter Summary**

A number of realistic sensor options were developed and evaluated for use in a sensor integrated tool holder. Signal conditioning and transmission methods were also developed for each sensing method. It was found that each sensing method had advantages and drawbacks for the specific environment however they all show potential for collecting meaningful data from the machine tool. In the case of the strain gauge applications, the tool holder dynamics are of significance since the location of the gauges is on the body of the tool holder. The accelerometer implementation is placed directly at the tool tip which makes it the most direct embodiment for sensing motion. The Bluetooth transmitter was introduced as the method for data transmission off the tool holder body.

Calibration of the strain sensors identified that while cross talk from bending forces was present, it is not significant enough to corrupt the torque information while the tool is AC coupled. Calibration of the electret accelerometer was discussed, with detail referenced to Appendix A. A thermocouple tool core temperature sensor described and characterized in Appendix B corroborates the temperature stability of the electret accelerometer for dry cutting tests since there is a phase delay between core temperature and the onset of cutting.

The acceleration and strain sensors coupled with various Bluetooth protocols have an

appropriate bandwidth ( $>3\text{kHz}$ ) for observing dynamic phenomenon in the milling system. The sensitivity varies between the sensor and location, but is greater than  $100\text{mV/g}$  for the accelerometer and  $4.3 \times 10^{-5} \text{ V/(N}\cdot\text{m)}$  for torsional strain. Chapter 3 will discuss the applications of both acceleration and strain for quantifying tool dynamics and the cutting process.

It is found that the scaled torque signal from the wired strain gauge sensor-integrated tool is in agreement with the magnitudes predicted by the cutting force model (see the above experimental and model plots).

## CHAPTER 3

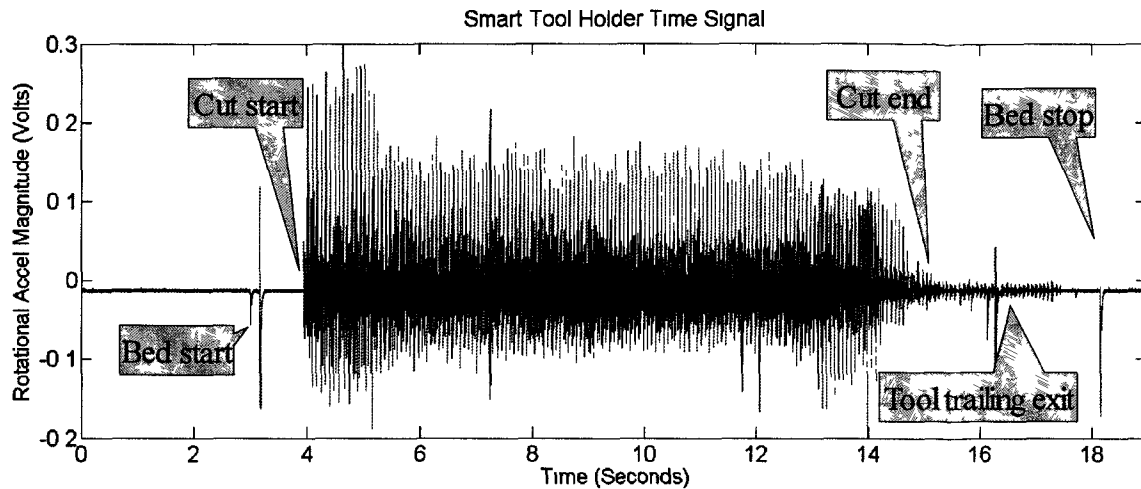
### Experimental Applications For Observation of Milling Phenomenon

#### **3.1 Electret Accelerometer Based Tool Tip Acceleration Measurements**

This chapter will demonstrate how the various sensors described in Chapter 2 and Appendix A can be used to detect the onset of chatter as explained in Chapter 1. Cutting tests were performed to investigate the correlation of the output signal with milling events.

First, the electret accelerometer Prototype 1 was tested. The tests performed were 75% immersion (57.15 mm radial immersion) linear upmill cuts through 6061 aluminum. The spindle speed for these tests was 800 RPM with a 2.54 mm axial depth and feed rate of 0.762 m/min. The cut length was 152.4 mm between workpiece entrance and exit. The output from the transmitter was recorded with a data acquisition PC sampling at 20 kHz.

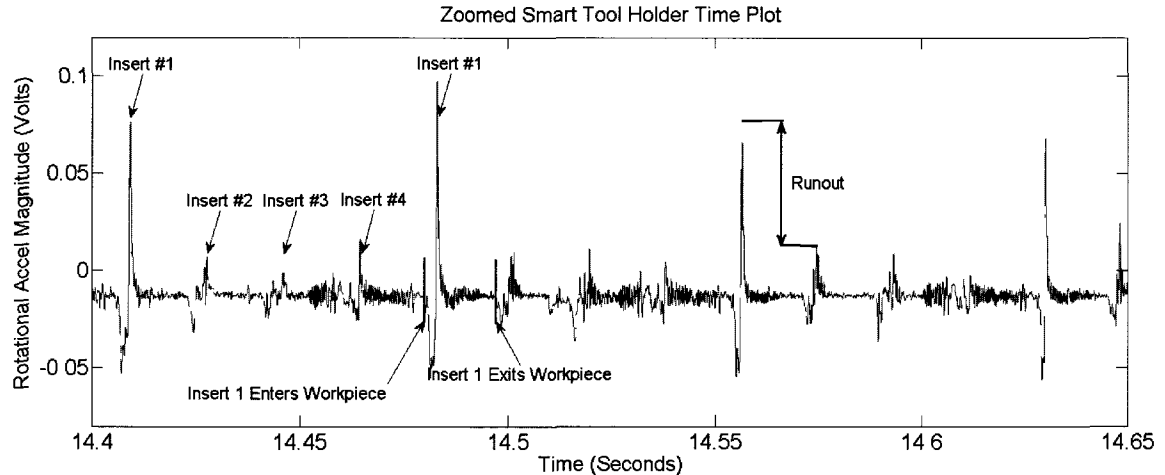
A plot of the recorded data is shown in Figure 3.1. The noise floor was very low, indicating that the transmitter effectively avoided motor noise and delivered an uninterrupted signal during the test. The low level of noise can be seen in Figure 3.1 before and after the cutting starts. The spindle speed ramps can be seen before and after the cut. Also, the tool trailing edge exit can be observed between 15-17 seconds. The trailing edge takes time to exit the workpiece because of the large diameter face mill tool.



*Figure 3.1: Time Signal From the Face Mill Acceleration Sensors*

Entrance and exit effects are clear, with higher magnitudes occurring during workpiece penetration (at 4 to 5 seconds) and decaying magnitudes as the tool exits the material (at 14 to 15 seconds). Signal spikes are observed at 2.6 and 18.2 seconds, corresponding to the instant at which the bed started and stopped. The detection of bed movement is not expected because the orientation of the sensors was intended to cancel X and Y components of acceleration. Since the tool only moves in the Z direction it must either be a vibration transmitted from the bed to the tool via the machine structure, or an electrical artifact. Further investigation is warranted.

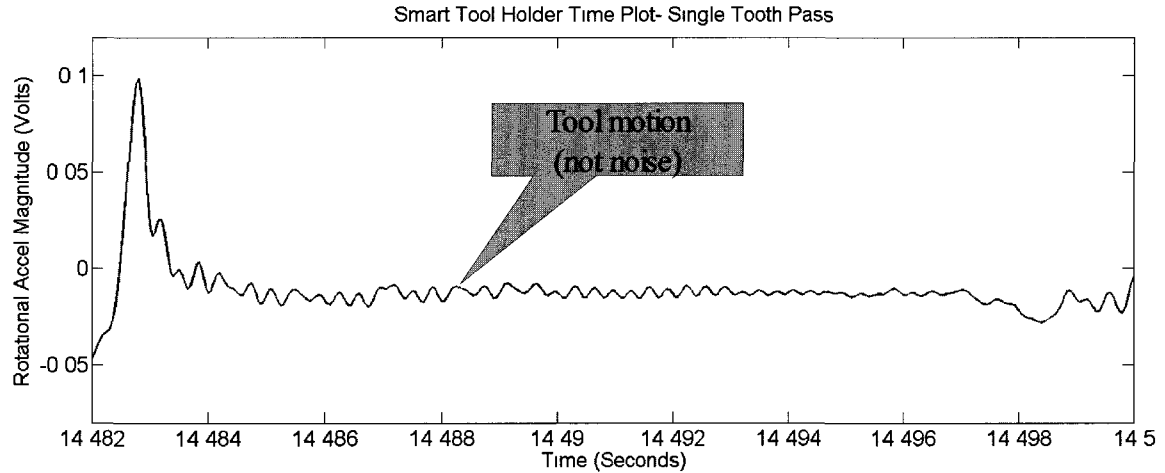
Sensor data for three revolution of the tool is shown in Figure 3.2. The toothpass frequency of 53.33 Hz is apparent in the time data with a period of 0.0187 seconds between inserts.



*Figure 3.2: Detailed Time Signal From the Face Mill Acceleration Sensors*

It is apparent that runout is present, with insert 1 producing a significantly larger vibration magnitude than inserts 2 through 4. The presence of runout was confirmed by physical measurement with a dial indicator showing a 0.23 mm difference between the high and low measurements. The recorded data correctly reflects the underlying physics. This is admittedly a rather large runout that would clearly have a negative effect on part accuracy and surface finish. We conjecture that the sensor would do an equally good job of detecting a broken tooth.

Machining a different material than aluminum would produce higher force magnitudes but the expected patterns of acceleration would remain similar. The material will affect workpiece stiffness, damping, and cutting force.

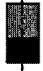
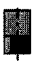







*Figure 3.3: Single Tooth Pass Time Response*

The sensor signal is further expanded in Figure 3.3 to show the cutting action during the time when a single insert is in contact with the workpiece.

To further expand on the information collected from Prototype 1, the axial electret Prototype 2 was used to further test the sensor output during a variety of cutting geometries and feed rates. Table 3.1 details the geometries of the tests conducted.

*Table 3.1: Electret Accelerometer Prototype Cutting Test Geometries*

Milling type	Slot	Down	Up	Down	Up	Down	Up
Radial	Full	75%	75%	50%	50%	25%	25%
Immersion							
Geometry of							
Immersion							
(Cross Section)							

All application tests were operated at a constant spindle speed of 3819 RPM, axial depth of 5.08 mm, and followed a linear path in 6061 T6 Aluminum. A single insert was placed on the tool. The material removal rate was varied by changing the feed rate three

times during each geometry test. Table 3.2 provides the three feed rates used during each cutting geometry test. The feed rates presented in Table 3.2 were calculated to maintain a uniform average chip thickness for different cutting geometries.

*Table 3.2: Electret Accelerometer Prototype Cutting Test Feed Rates*

	Slot	75% Down	50% Down	25% Down	75% Up	50% Up	25% Up
Feed 1 (in/min)	6.0	5.33	6.0	8.0	5.33	6.0	8.0
Feed 2 (in/min)	24.0	21.33	24.0	31.99	21.33	24.0	31.99
Feed 3 (in/min)	59.99	53.32	59.99	79.99	53.32	59.99	79.99

During this test, we compared upmilling and downmilling cuts. While testing, it was noticeable that upmilling caused higher vibration magnitudes in the data. As expected, this is seen in the average vibration magnitudes shown in Table 3.3. The upmilling cuts are observed to have higher absolute magnitudes for all tests. Figure 3.4 shows a time plot of both half immersion upmill and downmill cuts.

A positive acceleration bias was observed for up milling. A negative acceleration bias was observed for down milling. This was due to the orientation of the sensor sensing displacement of the tool tip when peak acceleration (tool impact) was causing either positive or negative acceleration on the sensor depending on how the tool was engaging the material. Figure 3.5 shows a plot of the data for a slot cut at the three feed rates shown in Table 3.2

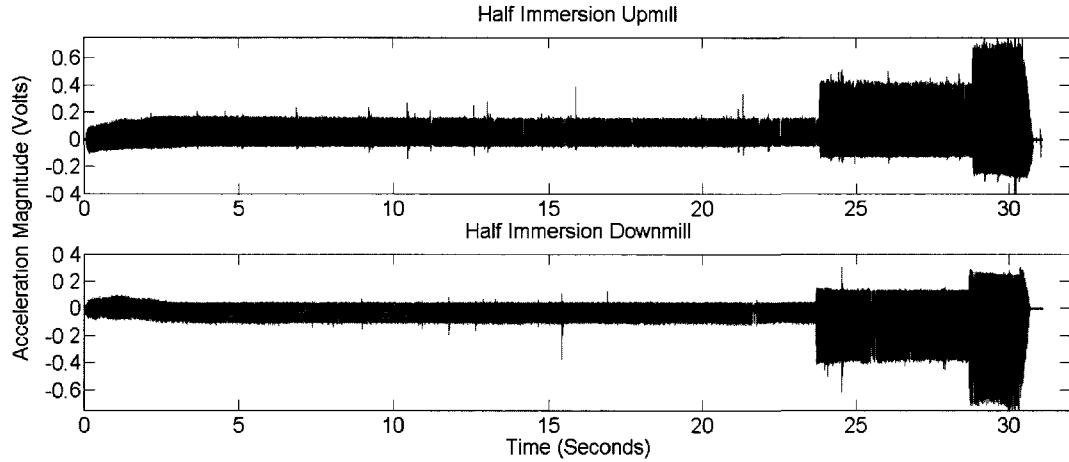


Figure 3.4: Half Immersion Upmill and Downmill Cuts

Table 3.3: Electret Accelerometer Prototype Cutting Test Vibration Magnitudes

	Slot	75% Down	50% Down	25% Down	75% Up	50% Up	25% Up
Feed 1 (Volts)	0.0186	0.0146	0.0135	0.0134	0.0191	0.0191	0.0159
Feed 2 (Volts)	0.0581	0.0443	0.0417	0.0412	0.0519	0.0527	0.0459
Feed 3 (Volts)	0.1218	0.0946	0.0806	0.0808	0.1034	0.1016	0.0874

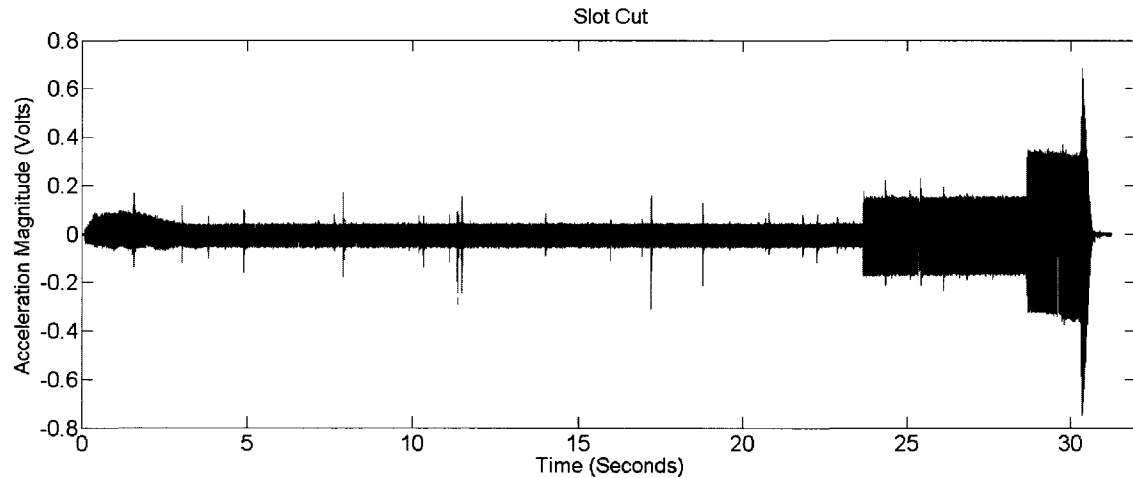


Figure 3.5: Slot Cut Acceleration at Three Feed Rates



### **3.2 Observing Chatter with Electret Accelerometer Based Tool Holder**

Regenerative chatter was observed during a slot cut. Using Prototype 1, the electret accelerometer tool, 6061 T6 aluminum was cut at a spindle speed of 3819 RPM, an axial depth of 10.16 mm, and feed rate of 12.7mm/sec (0.762 m/minute). This depth of cut and feed rate at 3819 RPM induced a chatter condition. The spindle speed was held constant so that frequency analysis of the data could be directly compared to lighter axial depth slot cuts conducted at the same tooth pass frequency.

Figure 3.6 shows the time response of the sensor during the development of chatter conditions. As expected, the vibration magnitude greatly increases as the chatter builds.

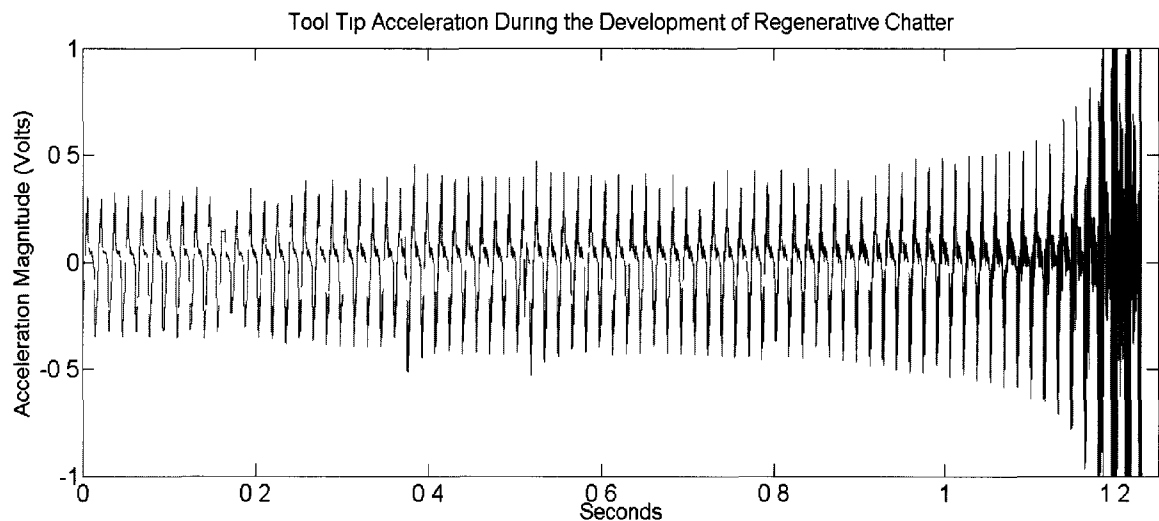


*Figure 3.6: Observing Tool Chatter with Electret Accelerometer*

To provide a visual interpretation of how the regenerative chatter begins, the acceleration data presented in Figure 3.7 is shown with a photograph of the workpiece slot cut during the development of instability. Figure 3.7 contains an overhead photograph of the slot cut accompanied by three acceleration frequency spectra. These three acceleration spectra are generated from the time data and are time-correlated to

each segment of the slot cut photograph.

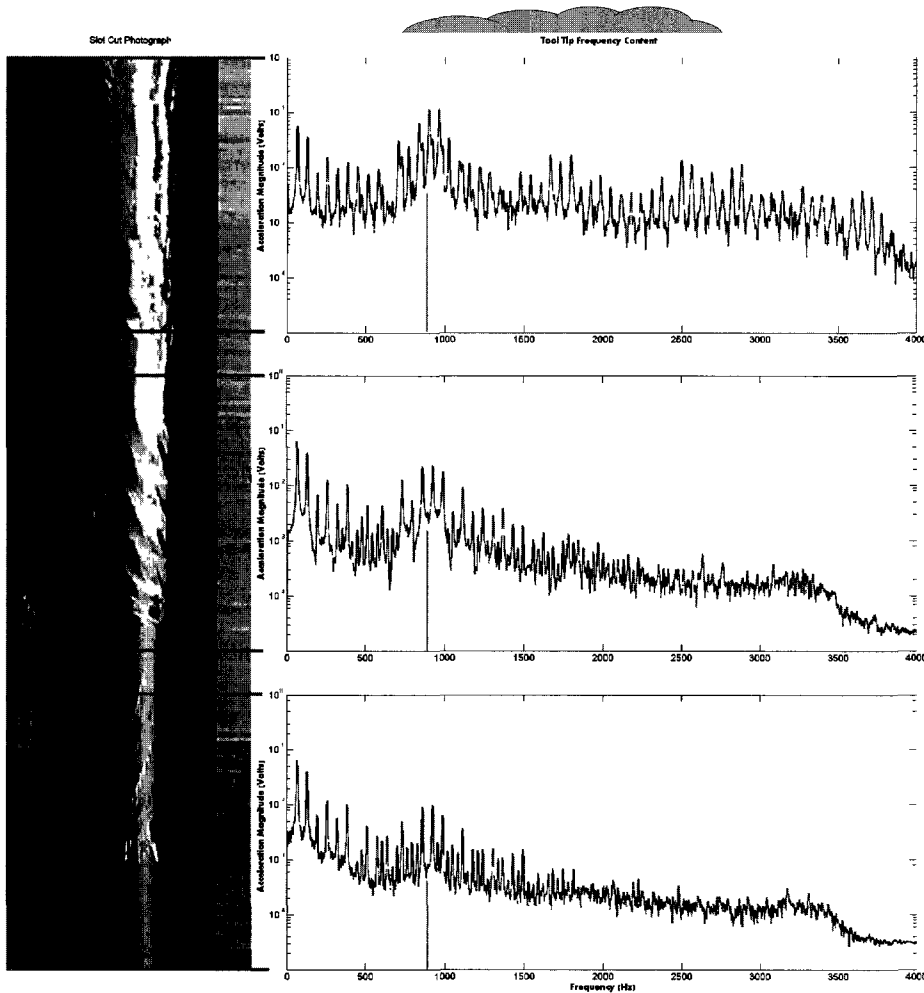


*Figure 3.7: Observation of Chatter Buildup Referenced to Workpiece Photo*

### **3.3 Chatter Prediction Using the Electret Sensor Integrated Tool**

The evolution of a chatter mode can also be observed in Figure 3.8 as a waterfall plot of frequency content over time (using Prototype 2). It is evident that the development of the chatter condition occurs over over a 1.2 second period in time, with rapid acceleration towards the onset of workpiece damage. However, during the early development period, the surface finish remains normal. Therefore, by tracking elevations in the chatter mode,

it may be possible to predict the onset of workpiece damage before it occurs. The ability to see the buildup of instability is crucial for control applications and chatter prediction possibilities. Observing the onset of regenerative chatter is possible because of the unique signal to noise ratio obtained from embedding sensors within the tooling body.

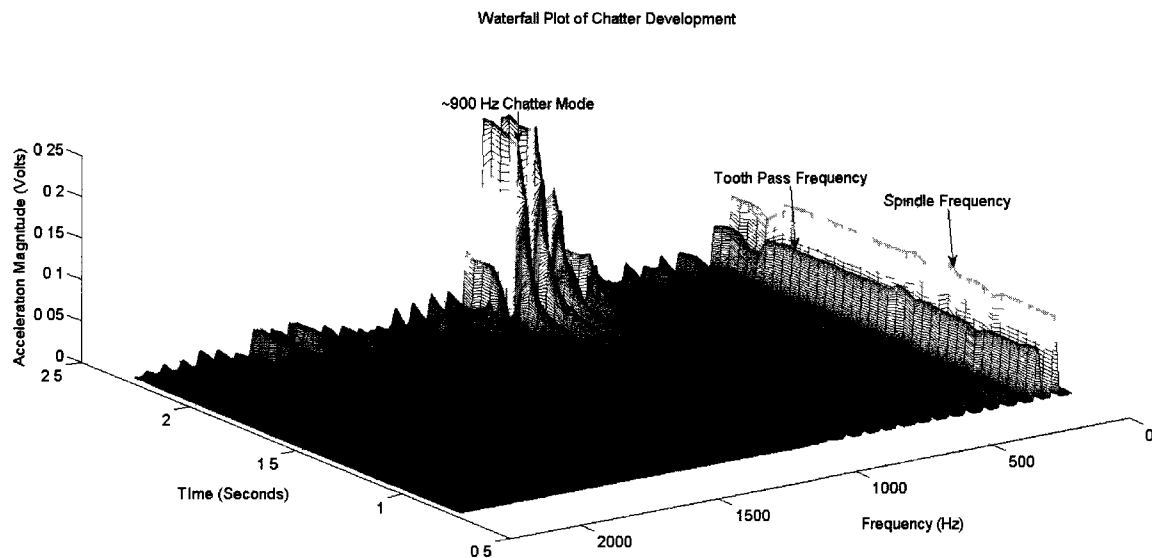


*Figure 3.8: Waterfall Plot of Chatter Development*

Alternative control methods such as the Harmonizer [53] product rely on inducing chatter and identifying the chatter frequency from an unstable cut; not during a cut or before chatter exists.

It has been shown that the sensor integrated tool Prototype 2 is sensitive enough to detect precursors to the onset of chatter in end milling. This success is due to the high signal integrity attributed with placing the sensor directly within the cutting tool. This monitoring ability is valuable and provides insight into the mechanisms of chatter development. The evolution of a chatter mode can be observed in Figure 3.8 as a waterfall plot of frequency content over time. This test is a slot cut at 10.16 mm (0.4 inch) axial depth, single insert cutter, a feed of 12.7 mm/sec (30 inches/minute), and

spindle speed of 3819 RPM (0.15 mm, 0.0039 inches, feed per tooth). Despite the aggressive cutting conditions used, chatter build-up is observed as early as 1.2 seconds before the onset of possible workpiece damage. Note that this buildup is specific to these cutting conditions and machining system, and may change for other cuts and other machines.

Although observing the early onset of chatter is suitable for an in-process safety measure, relying on this capability does not help with process planning. Ideally, cutting engagements and speeds would be chosen with prior knowledge of unstable conditions. In this way, process efficiency can be increased in an intelligent manner.

One goal of this work is to experimentally determine stable and unstable cutting speeds at various depths of cut. By doing so, it is possible to generate an experimental stability lobe diagram. A stability lobe diagram is a plot of spindle speed vs axial engagement, [25], that identifies depth and speeds at which regenerative tool chatter occurs. Figure 3.10 shows a typical stability lobe plot. In this work, we keep the geometry of the cut constant and sweep the spindle speed from low to high, causing the system to go in and out of chatter. In essence, we are locating the stability lobe points at a specific depth of cut.

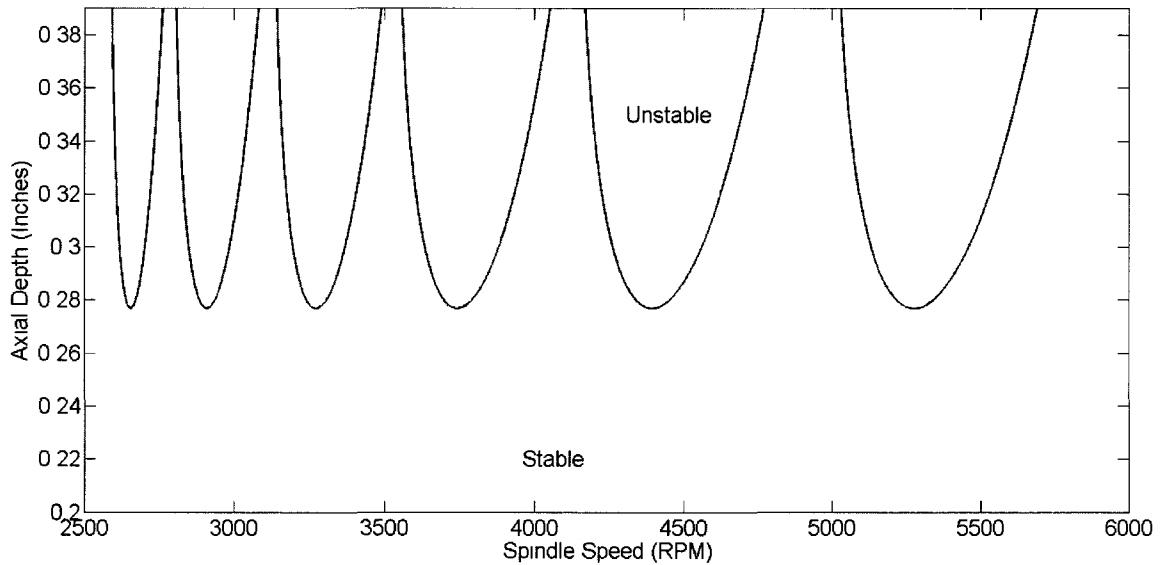


*Figure 3.9: A Typical Stability Lobe Diagram*

Stable and unstable cutting speeds can be determined using the vibration sensor integrated into the end milling tool. It is expected that this tool will provide sufficient resolution to detect the onset points of instability. The tests conducted are slot cuts in T6061 Aluminum with a 19.05 mm ( $\frac{3}{4}$  inch) two flute tool. The range of spindle speeds is between 2501 and 7376 RPM for each depth of cut in order to examine the reduction in stability associated with increasing axial depth. Four axial depths of cut have been chosen for this experiment.

From a practical perspective, it is necessary to consider the scope of testing a large number of spindle speeds. The maximum number of unique cuts required to fully determine stability fills a 4855 by 4 experimental matrix (corresponding to the number of spindle speeds and depths tested). Realistically, this number can be reduced, however the implication is an impractical number of cutting tests assuming each condition is to be tested individually. However, since it is desirable to maintain high resolution on the spindle speed, a solution is developed to minimize the number of cuts required, without

sacrificing resolution.

This solution is similar to using a sine chirp technique to evaluate system frequency response. A cutting test is designed to increase spindle speed from 2501 to 7376 RPM in 1 RPM increments, over the course of a 114.3 mm (4.5 inch) linear cut in the positive X direction. During this time, the material feed rate is also changed to maintain a constant feed per tooth of 0.0254 mm (0.001 inch). To avoid variations in cutting dynamics during material entrance and exit, the test is started and stopped while the tool is fully immersed in material. Specifically, in a 152.4 mm (6 inch) workpiece, the tool enters the material, travels 19.05 mm (0.75 inches) at 2501 RPM, the spindle speed is then swept until 133.35 mm (5.25 inches) reaching 7376 RPM, and then exits the material at 7376 RPM. This spindle speed sweep is repeated for each axial depth condition, from 8.255 mm (0.325 inches) to 10.16 mm (0.4 inches) in steps of 0.635 mm (0.025 inches).

Preliminary test results show that the onset of instability can be clearly discerned from the tool tip vibration signal. This is superior to using a microphone since the signal to noise ratio is greater. The onset of chatter modes are seen as rapid increases in the time signal magnitude. This confirms the hypothesis that chatter rapidly grows at unstable spindle speeds. At each unstable mode, after the rapid onset of chatter, instability slowly attenuates in the direction of spindle speed change. For instance, if the spindle speed were increasing from low to high, the instability would quickly onset at a particular frequency and then proceeds to decay as the spindle speed increased into a stable frequency range. Figure 3.10 shows this phenomenon for increasing spindle speeds. The test shown in Figure 3.10 is conducted at the 8.89 mm (0.35 inches) axial depth.

The spindle sweep method makes the assumption that the sweep rate is slow enough that chatter has the opportunity to build. Recalling that it can take time in an unstable condition for the instability to grow (Figure 3.6), the spindle speed sweep must be conducted slowly. There is opportunity for future work to study the rate of chatter build up during unstable cutting conditions.

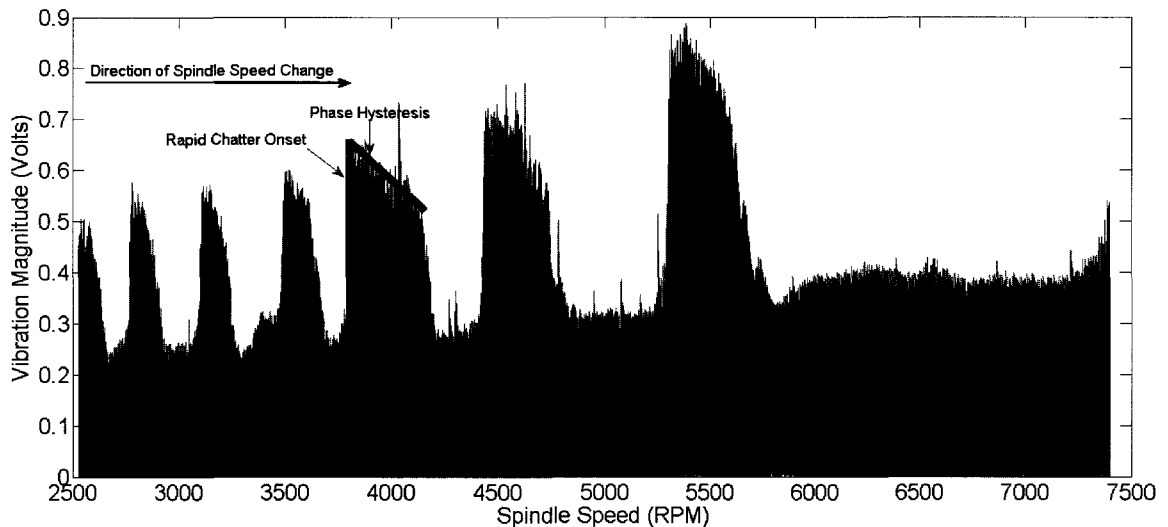


*Figure 3.10: Directional Chatter for Increasing Spindle Speed at 8.89mm Axial Depth*

Because of this observed effect, unstable spindle speeds can be recognized at their onset, but their trailing edge lacks definition as the spindle speed moves toward a more stable region. Therefore, it is necessary to reverse the change in spindle speed to see if this effect is related to increasing or decreasing the spindle speed sweep. It is found that the same effect is found to be true for the reversed spindle speed test. The direction of the spindle speed change (2501 to 7376 vs. 7376 to 2501) determines the persistence of instability after its onset. The

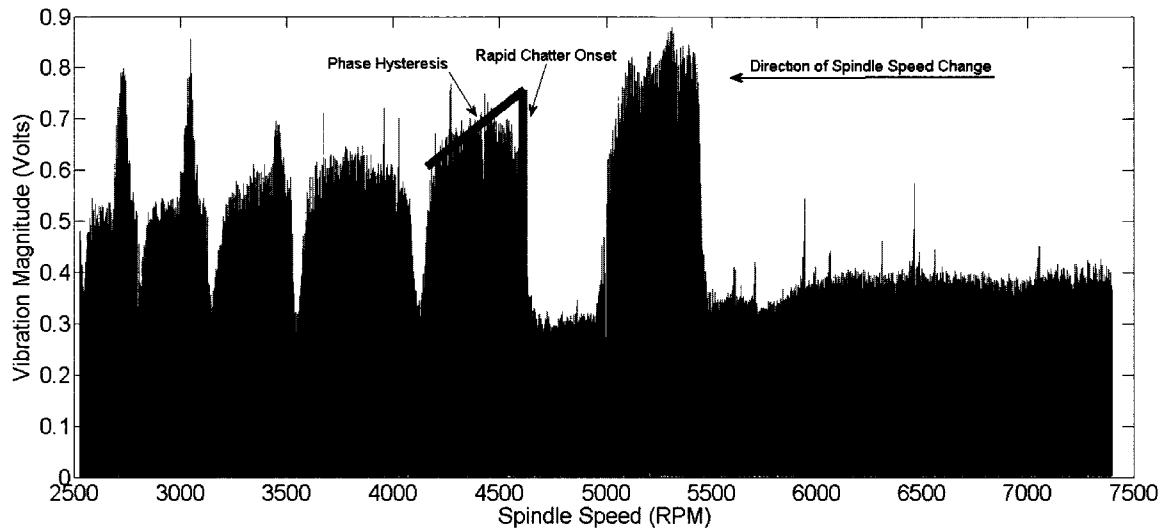


Figure 3.11: Directional Chatter for Decreasing Spindle Speed,  $AD=8.89\text{mm}$

The increasing spindle speed had a more pronounced effect of attenuating chatter into stable regions versus the decreasing speed. The attenuation happens with a faster slope in the increasing speed because more revolutions occur in a shorter time span (versus less when decreasing speed). Since chatter is replaying the surface finish, fewer tooth passes means a longer attenuation time.

This phenomenon makes physical sense since regenerative chatter is a playback of the surface finish waviness from previous cutting. Once the surface finish is out of phase with the tool vibration, the surface finish continues to excite the tool at the chatter frequency until the unstable surface finish is attenuated. Since regenerative chatter is caused by the surface finish being out of phase with the tooth pass frequency, we refer to this phenomenon as directional chatter. Figure 3.11 shows a vibration plot of the reversed spindle speed test. The test shown in Figure 3.11 is conducted at the 8.89 mm axial depth. Later in this paper, modeling efforts are shown to identify and explain the observations made in these tests.



From these initial experiments, it is found that a spindle speed sweep test is capable of producing useful results that estimate the spindle speeds at which regenerative chatter occurs. However, it is necessary to repeat the test for both increasing and decreasing spindle speeds due to the directional dependence phenomenon. For the tests described earlier, the final experimental space for this technique is 4 axial depths and 2 spindle sweep directions (an experimental space of 4855 spindle speeds by 4 by 2).

Although directional chatter occurs during the decay of instability, it is observed that the onset of chatter is sharply defined for both increasing and decreasing spindle speeds. These onset points identify the upper and lower bounds of the unstable modes. Because the test is conducted for both increasing and decreasing spindle speeds, the upper and lower boundaries of the unstable modes can be estimated. To test this hypothesis, stable and unstable spindle speeds were chosen based on the two tests. Figure 3.12 shows the absolute vibration magnitudes from both test types superimposed for clarity. The tests shown in Figure 3.10 and 3.11 are at an axial depth of 8.89 mm (0.35 inches). Recalling that the development of instability is a function of both depth and spindle speed, the plot in Figure 3.12 shows the instabilities that develop at the 8.89 mm inch depth. Vertical lines indicate the selected stable spindle speeds chosen for verification using constant spindle speed test cuts. Table 3.4 contains the selected stable speeds along with unstable speeds.

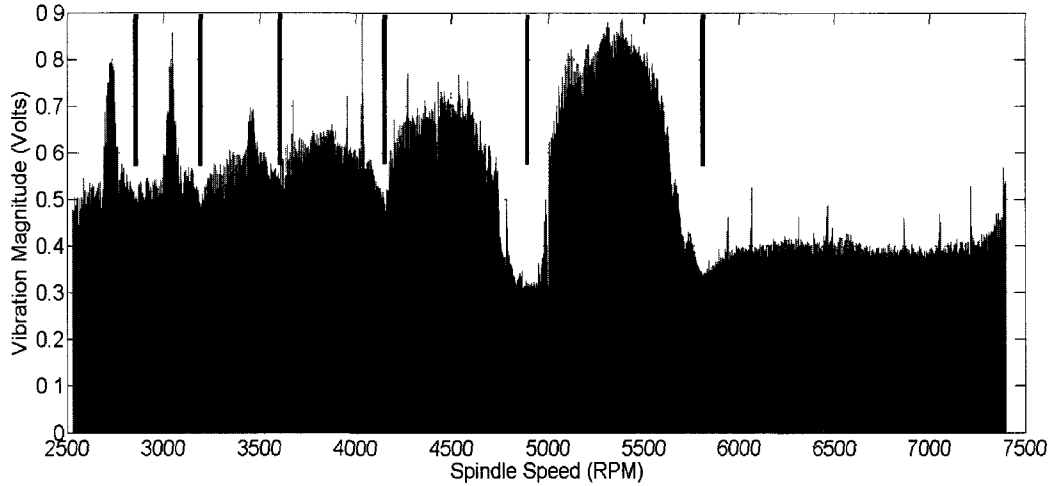


*Figure 3.12: Superimposed Absolute Vibration Magnitudes from the Frequency Sweep Tests*

*Table 3.4: Selected Stable and Unstable Spindle Speeds from Figure 3.12*

Stable (RPM)	2867	3197	3616	4153	4891	5808
Unstable (RPM)	2748	3063	3485	3850	4758	5340
Increasing speed Chatter Frequency (Hz)	918	927	923	930	932	929
Decreasing speed Chatter Frequency (Hz)	887	886	892	891	896	890

The spindle speeds in Table 3.4 are validated by steady state cutting tests. The spindle speed is held constant for each test while maintaining the same axial depth and 0.0254 mm (0.001”) feed per tooth as before. For all six stable conditions predicted, the cuts did not exhibit chatter. For all six unstable conditions predicted, chatter occurred. These tests were repeated three times with identical results.

These tests indicate that it is feasible to predict stable spindle speeds using the sensor

integrated tool. By understanding where instability occurs, a more productive combination of feed and speed can be chosen to increase material removal rate. In the range tested, the material removal rate between the lowest and highest stable cutting condition can be doubled while maintaining stability.

### **3.4 Chatter Frequency Using The Sensor Integrated Tool**

It is useful to identify the specific frequency at which chatter occurs. From the waterfall plot of chatter development (Figure 3.8), this frequency is shown to be approximately 900 Hz. Knowing the chatter frequency of the system, it is possible to predict stable and unstable spindle speeds [25]. The locations of these peaks should align with instabilities in the experimental data. By understanding the relationship between phase shift and spindle frequency, the locations of peak instability can be located according to the peak phase shift of the structural transfer function [25]. This phase shift can be calculated by :

$$\psi = \tan^{-1}\left(\frac{\sin(\omega_c T)}{1 - \cos(\omega_c T)}\right) \quad (3.1)$$

Where  $T$  is the tooth passing period and  $\omega_c$  is the chatter frequency in rad/s. Evaluating this function over a range of spindle speeds identifies the least stable speeds when

$\psi = \frac{\pi}{2}$  . Table 3.5 shows the estimated unstable speeds using Equation 3.1, assuming a

900 Hz chatter frequency. These values are estimated by  $\omega_c = 2\pi(900\text{Hz})$  and evaluating the tooth passing period  $T$  over the range of the spindle speed test.

*Table 3.5: Calculated Unstable Speeds*

Calculated Unstable (RPM)	2700	3000	3375	3860	4500	5400
Observed Unstable From Table 3.4	2748	3063	3485	3850	4758	5340

Using the peak phase angles to determine maximum instability corresponds strongly to the unstable conditions selected from the experimental data. Additionally, it is not necessary to know the FRF (frequency response function) to evaluate these conditions. Calculating  $\psi$  from Equation 3.1, it is feasible to compute the stable spindle speeds as well as the unstable speeds. A peak-trough plot of instability can be computed by [25]:

$$|\kappa| = |\tan(\psi)| = |\tan(\pi / 2 - \omega_c T / 2)| \quad (3.2)$$

where the absolute value is taken to observe the magnitude of the phase angle tangent as a function of tooth passing period. Equation 3.2 is calculated over the range of spindle speeds to produce the  $|\kappa|$  versus RPM curve shown in Figure 3.13. The peaks of this plot occur when the spindle speed and surface waviness are 90 degrees out of phase. This method is similar to the relationship in [25] where theoretical stability lobes are generated as a function of  $\kappa^2$ , a cutting force coefficient, and the dominant real system pole. Recall, this method is based on a 2<sup>nd</sup> order model and assumes there is a single real pole dominating the system. However, the absolute magnitude is sufficient to observe the peak unstable spindle speeds that occur at the asymptotes of  $|\kappa|$ . Figure 3.13 shows the tangent function in Equation 3.2 superimposed onto experimental vibration data. The tangent function plotted in Figure 3.13 is only to locate peak instability. While this is not a stability lobe diagram, it shows that the peak instabilities are close to those from the

experimental data. The stable spindle are listed in Table 3.6. The minima of this equation represent the most stable spindle speeds, and are shown in Fig 3.13.

Table 3.6 shows the results of evaluating Equation 3.2 and locating stable spindle speeds at the minima of the function. As with the unstable speeds in Table 3.5, the predicted stable speeds are close to the experimentally observed speeds presented in Table 3.4. This clearly illustrates how knowing the chatter frequency can potentially assist in choosing stable spindle speeds.

Table 3.6: *Stable Speeds Predicted by the Phase Shift Tangent*

Calculated Stable (RPM)	2850	3175	3600	4150	4900	6000
Observed Stable From Table 3.4	2867	3197	3616	4153	4891	5808

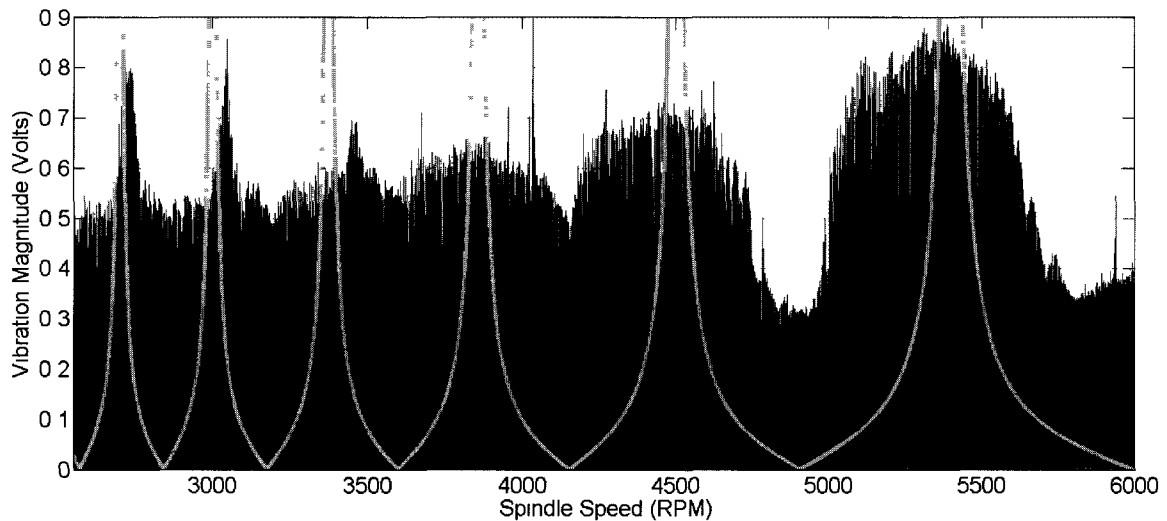
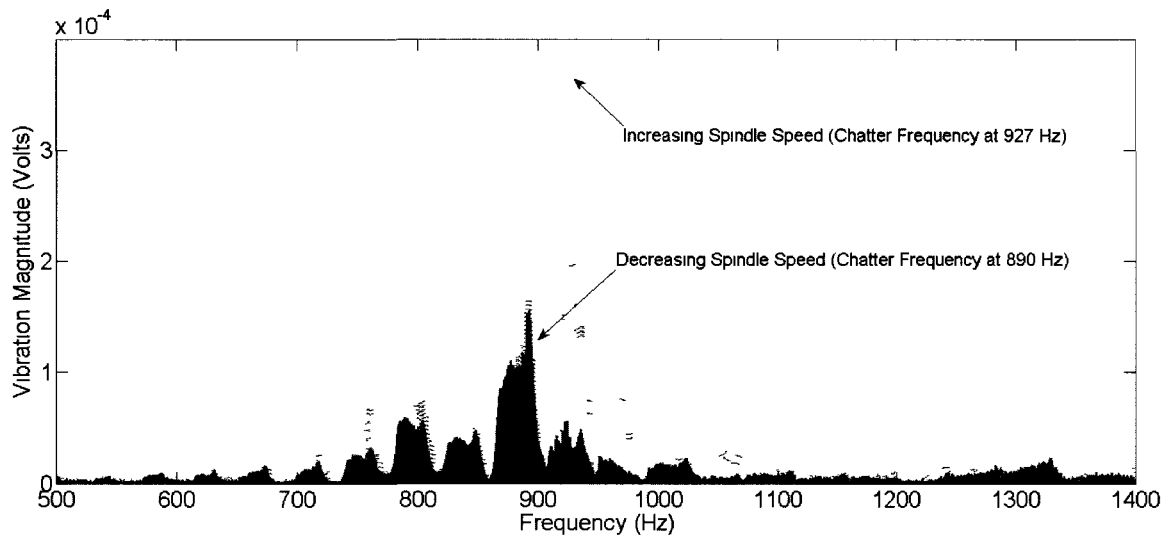


Figure 3.13: *Phase Angle Tangent Magnitude vs Spindle Speed*

### **3.5 Frequency Based Observations and Experimental Stability Lobe Diagrams**

For use in theoretical models such as the best speeds equation [48], it is critical to understand the chatter frequency of the system. To observe this frequency, an FFT is

performed on the spindle speed sweep data from the accelerometer sensor as shown in Figure 3.10 and 3.11. The chatter frequency is determined to be 927 Hz for the spindle speed sweep tests with increasing spindle speed and 890 Hz for the tests with decreasing spindle speed.



*Figure 3.14: Identifying Chatter Frequencies*

This is an unexpected result because increasing and decreasing speed tests are performed at identical feed rate and engagement. Moreover, the relative magnitude of the chatter frequency differs between increasing and decreasing spindle speeds. Although using the chatter frequency to predict stable speeds is convenient, the technique presumes the system response is repeatable. Since a change in the chatter frequency is observed for increasing vs. decreasing spindle speed, questions arise about the influence of cutting conditions on the chatter frequency.

A simple experiment is designed to explore the difference in observed frequencies. Like the previous tests, this experiment consists of two cuts with increasing and decreasing spindle speeds. All conditions, including the workpiece and tool, are identical

to the initial experiments, except the feed direction is reversed from positive X to negative X. The tests were slot cuts to avoid problems with up versus down milling. Specifically, this is identical to the initial tests, with a reversed feed direction. If the system is linear, this should not affect the outcome since the transfer function in the X direction is assumed constant. However, it is clear from Table 3.7 that the dynamics of the system change by reversing the feed direction. This is evident from both the time magnitudes and the frequency content of the vibration signal. Table 3.7 shows the chatter frequencies comparing these cutting conditions.

*Table 3.7: Chatter Frequency Dependency on Cutting Direction*

Increasing/Decreasing Spindle Speed	Feed Direction	Chatter Frequency (Hz)
Increasing	+ X	927
Decreasing	+X	890
Increasing	-X	940
Decreasing	-X	910

Because these cutting conditions are found to have a significant effect on the chatter frequency, it is possible that other cutting conditions such as engagements, feed rate, and workpiece geometry will also have an effect along with XYZ position of the machine tool. The observed difference in the chatter frequency cannot be explained by the simple models presented in the reviewed literature and will be the subject of further investigation.

The tool tip vibration signal from the electret sensor contains information about the entire spectrum of the machine response, including that of the chatter frequency. It is

desirable to inspect information at the chatter frequency to clearly note the onset and growth of instability. To make a clear observation, other frequency content in the signal must be de-emphasized. This can be done by generating a waterfall series of FFT's (as shown in Figure 3.8), or the chatter frequency can be extracted from the time data using a bandpass filter. The filter is designed to attenuate all frequency content except for the band around the observed chatter mode. This is a different approach than using a comb filter to eliminate the tooth pass frequency and its harmonics (e.g. the Harmonizer method). The band pass filtering approach is implemented so the data can be processed easily in the time domain. Such an approach has been used with commercial systems such as the Harmonizer (53), discussed in the Chapter 1 introduction of this dissertation.

The bandpass filter is rapid and more robust than the FFT. This is because it is computationally faster to implement the filter for streaming data, instead of waiting to collect segments of data for computing FFTs through time. The passband on this filter is defined as  $\omega_c - 50 < \omega < \omega_c + 50$  where  $\omega_c$  is the average chatter frequency of 900 Hz. A 100 Hz passband is chosen since the chatter frequency is observed to shift with speed changes (discussed earlier). Phase shift in the filtered data is avoided by passing the data forward and backwards through the filter. This forward-backward filtering effectively increases the Butterworth to a 4<sup>th</sup> order roll off. Isolating the chatter frequency in the time domain data makes it easier to observe and denote the onset and growth of the chatter mode by counting zero crossings and picking peak amplitudes. This saves complication of transforming the data to the frequency domain to observe the same information. Figure 3.15 shows a comparison of the unfiltered raw time data and the filtered chatter



frequency data for increasing spindle speed at the 8.89 mm axial depth of cut. After the data is filtered to isolate the chatter frequency range, it is easier to discern the onset points of instability. Filtering in this manner neglects other modes in the system and is used only to highlight changes in a specific frequency for this case.

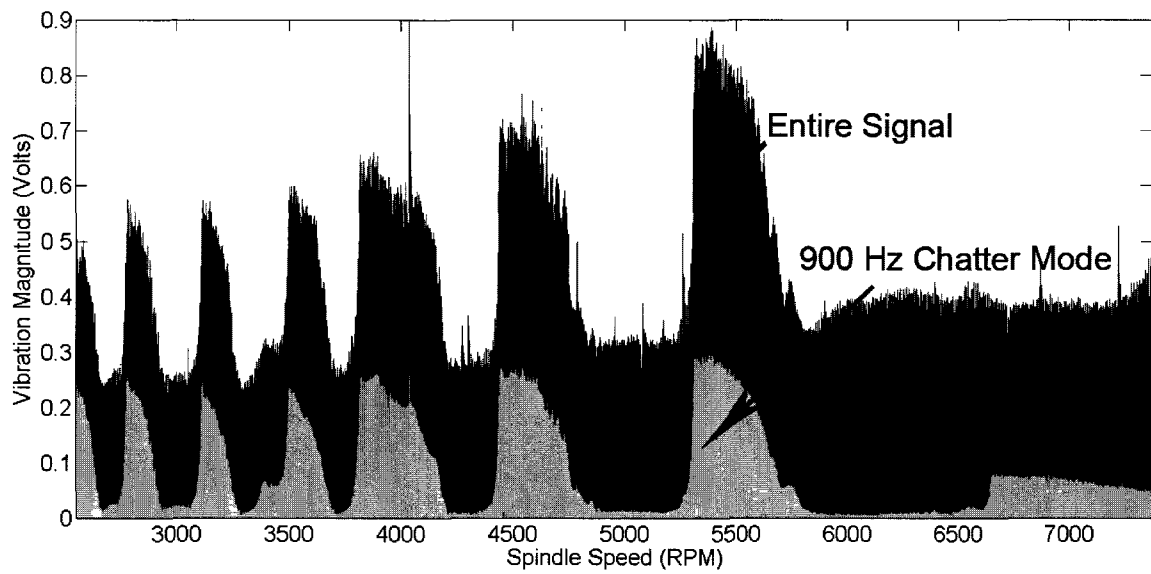


*Figure 3.15: Bandpass Isolation of the Chatter Frequency*

With knowledge of unstable spindle speeds, it is possible to generate an experimental stability lobe diagram. To this point, chatter frequency has been discussed, however, it is also important to know the exact spindle speed, time correlated to the vibration data. For many NC milling machines, the spindle motor control operates in open loop with the controller. In typical processes, the spindle runs at steady state during cutting operations and the motor speed accurately reflects the amperage and frequency applied by the control system. However, the spindle speed sweep experiments conducted for this work are not steady state cutting conditions. For this reason, the true spindle speed must be known. The vibration signal from the tool tip sensor contains information about the frequency content of the cutting process, including the spindle frequency. Therefore, it is

possible to know the true spindle speed from the vibration signal by isolating the spindle frequency component of the vibration signal. It is desirable to use the vibration signal to estimate spindle speed directly to maintain time alignment between the instantaneous spindle speed and the data.

Isolation of the spindle frequency is possible by defining a bandpass filter around the theoretical spindle speed designated by the controller. The theoretical speed is dictated by the G Code and is made in discrete steps as the cut progresses. These steps occur proportionally to the feed rate to maintain a constant feed per tooth of 0.0254 mm. In other words, the spindle speed is a function of feed rate to maintain a constant chip thickness and material removal rate.

With knowledge of the theoretical (controller reported) spindle speed over time, a filter is designed to isolate the spindle frequency for each step through the dataset. This filter is a second order Butterworth bandpass filter. The passband on this filter is defined as  $0.75 * \omega_s < \omega < 1.25 * \omega_s$  where  $\omega_s$  is the theoretical spindle frequency. This filter is designed to avoid the tooth pass frequency and allow for  $\pm 25\%$  deviations from the theoretical spindle speed. This should be sufficient considering that the spindle speed is expected to be within a few percent. A two flute cutter is used for this work, however the technique is applicable to tools with any number of flutes. After this filter is applied, the period of the spindle waveform is measured directly from the time data. This is done by locating the zero-crossings of the filtered waveform. It is found that this technique is robust and computationally fast.

A lag between the theoretical controller speed and the measured spindle speed is

observed as seen in Figure 3.16. Since the spindle controller operates in an open loop configuration, this is an expected outcome of continually changing the spindle speed. Although a lag is present during the spindle sweep, the controller is accurate within 1%-3% during steady state cutting, depending on load. This is verified by conducting several tests at constant spindle speeds. By knowing the true spindle speed throughout the test, a more accurate stability lobe diagram can be created. Moreover, extracting the spindle speed from the vibration signal improves the potential to automate the process, requiring only the sensor integrated tool and no additional interface to a rotation sensor.

Error in the spindle measured speed (shown in Figure 3.16) can be attributed to the method used to estimate the spindle speed from zero crossings in the data. During times of chatter, the zero crossings can be difficult to determine due to superposition of the chatter frequency in the data. Even though the bandpass filter attenuates the chatter frequency, it still has effect on the data. One method that can be investigated for future work is the use of hysteresis in the filtering method to make zero crossing estimation more accurate.

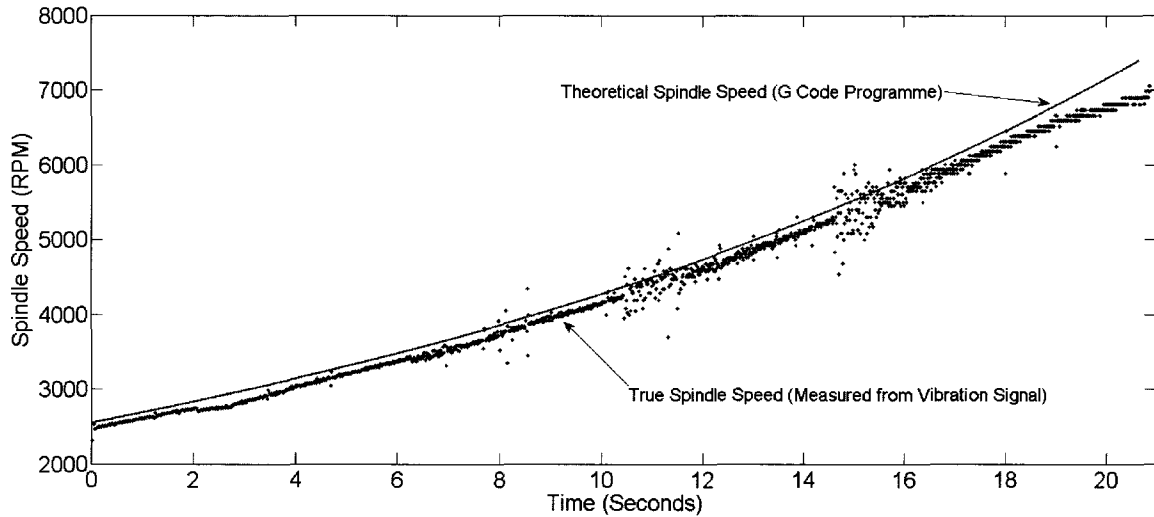


*Figure 3.16: Theoretical vs Actual Spindle Speed*

After isolating the chatter frequency in the time data and determining the true spindle speed, it is possible to identify instability onset for a particular cutting condition at various axial depths using Equation 3.1. For the 8.255 mm (0.325 inch) axial depth, chatter is not observed during the increasing spindle speed test, but is encountered during the same conditions with decreasing spindle speed. Although the specific cause is unknown, this may be related to nonlinearities like those responsible for changing the chatter frequency, or to the rate of change of the spindle speed. Another hypothesis is that the change in bed location influences the chatter frequency. For axial engagements lower than 8.255 mm, chatter only occurs at constant spindle speeds. This outcome suggests that the maturation (build-up) rate of the chatter mode differs as a function of depth.

Even though the 8.255 mm axial depth did not produce fully developed chatter during the spindle speed sweep, the higher axial depths provided clear onset points from both increasing and decreasing spindle speeds, from which an experimental stability lobe diagram can be created. These onset points define the upper and lower boundaries at

which instability occurs. Recalling the discussion of directional chatter, the upper boundaries are defined by the decreasing spindle speed sweep and the lower boundaries are defined by increasing spindle speed sweep. The experimental stability lobe diagram can be generated to 10.16 mm (0.4 inches) axial depth since this is the limit of the tool used for this investigation. Figure 3.17 shows the experimental stability lobe diagram plotted with the upper bounds represented by a downward pointing triangle (from the decreasing spindle speed tests) and lower bounds by an upward pointing triangle (from the increasing spindle speed tests).

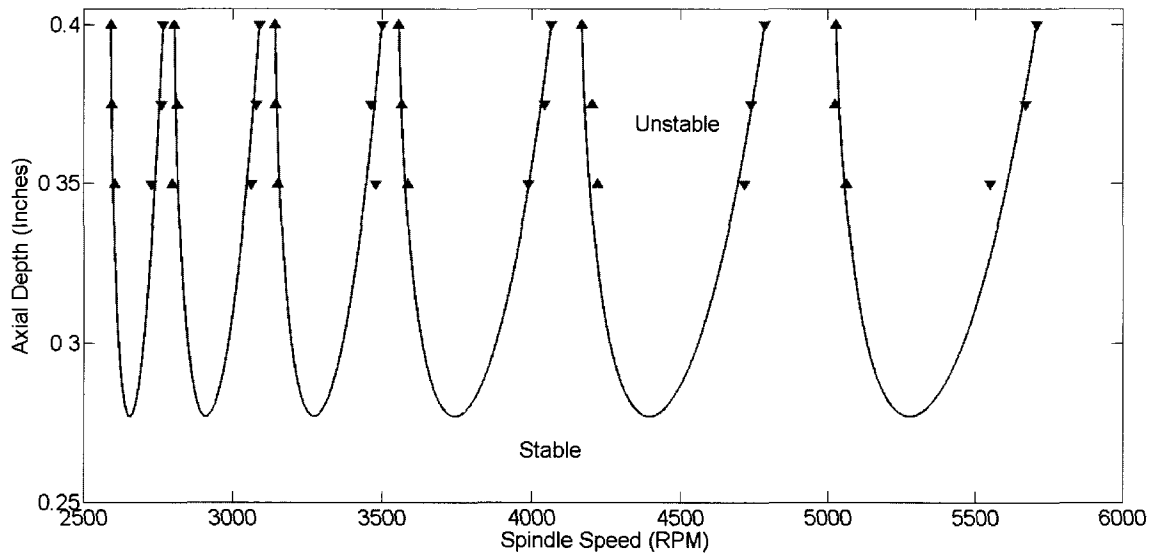


*Figure 3.17: Experimental Stability Lobes*

The plot presented in Figure 3.17 is a curve fit to the experimental chatter onset points. It is found that a second order tetration ( $2x$ ) function fit the data points well. For each unstable mode, the tetration [52] is computed over the interval 0 to 1 and scaled by the onset spindle speeds to fit the experimental data. Explicitly, this is defined as  $x(n)^{x(n)}$  where  $x = [0, 1/(\omega_2 - \omega_1), \dots, 1]$ ,  $\omega_2$  is the upper bound of an unstable mode, and  $\omega_1$  is the lower bound of an unstable mode. Although this function fits the existing data reasonably

well there is no guarantee that the portion of the curve away from the data points is accurate and further testing is warranted. With this sensor, the onset of tool chatter may be detected before workpiece damage occurs. By observing the growth and frequency of the chatter mode before workpiece damage, adaptive chatter control of the spindle speed is a promising area of future investigation.

Since chatter frequency changes with cutting conditions (i.e. increasing vs. decreasing spindle speed), questions emerge about chatter modeling techniques that assume the milling system plant to be repeatable. Future work will explore more advanced time domain simulation models, and adaptive control of the spindle speed using feedback from the sensor system to actively avoid chatter conditions.

### **3.6 Tool Torque Measurement**

By comparing the peak torque values measured with Prototype 3, the distribution of material removal rate (MRR) can be approximated. Although this requires more verification and subsequent study, the results are important to touch on because of implications for feed rate override control and tool failure detection. During the case shown in Figure 3.19, insert 1 is contributing 27% of the MRR capacity while insert 2 is contributing 73% of the MRR. The average feed per tooth of this test was 0.122 mm/tooth. As a result of insert run out, insert 1 cuts at an effective 0.0329 mm/tooth and insert 2 cuts at an effective 0.0891 mm/tooth.

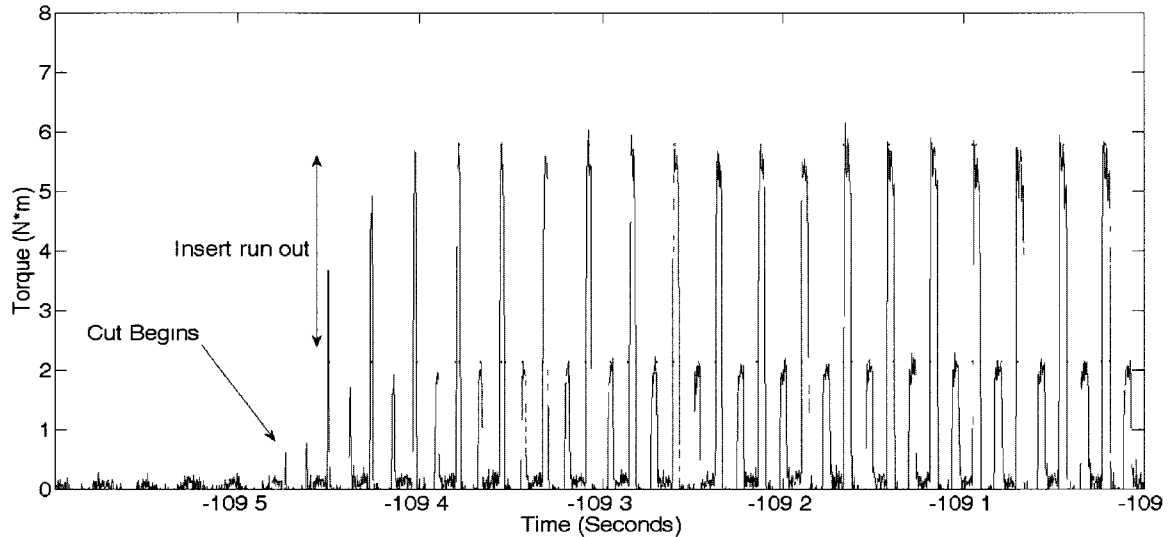


*Figure 3.18: Torque Signal Showing Insert Run Out*

A use of the torque sensor can be found in estimating tool run out. On a two insert cutting tool, the chip load is ideally distributed at 50% material removal rate (MRR) on each insert. Realistically, run out exists on the tools and it must be quantified. This eccentricity is expected on insert type tools and with set screw tool holding systems. The effect of run out is greatest after tool changes before the tools are 'broken in'. By knowing the torque, it is possible to understand the true distribution of MRR on the insert cutting tools.

Possibly the most interesting application of this torque sensor integrated tooling system is the observation of tool tip dynamic effects. Previously the electret tool tip vibration sensor, Prototype 2, was used to observe the signal frequency content during regenerative tool chatter. Although vibration is a useful source of information to inspect frequency components of the cutting signal, it does not provide magnitude information. With the torque dynamometer integrated tool, a direct observation of the cutting torque during tool engagement is possible. Unlike commercial rotating dynamometers, this

sensor is integrated with a commercial cutting tool and the stiffness is not affected. Thus, modes are not artificially introduced into the cutting system.

Since previous work investigated tool chatter with tool tip vibration (Prototype 2), a test is conducted to observe chatter with the torque sensor integrated tool (Prototype 3). A cut is conducted in tool steel with a 14.2875 mm radial engagement and 3.175 mm axial depth, using two inserts. At a spindle speed of 2500 RPM, a light chatter condition was encountered. Figure 3.19 shows a waterfall plot of this test. The evolution of the chatter mode supports the results found with the electret accelerometer. However, unlike previous vibration studies, the torque magnitude is measured. Over a time period of approximately 0.5 seconds, the amplitude of the chatter mode grows to about 0.5 N\*m/Hz.

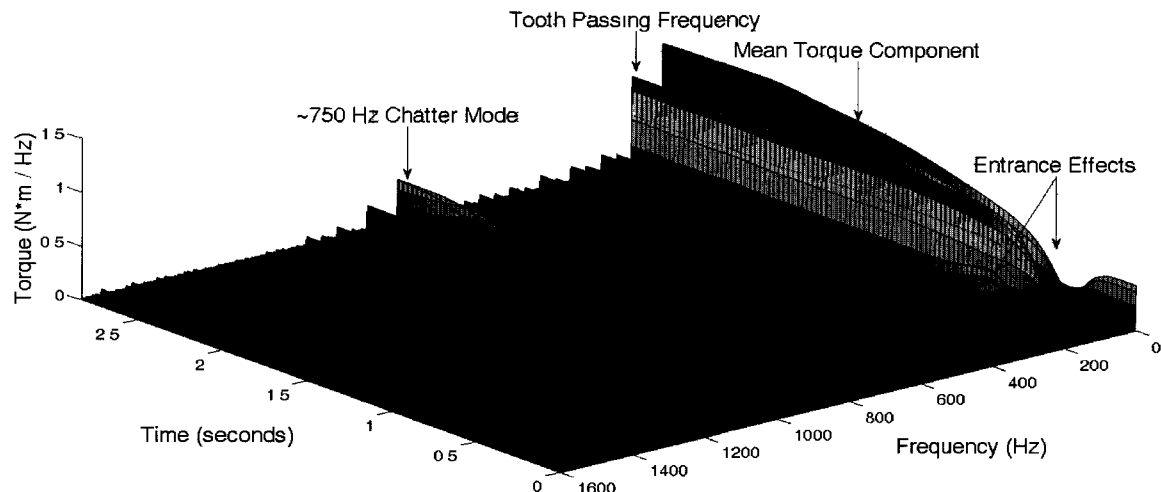


*Figure 3.19: Torque Signal Showing Entrance Effects and Regenerative Tool Chatter*

In addition to tool chatter, torque during workpiece entrance and exit are shown. Specifically, when the milling tool initially contacts the workpiece, the behavior is notably different than during steady state cutting. Although this effect influences surface quality, the author is not aware of any literature thoroughly documenting the behavior of



the tool during this period of rapidly changing engagement. Figure 3.19 highlights the workpiece entrance effects at the beginning of the test. The frequency content of the torque data suggests that the response of the milling system experiences substantial changes during the entrance. It should be noted that Prototype 3 was not fully characterized for bending cross talk in the torque data. While this does not affect the frequency information, the effects of bending in the data are not explored with this tool.

### **3.7 Chapter Summary**

The electret accelerometer based measurements were shown to capture features of the cutting process including tooth passing behavior, tool run out, and tool chatter. Instabilities in the system are detected before onset of chatter due to the signal to noise ratio of the sensors. The electret sensor integrated tools were found to identify build up of instabilities with significant time before escalation of the magnitude. The ability to see the buildup of instability is a significant step towards avoiding unstable conditions and taking corrective action with machine control. This would not be possible without a high signal to noise ratio of placing the sensor inside the tool holder. Spindle speed sweep testing, a novel experimental approach to evaluating stability, was designed for use with the sensor integrated tool holder. Using the electret accelerometer based tool holder, best speeds were predictable and experimental stability lobe diagrams could be created from the spindle speed sweep data. Interesting behavior was seen during the spindle speed sweeps regarding the onset of stability and the decay of unstable modes after the spindle speed has entered a stable condition.

Tool torque was monitored using strain gauge sensors. Torque data was compared to cutting force models as well as a bed dynamometer and power sensor. Similar behavior to the accelerometer tests was observed in the frequency content of the strain sensor signal. The buildup of an unstable condition was observed at high resolution. Entrance effects (when the tool enters the workpiece) were observed. The advantage of using torque over acceleration is a more direct sensing approach to monitor the strain of the material. Torque information is directly correlated to cutting force, thus, its magnitude is more meaningful than acceleration. Moreover, torque does not involve XYZ vector information because it is a couple around the axis of the tool holder. Similar to the acceleration tests, torque was shown to expose system instabilities before escalation to full blown chatter.

## CHAPTER 4

### In situ Chatter Frequency Prediction Using Torque Data

This chapter describes a method to extract chatter frequencies from stable (non-chatter) cutting data by applying system identification methods used in speech recognition. Because the smart tools provide a high SNR, these closed loop frequencies can be estimated without encountering tool chatter. The method explored is called linear predictive coding (LPC) and is used to generate formant frequencies. LPC is an autoregressive technique that creates a simplified model of the data from which frequency tracking can be easily achieved.

As applied to machine tool dynamics, the goal of frequency prediction and frequency tracking is to estimate chatter frequencies from the data before encountering an actual chatter condition. The torque data captured by the sensor integrated tool is proportional to the instantaneous chip thickness during cutting. The instantaneous chip thickness is a function of both the nominal chip thickness and the machine tool system dynamics. The torque data can be approximated as the output from a LTI (linear time invariant) system with the time domain torque signal equal to the periodic chip thickness input signal convolved with the frequency response function (FRF) of the cutting system. This is defined in the time domain as:

$$\tau(t)=p(t)*f(t) \quad (4.1)$$

and in the Laplace domain as:

$$T(s)=P(s)\cdot F(s) \quad (4.2)$$

where  $p$  is the instantaneous tooth passing chip thickness signal (input),  $f$  is the frequency response function, and  $\tau$  is the output torque signal from the sensor data. The cutting system is not the entire machining system and (in the system schematic, Figure 1.3) the smart tool is recording data between the force model and compliance model of the milling system. Linear Predictive Coding (LPC) methods are used to estimate the frequencies in  $F(s)$  which are a result of the entire machine dynamics acting on the chip thickness. While the cutting system transfer function  $F(s)$  could be determined using LPC if the input  $p(t)$  was white noise, it is a periodic signal at the tooth passing frequency. Further, the chip thickness signal is not recorded. Without the chip thickness signal, the major closed loop frequencies can be located, but it does not allow us to determine the transfer function. An important distinction is that LPC is being used to locate the closed loop frequencies during cutting. Since the chip thickness signal is not known, this method does not determine the tool holder, i.e. structure, or work piece FRF.

#### **4.1 Linear Predictive Coding and Formant Frequency Tracking**

Linear predictive coding is a method of creating a frequency spectrum from a model of the data to capture the spectral shape of a data set while disregarding detailed harmonic structures [44,45]. The harmonics of an input signal are not of interest and the

model intentionally lacks resolution on these features so that frequency tracking identifies system modes and not harmonics of the input signal. In a traditional example, it is used to estimate the formant frequencies of lung-mouth-nasal systems for human speech recognition. This technique has never before been applied to machining data. We propose to use the method to determine the dominant vibration modes in the torque signal obtained from the smart tool during a cut. In an end milling system, significant tooth passing harmonics exist throughout the torque spectrum  $T(s)$ . LPC provides a method to distinguish the significant system frequencies from the harmonics of the tooth passing frequency.

The autocorrelation method of LPC chosen for this work is detailed in [44]. Assuming for a given window of torque,  $\tau$ , and model order  $M$ , the present sample is predicted by autoregressing the historical samples of torque data:

$$\begin{aligned}\tilde{\tau} &= a_1 \tau(n-1) + a_2 \tau(n-2) + \dots + a_M \tau(n-M) \\ &= \sum_{i=1}^M a_i \tau(n-i)\end{aligned}\quad (4.3)$$

where  $\tau$  is the prediction of  $\tau(n)$ ,  $\tau(n-i)$  is the  $i^{th}$  step historical sample, and  $\{a_i\}$  are linear coefficients. The sum of squared prediction error takes the form:

$$\begin{aligned}E &= \sum_n \epsilon(n)^2 = \sum_n (\tau(n) - \tilde{\tau}(n))^2 \\ &= \sum_n \left( \tau(n) - \sum_{i=1}^M a_i \tau(n-i) \right)^2\end{aligned}\quad (4.4)$$

By minimizing the sum of squared error,  $E$ , it is feasible to solve for the prediction coefficients  $\{a_i\}$  by setting the derivative of  $E$  with respect to  $\{a_i\}$  equal to zero:

$$\sum_n 2\tau(n-k) \left( \tau(n) - \sum_{i=1}^M a_i \tau(n-i) \right) = 0 \quad (4.5)$$

for  $k=1,2,\dots,M$

This form contains  $M$  unknowns and  $M$  equations:

$$\begin{aligned} \sum_n \tau(n-k)\tau(n) &= a_1 \sum_n \tau(n-k)\tau(n-1) + \dots \\ &\dots + a_2 \sum_n \tau(n-k)\tau(n-2) + \dots + a_M \sum_n \tau(n-k)\tau(n-M) \end{aligned} \quad (4.6)$$

Assuming that there is a finite number  $N$  of discrete samples in the data window  $\tau$ ,

Equation 4.6 can be approximated in Yule Walker matrix form:

$$\begin{bmatrix} r(0) & r(1) & \dots & r(M-2) & r(M-1) \\ r(1) & r(0) & \dots & r(M-3) & r(M-2) \\ \vdots & \vdots & \ddots & \vdots & \vdots \\ r(M-2) & r(M-3) & \dots & r(0) & r(1) \\ r(M-1) & r(M-2) & \dots & r(1) & r(0) \end{bmatrix} \begin{bmatrix} a_1 \\ a_2 \\ \vdots \\ a_{M-1} \\ a_M \end{bmatrix} = \begin{bmatrix} r(1) \\ r(2) \\ \vdots \\ r(M-1) \\ r(M) \end{bmatrix} \quad (4.7)$$

or  $Ra=r$ , where  $\{r(1)\dots r(M)\}$  is an autocorrelation estimate for  $\tau$ :

$$r(k) = \sum_{n=0}^{N-1-k} \tau(n)\tau(n+k) \quad (4.8)$$

The matrix form of Equation 4.7 is solved with the Levinson-Durbin recursive method to minimize the required computation to solve  $\{a_i\}$ . This algorithm is described fully in [45, 46, 47]. Once the coefficients  $\{a_i\}$  are solved, the roots of the model can be found. The poles of the frequency response function,  $F(s)$ , are estimated by treating the model as an all-pole (infinite impulse response) IIR filter:

$$F(z) = \frac{1}{A(z)} = \frac{1}{1 + a_2 z^{-1} + \dots + a_{n+1} z^{-n}} \quad (4.9)$$

The location of the LPC poles can be estimated in real time from a window of the experimental cutting torque data,  $\tau$ . The set of system poles,  $R$ , are found as the

polynomial roots of the filter denominator (Equation 4.9). Recall that the actual system poles can only be determined if  $p(t)$  were white noise. Our use of LPC is to find the dominant system frequencies, referred to as Formant Frequencies.

Formant frequencies are calculated by the phase angle of the LPC poles and scaled by the discrete sampling frequency,  $F_s$  :

$$Fr = \frac{\angle R}{2\pi(F_s/2)} \quad (4.10)$$

where  $R$  are the LPC poles,  $F_s$  is the discrete sampling frequency of  $\tau$ , and  $Fr$  is in units of Hz. The phase angle is calculated by the arctan between the real and imaginary part of  $R$ . For further information, see the MATLAB function “angle” [54].

For the LPC method, it is important to note that we assume our data is both linear and time invariant over a short data window. However, a system that is not assumed to be time-invariant can be solved using other approaches such as the Green function method [47].

## **4.2 Impulse Response Testing**

Several experimental tests are presented to demonstrate the efficacy of the formant tracking method. The first experiment establishes the baseline “static” FRF of the end milling machine structure using the traditional 'hammer test' in X and Y linear directions. The impulse response is measured with a piezoelectric accelerometer mounted to the milling tool. Prototype 4 is struck by a modally tuned hammer and both input and output response is recorded, as detailed in [35-38]. The FRF is estimated as the transfer function between the input and output signals. Both X and Y axes are examined independently.

It is important to have this baseline to validate and contrast estimated system

frequencies with those observed from the LPC method. Although it is not expected that these will exactly match the in-cut results, they should corroborate the number of system modes. Of course, this is dependent on the spindle speed since it is known that chatter frequencies can be different than the open loop natural frequencies of the system [48]. The baseline FRF's are a 'static' (non-rotating and non-cutting) representation of the tool, spindle and machine structure, without workpiece dynamics. Moreover, the spindle is treated as a cantilever, free from engagement with the workpiece material. Figures 4.1 and 4.2 illustrate the baseline FRF for both X and Y directions.

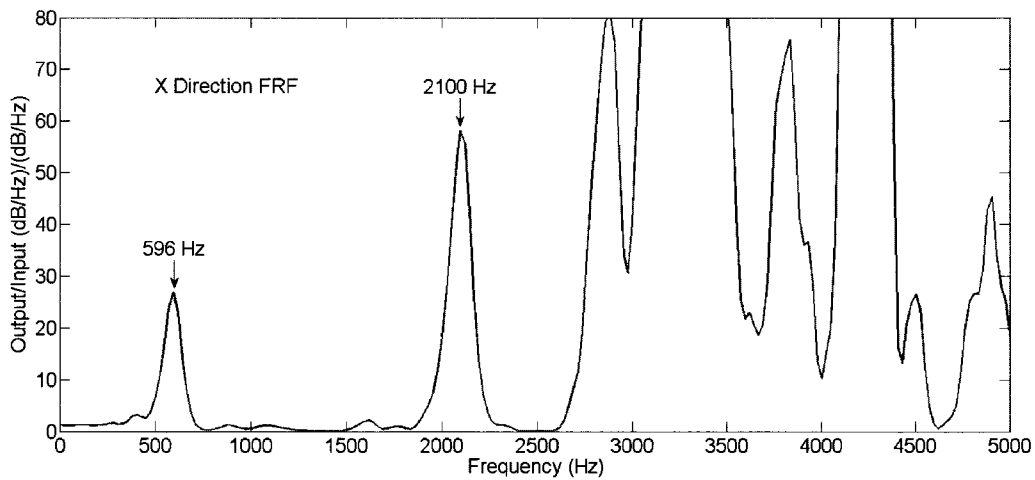


*Figure 4.1: Baseline X Direction Tap Test*

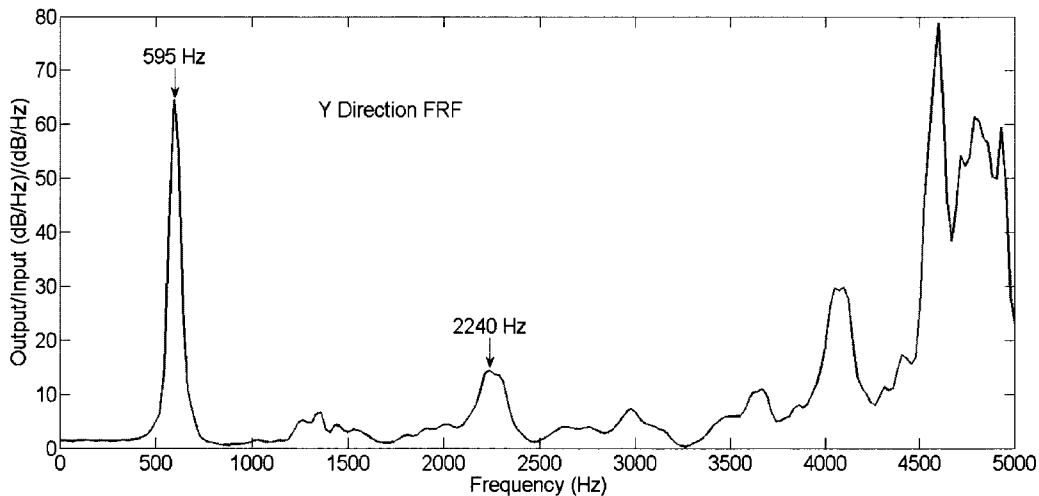


*Figure 4.2: Baseline Y Direction Tap Test*



From analyzing the baseline FRF's, two modes are observed that may be close to the actual chatter frequencies. At approximately 595 Hz, a natural frequency occurs in both X and Y directions. This mode is attributed to the cutting tool compliance which we anticipated to be the most compliant part of the machining system. The second mode may be the result of machine spindle dynamics. The second mode has slight variation between X and Y (2100 vs. 2240 Hz). Frequency content above 2500 Hz for the X direction, and 3500 for Y, is not considered reliable since the input signal did not contain significant energy at these frequencies. A nylon tip was used on the impact hammer to concentrate energy at low frequencies and avoid double taps of the hammer. As a result, the magnitude of the FRF contains no coherent information at high frequencies. It should be noted that for short overhang tools where the spindle contributes substantial response, it is necessary to use a steel tip and supply an impulse that captures higher frequencies [25].

#### **4.3 Application of LPC Methods to Estimate Chatter Frequencies**

A slot cutting test at 45 degrees in the X-Y plane is designed to excite the machine system in X and Y directions (see Figure 4.3). The chatter frequency (or frequencies) are expected to occur near the lowest modes of the system. Recalling that our goal is to estimate the system chatter frequencies from the torque data *before encountering chatter*, the test is run with a shallow axial engagement. Moreover, the test is conducted in a solid clamp-anchored workpiece to minimize the influence of workpiece dynamics. The test conditions are 2501 RPM, axial depth 3.81mm (0.15 inch), at a feed rate of 254 mm/min (10 ipm). The cutting tool selected for this test was a Kennametal Mill 1-10 with a

19.05mm (0.75 inch) cutting diameter and single insert. The material was 6061-T6 aluminum alloy.

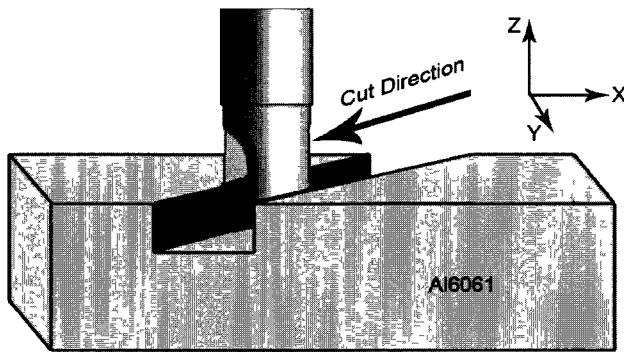


*Figure 4.3: XY Slot Cutting Experimental Orientation*

The torque data collected for this test is shown in Figure 4.4. Prototype 4, the semiconductor based torque sensing smart tool (Prototype 4), was used in this application due to its high sensitivity. No chatter build up was encountered and the workpiece finish remained acceptable. The torque magnitudes are comparable to theoretical estimations from an infinitely stiff mechanistic cutting force model. It should be noted that no run out was present since a single insert cutter was used for the test.

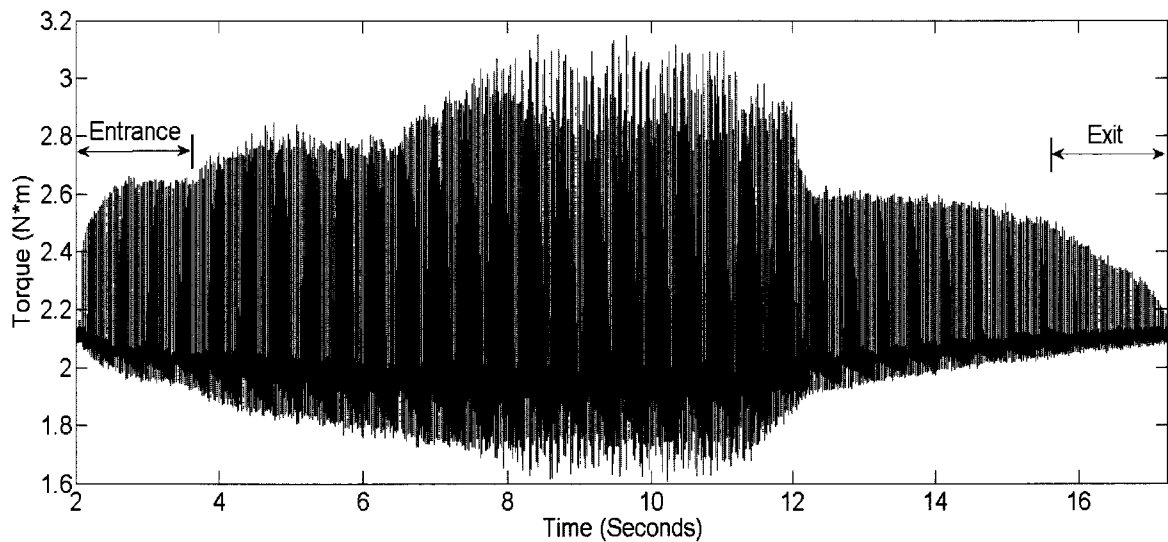


*Figure 4.4: Torque Plot from the XY Slot Cut*

This data is interesting, because the peak torque values increase for a period of time between 7 and 12 seconds. The increase in peak value is during the steady state part of the cut. The root mean square of this data does not change during the period, indicating that the material removal rate (average chip thickness) is unchanged. Peak torque (peak chip thickness) increases during this time suggesting that the system has changing response during the steady state cut. This is supporting evidence that the milling system can undergo changes during a steady state cut. From this torque data, Equations 4.3 through 4.10 are used to generate a set of formant frequencies locating the peaks of the estimated LPC poles. Figure 4.5 shows Equation 4.9 evaluated for a 10 pole model (the four lower formant frequencies shown). These formant frequencies track possible chatter frequencies throughout the cutting process, updated at each window of  $\tau$ . Each window contains 1024 data points collected at 10.24 kHz. 0-4 Seconds and 12-16 seconds contain data from entrance/exit effects.

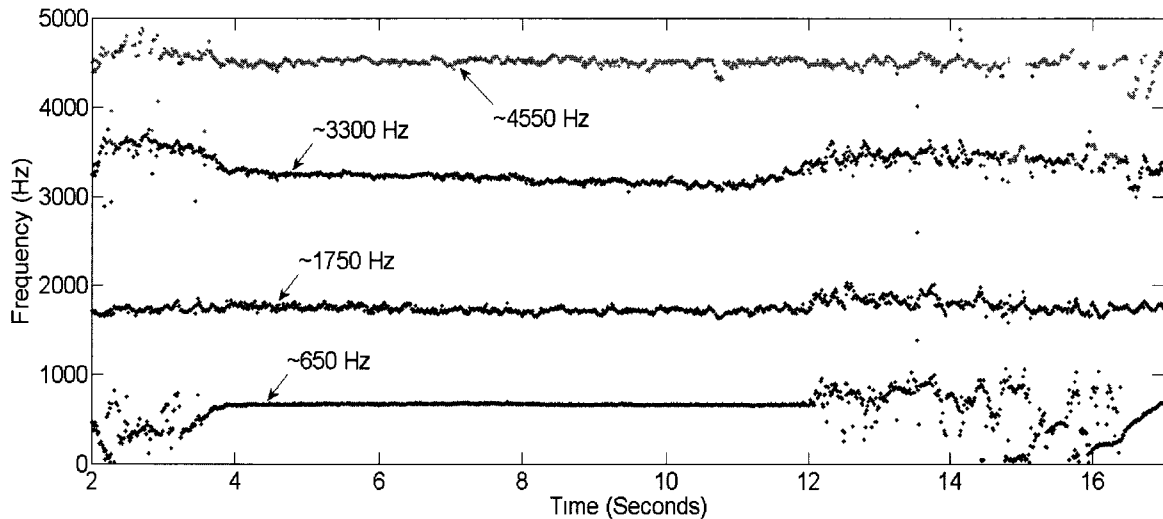


*Figure 4.5: Dominant Formant Frequencies of the XY Slot Cut*

Plots of the formant frequencies agree with the behavior discussed in page 204 of Schmitz/Smith [48], identify that multiple chatter frequencies exist at a given spindle

speed. Drawing a vertical line through the Schmitz plot at any spindle speed intersects multiple chatter frequencies similar to those identified by the LPC method. This plot also shows that chatter frequencies,  $f_c$ , are not always equal to the machine tap test FRF.

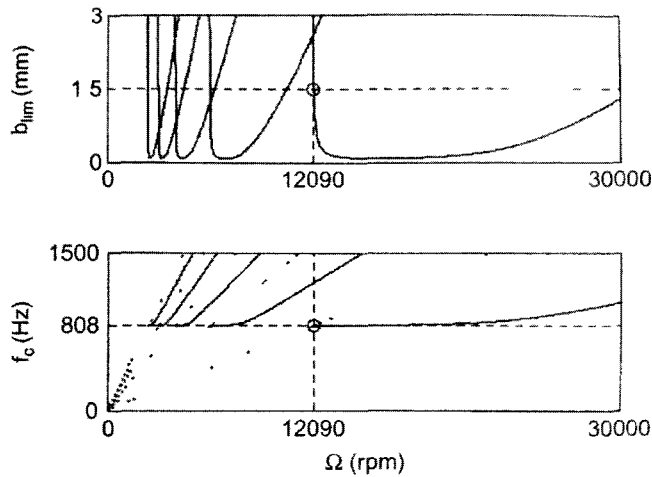
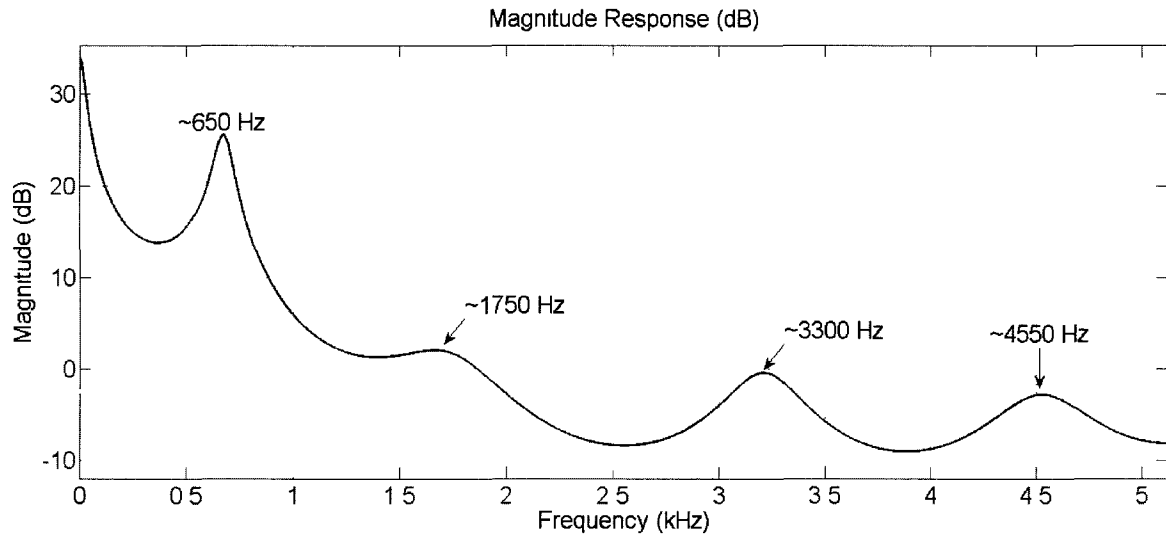


Figure 4.6: Multiple Chatter Frequencies (Schmitz/Smith [48] pp 205)

The formant frequencies represent the peak magnitude locations in the LPC model frequency response. It is observed that the LPC dominant frequencies of  $F(z)$ , are different than the dominant modes in the baseline tap test FRF's (Figure 4.1-4.2). *This is to be expected for several reasons.* Most importantly, the **LPC measures the dominant frequencies such as chatter frequencies, which are not the same as system natural frequencies.** Appendix I expands some justification for tool-engaged boundary conditions that may also contribute to this effect. Figure 4.7 shows a 10th order (five pole) LPC model of the system, estimated from the cutting torque signal,  $\tau$ . Figure 4.7 was generated with the MATLAB Filter Visualization Tool, treating the LPC model as an IIR (infinite impulse response) filter.



*Figure 4.7: 10th Order Model Frequency Response From Cutting Torque Data*

A reader may question the validity of the 10th order model, without a discussion of minimally sufficient model order. Therefore, a 64th order LPC model is presented for the same data window and is shown in Figure 4.8. Based on this comparison, it is evident that there is no substantial improvement in frequency resolution of most modes. However, there is an arguable improvement on the resolution of the second dominant mode, recalling that there are two distinct frequencies for the X and Y transfer functions. It is important to use information from both X and Y directions to determine stability. Altintas [25] discusses the use of a resolved transfer function that combines both X and Y responses depending on the direction cosine of the forcing input. The 64<sup>th</sup> order model has much higher resolution on the system than the 10<sup>th</sup> order model, however this is not helpful since the higher order creates difficulties interpreting the data. One problem with using an extremely high model order is that the tooth passing frequency is captured in the LPC model and could lead to a false-positive identification of a chatter frequency. As the model order grows, the LPC model spectrum approaches the spectrum of the actual data

and no useful filtering of cutting frequencies and harmonics is achieved. It is found that using a minimum model order is preferable to intentionally ignore resolution on the tooth passing frequency and associated harmonics.

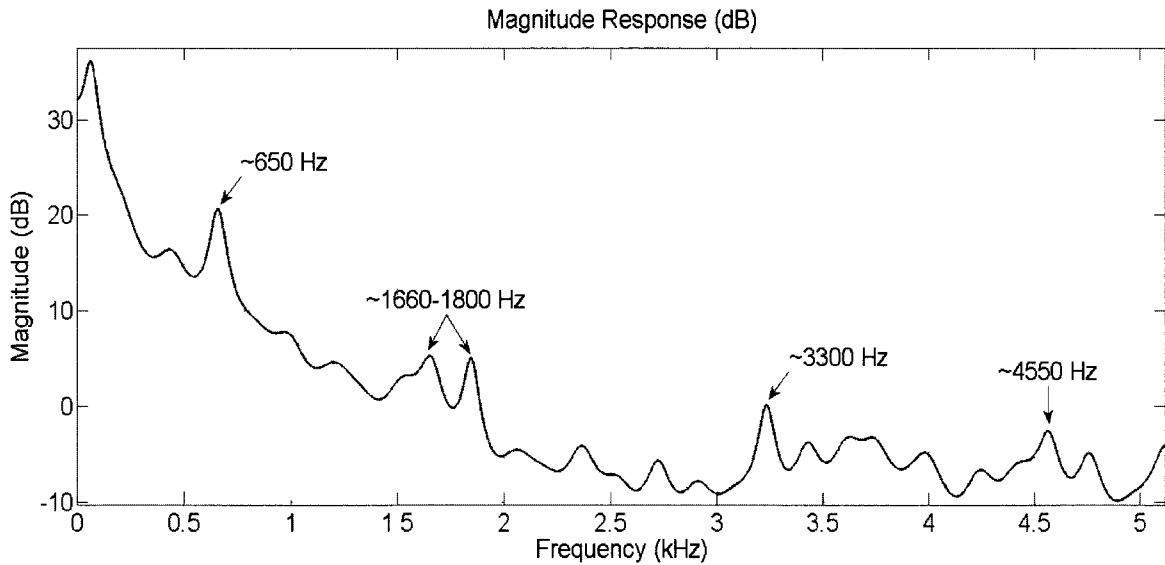


*Figure 4.8: 64th Order Model Frequency Response From Cutting Torque Data*

Figure 4.9 shows the power spectrum of the raw torque data,  $\tau$ , for the stable cut at 3.81mm (0.15 inch) axial depth. Unlike the model spectrum, the raw spectrum is dominated by tooth passing harmonic frequencies and is difficult to interpret to determine the location of dominant system frequencies. By comparing Figure 4.7 to Figures 4.8 and 4.9, it is clear that the LPC method is smoothing the frequency such that tooth passing harmonic frequencies are eliminated while preserving the system's overall response shape. Specifically, the system shape is not readily apparent in Figure 4.9 since the data is dominated with tooth passing harmonics. Removing the tooth passing frequency and its harmonics is the method used in applications such as the Harmonizer (53), however, knowledge of the tooth passing frequency is required. There are also hardware benefits to the LPC methods, since speech recognition has been optimized for use on

microprocessors with DSP functionality. Comb filters require reformulation for changes in spindle speed, which is slower than LPC methods which do not require updated filters in response to the input signal. In control applications, where time delay is critical, the LPC methods are preferable.

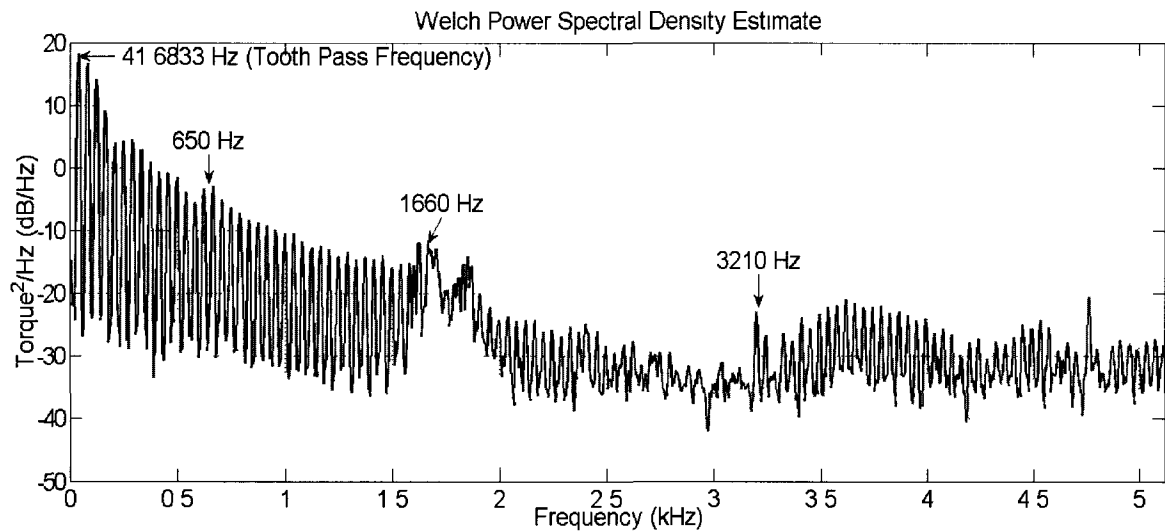
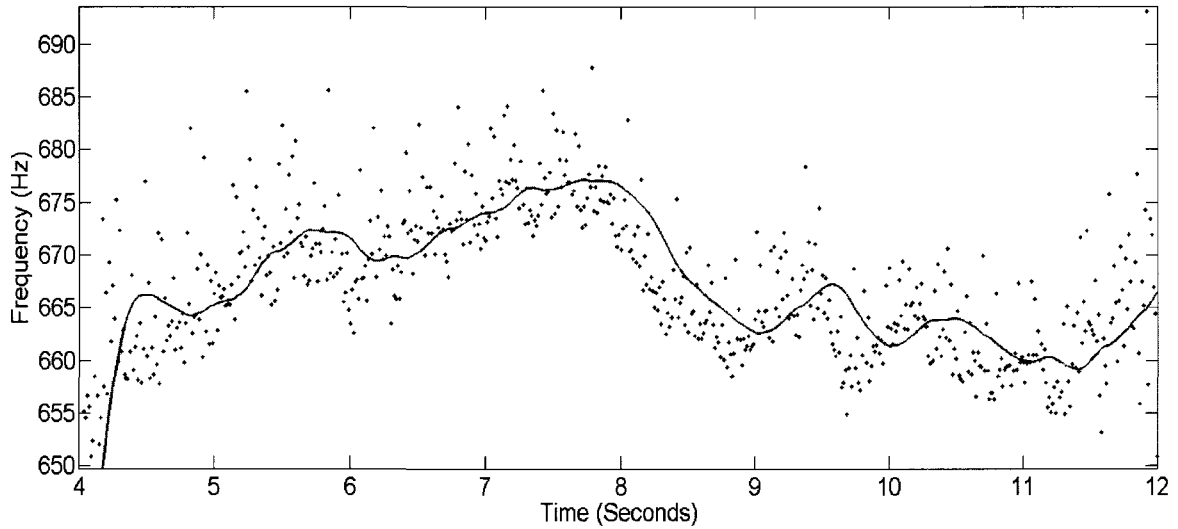


Figure 4.9: PSD of Stable (no chatter) Raw Torque Data

#### **4.4 Time Varying Effects on LPC Frequencies and Predicting Stable Cutting Speeds**

Because the LPC frequencies are estimated from the streaming torque data, time varying effects in the modes can be observed. An interesting phenomenon is drift captured in the formant frequencies during steady state cutting. This suggests that the chatter frequency, hence modes of the system, may be shifting throughout the cutting process. Figure 4.10 shows the lowest formant frequency from Figure 4.5, corresponding to the ~650 Hz mode of the cutting tool. This frequency is observed to drift within a 15 Hz envelope of its mean value. This effect is fascinating and warrants further investigation. This may occur due to changes in the XYZ position of the machine bed, changes in the workpiece location, and changes related to compliance from workpiece

clamping unit.



*Figure 4.10: Drifting System Poles During Steady State Cutting*

The literature [48] describes difficulties in accurately predicting stable spindle speeds at low RPM. One cited cause is that bearing stiffness rapidly changes at low spindle speeds. An added issue is close lobe proximity at low spindle speed. The drift we observe in the LPC poles may reflect the bearing stiffness or machine position.

At low spindle RPM, the stable parameter space is highly sensitive to small variations in the chatter frequency,  $\omega_c$ . Thus, for closely spaced lobes a small change in the chatter frequency can indicate a large shift in stability (see Chapter 1 for a discussion of stability lobes). For this reason, estimating the LPC frequencies is critical to maintaining stability at low spindle speeds.

#### **4.5 Validating the LPC Frequencies by Inducing Chatter**

Finally, the validity of the LPC model is tested by conducting an identical cut at an increased axial depth of 7.62 mm (0.3 inches). By increasing the axial depth, chatter is induced and the actual chatter frequency can be observed. The true chatter frequency is



observed in the power spectrum of the raw torque data at  $650 \pm 10$  Hz, plotted in Figure 4.11.

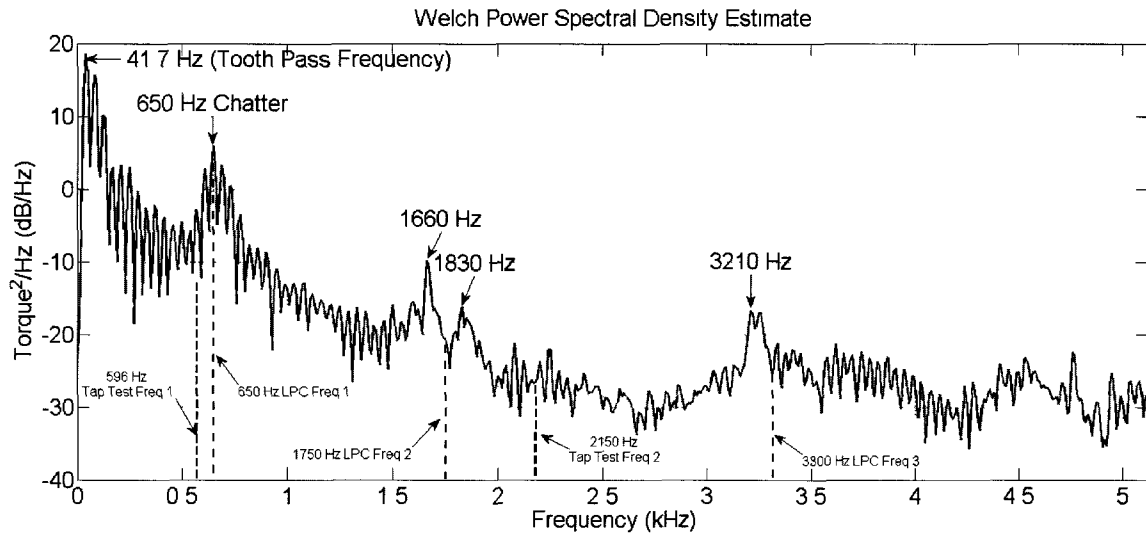


Figure 4.11: PSD of Raw Torque Data Under Induced Chatter

Based on the experimentally obtained results, the LPC model low frequency mode of 650 Hz matches the significant chatter frequency shown in Figure 4.11. The results of the tap tests, i.e. the baseline FRF's, give little indication of the actual chatter frequency. Obviously, because of the accurate chatter frequency prediction, the LPC model would give an estimation of stable spindle speeds for safe cutting when the formant frequencies are used to estimate best speeds.

#### **4.6 Changes in the LPC Frequencies as a Function of Spindle Speed**

With an in-process estimation of the LPC frequencies, a feedback control mechanism can be developed to adapt machine tool process parameters in response to predicted chatter conditions. For this reason, it is important to understand the effect of machine tool process parameters, most importantly spindle speed, on the accuracy of the LPC mode

estimation method. Because spindle speed is a control variable with respect to machine tool stability, its effect on the chatter frequency is important. To explore this, a suite of slot cutting tests is repeated at two axial depths of cut. The first depth, 2.54 mm (0.1 inches), is intended to test the ability of the prediction method to forecast the chatter frequency without encountering a tool chatter condition. The second depth, 7.62 mm (0.3 inches), is designed to induce regenerative chatter and validate the chatter frequency predictions made from the first depth. Figure 4.12 is a conceptual model of the experimental setup for this test.

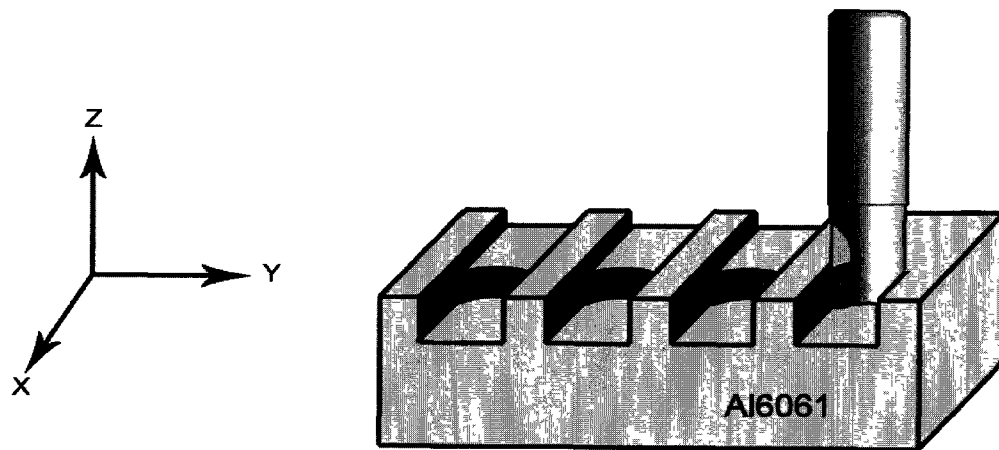


*Figure 4.12: Multi-Depth Slot Cutting Experimental Orientation*

Table 4.1 shows the predictive (2.54 mm depth) versus the induced chatter frequencies as a function of spindle speed. The average chatter frequencies are shown. The drift present around the average frequencies is within a 15 Hz envelope of a 10 point moving average. The outcome of these tests further validates the ability of the LPC method to estimate the correct chatter frequency locations from the cutting torque data. In all cases, the chatter frequency is estimated as the lowest formant frequency from the LPC model.

Table 4.1: *Predicted and Actual Chatter Frequencies as a Function of Spindle Speed for Slot Cuts*

		Spindle Speed (RPM)						
	Axial Depth	2501	2750	3000	3250	3500	4250	4750
Predicted (Hz)	2.54 mm (0.1")	649	664	673	675	678	686	693
Actual (Hz)	7.62 mm (0.3")	655	667	679	683	679	686	680

The predicted versus actual chatter frequencies are consistent, acknowledging that these are average values and the actual values drift in an envelope (see Figure 4.10).

Plotting the induced chatter frequencies over the range of spindle speeds produces a nonlinear relationship. This effect is documented in time domain simulations by Schmitz [48] where chatter frequency becomes a function of spindle speed. In their work, tap test data is used in the model but it has been shown by [49,50,51] that the spindle frequency response changes with spindle speed. This would change the chatter frequency prediction of the simulation. Although the change in chatter frequency is within 30 Hz, system stability is highly influenced by small changes at low spindle speeds. Figure 4.13 shows the relationship between observed chatter frequencies and spindle speed. The literature [49,50,51] documents that the tap test FRF does change as a function of spindle speed, affecting stability estimation and increasing the difficulty of selecting stable process parameters. Hence, there is need for an “in-process” estimation of the chatter frequencies to potentially update cutting parameters to reflect real conditions.

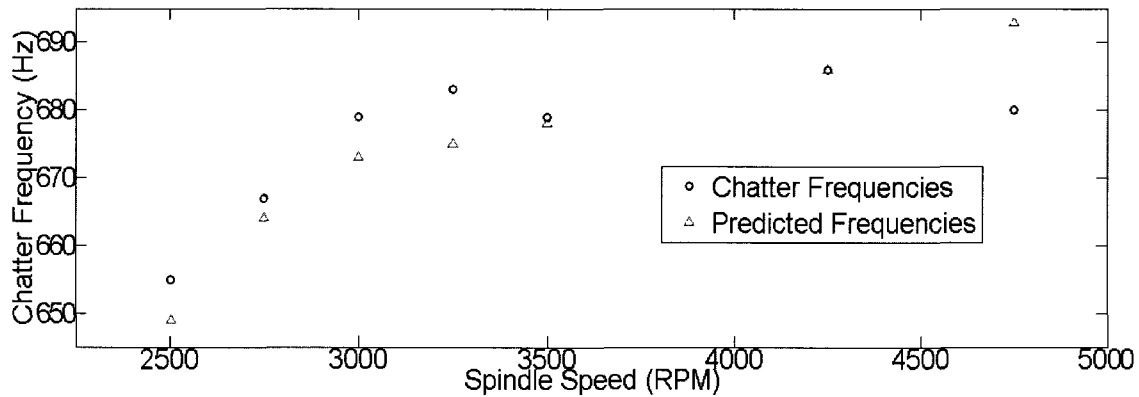


Figure 4.13: Chatter Frequencies vs. RPM

#### **4.7 Estimating Chatter Frequency with LPC during Partial Engagement Cutting**

To this point, we have discussed examples of estimating an in-process chatter frequency based on torque data from various slot cutting scenarios. It is also necessary to demonstrate the method for partial engagement cutting. To do so, partial radial immersion cuts in the X machine direction were conducted at 4.7625 mm (0.1875 inch) radial depth and 2501 RPM. Figure 4.14 is a conceptual model of the experimental setup for this test. Figure 4.15 shows the LPC model spectrum and peak formant frequencies for this test.

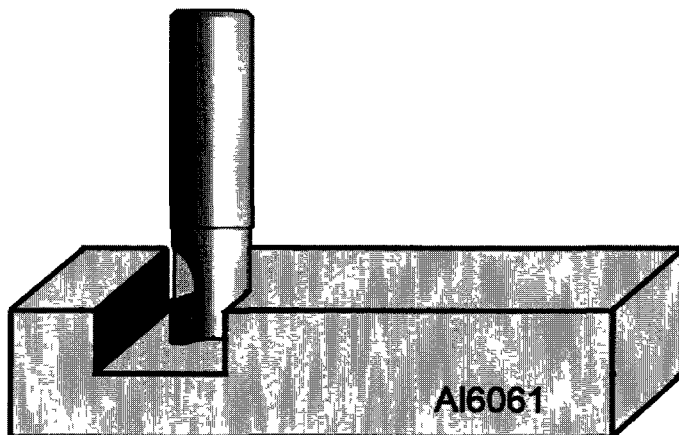
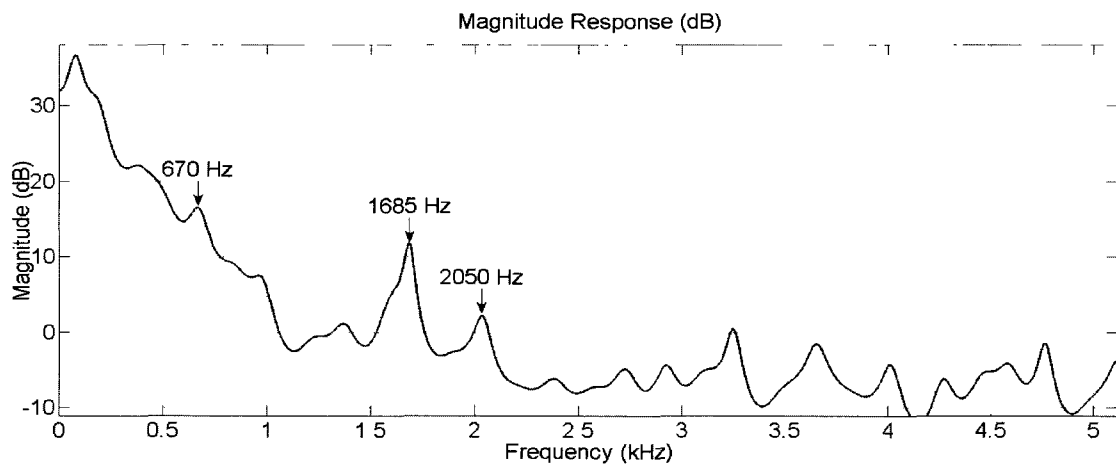


Figure 4.14: Quarter Radial Immersion Experimental Orientation

For the  $\frac{1}{4}$  immersion cutting experiments, the model shows frequencies that are similar to those present in the baseline FRF (obtained by the hammer test). Unlike the slot cutting examples, this system does not chatter in radial immersions under 9.5250 mm, regardless of axial engagement. This was observed for both up milling and down milling experiments. However, despite the inability to produce chatter at light radial engagement, the estimated chatter frequencies correlate with those obtained from the slot cut. While chatter frequencies can be determined from the  $\frac{1}{4}$  immersion cut as shown in Figure 4.15, it is much more difficult to select a dominant chatter frequency. More experiments are needed to determine the cutting conditions necessary to accurately determine the dominant chatter frequencies.



*Figure 4.15: 64th Order Model Frequency Response From Quarter Radial Immersion Cutting Torque Data*

#### **4.8 Chapter Summary**

The machining system chatter frequencies can be estimated from cutting torque data collected from a wireless sensor integrated end milling tool holder. Using LPC methods, the model frequencies, (i.e. chatter frequencies) can be estimated in real time from windows of cutting data, revealing the chatter frequencies during highly stable cutting

conditions. This is an exciting advance from traditional methods that estimate chatter from the impulse response (tap test) of the machine, particularly for low spindle speeds where stability becomes highly sensitive to small changes in the spindle speed. The traditional tap test method neglects aspects of the rotating/cutting system and gives a less accurate representation of the system frequencies. The ability to exploit formant frequency tracking to follow changes in the closed loop modes and hence chatter frequencies has also been demonstrated. The techniques are computationally efficient since low model orders provide sufficient system resolution, processing in under a millisecond per data window on a modest PC laptop. The ability to predict unstable frequencies from highly stable cuts is beneficial to *ad hoc* process planning and adaptive adjustment to the process parameters.

LPC estimates the frequency response of the system assuming white noise input to the system. In this application, **the closed-loop frequencies identified by the LPC method are not the same as the frequencies associated with the open-loop system poles.** An LPC pole is located at a possible chatter frequency, not an actual open-loop system pole, as found by the traditional tap test. Thus, the LPC poles can be thought of as the closed-loop poles identified by chatter frequencies. Often, particularly for low cutting speeds, the chatter frequency is very close to the natural frequency of the system.

The LPC poles (i.e. chatter frequencies) are a function of both spindle speed and radial depth. Figures 4.15 and Figure 4.8 demonstrate the differences between two radial immersion cases. The prediction of varying chatter frequencies over spindle speed is documented in the literature [48], however, the effect of radial depth requires more investigation. This leads one to believe that axial depth may also have an effect on chatter frequency, another avenue for future work. Clearly, engagement has an effect and could be attributed to boundary conditions (discussed in Appendix I).

Using the LPC method, there are a number of issues demonstrated with static tap tests regarding changing system response. The tap test is insufficient for selecting system conditions, particularly at low spindle speeds and can be assisted or improved by an online updating method such as LPC.

## CHAPTER 5

### Predicting Chatter Frequency With Coupled Workpiece and Tool Holder Dynamics

The machining of complex geometries, thin walls, and work holding arrangements leads to a complicated scenario of multiple natural frequencies contributed by different components of the machining system. The interaction between the dynamics of these different systems is difficult to predict. The smart tool holder can be used for frequency-based analysis of a multiple compliance system to study the interaction between workpiece and tool holder dynamics. This is an extension and application of the Linear Predictive frequency based analysis presented in the previous chapter. By introducing multiple frequencies of interest, the value of the LPC techniques can be evaluated using a system with multiple feasible chatter frequencies.

A series of experiments was conducted using the torque-measuring smart tool Prototype 4, a slender aluminum workpiece (cross section of 1.5" by 0.875"), and a bed vice clamp. The setup (see Figure 5.1) was designed to anchor the workpiece in a cantilever orientation, such that its natural frequency could be controlled based on overhang length. The test setup included slot cuts in the workpiece at a depth of 0.15" (3.81mm). Cuts were made in the Y direction starting at the top of the beam. This depth



was not sufficient to cause chatter, but was close to an unstable depth at longer workpiece overhang lengths. This depth was chosen from empirical observation. Material was removed from the workpiece after each test cut to clean the face of the workpiece.

A second set of tests, discussed in Section 5.2, was run to evaluate chatter when the axial depth was increased to 0.175”.

Figure 5.1 shows the cantilever workpiece and bed vice. Before each test, a tap test was conducted using a National Instruments PXI data acquisition computer, impact hammer, and accelerometer fixed to the workpiece. The accelerometer setup can be seen in Figure 5.2. The vibration data collected from the tap tests gives an estimate of the cantilever's natural frequency at the various overhang lengths.

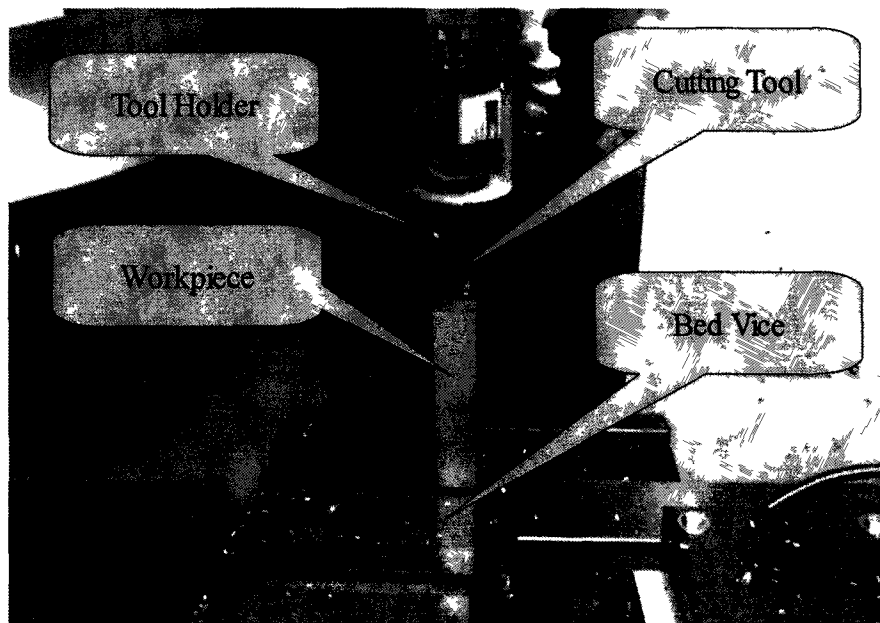


*Figure 5.1: Cantilever Workpiece and Tool Holder*

The parameters of these experiments are constant with the exception of cantilever

length. The feed rate was held at 10 ipm, spindle speed was held at 2501 RPM, a single tooth Sandvik R390-11 T3 08E-NL tool with 3/4" (19.05mm) cutter diameter was used. Table 5.1 identifies the cantilever lengths, in increments of 0.15" (3.81mm). The first fundamental frequency from the tap test data are also shown, for reference. No second fundamental frequency was observed. Figures 5.2 and 5.3 show example cantilever tap test data.

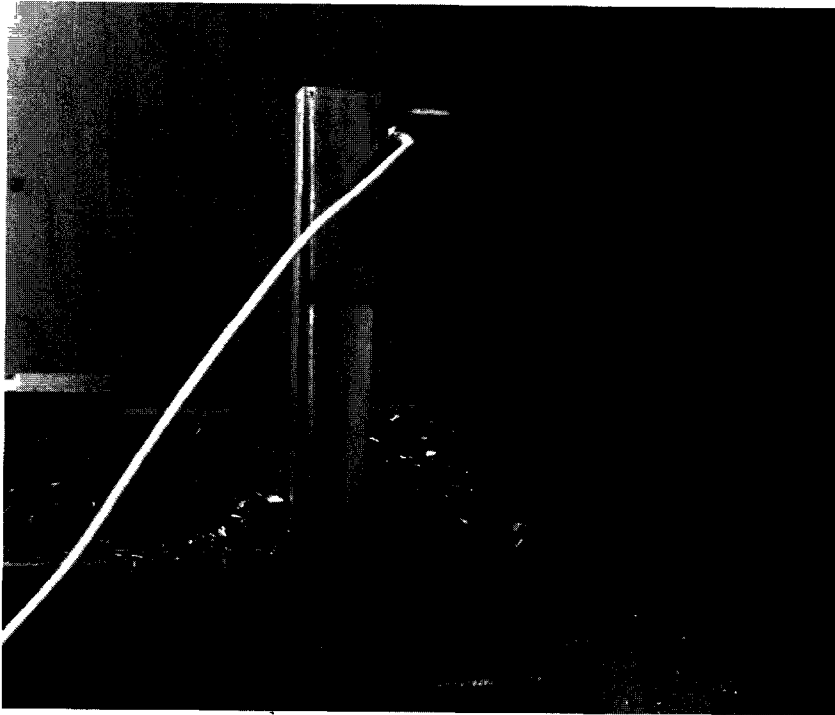


*Figure 5.2: Cantilever with Tap Test Accelerometer*

*Table 5.1: Cantilever Workpiece Lengths*

Bar Length (mm)	Bar Tap Test Frequency (Hz)	Tool Tap Test Frequency (Hz)	1 <sup>st</sup> LPC Frequency (Hz)	2 <sup>nd</sup> LPC Frequency (Hz)
55.37	3025	595	651	-
59.18	2750		655	-
62.99	2384		653	3409
66.80	2294		649	3200
70.61	1968		664	2750
74.42	1813		675	2589
78.23	1690		2469	4587
82.04	1565		2391	4406
85.85	1470		2353	4390
89.66	1370		1901	4500
93.47	1275		1808	3490
97.28	1203		1750	3421
101.09	1150		1605	3204
104.90	1075		1510	2902
108.70	1005		1450	2751

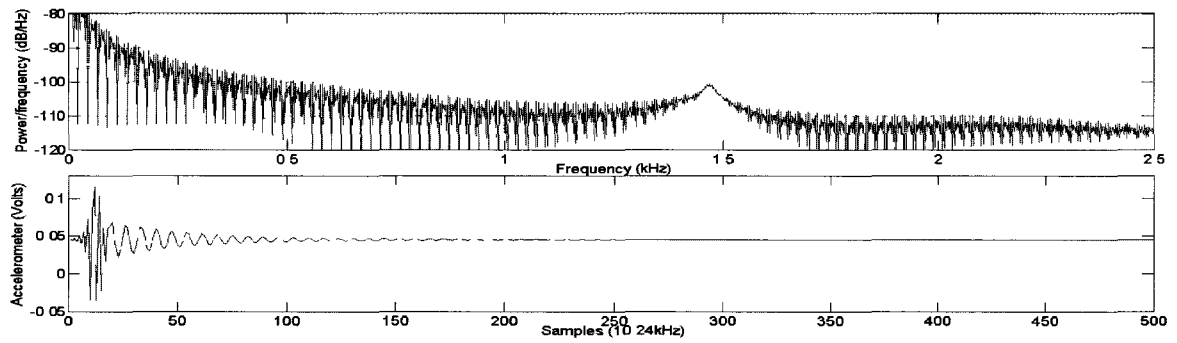


*Figure 5.3: 85.85mm Cantilever Tap Test*

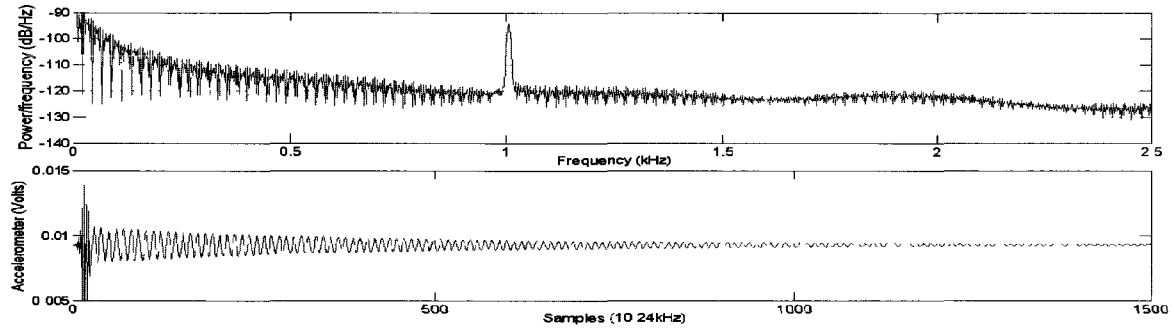


Figure 5.4: 108.70mm Cantilever Tap Test

### **5.1 Using the LPC Model as an Adaptive Filter**

The previous discussion of LPC focused strictly on tracking the frequency content of the torque signal through time. Though it is useful to predict the movement of a particular mode, the behavior of the entire system is not observed at a single frequency. A more comprehensive view of the dynamics is presented if the LPC coefficients are used to track the dominant frequencies through time. Evaluating the impulse response of Equation 4.9 produces the LPC model output, which can be tracked through time. Because the LPC model is recalculated at each time window of data, the time-updated model is representing the changing dynamics in the system. It is important to understand the validity of frequency analysis with the LPC methods is dependent on a small time window in which the assumption of linear time invariant data is valid. The LPC model is created from autoregression of the data over a small time window. The model assumes the torque signal is the output from a fictional system excited with white noise. The model represents the torque signal at a small instance in time and does not incorporate the time delay or feedback present in the real system.

Because the LPC model is data dependent, it adapts to changes in the dynamic system due to variables in the cutting system. These variables include bed location, workpiece

fixturing, workpiece dynamics, and perturbations in the spindle speed. The LPC autoregressive technique assumes the system is linear and time invariant (LTI) with a white noise input and measured torque or vibration. Autoregression system identification techniques consider the data to be the output from a black box system with a white noise input. This modeling approach does not explicitly contain the time delay responsible for tool chatter, nor any feedback of the real system. However, the torque data output does contain the effects of the time delay. The LPC creates a linear model that is representative of the cutting torque signal at the time of data measurement. As cutting conditions change, the linear system model will change. For this reason the LPC model is updated continually through time so that each LPC model is an accurate model of the torque signal for the short time window being represented. The resulting LPC model can be thought of as an adaptive filter, since the frequencies of the LPC model change along with data from the cutting system. The LPC model captures the torque signal frequency, which result from both time delay and changing system dynamics. Tracking changes in the LPC model response through time shows that changes are occurring in the cutting system. It should be understood that these changes take place during 'steady state' cutting and unmeasured variables are changing during cutting. These variables may be as simple as XYZ stiffness, or more involved phenomenon such as built up edge, workpiece material variations, temperature effects, or system damping.

Figure 5.5 shows the LPC model frequencies from a steady state cantilever cutting test at a workpiece length of 108.70mm. Recall that the workpiece tap test for this experiment identified a workpiece natural frequency of 1005 Hz. The cutting tool natural

frequency is approximately 595Hz as shown by the tap test. However, the cantilever cutting data shows the first dominant mode to be approximately 1500 Hz. The cutting force is being generated between two cantilevers, and can be modeled as a force applied to two springs in series. However, since two cantilevers (i.e. the workpiece and the tool) are in end contact through the cutting engagement, the real boundary conditions are more complicated. Appendix I expands the evidence for a change in frequency, according to the boundary conditions of cantilevers with different support types at the tool-workpiece interface. The frequency increase is too great to be explained simply by the change in boundary condition, particularly since the frequency is higher than slotting in a solid block. By no means is a full explanation offered, beyond postulating that boundary conditions need to be further explored as future work. This is a nonlinear system and would require modeling and simulation to predict the behavior.

The most interesting effect that is observed from Figure 5.5 is the changing frequency and magnitudes estimated by the LPC method. If the cutting system variables were truly steady state, the frequency and magnitude would remain constant once entrance effects were completed. Instead, the modes are seen to shift in magnitude, peak location, and half-power points (the width of the modes changes through time). Again, this may be attributed to nonlinear effects in the system that could be the subject of future work.

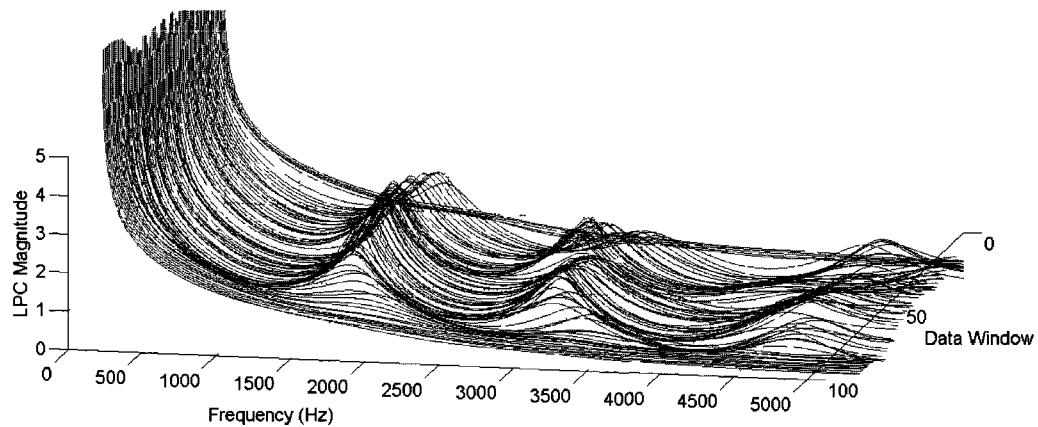


*Figure 5.5: LPC Predicted System Frequencies Throughout Cut (Cantilever 108.7mm)*

Similar results are observed on other cutting tests, Figure 5.6 is an example from a smaller cantilever workpiece overhang of 85.85mm. It was expected that the smaller cantilever length would produce a higher frequency response and this was confirmed by the LPC method. Note that the abrupt change in frequency shown in Table 5.1 is based on the system chatter frequency jumping from that of the workpiece to the tool holder system. Before this point, there was a consistent increase in system frequency as the cantilever was cut shorter.

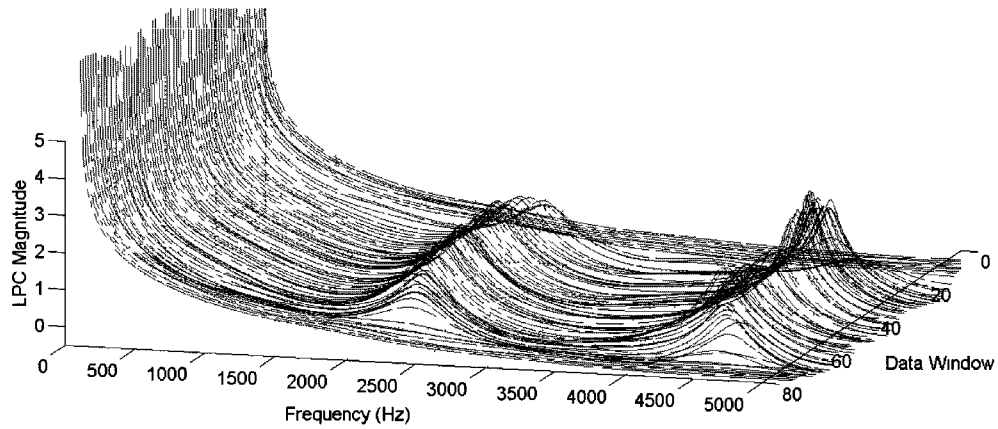


*Figure 5.6: LPC Predicted System Frequencies Throughout Cut (Cantilever 85.85mm)*

The frequencies predicted by LPC can be used to estimate an idealized linear system stiffness, given assumptions about the mass of the system. To make an estimate of stiffness, an LPC frequency is associated with a specific component in the system and the distributed mass of the component is used to approximate the stiffness value. This method assumes that the LPC frequency is close to the natural frequency of the mechanical system. It does not consider damping; the influence of damping is small and the approximation shows the behavior of the stiffness. The ideal linear stiffness predicted by the closed loop LPC frequency is approximately  $5e6$  N/m. The actual and linearized model stiffness may have significant differences as a result.

For example, for the cantilever case of 85.85mm, the cantilever has a total mass of 81gm (0.081kg). The dynamic mass is approximately 0.243 the total mass in a cantilever, 0.0196 kg. For a derivation of dynamic mass, see Appendix I. The lowest LPC frequency observed in the 85.85mm cutting test is 2350 Hz. The natural frequency of the cantilever at 85.85mm is 1470Hz. Using the LPC frequency, the stiffness of the system is estimated at 4,360,000 N/m (  $k=(2350*2\pi)^2*0.0196$  ). Using the natural frequency of the



cantilever tap test, the stiffness is 1,706,000 N/m (  $k = (1470 * 2\pi)^2 * 0.0196$  ). There is a significant difference between the stiffness estimated by the LPC frequency and the workpiece tap test frequency. A difference is expected, as the LPC frequency is the frequency of the lowest closed-loop mode. The workpiece tap test only estimates the open loop mode of the workpiece system.

It is understood that the linearized stiffness estimated from the LPC frequency does not reflect the actual stiffness(es) in the real system. However, it has been computed to demonstrate a point regarding the statistical spread in system variables. Repeated calculation of the stiffness shows that there is a statistical distribution around the average stiffness in the cut. This corroborates with the data plotted in Figure 4.10 which shows drift in the predicted frequency. This is useful, for instance, in modeling the system and providing a way of increasing model accuracy. Figure 5.7 shows the distribution of estimated stiffness for constant cutting conditions. This is an important concept to digest, since the LPC model can be used to generate a distribution of stiffness values for a steady state cut. Hence, this information is used in the future work section to generate a statistical distribution of stability lobe diagrams. An example distribution of calculated stiffness is given in Figure 5.7 for the 85.85mm cantilever length.

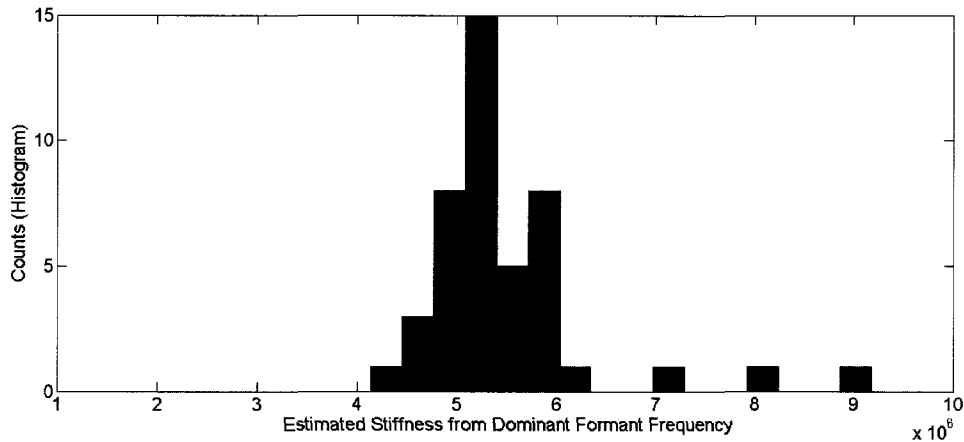


*Figure 5.7: Statistical Variation of Stiffness Estimated from Chatter Frequency*

## **5.2 Closed Loop Pole Magnitude and Bifurcation of the Chatter Frequency**

The results from the cantilever cutting test are intriguing, and show that there is an exchange of energy between workpiece and tool-based response favoring the most compliant mode. This jump in the lowest LPC frequency is evident from Table 5.1. Although this is intuitively true, the point at which this exchange happens could not be predicted. Specifically, the rotating stiffness of the tool holder/spindle cannot be measured accurately while rotating. Using frequency data from the smart tool holder, the observed chatter frequency can be recorded throughout cutting. It is then possible to determine which system (tool holder, or workpiece) is contributing the dominant chatter mode.

An abrupt transition between workpiece-dominated and tool-dominated response can be seen when the cantilever workpiece has become short. This happens around 75mm in cantilever length. By applying position controlled force to the dynamometer, the static stiffness of the tool is measured to be 4,728,424 N/m in the X direction and 6,304,566 N/m in the Y direction. The measurement of cantilever frequency suggests that the tool

and workpiece shows that the cantilever and tool have a natural frequency in the same order of magnitude. It is possible that a bifurcation of chatter frequency could occur at any point within this range. The rotating stiffness of the tool, as stated previously, is different than the static stiffness. The inability to measure the rotating stiffness of the tool makes it difficult to estimate the exact point where chatter frequency transitions from tool-dominant to a workpiece-dominant regime.

To make sense of this transition/bifurcation, it is helpful to observe the behavior plotted on the same scale, vs. cantilever length. Prior information, collected from the workpiece tap tests, gives the trend in cantilever natural frequency. Cuts were conducted at an increased axial depth of 0.175" so that chatter was encountered. Torque information collected during the cut and processed with LPC shows the trend in the system frequencies. From a workpiece length of 100mm to 75mm, the workpiece chatter frequency follows the trend of workpiece natural frequency. Unlike the workpiece, the tool holder frequency is relatively consistent and does not exhibit large changes associated with changing length and mass. Once the chatter frequency transitions between workpiece and tool holder frequencies, the chatter frequency is shown to stabilize around that of the tool holder. The LPC pole magnitudes are plotted for both the tool holder and workpiece. Although the LPC magnitudes are relative, they can be compared to each other and their trend is helpful in determining the dominant mode in the system. The observed dominant chatter frequency can be superimposed onto this plot to highlight the point at which chatter jumps from workpiece-based to tool-based motion. The LPC frequency of highest magnitude is used to identify the "dominant" frequency.

Figure 5.8 shows this information plotted against cantilever length.

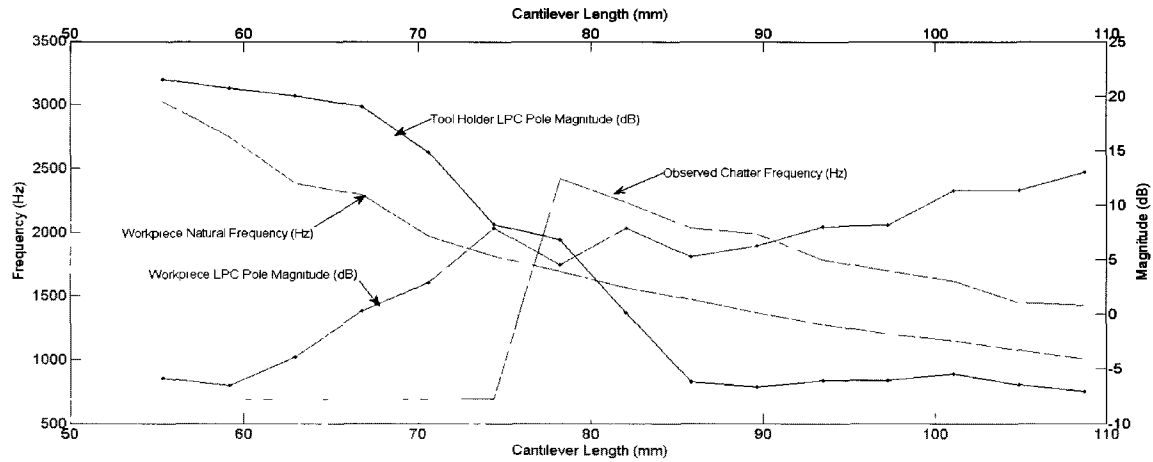


Figure 5.8: Transition between tool and workpiece chatter during cantilever cutting experiments

### **5.3 Chapter Summary**

The system dynamics are evaluated in terms of the LPC model coefficients. A suite of cantilever cutting tests was performed to ensure that LPC was correctly following changes in the system frequencies resulting from the changes in the stiffness of the system. It was found that the coupled cantilever-tool LPC frequency was different than that of the tool or cantilever natural frequencies. Inducing chatter confirms that the LPC frequency is the observed chatter frequency. Chatter frequency versus LPC pole frequency and magnitude is presented to highlight the bifurcation between tool-based chatter and workpiece-based chatter frequencies over a changing workpiece stiffness.

## CHAPTER 6

### Time Domain Modeling of Tool Chatter to Capture System Behavior

#### **6.1 Time Domain Cutting Tool 2DOF Model**

A time domain model was created to replicate the spindle speed sweep testing described in Chapter 3 and to investigate the phenomenon of phase hysteresis observed in the sweep experiments. In this model the workpiece is infinitely stiff.

The model developed for this analysis is a second-order two degree of freedom system with unique directional properties for each axis and a delayed feedback of surface profile. The dynamic model is a spring-mass-damper in each axis, X and Y. The dynamics of each axis are coupled by the direction cosines of force input, the magnitude of which is a function of the instantaneous chip thickness. To simplify the model, it was restricted to a zero helix angle cutter with one or two teeth. This assumption is reasonable because the cutting tools used for experimental testing are steep angle insert cutters. However, assuming a straight flute introduces some error.

The parameters for this system were measured from static tests conducted on the Fadal mill spindle. As a result, the physical parameters of stiffness and damping are presumably different from those during experimental tests when bearings are in motion and workpiece engagement occurs. Regardless, the static parameters have a sufficient

accuracy (similar order of magnitude) to produce a realistic simulation. The stiffness was measured by displacing the axes in small increments while the spindle was fixed against the bed dynamometer. The stiffness includes both the stiffness of the spindle and the tool holder fixed in the spindle. The stiffness was notably different in X versus Y directions, possibly due to the geometry of the spindle and the tool. The spindle is stiffer in the Y direction which can be understood by the way the spindle is supported in Y. This test was conducted for both X and Y axes to obtain force vs. displacement points to estimate the stiffness (Figured 6.1 and 6.2).

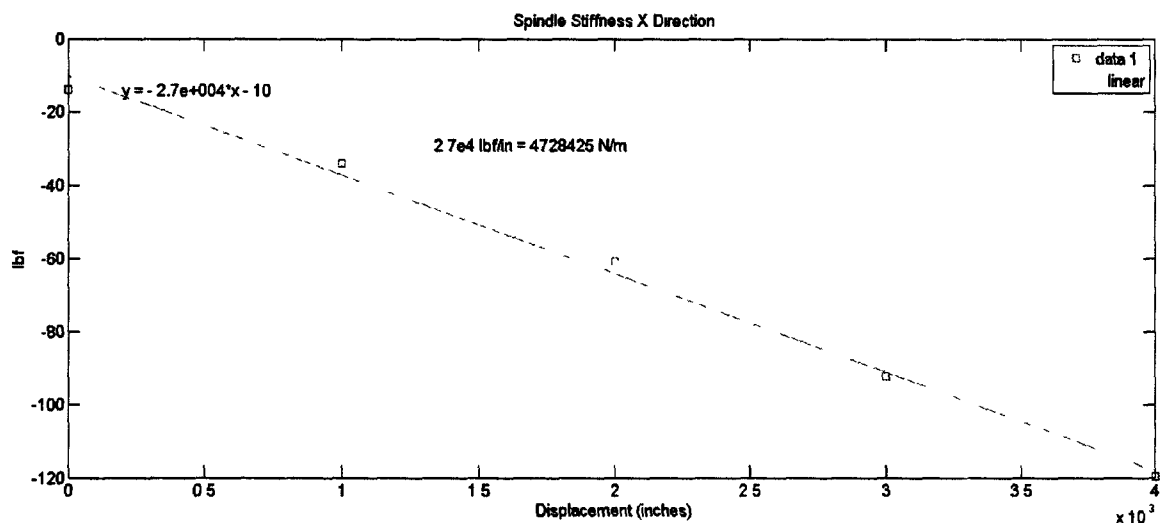


Figure 6.1: Spindle+Tool Stiffness X Direction

Nonlinearity in the response may be attributed to loading of the spindle bearing.

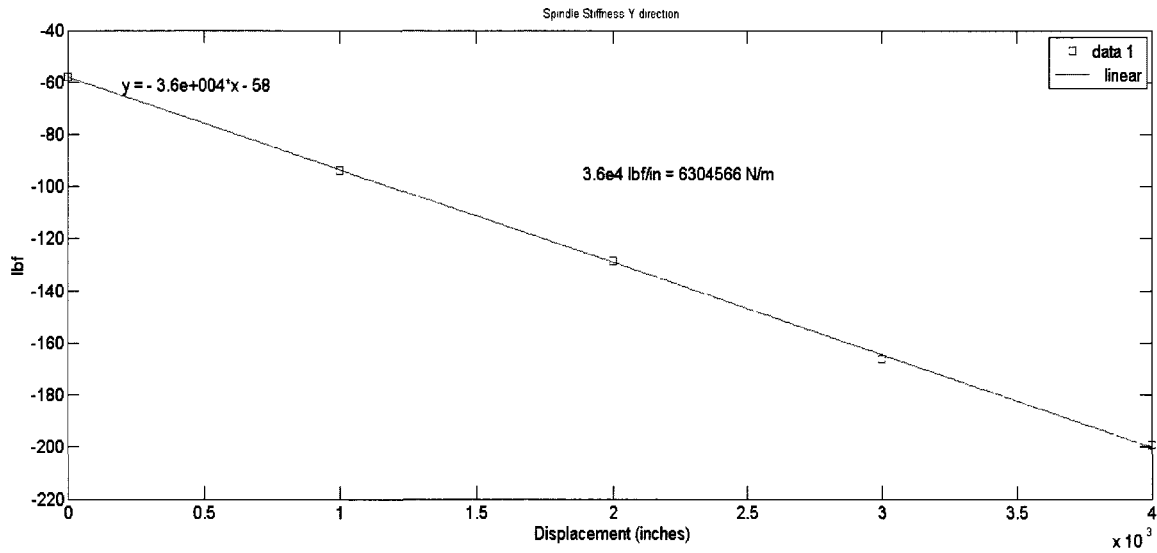


Figure 6.2: Spindle+Tool Stiffness Y Direction

Although stiffness can be directly measured, the effective mass in each axis must be estimated. To do so, the assumption is made that the first natural frequency of the system can be related to the stiffness through the approximation  $\omega = \sqrt{k/m}$  ;  $m = k/\omega^2$  . The natural frequencies in both X and Y were similar and were estimated from impulse response testing of the cutting tool. Figure 6.3 shows the result of an impulse response on the mill spindle.

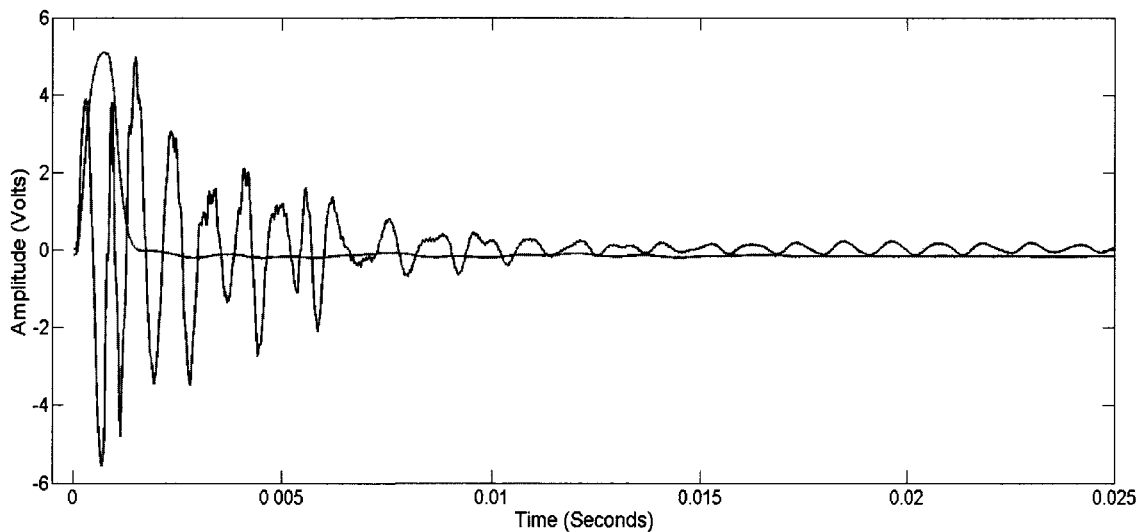


Figure 6.3: Impulse response of the tool and spindle

From the period of the impulse response, the natural frequency for both X and Y axes is found to be 1183 Hz. Given this frequency, the effective masses are estimated as  $m_x=3.3787$  and  $m_y=4.5049$  kg. The damping was observed from log decrement of the tool response. This produced damping ratios,  $\zeta_x=0.0625$  and  $\zeta_y=0.0488$  . The damping ratio was used to estimate the damping coefficient,  $c$ , in units of kg/s, as  $c=2\zeta\sqrt{km}$  ,  $c_x\approx 500$  , and  $c_y\approx 450$  .

The governing dynamic equations for this model are the differential equations of motion evaluated to solve for acceleration in the X and Y directions:

$$\ddot{x}(n)=\frac{F_x(n)-c_x*\dot{x}(n)-k_x*x(n)}{m_x} , \quad \ddot{y}(n)=\frac{F_y(n)-c_y*\dot{y}(n)-k_y*y(n)}{m_y} \quad (6.1)$$

where  $n$  represents the current discrete time step in the model.

To estimate the resulting displacement at the next time step as a function of the current deflection and current dynamics, these equations can be integrated two times using Euler integration:

$$\dot{x}(n+1)=\dot{x}(n)+\ddot{x}(n)*dt , \quad x(n+1)=x(n)+\dot{x}(n)*dt \quad (6.2)$$

$$\dot{y}(n+1)=\dot{y}(n)+\ddot{y}(n)*dt , \quad y(n+1)=y(n)+\dot{y}(n)*dt \quad (6.3)$$

While Euler integration accumulates error through time steps, it is computationally simple and employed in this 2DOF model. A Runge-Kutta based integration method is used in the 4DOF model discussed in the next section.

The radial displacement on every tooth is calculated by the sum of the projections of the displacements in x and y on the tooth radius

$$z=x(n)*\sin(\phi)+y(n)*\cos(\phi) \quad (6.4)$$



Where  $\phi$  is the rotational angle of the cutter at iteration  $n$ . For an image of the rotation angle vs radial displacement, refer to [25]. Figure 6.4 shows a diagram of radial force,  $F_r$ , tangential force,  $F_t$ , entrance angle, and exit angle.

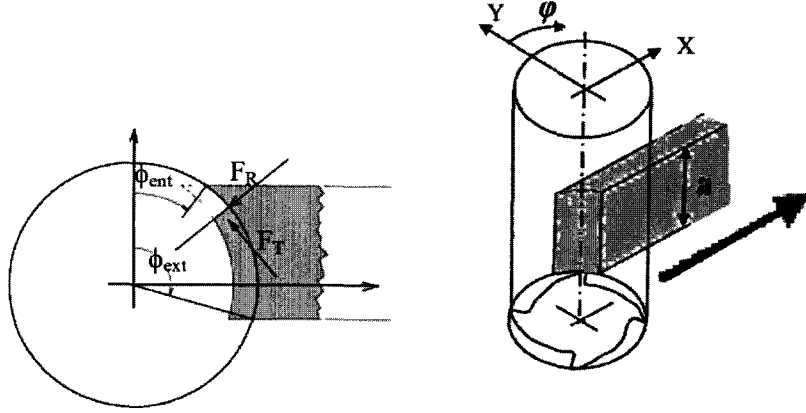


Figure 6.4: Geometry of Cutting Forces, Entrance, and Exit Angles

Along with the equations of motion, the radial displacement is recalculated at every iteration,  $n$ . The tooth rotation is discretized into 160 time steps. Therefore, the instantaneous chip thickness is recalculated at each  $n$  as:

$$h = c * \sin(\phi) - (z - z_{old}(n - 160)) \quad (6.5)$$

where  $\phi = n \times (\pi / 160)$ ,  $c$  = feed per tooth.

This equation describes the interaction of the previous cutting engagement, at  $n-160$ , with the new chip thickness at time  $n$ . The first part of this equation is the non-dynamic instantaneous chip thickness which is approximated as a function of the feed per tooth  $c$  and the angle of engagement. If  $h$  is less than or equal to zero the tool deflection is outside the workpiece and the cutting force is set to zero.

In order to simulate a spindle speed sweep, the time step was made a function of RPM. This was done to maintain the discretization resolution of 160 steps per tooth pass. The model is designed to accept a range of RPM values over which the sweep is computed. The RPM values are related to the time step as:

$$dt = \frac{60}{320 * RPM(n)} \quad (6.6)$$

Where RPM is a function describing how the spindle speed changes as a function of the iteration  $n$ . The minimum  $dt$  is equal to the reciprocal of the simulated Nyquist frequency. For example, at 2500 RPM, the sampling frequency is  $1/7.5e-005$ , or 13.33 kHz. In this case, the Nyquist frequency is 6.665 kHz. This method is sufficient for sampling because the sampling frequency is more than ten times the natural frequency of the simulated system ( $\sim 1200$  Hz). The reasoning behind this method of step calculation is the RPM values can be given as a vector of curve fit points based on the actual RPM of the experimental test (see Figure 3.17). There is no observed difference in the output of the model when the model is oversampled at 110 kHz (approximately 100 times the natural frequency of the system), however the computing time is significantly increased.

Because of the way the model sampling period is designed (based on the RPM of the input spindle speed) the model is sufficient for testing at RPM values determined by

the number of sampling points allowed. Extremely low spindle speeds require a large number of sampling points. If the model were changed to not accept spindle speed sweeps, this could be altered. However, the model was written to reflect the spindle speed sweep range discussed in Chapter 3.

The model is set up for slotting cuts, as done in the experimental tests. Axial depth is an input parameter in the model, alongside spindle speed sweep range and the number of time steps. The model has the option of applying “noise” perturbations to X and Y damping and stiffness, however for this dissertation this functionality is not explored. This is an interesting area for future work, since the additions of perturbations to the model parameters may replicate the drifting closed loop pole behavior observed in the LPC frequency tracking. Appendix C shows the model code, with a commented input example. Figures 6.5 and 6.6 show the results of radial displacement,  $z$ , from this model over a range of spindle speed from 500 to 7500 RPM at an axial depth of 10mm. The model was computed for both increasing and decreasing speeds and the effect of phase hysteresis is clearly observed and corroborates with the experimental tests. By sweeping the spindle speeds in the model, the experimental spindle speed sweeps are recreated, with greater control of parameters.

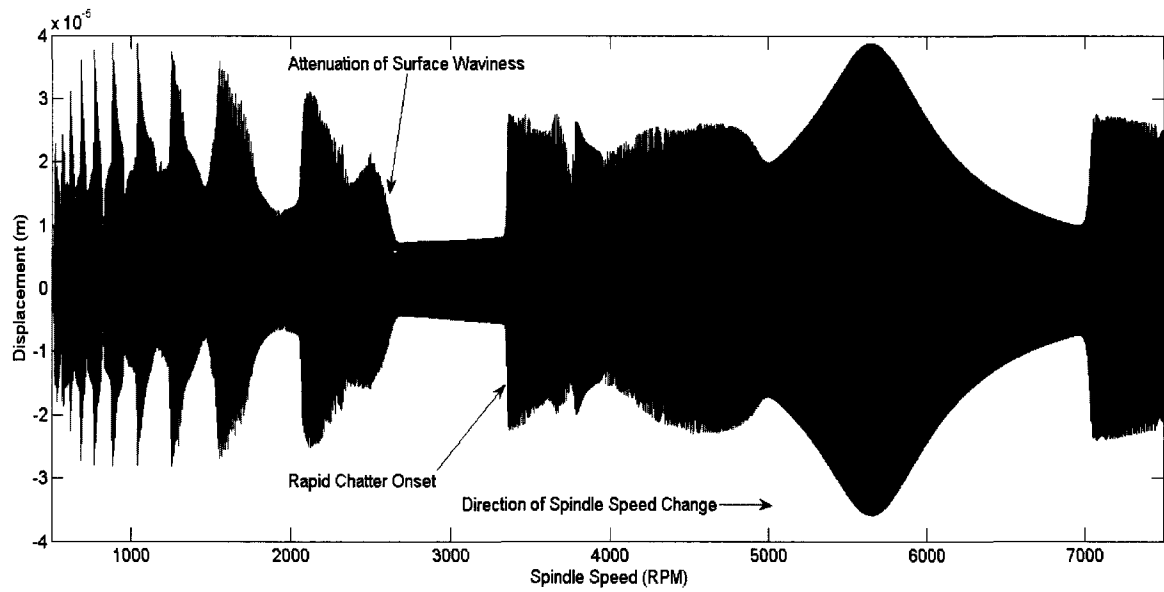


Figure 6.5: Simulated radial displacement observed for increasing spindle speed.

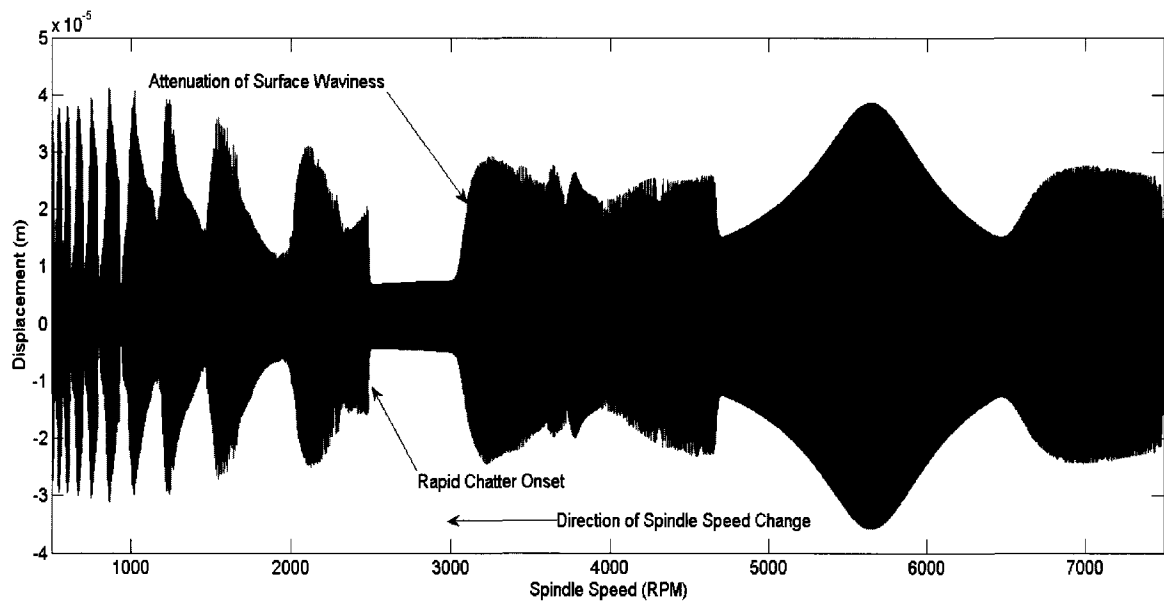


Figure 6.6: Simulated radial displacement observed for decreasing spindle speed.

In addition to the phase hysteresis effect, a number of features are observed in the model output that are similar to the experimental vibration data. At approximately 5750RPM, there is an area responding to forced vibration. This area in the response does not behave with phase hysteresis because it is not caused by passing in and out of a stability lobe region. The presence of smaller “beat” instabilities are reflected by both the time simulation and experimental spindle speed sweeps. Figures 6.7-6.9 shows this effect in both simulated and experimental instabilities. The smaller instabilities are attributed to mode coupling between X and Y axes. This hypothesis is supported by inspecting the exchange of magnitude between forces in the X direction vs the Y direction coinciding with the peak of the beat instabilities. The model produces both X and Y force data for this comparison. In the figures, these are pointed out in the X direction to illustrate one of the degrees of freedom, the resolved displacement of the X and Y direction, and the experimental vibration data.

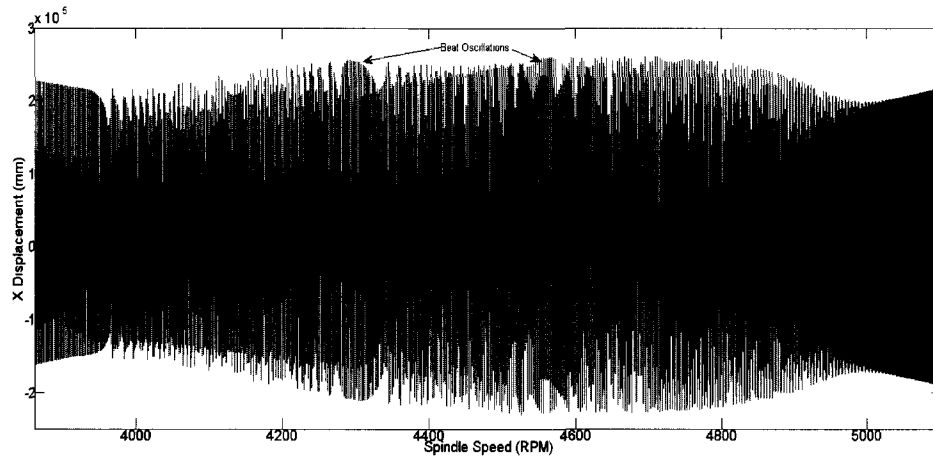


Figure 6.7: Instabilities for simulated data

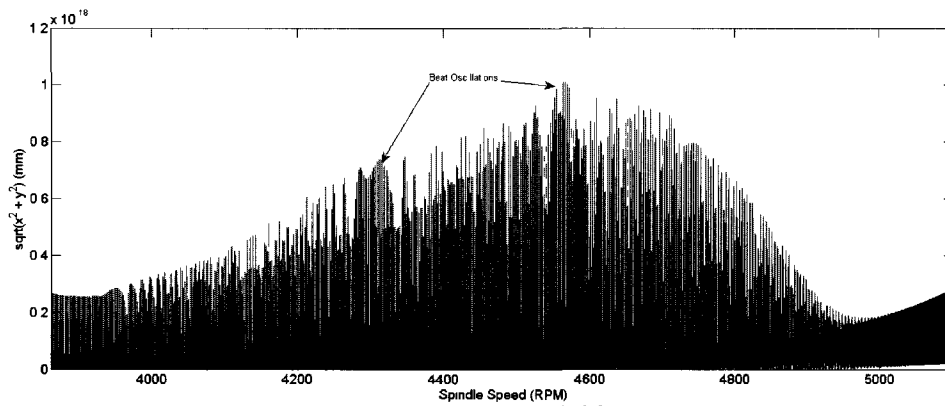


Figure 6.8: Resolved Instabilities  $(x^2 + y^2)^{0.5}$

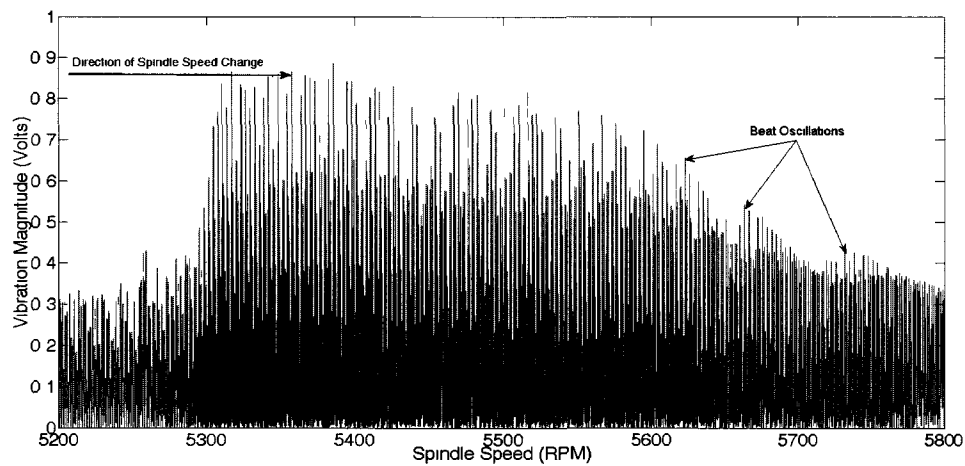
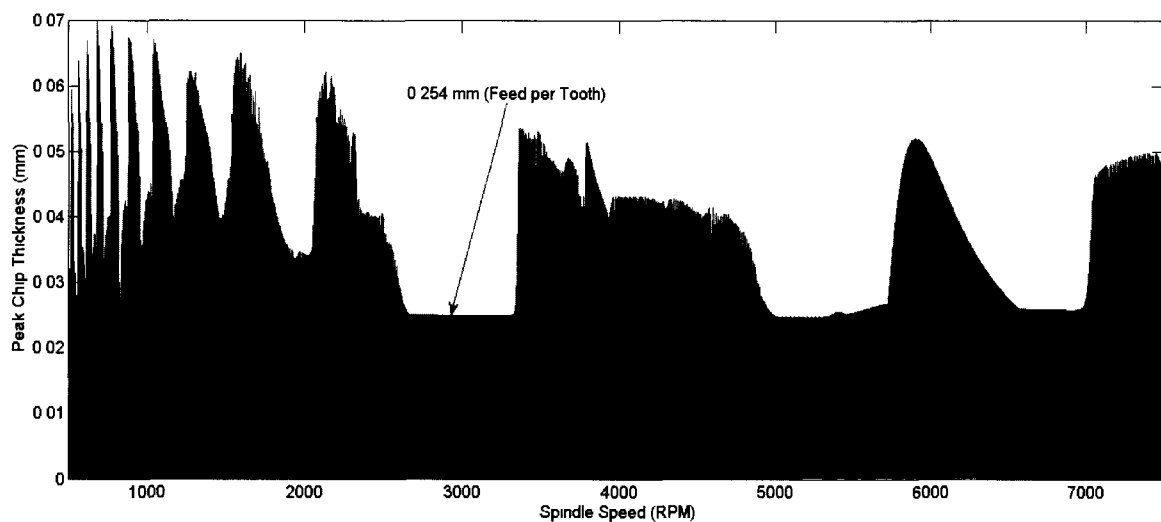


Figure 6.9: Instabilities for experimental data.

The model is also shown to reflect changes in the chip thickness over the spindle speed sweep. The dynamic effects contribute to higher chip thicknesses during areas of peak phase shift between the surface profile and tooth passing input force. It is useful to observe how the peak chip thickness reflects the the dynamics when the second term of Equation 6.5 is superimposed on the nominal chip thickness values. Figure 6.10 shows the chip thickness calculated by the simulation, highlighting the departure from nominal chip thickness with feed per tooth as a reference point.



*Figure 6.10: Simulated chip thickness*

It can be seen in Figure 6.10 that the areas of instability create peaks in the material removal rate above the nominal feed per tooth. Although the nominal feed per tooth remains constant, the peak material removal and subsequent forces are much greater during unstable conditions.

## **6.2 Conclusions about the Time Domain Cutting Tool 2DOF Model**

The time domain simulation was useful for identifying which variables were affecting the phase shift phenomenon and confirming that the chip thickness (i.e. surface finish) attenuated as the sweep changed from an unstable to stable mode. The presence of oscillations nested within instabilities was also observed in the simulation and corroborates the experimental tests. Although the physical parameters for the model were based on static tests of the actual system, the chatter modes were not similar in frequency to the experimental test. This is presumably due to the change in dynamics that are associated with static vs dynamic bearing stiffness, workpiece dynamics, and bed dynamics. At higher spindle speeds, the modes began to align with the experimental tests, but for low spindle speeds, the fit was poor.

The results were satisfactory for describing the phenomenon of 'phase hysteresis'. The model demonstrated that this effect was dependent on the direction of spindle speed change. The hysteresis effect was captured in the model displacement as well as in the calculated chip thickness. By investigating the effects captured in this time domain model, the phase hysteresis phenomenon is confirmed to be the decay of surface waviness after the dynamics have entered a stable mode. Once the dynamic component of the model is in phase with the non-dynamic chip thickness, the instantaneous chip thickness attenuates.

## **6.3 Time Domain Coupled Cutting Tool & Work Piece 4DOF Model**

The 2 DOF time domain model specified in the previous section was expanded by



the introduction of the workpiece compliance coupled through forcing interaction with the tool holder system. Similar to the 2 DOF model, the forcing behavior of the system is calculated from the equations of motion. The introduction of a second system requires added notation. The tool holder is the first system and its parameters are denoted by the subscript '1', such as  $x_1$  ,  $y_1$  ,  $c_{x1}$  ,  $c_{y1}$  ,  $k_{x1}$  , etc. Likewise, the workpiece system is the second system and its parameters are denoted by the subscript '2'. Figure 6.11 shows a drawing of the model, with a simplification of the forcing function linking the independent degrees of freedom.

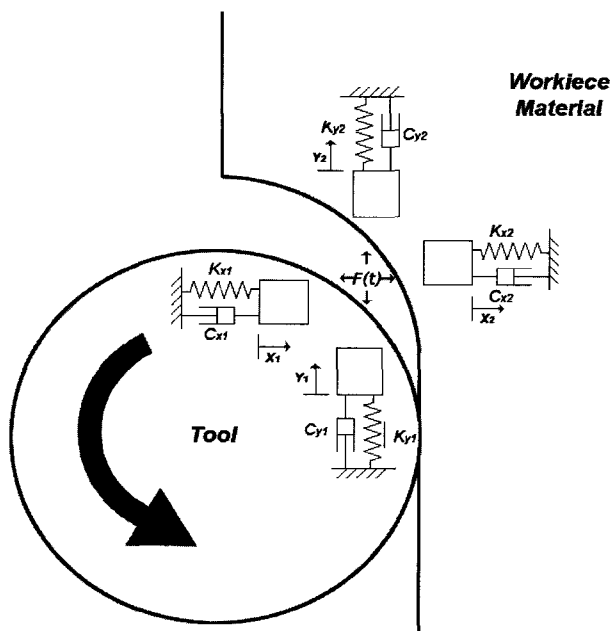


Figure 6.11: 4DOF System Model

The equations of motion for these systems are related through equal and opposite forcing functions in each direction.

$$\ddot{x}_1(n) = \frac{-F_x(n) - c_{x1} * \dot{x}_1(n) - k_{x1} * x_1(n)}{m_{x1}} \quad (6.7)$$

$$\ddot{x}_2(n) = \frac{F_x(n) - c_{x2} * \dot{x}_2(n) - k_{x2} * x_2(n)}{m_{x2}} \quad (6.8)$$

$$\ddot{y}_1(n) = \frac{-F_y(n) - c_{y1} * \dot{y}_1(n) - k_{y1} * y_1(n)}{m_{y1}} \quad (6.9)$$

$$\ddot{y}_2(n) = \frac{F_y(n) - c_{y2} * \dot{y}_2(n) - k_{y2} * y_2(n)}{m_{y2}} \quad (6.10)$$

As with the 2DOF model, integration is performed on these equations of motion to identify the position variable. However, for added accuracy, a 4<sup>th</sup> order Runge-Kutta integration technique was used to estimate the integration. To see example code for this integration routine, refer to Appendix E. For the sake of brevity, only the  $x_1$  integration is shown in equations 6.11 and 6.12.

$$\dot{x}_1(n+1) = \dot{x}_1(n-1) + dt(\ddot{x}_1(n-1) + 4\ddot{x}_1(n) + \ddot{x}_1(n+1))/3 \quad (6.11)$$

$$x_1(n+1) = x_1(n-1) + dt(\dot{x}_1(n-1) + 4\dot{x}_1(n) + \dot{x}_1(n+1))/3 \quad (6.12)$$

The chip thickness is calculated as a difference in the deflection of both systems in each degree of freedom. The difference is calculated since the deflections have the same sign but in opposite direction. For example, in the x direction, the total deflection between the cutting tool and workpiece is calculated as:

$$\Delta x(n+1) = x_2(n+1) - x_1(n+1) \quad (6.13)$$

$$\Delta y(n+1)=y_2(n+1)-y_1(n+1) \quad (6.14)$$

Once this total deflection is calculated for both x and y directions, the procedure for calculating forces is the same as the method described in the 2DOF. After calculating the deflections,  $x(n)$  and  $y(n)$  are replaced with  $x(n+1)$  and  $y(n+1)$ . The chip thickness is formulated based on feed per tooth and delayed chip thickness. If the chip thickness is less than zero the tool is considered out of the workpiece and the force is set equal to zero.

The results for this model reflects the input stiffness and mass for each degree of freedom. For example, the lowest stiffness and mass combination was 2.05e6 N/m and 3.6 kg, giving a natural frequency of approximately 120 Hz. The model was run for similar conditions to the 2DOF model. While the behavior is similar, the results are different when the workpiece is compliant.

The frequency content of the model can be evaluated by calculating the power spectral density (PSD) of the data. Peaks exist at locations of natural frequencies.

There are interesting effects that can be observed in this model, namely the presence of other frequencies (for instance, at 500Hz in Figure 6.12) that may represent interaction between modes of the system.

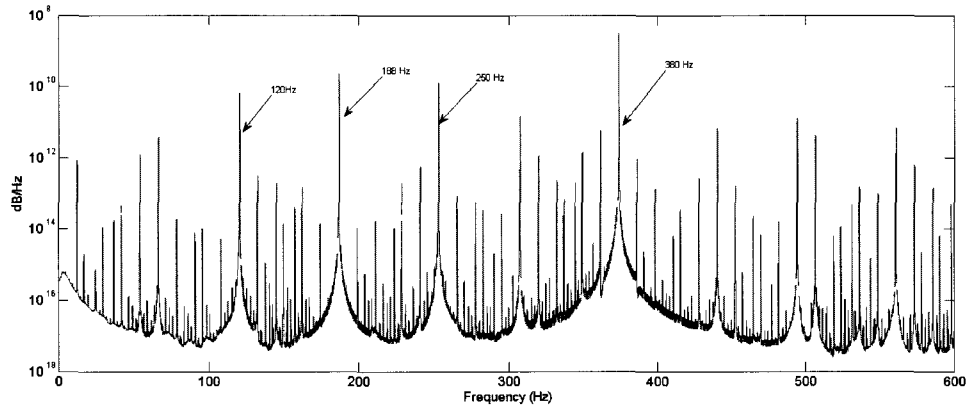


*Figure 6.12: 4DOF Model Frequency PSD*

This model also retains the ability developed in the 2DOF model to conduct frequency sweeps over a range of spindle speeds. The total deflection between the workpiece and the tool are plotted for a spindle speed sweep in Figure 6.13. The X and Y directions are related, but independent in their behavior, reflecting the different parameters for stiffness and mass entered in the model.

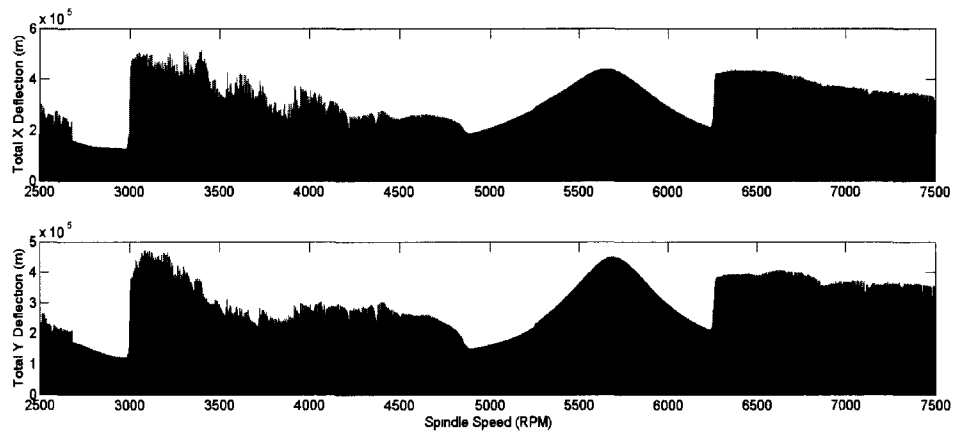


*Figure 6.13: 4DOF Model Spindle Speed Sweep*

The 4 DOF model shows significant difference in the chatter frequencies, while maintaining the natural frequency of the 2DOF system (which causes forced response around 5750 RPM). These results are similar to the cantilever experimental results, where the natural frequency of the tool and workpiece was lower than the observed chatter frequency. However, the models were not capable of replicating the same frequencies observed during the cutting tests without editing the model parameters for stiffness and mass. The static measurements of stiffness may not be sufficient as model inputs to accurately reproduce frequencies that occur during spindle rotation.

There are both similarities and differences between the 2DOF and 4DOF models. A significant difference is the integration methods used in each. The 2DOF model uses Euler (rectangular) integration that is prone to error compounding over many time steps. In Euler integration, error approaches zero as the time steps approach zero, however it is not possible to achieve this case. The 4DOF model uses an integration based on Runge Kutta, which has error significantly less than the Euler method. Specifically the compounded error over a given number of time steps is worse for the polygonal approximation made at each step by the Euler first order integration. To compare the difference in the models, the 4DOF model can be made into a 2DOF model by setting the workpiece system to have infinite stiffness so that it does not have compliance contributing to the chip thickness. Conditions are chosen to compare the two models with the same input. An axial depth of 2mm, spindle speed sweep between 2500 to 7500 RPM, tool stiffness of  $k_x=4.7\text{e}6\text{ N/m}$   $k_y=6.3\text{e}6\text{ N/m}$  , and tool mass of  $m_x=3.38\text{ kg}$   $m_y=4.5\text{ kg}$  . 2 Million data points were calculated for both models with an increasing

(upward) sweep direction.

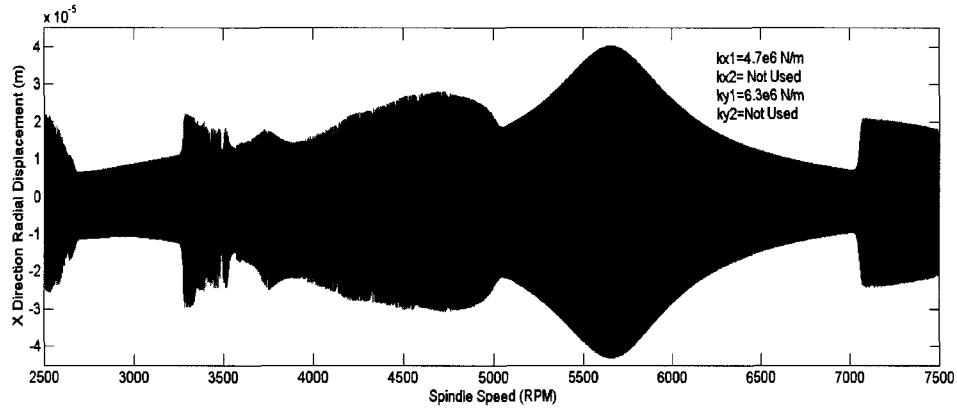


Figure 6.14: 4 DOF Model with Infinitely Stiff Workpiece

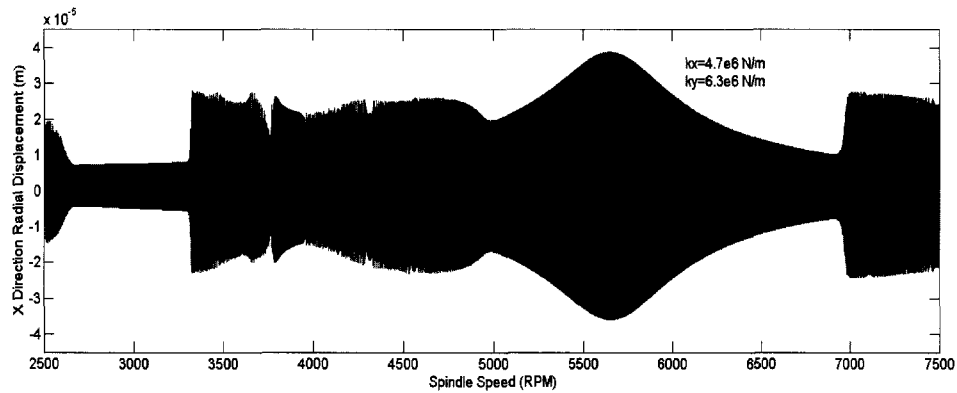
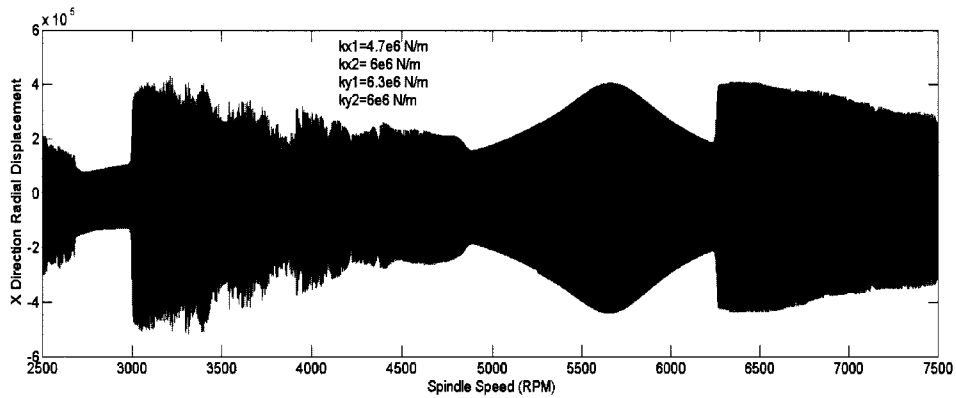


Figure 6.15: 2DOF Model for Comparison to 4DOF Model

Similarity between the model behavior was observed but the results were not identical. This is not surprising due to the significant difference in numerical error between the two solution methods. Considering numerical accuracy, the 4DOF model is superior to the 2DOF model and thus is closer to representing a real system. However, the behavior exhibited in the real system is replicated by both models. The 4 DOF model can be evaluated with workpiece stiffness and gives significantly different results demonstrating the importance of modeling the workpiece interaction. It is important to model the workpiece compliance, particularly when the workpiece has a stiffness in the same order

of magnitude as the tool holder.



*Figure 6.16: 4 DOF Model With Workpiece Compliance*

#### **6.4 Replicating the Cantilever Cutting Test with the 4DOF Model**

The final application of the 4DOF model is to apply the model to inspect the results of the cantilever cutting tests. In particular, the model is shown to replicate the behavior in Figure 5.8 where chatter frequency jumps suddenly as the cantilever is cut shorter.

A simulation is set up with a fixed tool holder mass of 4kg and stiffness of  $5e6$  N/m. Both the X and Y directions of the tool holder are given the same stiffness and mass parameters to simplify analysis. This model tool holder has a natural frequency of 178Hz. The cantilever system is given a varying mass and stiffness related to the length. This mass and stiffness are entered into the model and the model is re-run for each set of cantilever parameters. As with the actual cutting data, the chatter frequencies are determined by the dominant LPC frequency in the data.

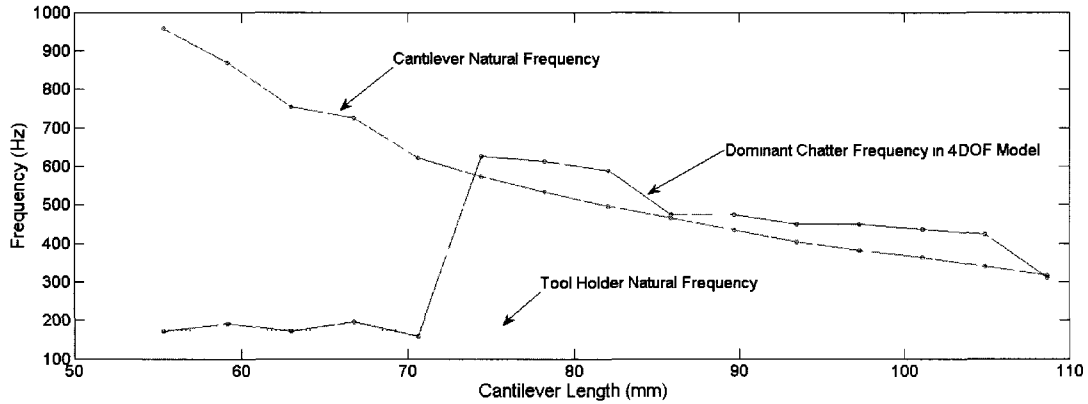


Figure 6.17: 4DOF Model Changing Cantilever Length

The results are encouraging, that the 4DOF model is capturing the behavior of the real system. The model does not replicate the exact points of the real system, but the behavior is similar. The chatter frequency changes from a workpiece based frequency to the tool holder frequency.

### **6.5 Chapter Summary**

Time domain models were capable of replicating the spindle speed sweep experiments and recreating the phenomenon observed in the experimental cutting data. The spindle speed sweep simulations show that chatter has a rapid build up into an unstable region and dies out gradually once the tooth passing frequency has progressed into a stable regime. The sweep functionality was helpful in studying the die-out of the chatter frequency into a stable mode. It was found that the surface finish attenuates gradually as the phase between the surface finish and tool vibration enters a stable region. The two degree of freedom model was capable of replicating effects seen on the tool-based chatter in a stiff workpiece. This model was found to exhibit beat frequency behavior between the X and Y degrees of freedom. The beating was compared to experimental data which shows similar behavior. Unlike the experimental data, the model



could be separated into X and Y coordinates separately to confirm that the beats were exchanges of energy between the X and Y systems. Resolving the model displacements into a single resultant produced displacement plots which were very similar to the experimental data. Although the 2DOF model was enlightening, it was not able to capture the behavior of a system with a compliant workpiece.

A four degree of freedom model was made to address the behavior of a workpiece and tool with compliance in the X and Y directions. This model used an integration technique based on Runge Kutta instead of the Euler integration used on the 2DOF model. The benefit of this change was questionable for non-chattering simulations, since the error in rectangular integration is zero for periodic functions (such as slot cuts). However, the benefit exists to reduce error in non periodic simulations (i.e. when the simulation is chattering integration error is reduced). The workpiece and tool are coupled by the cutting force equal and opposite between the workpiece and tool. This model behaved with significant differences to the two degree of freedom model, identifying that the systems interact to produce different chatter frequencies than either individual system would experience without the interaction. This effect was observed during the experimental tests using a cantilever workpiece.

For both the 4DOF and 2DOF models, trends and behavior observed during the experimental tests are successfully reproduced. Although behavior was reproduced, the models did not match the specific frequencies of the experimental system. This was not of particular concern since differences between static and rotating stiffness are acknowledged and the point of the models was to reproduce phenomenon recorded in the physical experiments. The purpose of these models was not to predict specific frequencies, but to replicate the complex behavior that was observed during experimental spindle speed sweeps and cantilever cutting tests.

## CHAPTER 7

### Conclusions

#### **7.1 Conclusions and Outcomes**

The development of smart tool holders can change the way cutting data is collected and observed. Cutting processes can be monitored in a non invasive way without compromising the stiffness of commercial tool holder bodies. No longer is it necessary to collect data from large and compliant bed mounted dynamometers. The bandwidth on the smart tool is mechanically superior to traditional dynamometer systems. While the bed dynamometer introduces its response into the cutting system, the smart tool does not add any additional dynamics to the standard tool holder system. The feedback from a tool holder-based sensor circumvents problems associated with spindle and motor power data; namely, the lack of bandwidth and susceptibility to changes in system efficiency over time.

The smart tool holder is used to evaluate dynamic phenomenon of the end milling system. Specifically, tool chatter is observed and investigated using data collected from the smart tool. This data has given new insight to the development of tool chatter as well as the stochastic behavior of tool chatter during steady state cutting.

Using an autoregressive technique called Linear Predictive Coding, data from the

smart tool is analyzed. The output are formant frequencies associated with the closed-loop poles. These frequencies are determined by calculation of formant frequencies from the LPC model, similar to the calculation of formant frequencies from speech recognition techniques. The formant frequencies are found to locate the frequency of tool chatter, from non-chattering stable cutting conditions. The smart tool high signal to noise ratio enables resolution sufficient for determination of the chatter frequencies before the onset of tool chatter.

Four tooling prototypes were used during the course of this work. These prototypes consisted of two acceleration sensing tools and two torque based tools. Of the torque sensing tools, the fourth prototype (a semiconductor strain sensing tool) was used to explore the LPC method. The semiconductor tool was used due to its high signal to noise ratio.

Although the semiconductor tool was set up to measure only torque, the tool also detected some bending strain. This is known as cross talk between the torsion and bending strains and is caused by alignment of the gages. The cross talk was measured and analyzed using a test jig on a force controlled input and determined to be worth noting for future development. In future iterations of the tool it will be critical to locate the gages in a position on the holder body that is less prevalent for bending strain.

Using the smart tool holder a series of experiments were conducted to observe the buildup of chatter during cutting. These experiments were informative about the way in which chatter develops through time. With the high SNR of the smart tool, chatter was

observed building over time periods of up to 2 seconds. This is a positive result and opens the door for future work in control methodologies.

In addition to studying the build up of tool chatter, experiments were designed to sweep the spindle speed during a cut to excite chatter across a range of spindle speeds. This technique was able to generate experimental stability lobe diagrams. Because of interesting behavior observed during the spindle speed sweeps, time domain models were the next area of focus (in order to explain observations).

Modeling efforts have replicated behavior observed from the smart tool holder data. Two models were created to observe a tool holder dominated system with freedom in X and Y directions, and a tool holder system with a compliant workpiece with freedom in X and Y directions. These models were written with the capability of reproducing spindle speed sweep tests. The results of the models shows coherence to the behavior of the real system, however, the chatter frequencies did not match the real cutting system since static measurements of stiffness are not the same as the spindle stiffness during rotation.

In summary, this work has resulted in several novel contributions to metal cutting research.

- A smart tool holder was made for recording information from the live cutting process. There is a substantial improvement over the traditional methods of using external sensors or force sensing based on bed dynamometer. Problems with external sensing are circumvented because the measurements are more direct.
- Cutting dynamics have been observed from the tool holder. High signal-to-noise

ratio enable clear observation of frequency content and how the cutting signal behaves throughout cutting. Drift in the frequency content during cutting provides an explanation for the difficulty predicting stable cutting speeds from traditional methods (i.e. tap tests).

- Chatter frequencies are observed in stable cuts before the onset of chatter. The closed loop frequency content of the system is of great importance to the optimization of cutting processes in real time. This is a significant advance to the state of the art.
- Time domain modeling efforts capture trends and behavior observed in the cutting system.

## CHAPTER 8

### Future Work

#### **8.1 Suggested Directions and Topics for Future Work**

A probability distribution function can be based on the drifting system poles during steady state cutting. The variables affecting variation in the system can be investigated, according to the results of statistical changes in the probability distribution. For example, spindle bearings and bed ball screws can be replaced with higher precision components and the effect on the distribution of the estimated system poles can be quantified. Tool clamping and bed attachment can be analyzed. This is one proposed way to approach a sensitivity analysis of what causes the variation to occur in a “steady state” cutting experiment.

A second area of promising future work is the investigation of boundary conditions and the forcing input between the cutting tool and workpiece during cutting. It is the opinion of the author that the cutting is introducing a boundary condition to the tool holder and workpiece which is not simply explained by a forcing function between two cantilever structures. The tool engagement may have an effect on the behavior of the system and has not been captured. It is likely that the boundary conditions and forcing could contain non linear behavior leading to some of the effects discussed in this dissertation.

A third area of future work is expanding the use of autoregressive system models to calculate FRF's. This work is initiated in the future work section of this dissertation when the LPC model is used to generate model FRFs and estimate a model stability lobe diagram. The benefit of using the LPC model information to generate stability lobe diagrams is parallel to the study of statistical distribution of drift around predicted chatter frequencies. Producing stability lobes is a subsequent step towards defining a “stable”, “possibly stable”, and “unstable” parameter space, with a distribution to define “possibly stable”.

The LPC model coefficients could be used to approximate the denominator of the system FRF under the assumption that  $\omega_c \approx \omega_n$ . For cases where  $\omega_c \neq \omega_n$  due to spindle speed,  $\omega_n$  can be calculated with knowledge of the spindle speed and  $\omega_c$ . This method is an exploratory use of the LPC model method and has shown intriguing results that can be the framework for future work. Because the LPC model is updated through time, the model stability lobes can be regenerated at each time window to produce plots showing a distribution of stability lobes and what appears to be a probability distribution around the stable/unstable transition. Section 8.3 outlines a mathematical method to generate stability lobe diagrams from LPC information.

## **8.2 Mathematical Method for Estimating Stability Lobes from LPC Model**

An extension of this work is to use the LPC model to approximate for the system poles and generate a stability lobe diagram. LPC has been experimentally shown to predict chatter frequencies. Thus, for cases where  $\omega_c \approx \omega_n$  it is possible to generate



stability lobe diagrams using the LPC pole parameters to create a model FRF. For cases where  $\omega_c \neq \omega_n$  due to spindle speed [48],  $\omega_n$  can be calculated with knowledge of the spindle speed and  $\omega_c$ . For the discussion presented in this dissertation, it is assumed  $\omega_c \approx \omega_n$ . However, a worthwhile extension of this work is to apply the method to cases where  $\omega_c \neq \omega_n$  and  $\omega_n$  is calculated based on  $\omega_c$ .

Because the LPC generates an all pole model, parameters such as natural frequencies and damping (pole half power widths) can be acquired from inspection. However, since the LPC analysis does not correctly identify pole magnitude, the modal masses must be known before a complete FRF can be generated.

For estimating FRFs, the system is split into two degrees of freedom. The system will have a unique FRF for each degree of freedom. All of these FRFs influence the stability of the system. Consider the example discussed previously for a cantilever workpiece and tool. This system has two compliant members, the tool and work piece, that have freedom in both X and Y direction; i.e., there are four degrees of freedom ( $x_{tool}$ ,  $y_{tool}$ ,  $x_{workpiece}$ ,  $y_{workpiece}$ ).

After the DOF's are identified, the modal mass must be known for each DOF. For a XY symmetrical cantilever, this is trivial and is approximately 0.243 times the overhanging mass of the cantilever tool (see Appendix I). Next, estimate stiffness from each DOF, based on the dominant pole location (frequency) and the estimated mass. (Note: an important assumption is made here that chatter occurs only around the dominant pole of a system. ) For our four DOF system, there will be

$k_{x_{tool}}, k_{y_{tool}}, k_{x_{work\ piece}}, k_{y_{work\ piece}}$  according to:

$$k_{xx} = \omega_{nxx}^2 m_{xx} \quad (8.1)$$

where the subscript 'xx' indicates that the computation is applicable for x tool, y tool, x work piece, and y workpiece.

The above assumption about the chatter frequency and lowest pole dominating is typically acceptable. However, LPC will generate a number of poles specified by the user, giving a 4th order or higher system. The natural frequency, resonant frequency, and damping ratio apply to each pair of complex conjugate poles. Another (more involved) way to calculate both damping and stiffness without the above assumption, is to compute the eigenvalues. For reference, the MATLAB function “damp” can analyze the LPC all-pole model as a transfer function and provide a list of eigenvalues. This is also a way to estimate damping for individual poles. The damping ratio is computed from each complex eigenvalue as the ratio of the real part over the magnitude of the eigenvalue:

$$\zeta_{xx} = \frac{\Re \lambda_{xx}}{\sqrt{\Re \lambda_{xx}^2 + \Im \lambda_{xx}^2}} \quad (8.2)$$

Once the stiffness and damping is calculated for each DOF, define the specific cutting force and the force angle using a cutting force model. It is appropriate to use a single coefficient model that defines specific cutting force in N/mm<sup>2</sup> since other coefficients are not of interest to chatter modeling. Typical values for the specific force coefficient,  $K_s$ , are 300-750 N/mm<sup>2</sup>, depending on the type of work piece material and tool type. The force angle,  $\beta$ , is based on the tool geometry. Typical values for steep helical end mills are 60-80 degrees.

The FRF is generated, normalized by the natural frequencies for each DOF. The FRF

will be computed using the normalized frequencies:

$$r_{xx} = \omega / \omega_{nxx} \quad (8.3)$$

The real and imaginary parts of the FRF are generated by:

$$\Re[FRF_{xx}] = \frac{1}{k_{xx}} \frac{1 - r_{xx}^2}{(1 - r_{xx}^2)^2 + (2\zeta_{xx}r_{xx})^2} \quad (8.4)$$

$$\Im[FRF_{xx}] = \frac{1}{k_{xx}} \frac{-2\zeta_{xx}r_{xx}}{(1 - r_{xx}^2)^2 + (2\zeta_{xx}r_{xx})^2} \quad (8.5)$$

There should be a FRF generated for each DOF in the system. After the FRFs are calculated, they must be weighted by a direction orientation coefficient. This is the direction cosine in the XY coordinate system, based on the direction that the cut is being made. For example, for a slot cut in the X direction, the orientation coefficients would be:

$$u_x = \cos(\beta\pi/180) \quad \text{and} \quad u_y = 0$$

The resultant FRF, or “oriented FRF”, is given according to:

$$\Re[FRF_{orient}] = u_x \Re[FRF_x] + u_y \Re[FRF_y] \quad (8.6)$$

$$\Im[FRF_{orient}] = u_x \Im[FRF_x] + u_y \Im[FRF_y] \quad (8.7)$$

Bringing the derivation back to our tool and cantilever example, there will be a resultant FRF for the tool and a resultant FRF for the cantilever. For these FRFs, the range of frequencies in which chatter is possible corresponds to when  $\Re[FRF_{orient}] < 0$ . Book keeping must be done at this point to relate the physical number of flutes on the tool,

$N$ , to the average number of flutes,  $N_{avg}$ , immersed in the cut. This is based on the entrance and exit angles,  $\phi_s$  and  $\phi_e$ , for the cut.

$$N_{avg} = \frac{N}{360} (\phi_e - \phi_s) \quad (8.8)$$

For a slot cut,  $\phi_s$  and  $\phi_e$  are 0 and 180 degrees. At this point, there is enough information to calculate the stable depth limit for the stability lobe diagram,  $b_{limit}$  :

$$b_{limit} = \frac{-1}{2 K_s \Re[FRF_{orient}] N_{avg}} \quad (8.9)$$

The final steps are to generate the lobe shapes and determine the conglomerated shape of the stability lobe diagram. To do so, the phase angle of the oriented FRFs must be calculated:

$$\epsilon = 2 * pi - 2 \tan^{-1} \left| \left( \frac{\Re[FRF_{orient}]}{\Im[FRF_{orient}]} \right) \right| \quad (8.10)$$

From this angle, the spindle speeds can be calculated for each  $i^{th}$  individual lobe:

$$\Omega_i = \frac{\frac{\omega}{(2\pi N)}}{(i + \frac{\epsilon}{(2\pi)})} \quad \text{where } i = [0, 1, \dots] \quad (8.12)$$

The resulting union of the spindle speeds  $\Omega$  , can be plotted to create the conglomerated stability lobe diagram.

The results from an example computation are shown below, with the multiple lobes superimposed on a single graph to form a stability diagram.

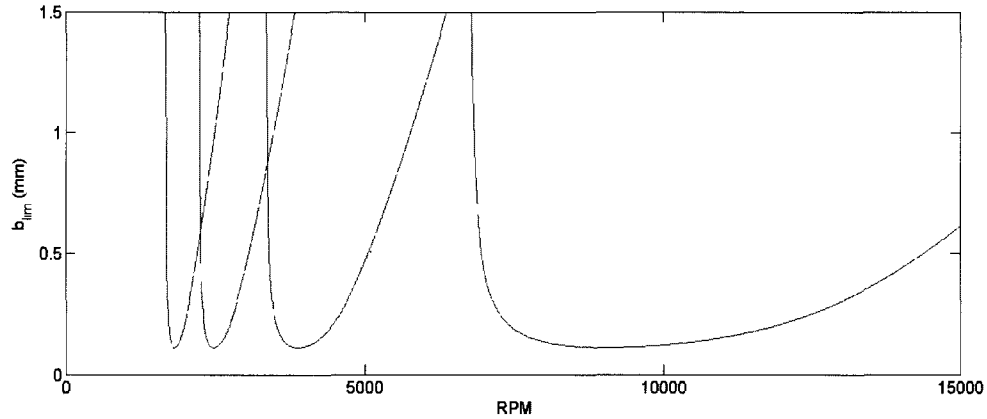


*Figure 8.1: Stability Lobe Diagram Generated From LPC Coefficients*

### **8.3 Variation in the Stability Lobes Throughout Cutting**

The continuous adaptation of the LPC model throughout the cutting enables an opportunity to update the stability lobe computation with data from cutting. Monitoring the changes in the stability lobe throughout steady state cutting provides a number of benefits for real-time application as well as offline process planning. From an offline perspective, understanding the distribution of the stability lobes superimposed through time is advantageous to predict stable, sometimes stable, and never stable regions of the lobe diagram. Section 5.1 discusses the adaptive change in the LPC model through time. The change in the LPC model is reflected in the stability diagram and can be similarly plotted through time.

Using the method of section 5.3 to generate stability lobe diagrams, the diagrams can be recreated through time for sequential data windows. The effect is fascinating and corresponds to the observed change in LPC poles (shown in Figure 8.2). Thus, a

distribution of stability can be seen for a steady state cut. This information is useful for process planning since a specific workpiece/clamping/tool combination could be characterized and safety margins applied to the stability lobes.

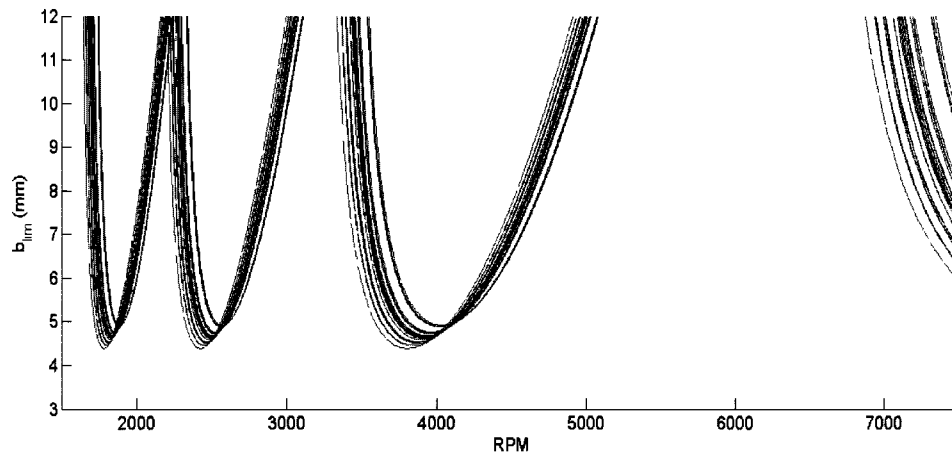


*Figure 8.2: Stability Lobe Distribution*

#### **8.4 Including Stochastic Noise Effects to Time Domain Models**

Another avenue for future work is exploring the addition of perturbations (both stochastic and deterministic) to the time domain models. Work was already done to add this functionality into the 2DOF model shown in Appendix C. This could help to capture effects from bed location and/or variation in the spindle system during cutting.

## LIST OF REFERENCES

- [1] Schuyler, C.K., M. Xu, R.B. Jerard, and B.K. Fussell (2006). "Cutting Power Model-Sensor Integration for a Smart Machining System." Transactions of the North American Manufacturing Research Institution of SME, Vol. 34, pp. 47-54.
- [2] Byrne, G. and G.E. O'Donnell (2007) "An Integrated Force Sensor Solution for Process Monitoring of Drilling Operations." CIRP Annals- Manufacturing Technology, Vol. 56, Issue 1, pp. 89-92.
- [3] Park, S.S. (2006). "Identification of Spindle Integrated Force Sensor's Transfer Function for Modular End Mills." Journal of Manufacturing Science and Engineering, Vol. 128, Issue 1, pp. 146-153.
- [4] Rehorn, A.G., J. Jiang, and P.E. Orben (2005). "State-of-the-art methods and results in tool condition monitoring: a review." The International Journal of Advanced Manufacturing Technology, Vol. 26, Numbers 7-8, pp. 693–710.
- [5] Suprock, C.A., J. Piazza, and J.T. Roth (2006). "Directionally Independent Failure Prediction of end milling Tools during Pocketing Maneuvers." ASME International Conference on Mfg. Science and Engr., MSEC2006-21089, 10 pp.
- [6] Jerard, R.B., B.K. Fussell, M. Xu, C. Schuyler, and D. Esterling (2006). "Development of a testbed for research on smart machine tools." NSF DMII Grantees Conference, St. Louis, July, 2006.

- [7] Sessler, G.M. and J.E. West (1966). "Foil-Electret Microphones." The Journal of the Acoustical Society of America, Vol. 40, Issue 6, pp. 1433-1440.
- [8] Oppenheim, A.V. and R.W. Schaffer 1989 Discrete-Time Signal Processing Prentice-Hall, pp. 611-619.
- [9] Proakis, J.G. and D.G. Manolakis 2007 Digital Signal Processing- 4th Edition, Prentice Hall, pp. 69-80.
- [10] Nichols, J.S. (2009). "Design and Application of a Wireless Torque Sensor for CNC Milling" Masters Thesis. University of New Hampshire. Department of Electrical Engineering.
- [11] NTIA "Manual of Regulations and Procedures for Federal Radio Frequency Management" US Govt. Printing Office. 2010. ISBN: 0-16-016464-8
- [12] Callaway, E.H. (2004), "Wireless Sensor Networks: Architectures and Protocols" CRC Press, September 2003 ISBN-13: 9780849318238
- [13] Sudararajan, V., Redfern, A., Schneider, M. and Wright, P. (2005) 'Wireless sensor networks for machinery monitoring', ASME International Mechanical Engineering Congress and Exposition, Orlando, Florida, USA.
- [14] Wright, P. K., Dornfeld, D. A., Hillaire, R. G., and Ota, N. K. (2006), "A Wireless Sensor for Tool Temperature Measurement and its Integration within a Manufacturing System", Trans. North American Manufacturing Research Institute, 2006, vol. 34
- [15] Dini, G., and Tognazzi, F. (2006), "Tool condition monitoring in end milling using a torque-based sensorized toolholder", Proceedings of IMechE: J. Engineering



Manufacture, Vol. 221 Part B, pp 11-23 DOI:10.1243/09544054JEM559

[16] Cheng, C.H., Schmitz, T.L., Duncan, G.S. (2007), "Rotating Tool Point Frequency Response Prediction Using RCSA", Machining Science and Technology, Vol. 11, Issue 3, July 2007 , pp 433-446

[17] Bluetooth Special Interest Group. January 2011. Web: [www.bluetooth.org](http://www.bluetooth.org)

[18] Bluetooth Special Interest Group (2007) "Advanced Audio Distribution Profile Specification" Revision 12. Document A2DP\_SPEC. April 2007

[19] Suprock, C.A., Fussell, B.K., Roth, J.T. (2008) "A Cost Effective Accelerometer and DAQ for Machine Condition Monitoring: A Feasibility Study." Transactions of the North American Manufacturing Research Institution of SME, Vol. 36

[20] Xu, M., Jerard, R.B., and Fussell, B.K., (2007) "Energy Based Cutting Force Model Calibration for Milling" Computer aided design and applications Vol 4, Nos. 1-4, 2007 pp 341-351.

[21] Suprock, C.A., Roth, J.T., Downey, L.M., (2007) "Failure Forecasting for Flat, Ball-Nose, Roughing, and Tapered end mills Using Acceleration Data" Transactions of the North American Manufacturing Research Institution of SME, Vol. 35

[22] Suprock, C.A. (2008) "Wireless Sensor Integrated Smart Tool Holder and Tooling for Metal Cutting" United States Patent and Trademark Office, Provisional Patent Application No. 61037033.

[23] University of New Hampshire, Design and Manufacturing Lab. February 2010. Web: <http://unh.edu/dml>

[24] Hosiden Online Electret Microphone Catalog. January 2008. Web:

[http://www.hosiden.co.jp/web/english/web/products/pdf/e\\_on06\\_mic.pdf](http://www.hosiden.co.jp/web/english/web/products/pdf/e_on06_mic.pdf)

[25] Altintas, Y. (2000) "Manufacturing Automation" Cambridge University Press, New York. ISBN: 0-521-65029-1

[26] Suprock, C.A., Fussell, B.K, Jerard, R.B., Hassan, R.Z., (2008) "A Low Cost Wireless Tool Tip Vibration Sensor for Milling" ASME MSEC 2008, MSEC\_ICMP2008-72492

[27] Suprock, C.A., Fussell, B.K, Jerard, R.B., Hassan, R.Z., (2008) "Predicting end mill Tool Chatter with a Wireless Tool Tip Vibration Sensor" 11th CIRP Conference on Modeling of Machining Operations

[28] Jones, J.J., McNeal, T.A., Salandro, W.A., Roth, J.T., Suprock, C.A., Fussell, B.K., (2008) "A Comparability Study of a Wireless Electret Accelerometer to a Traditional Piezoelectric Accelerometer" ASME MSEC 2008, MSEC\_ICMP2008-72203

[29] Roth, J.T. (2006) "Using the Eigenvalues of Multivariate Spectral Matrices to Achieve Cutting Direction and Sensor Orientation Independence" Journal of Manufacturing Science and Engineering, Volume 128, Issue 1, pp. 350-354

[30] EE Times Asia "Kistler rotating cutting force dynamometer performs up to 25,000rpm" January 2010. Web:

[http://www.eetasia.com/ART\\_8800211379\\_480200\\_NP\\_037c5295.HTM](http://www.eetasia.com/ART_8800211379_480200_NP_037c5295.HTM)

[31] Suprock, C.A., Fussell, B.K, Jerard, R.B., Roth, J.T., (2008) "The Performance of Electret-Based Accelerometers and the Feasibility of Their Application in a Smart End Mill Tool Holder" ISFA2008U\_136, ASME ISFA 2008

[32] Filiz, S., Cheng, C.H., Powell, K.B., Schmitz, T.L., Ozdoganlar, O.B. 2008, "An

improved tool-holder model for RCSA tool-point frequency response prediction”, Precision Engineering, Vol. 33, Issue 1, July 2007 , pp 433-446

[33] Robert G. Landers, A. Galip Ulsoy., 2008 “Nonlinear Feed Effect in Machining Chatter Analysis” Journal of Manufacturing Science and Engineering Vol. 130, Issue 1 2008, pp 1-8.

[34] V. Gagnol et al, 2007 “Model-based chatter stability prediction for high-speed spindles” International Journal of Machine Tools & Manufacture, Vol 47, (2007), pp 1176–1186.

[35] Y. Altintas et al 1999, “Analytical Prediction of Stability Lobes in Ball End Milling” Journal of Manufacturing Science and Engineering, Vol. 121, 1999, pp 586-592

[36] Y. Altintas et al 1998 “Analytical Prediction of Chatter Stability in Milling—Part II: Application of the General Formulation to Common Milling Systems”, Journal of Dynamic Systems, Measurement, and Control, Vol. 120, 1998, pp 31-36.

[37] Y. Altintas et al 2004 “Multi Frequency Solution of Chatter Stability for Low Immersion Milling”, Journal of Manufacturing Science and Engineering, Vol. 126, 2004, pp 459-466

[38] Y. Altintas et al 2003 “An Improved Time Domain Simulation for Dynamic Milling at Small Radial Immersions”, Journal of Manufacturing Science and Engineering, Vol. 125, 2003, pp 416-422.

[39] Gray, P.R., et al 2009 “Analysis and design of analog integrated circuits” Fifth Edition. Wiley, New York. ISBN:978-0-470-24599-6 . Pages 47-48

[40] CRC Materials Science and Engineering Handbook, p.279 & p.281

[41] University of New Hampshire, Design and Manufacturing Lab, 23 January 2011.

Web. <http://unh.edu/dml>

[42] Drozda, T., Wick, C., Benedict, J.T., Veilleux, R.F., Bakerjian, R. "Tool and manufacturing engineers handbook : a reference book for manufacturing engineers, managers, and technicians", 4th ed. Society of Manufacturing Engineers, 1983.

[43] Johnson, K. (2003) , "Acoustic and Auditory Phonetics" Wiley-Blackwell; 2 edition, ISBN: 978-1405101233

[44] Park, S. "Linear Predictive Speech Processing", 15 February 2010. Web:

<http://www.engineer.tamuk.edu/SPark/chap7.pdf>

[45] Jackson, L.B., *Digital Filters and Signal Processing, Second Edition*, Kluwer Academic Publishers, 1989. pp.255-257.

[46] Ljung, L., *System Identification: Theory for the User*, Prentice-Hall, 1987, pp.278-280

[47] Pandit, S.M., (1991), *Modal and Spectrum Analysis: Data Dependent Systems in State Space*, John Wiley & Sons, Inc., New York.

[48] Schmitz, T.L., Smith, K.S., "Machining Dynamics- Frequency Response to Improved Productivity" Springer Science, New York. ISBN: 978-0-387-09644-5\

[49] Faasen, R.P.H., N. van de Wouw, J.A.J. Oosterling, H. Nijmeijer, (2003) "Prediction of regenerative chatter by modeling and analysis of high-speed milling," *International Journal of Machine Tools & Manufacture*, 43 (2003) 1437-1446.

[50] Abele, E. and U. Fiedler, (2004) "Creating Stability Lobe Diagrams during Milling",

Annals of the CIRP, 53/1/2004, pp. 309-312.

[51] Abele, E., Kreis, M., Roth, M., "Electromagnetic Actuator for in Process Non-Contact Identification of Spindle-Tool Frequency Response Functions". CIRP (Ed.), Second International Conference on High Performance Cutting, 12–13 June 2006.

[52] R. L. Goodstein (1947). "Transfinite ordinals in recursive number theory". *Journal of Symbolic Logic* 12 (4): 123–129. doi:10.2307/2266486

[53] The Harmonizer "Correct chatter problems quickly and easily" Manufacturing Labs. 23 January 2011. Web. <http://www.mfg-labs.com/mfg-labs/Harmonizer/index.html>

[54] MATLAB Software Help. "Revision 7.11.0 (2010b), Function Browser" 2010. Mathworks Inc.

[55] S. S. Rao, "Mechanical Vibrations" Addison-Wesley. 1991. ISBN: 0-201-50156-2

## APPENDIX A

Placement of an accelerometer at the tool tip requires a combination of size, low cost, and simplicity. At first, it was desirable to choose an off-the-shelf sensor to work with as this offered conveniences of calibration and data sheets. It was quickly realized that the tool tip environment was inappropriate for commercially offered acceleration sensors. Piezoelectric accelerometers offer satisfactory range, but have unacceptable size. Micro electrical mechanical (MEMs) accelerometers offer an acceptable size, but experience problems with saturation and ringing under the acceleration and frequencies encountered during cutting. For these reasons, alternatives were explored. It was discovered that an electret element microphone could be converted into an accelerometer with acceptable range and size characteristics. Development and evaluation of this sensor were conducted to satisfy questions about response and calibration. To do so correctly, a test bed was constructed and the sensors were developed on a wired connection outside of the cutting tool body. Because this sensor was developed as part of research, extensive evaluation was made to determine the true effectiveness of the sensor both for linearity and statistical variation.

An electret condenser responds to vibration input by changing its capacitance. The electret used for this study is a Hosiden # KUB2823 and is characteristic of a commercially available electret condenser. This particular electret employs a diaphragm and is similar to the design detailed in Sessler et al., [7]. A 1/8" mono male connector is

used to connect to the microphone port and 3' of ground-shielded microphone cable is used to connect the electret.

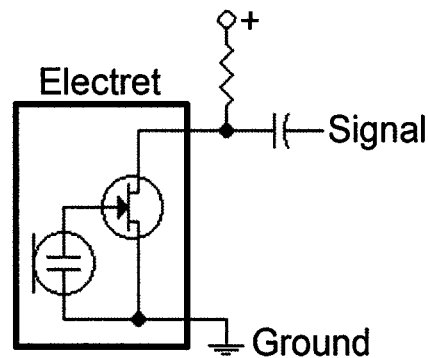


*Figure A1: Electret Condenser Microphone*

An electret condenser module contains a field effect transistor with an externally applied positive voltage bias. The resistor between this external voltage and the FET determines the gain impedance. The electret material contains a permanent electrostatic charge which applies a voltage to the FET as a function of proximity to a fixed ground plate. A capacitor is used to eliminate the DC offset within the output signal.

The retail electret sensor components are, together, \$1.10 USD in cost, which makes the electret accelerometer an attractive alternative to a piezoelectric sensor if the appropriate response characteristics are possible.

**Table A1: Electret Accelerometer Component Cost**

Component	Cost (USD)
Hosiden#KUB2823 Electret	\$0.50
3' Microphone Cable	\$0.50
1/8" Mono Male Connector	\$0.10

This electret sensor was sampled using a PC sound card and bench marked alongside a traditional piezoelectric accelerometer sampled on a NI PXI1031 DAQ computer. The data sampling rate on a standard PC sound card reaches 192 kHz while the frequency response range is 20-20,000 Hz. The native A/D conversion resolution is commonly 16 bit over a 1 volt range. However, many newer cards are available with 24 bit capability. Although the resolution of a PC sound card is sufficient to capture high bandwidth data, using the device for data acquisition on a machine tool system is futile without a robust sensor. Equally as important is the calibration of the sensor/sound card system. Questions such as “Is the system response linear?” and “Can the system replicate the performance of a traditional accelerometer/DAQ system?” must be answered before the sensor can be implemented for condition monitoring purposes.

An example of the electret sensor assembly, similar to the one used in this study, is shown in Figure A2. The electret sensor housing used in this study is fabricated as a solid 6 mm cylindrical body with the electret unit located at the center of the device, oriented along the axis. The electret diaphragm is completely embedded within the epoxy such that no external acoustic signals can be received. Thermal-set epoxy is used to fabricate the sensor housing. The figure below shows the sensor assembly.

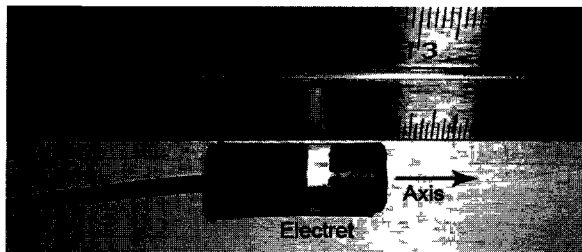


*Figure A2: Electret Accelerometer Assembly*



After embedding the electret condenser into a solid assembly, the dynamics of the sensor are significantly altered from the manufacturer's specifications. Specifically, the electret diaphragm can no longer respond to air pressure fluctuations, but instead, responds mechanically to vibrations of the solid assembly. Therefore, it is necessary to explore the dynamic response of this new sensor assembly.

To accomplish this, a sinusoidal vibration input is generated using a shaker table. A single-axis PCB piezoelectric accelerometer (Model 320 C33, serial number 5901) is fixed to the table at the same reference point as the electret sensor. The output sensitivity of this piezoelectric accelerometer is 100mV/g with a maximum range of 50g's. This piezoelectric accelerometer is amplified through a PCB charge amplifier. The corresponding voltage signal is monitored through a traditional DAQ system. The electret sensor is sampled through the mono-channel microphone port on a PC laptop. Both the piezoelectric accelerometer and the electret sensor signals are sampled at 20 kHz. Figures A3 and A4 detail the shaker table and attached sensors and corresponding DUT block diagram.

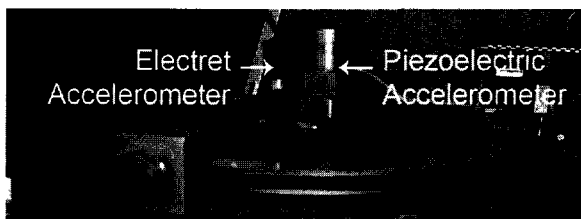


*Figure A3: Electret Accelerometer Test Setup*

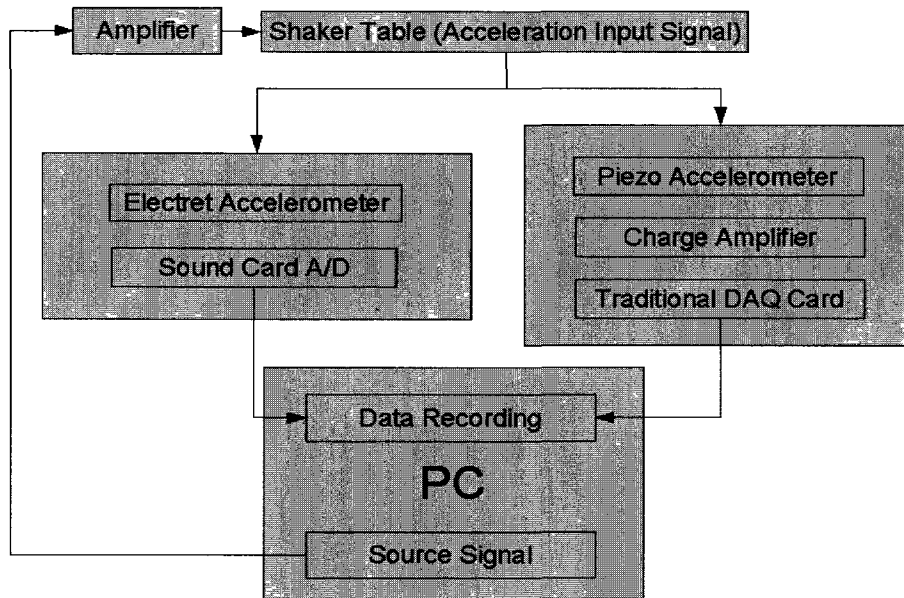


Figure A4: Block Diagram of Electret Test Setup

The PCB accelerometer has a known flat frequency response to 4 kHz and provides the baseline from which the electret sensor is benchmarked. Consequently, the specific response of the shaker table system is not of interest, since the piezoelectric accelerometer acts as the reference signal. For this work, multiple shaker gains are used and are identified according to peak acceleration amplitude in Table A1.

Table A1: Shaker Gains and Measured Acceleration

% Shaker Gain	Peak G's (x 9.81m/s <sup>2</sup> )
100%	6.56
80%	5.30
60%	3.91
40%	2.64
20%	1.31

A dynamic range of approximately 5.35g's, the limit of the shaker table, was investigated for this feasibility study.

To test the frequency response of the electret sensor/sound card system, a sine sweep voltage was input to the shaker motor. The frequency of this signal varied from 0 to 10 kHz in a linear sweep from 0 to 10 seconds. During this sweep, signal outputs from the electret sensor and piezoelectric accelerometer were recorded. The sensors were compared over 0 to 5kHz.

After the data was acquired, an amplitude spectrum was generated for both sensor types (Figure A4). This spectrum was created using the fast Fourier transform such as detailed in [8]. As expected, the outcome of the test shows the stable frequency response of the commercial piezoelectric accelerometer. As can be seen, the electret accelerometer also produces a repeatable frequency response.

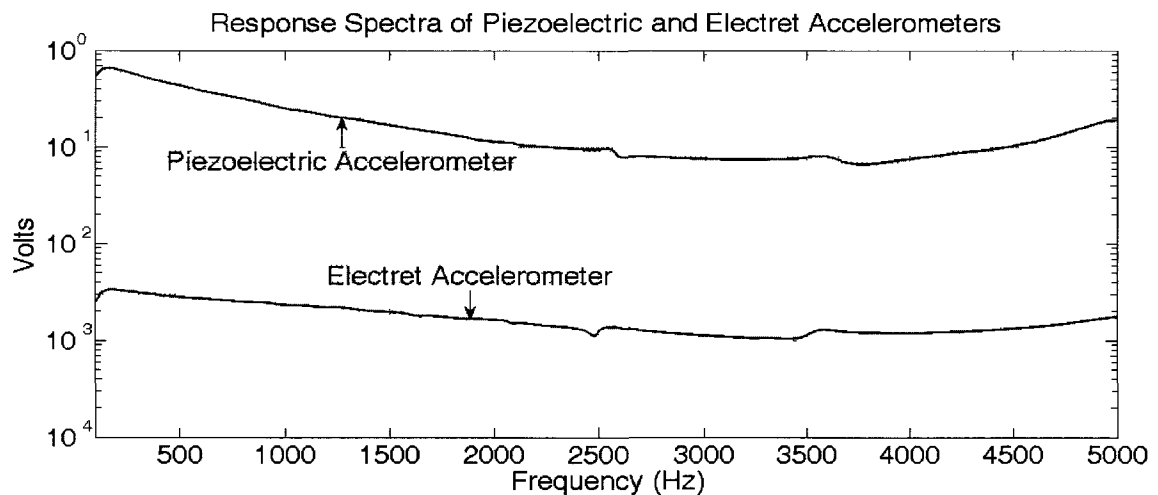


*Figure A4 Response Spectra for Piezoelectric and Electret Accelerometers*

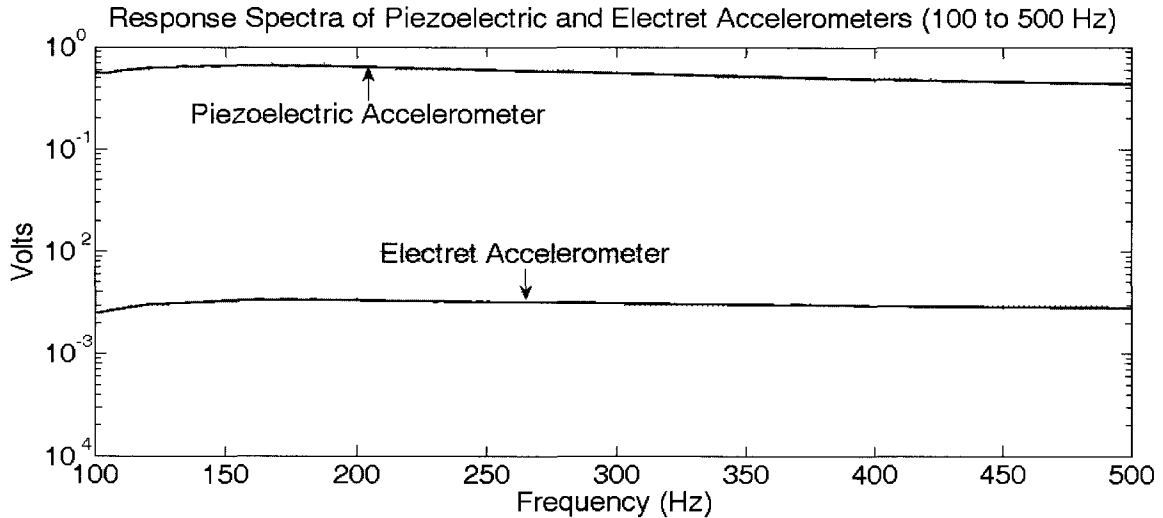


*Figure A5: Detail of 100 to 500 Hz Response Spectra*

As detailed in Figure A5, the response characteristics for both sensors show high similarity from 100 to 500 Hz. As a result of the electret relying on a mechanical diaphragm, it is anticipated that natural frequencies would exist as a function of the stiffness and mass of the diaphragm disk. For the 6 mm diameter electret tested, the diaphragm is small enough such that no natural frequencies are encountered within the observed range. Through an impulse test, the electret sensor's lowest natural frequency was determined to be 6800 Hz.

To test the hypothesis that the frequency response spectrum of the electret sensor does not vary as a function of input magnitude, several tests are conducted at different shaker gain levels. It is observed that the electret accelerometer does not change the shape of its response spectrum as a function of input acceleration amplitude. Figure A6 details five tests with the shaker gain set at 20, 40, 60, 80, and 100% respectively.

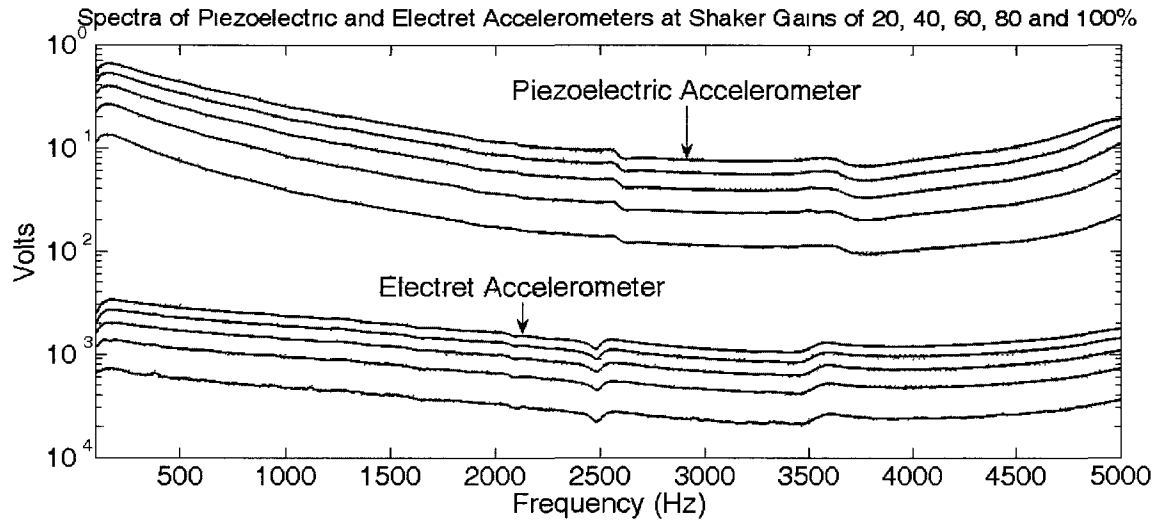


Figure A6: Linear Response of the Electret Accelerometer

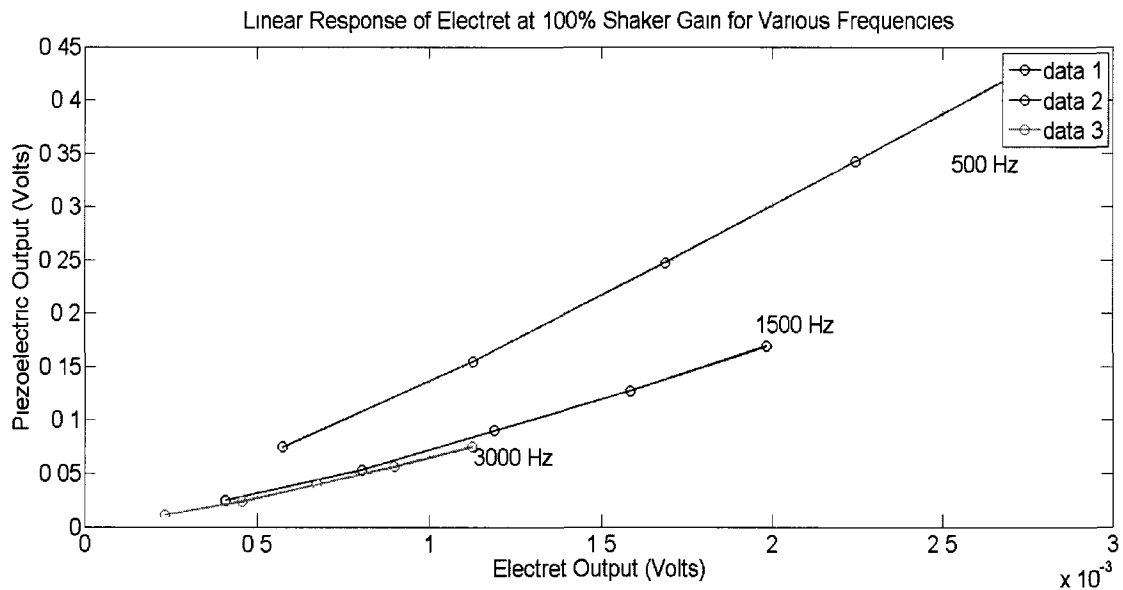


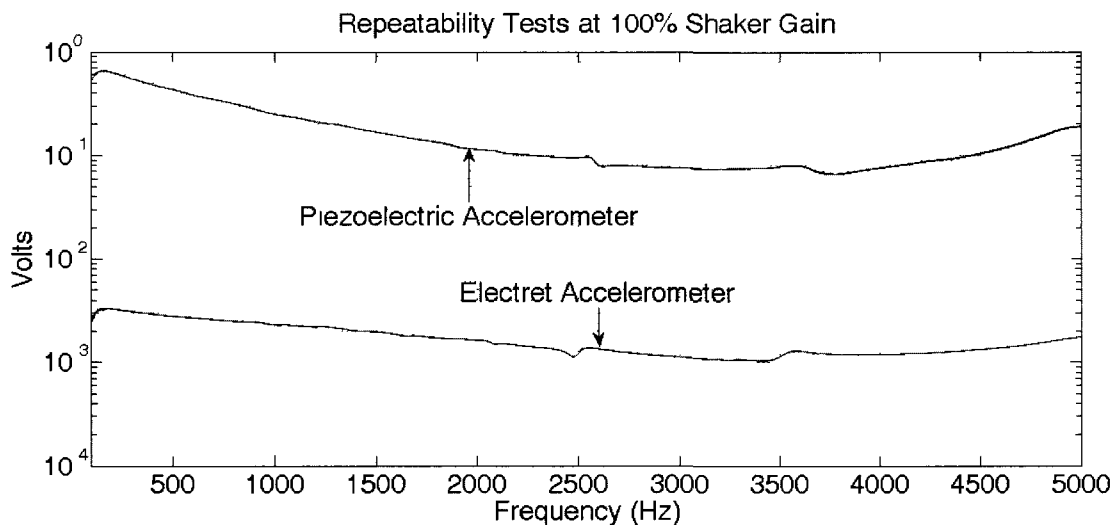
Figure A7: Linear Response of the Electret Accelerometer at Specific Frequencies

Figure A7 illustrates confirmation that the output from the electret corresponds directly to the acceleration input measured by the piezoelectric accelerometer. The curves at various

frequencies vary linearly with respect to acceleration amplitude, indicating that the gain of the electret is constant at all frequencies of interest.

After identifying that the electret accelerometer has a response that is linear with respect to input amplitude, the response repeatability was investigated. Fifteen tests were conducted at each shaker gain. As with the linearity response tests, a sine chirp was produced through the shaker motor. The resulting sensor spectra were observed for similarity.

Figure A8 illustrates the repeatability tests at 100% shaker gain plotted for both the piezoelectric and electret accelerometers.



*Figure A8: Electret Repeatability Tests at 100% Shaker Gain for 15 Tests*

From the outcome of these tests, it is evident that the response spectra of both sensors are nearly stationary over fifteen consecutive experiments. However, it is of interest to note that the spread seen in these spectra is a function of the number of

sequential tests performed. In particular, the amplifier and shaker motor produce a slightly different input amplitude as a function of operational temperature. This phenomenon was recorded by both the piezoelectric and electret accelerometers.

In addition to confirming a robust response, these repeatability tests identify the lower limit of the sensor's response reliability. As with the Piezoelectric accelerometer, this limit occurs between 0 and 100 Hz. Figure A9 details the 100 to 500 Hz range.

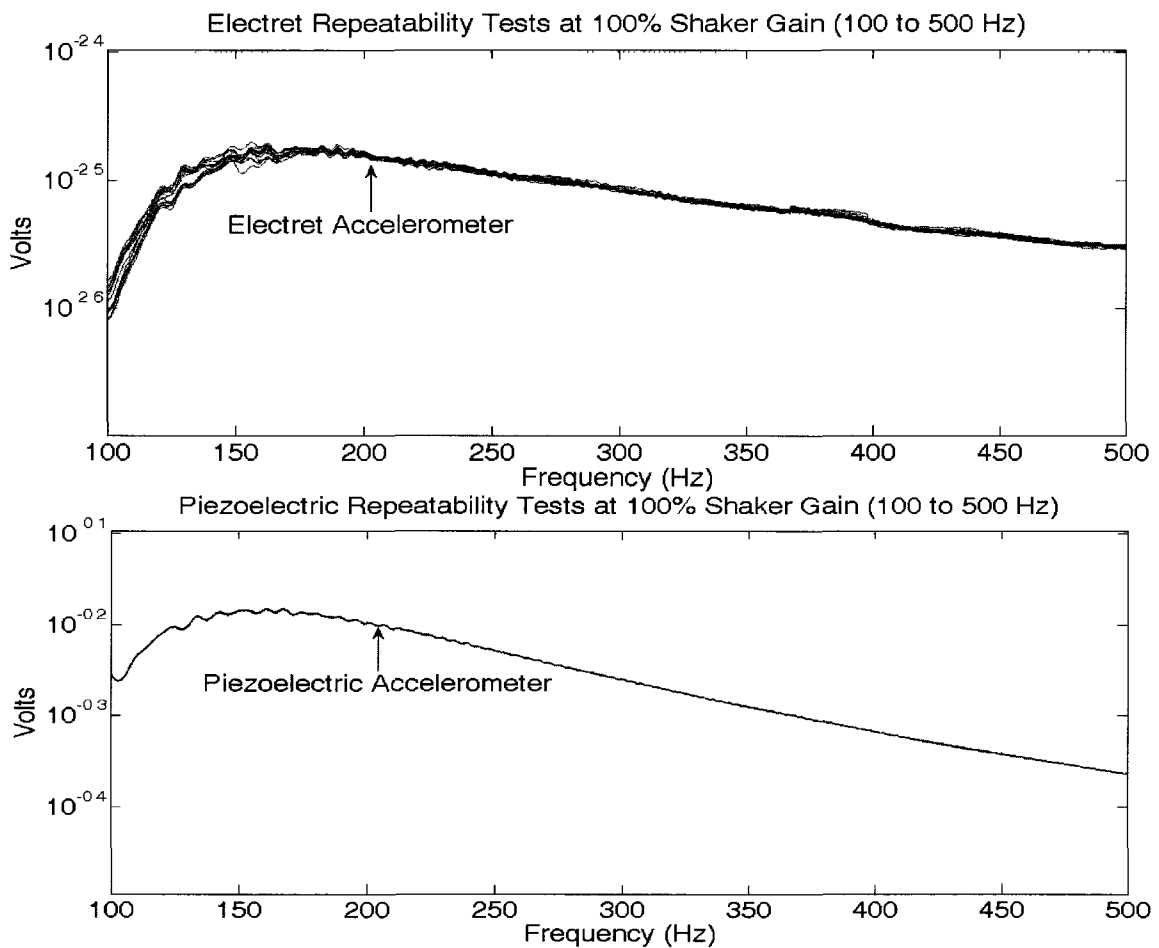


*Figure A9: Detail of 100 to 500 Hz Repeatability Tests at 100% Shaker Gain*

The final objective for the repeatability testing was to create a test-averaged response for

the electret accelerometer. This response represents the expected frequency spectrum of the sensor. Figure A10 shows the mean response of the sensor over all fifteen repeatability tests at 100% shaker gain.

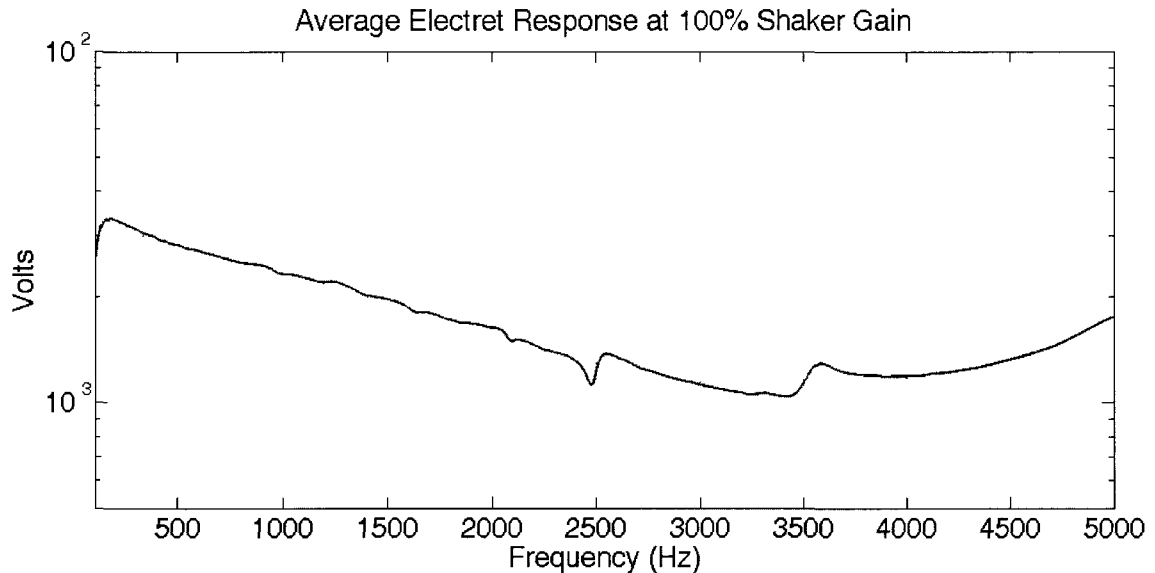


*Figure A10: Average Electret Response over 15 Repeatability Tests.*

Since the electret response spectrum is linear, the frequency response of the electret accelerometer can be mapped to the known flat response of the piezoelectric accelerometer. The objective of this process is to replicate the flat response of the piezoelectric sensor from the input signal of the electret accelerometer. This mapping assumes that the electret accelerometer response at each input frequency is equal to that of the input (piezoelectric) response scaled by a ratio. Using the measured electret response and piezoelectric response, this ratio can be derived as a function of frequency. Digital signal processing refers to the separation or combination of two signals in the frequency domain as convolution [9]. It is essentially a discrete transfer function between



one signal and the other.

In addition to amplitude linearity, assumptions are made that the sensor system is stationary and that the system contains little noise. Both of these assumptions are valid since the sensor system response does not change as a function of time and the signal to noise ratio is over 58 dB for all frequencies of interest.

First, the acquired time signals from both the electret and piezoelectric accelerometers are transformed into the frequency domain. The time signals are represented as  $e_g$  and  $p_g$  respectively. The subscript  $g$  represents the particular input gain level at which each data set was recorded. Specifically, this is the shaker table gain level. These signals are transformed according to the discrete Fourier transform as:

$$P_g(\omega) = \sum_{k=0}^{N-1} p_g(k) \exp\left(\frac{-2\pi i k \omega}{N}\right) \quad (A1)$$

$$E_g(\omega) = \sum_{k=0}^{N-1} e_g(k) \exp\left(\frac{-2\pi i k \omega}{N}\right) \quad (A2)$$

where  $E_g$  and  $P_g$  are spectra of the time signals evaluated over  $\omega=0, \dots, Nyquist$ . In the case of this experiment, the Nyquist frequency is 10 kHz since the time sampling rate was 20 kHz. However, the piezoelectric accelerometer bandwidth is 1 to 4000 Hz ( $\pm 5\%$ ). Since this sensor acts as the baseline for benchmarking the electret accelerometer, the spectra are evaluated over the range  $\omega=0, \dots, 5000 \text{ Hz}$ .

Recalling from the Linear Response section, the response of the electret accelerometer retained the same characteristics over multiple amplitude inputs. Therefore, the gain at any particular frequency is constant with respect to input

amplitude. Consequently, at any particular input gain level, there exists a ratio spectrum between the outputs of the electret and piezoelectric accelerometers. The ratio function is defined by:

$$R_g(\omega) = \frac{P_g(\omega)}{E_g(\omega)} \quad (\text{A3})$$

A mean frequency ratio function,  $\bar{R}$ , can be defined over the different gain levels as:

$$\bar{R}(\omega) = \frac{1}{G} \sum_{g=1}^G \frac{P_g(\omega)}{E_g(\omega)} \quad (\text{A4})$$

where  $G$  is the number of unique gain levels tested and  $g$  represents each single gain level. For the case presented in this work, gain levels of 20, 40, 60, 80, and 100% were observed. This represents  $G=5$  and  $g=1, \dots, 5$ .

Through the transformation by  $\bar{R}$ , error is distributed evenly over the range of input gains tested and a constant transform error can be expected. Figure A11 shows  $\bar{R}$  plotted with respect to frequency.

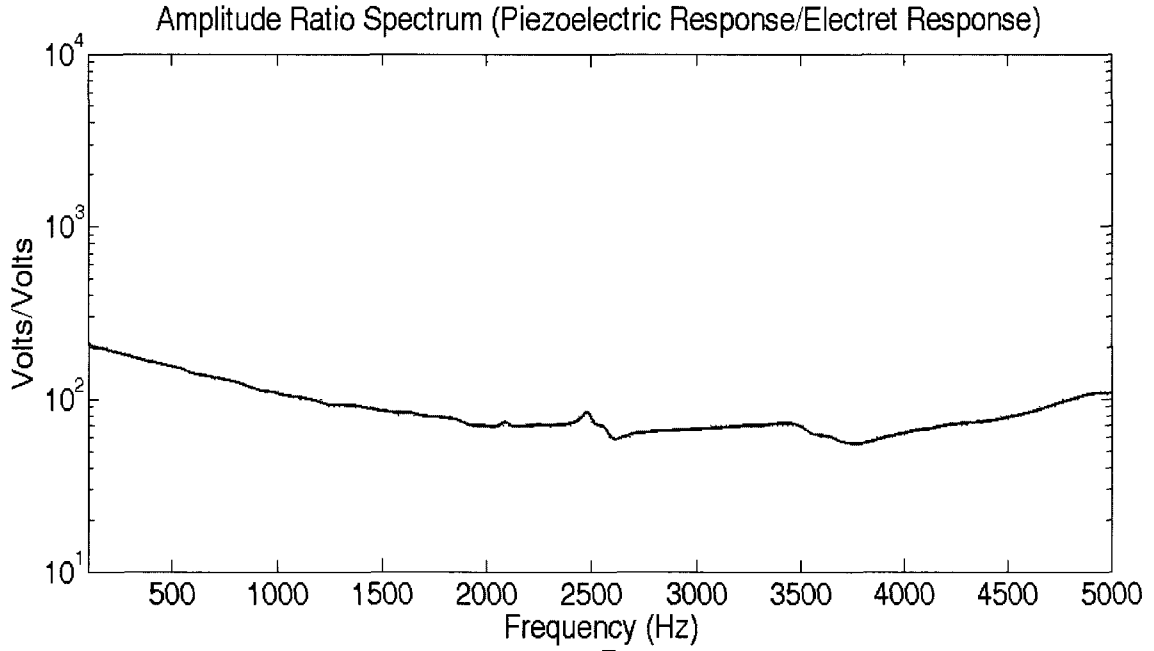


Figure A11: Calibration Transfer Function,  $\bar{R}$

After the derivation of  $\bar{R}$ , any output signal,  $E$ , from the electret accelerometer can be mapped to the flat response of the piezoelectric accelerometer according to:

$$E'(\omega) = \bar{R}(\omega) E(\omega) \quad (A5)$$

where  $E'(\omega)$  is the corrected electret frequency response. However, the ideal corrected spectrum  $E'$  does not reflect error present in the real system.

#### **Accounting for Electret Accelerometer Measurement Error**

Recalling that each of the five gain levels was tested fifteen times, the standard deviation in the piezoelectric and shaker table response can be assessed at each gain level  $g$  as:

$$SP_g(\omega) = \left[ \frac{1}{T} \sum_{i=1}^T (P_{ig}(\omega) - \bar{P}_g(\omega))^2 \right]^{\frac{1}{2}} \quad (A6)$$

where  $\bar{P}_g(\omega) = \frac{1}{T} \sum_{t=1}^T P_{gt}(\omega)$  ,  $t$  represents the test repetition  $t=1, \dots, 15$  and  $T=15$  .

Similarly, the electret and shaker table response error,  $SE_g$  , can also be computed through this method.

After the error is known at each gain level, the error can be propagated to the ratio spectrum,  $\bar{R}$  . Since the sensors were sampled on independent systems they have no covariance and the error propagation takes the form:

$$\bar{SR}_g^2(\omega) = SE_g^2(\omega) \left( \frac{\delta \left( \frac{\bar{P}_g(\omega)}{\bar{E}_g(\omega)} \right)}{\delta \bar{E}_g(\omega)} \right)^2 + SP_g^2(\omega) \left( \frac{\delta \left( \frac{\bar{P}_g(\omega)}{\bar{E}_g(\omega)} \right)}{\delta \bar{P}_g(\omega)} \right)^2$$

or:

$$\bar{SR}(\omega) = \left[ \left( SE \frac{\bar{P}_g}{\bar{E}_g^2} \right)^2 + \left( SP \frac{1}{\bar{E}_g} \right)^2 \right]^{\frac{1}{2}} \quad (A7)$$

This error is computed for the highest gain value tested (  $g=5$  ; 6.56g's). Figure A12 illustrates the ratio spectrum,  $\bar{R}$  , along with its corresponding full-scale error bars  $\bar{R} \pm \bar{SR}$  .

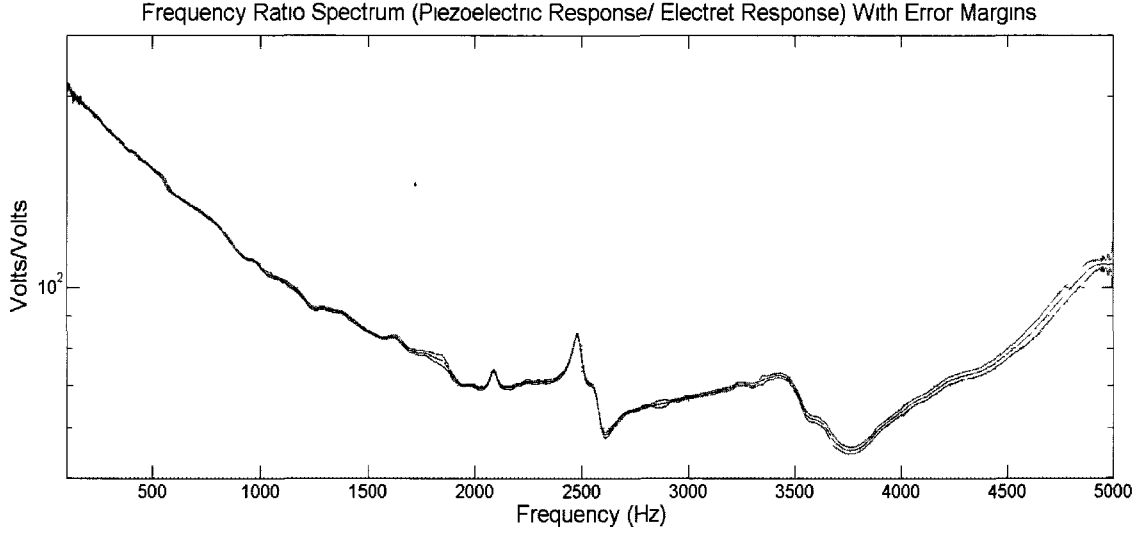


Figure A12: Calibration Transfer Function  $\bar{R}$  , with Error Bounds  $\bar{R} \pm \bar{S}\bar{R}$  .

Similar to the ideal case (Equation A5), any electret accelerometer signal and it's associated error band,  $E \pm SE$  , can be mapped to the equivalent response of the piezoelectric accelerometer:

$$E'(\omega) \pm SE'(\omega) = \bar{R}(\omega) E(\omega) \pm [\bar{R}(\omega) SE(\omega)]^{\frac{1}{2}} \quad (A8)$$

Therefore, the relationship between the piezoelectric response and electret response (considerate of both sensor errors) is given as:

$$P \pm PE \approx E'(\omega) \pm SE'(\omega) \quad (A9)$$

As calculated over the experimental tests, the corrected electret response spectrum has the highest spread at 5000 Hz during 100% shaker gain. Because the baseline piezoelectric sensor is stable to 4000 Hz, the error will be computed at this frequency. This value,  $E'(4000) \pm SE'$  , is  $0.0755 \pm 0.0008$  volts, corresponding to an error margin of

approximately 1% from the piezoelectric frequency response. This value includes variability from the electret sensor, piezoelectric accelerometer, and shaker table. As a result, this represents the error with respect to the piezoelectric sensor used as the reference source.

Using the mean transfer function  $\bar{R}$  as shown in equation A5, the corrected electret accelerometer response,  $E'$ , is highly similar to that of the piezoelectric accelerometer. Figures A13 through A15 show examples of the procedure applied at different shaker gain settings along with the piezoelectric response. The low frequency response of the sensor from 100 to 500 Hz is shown in Figure A16.

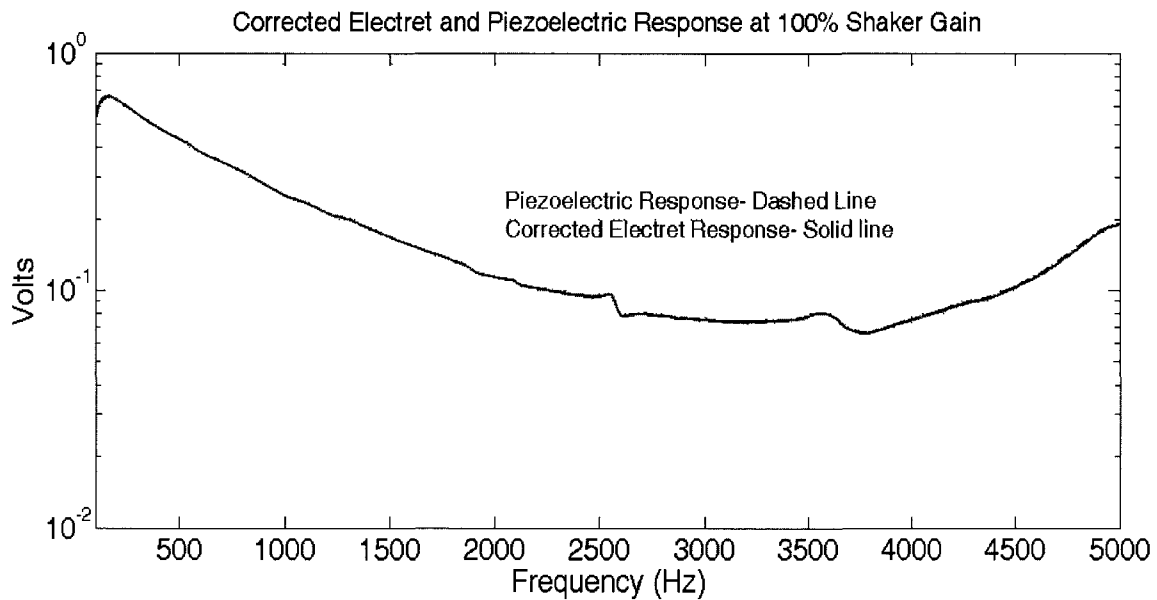


*Figure A13: Corrected Electret Response at 100% Shaker Gain*

The results at 100% shaker gain are representative of the results found over the other gains tested. Figures A15 and A16 show magnifications of both 80 and 20% gains respectively.

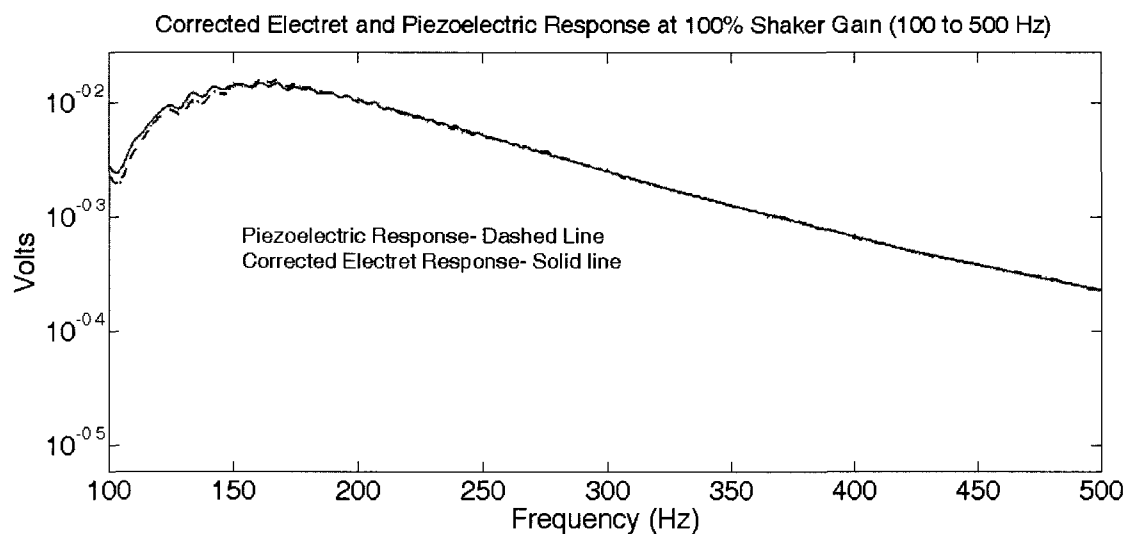


Figure A14: Corrected Electret Response at 100% Shaker Gain (100 to 500 Hz)

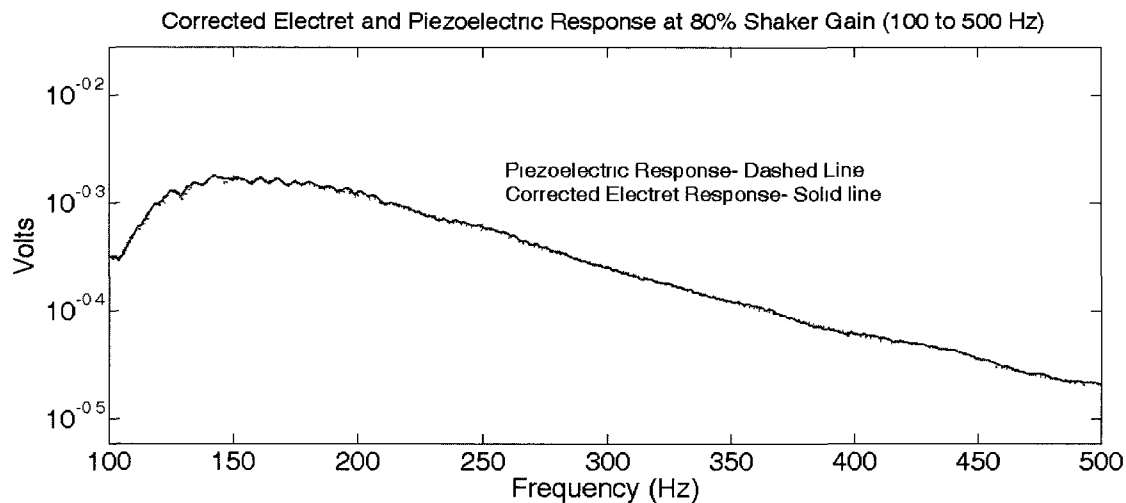


Figure A15: Corrected Electret Response at 80% Shaker Gain (100 to 500 Hz).



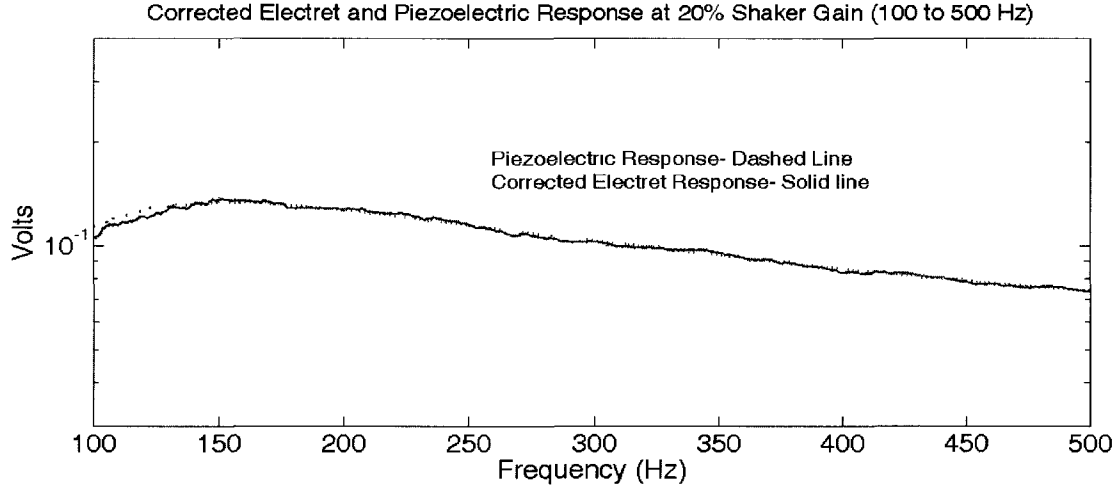


Figure A16: Corrected Electret Response at 20% Shaker Gain (100 to 500 Hz)

Since the response of a single electret is linear (Figure A7), the sensor must be tested for repeatability. Repeatability is investigated over a population of sensors from the same manufacturing batch. This shows how consistent the sensor response is between individual electret units. By repeating each individual sensor test multiple times,  $T$ , a mean ratio spectrum,  $\bar{R}$ , is given by repeated testing of one sensor at full scale shaker gain:

$$\bar{R}(\omega) = \frac{1}{T} \sum_{t=1}^T \frac{P_t(\omega)}{E_t(\omega)} \quad (\text{A10})$$

This mean ratio spectrum is generated for repeated tests of each individual sensor in the population. Specifically, there is a unique  $\bar{R}$  for each sensor tested. This is similar to Equation A4, but is performed over tests instead of gain settings.

After the derivation of  $\bar{R}$ , any output signal,  $E$ , from the electret accelerometer can be mapped to the equivalent response of the piezoelectric accelerometer according to:

$$E'(\omega) = \bar{R}(\omega) E(\omega) \quad (\text{A11})$$

where  $E'(\omega)$  is the corrected electret frequency response. In this sense,  $\bar{R}$  is the

calibration spectrum (gain ratios at discrete frequencies) that scales the spectrum of a particular electret sensor to the correct response shape. However, the ideal corrected spectrum  $E'$  does not reflect error or statistical deviation present in the system.

The observation of statistical variability must consider both error present in the repeatability of each individual sensor and in the repeatability of the population. For this study, 12 electret accelerometers were fabricated and benchmarked against a single piezoelectric accelerometer. Each of the 12 individual sensors was tested 32 times. Because the electret sensors were benchmarked against an imperfect signal from a piezoelectric accelerometer, the error present in the piezoelectric signal must also be propagated to the resulting variability. Because the piezoelectric sensor is the baseline, it is necessary to consider the variability of the piezoelectric sensor to confidently estimate the error bounds on the electret accelerometer. Standard deviation is used to define population spread over identical repeated tests. For each individual sensor, the population of 32 repeated tests is assumed to be normally distributed.

#### Step 1: Calibrate Sensor Population

By conducting repeated response tests for each of the 12 electret sensors, Equation A3 produced mean calibration spectra for the population. Recalling that each individual sensor was tested 32 times ( $T=32$ ), these mean ratio spectra,  $\bar{R}$ , represent a population of tests for each sensor. Corresponding to these mean ratio spectra, a standard deviation spectrum was also calculated for each sensor (discussed in the following section).

Although each calibration spectrum was slightly different, their trends were similar. Figure A17 shows a plot of the 12 ratio spectra,  $\bar{R}$ , for this population of sensors.

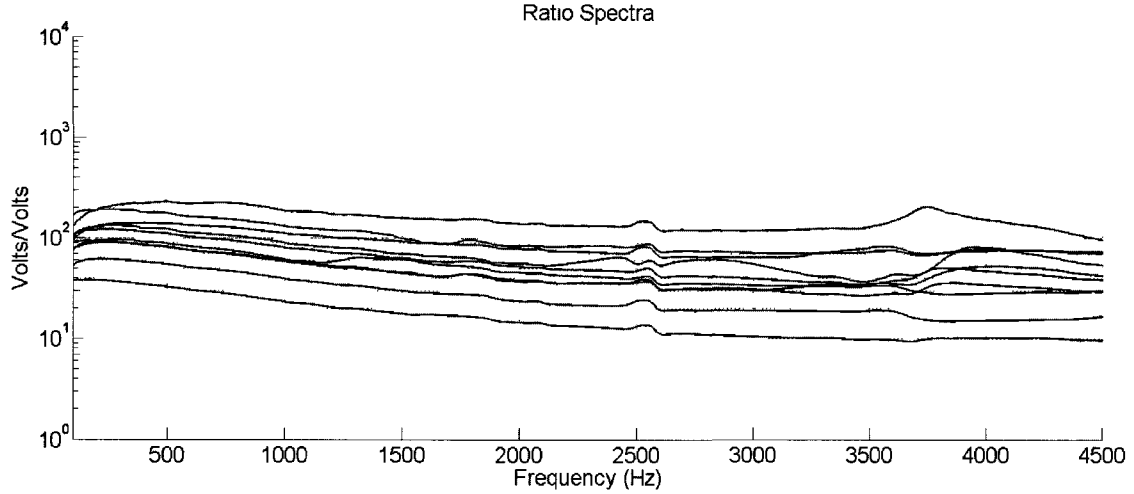


Figure A17: Transfer Function,  $\bar{R}$ , for the Population of Electret Sensors.

As found, the gains for the electret accelerometers varied as a function of frequency. This was to be expected since variability is introduced by the manual fabrication process. Although there is a range in the magnitude of the gains, the ratio spectra exhibit a strong trend in behavior over all 12 sensors.

#### Steps 2 and 3: Calculating the Standard Deviation Spectra of Individual Sensors

Similar to the gain, the standard deviation for each individual sensor is treated as a function of frequency. This is done since, in a typical sensor system, variability is seen to change throughout the response spectrum. However, deviation in both the electret accelerometer and the source (piezoelectric) signal must be accounted for. Therefore, this process involves an error propagation based on the standard deviation spectra.

The standard deviation present in the piezoelectric response can be represented as a function of discrete frequencies,  $\omega$ , as:

$$SP(\omega) = \left[ \frac{1}{T} \sum_{t=1}^T (P_t(\omega) - \bar{P}(\omega))^2 \right]^{\frac{1}{2}} \quad (A12)$$

where  $\bar{P}(\omega) = \frac{1}{T} \sum_{t=1}^T P_t(\omega)$ ,  $t$  represents the test repetition  $t=1, \dots, 32$  and  $T=32$ . Since standard deviation is being used as the definition for spread, a significant population of 32 repeat tests was performed.

Likewise, the standard deviation of the electret sensor response spectrum is defined as:

$$SE(\omega) = \left[ \frac{1}{T} \sum_{t=1}^T (E_t(\omega) - \bar{E}(\omega))^2 \right]^{\frac{1}{2}} \quad (A13)$$

where  $\bar{E}(\omega) = \frac{1}{T} \sum_{t=1}^T E_t(\omega)$ ,  $t$  represents the test repetition  $t=1, \dots, 32$  and  $T=32$ . Figure A18 shows a plot of the uncorrected mean electret spectrum,  $\bar{E}$ , and its corresponding standard deviation spectrum  $\bar{SE}$  for an individual sensor over 32 tests.

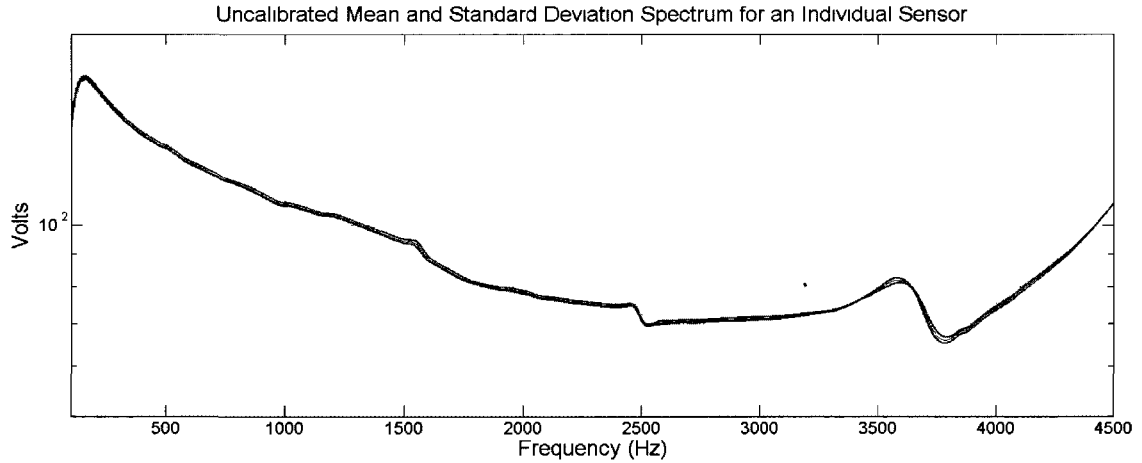


*Figure A18: Uncorrected Electret Spectrum and Corresponding Standard Deviation Spectrum.*

After these two standard deviation spectra are calculated, a ratio spectrum can be derived between that of the piezoelectric and electret accelerometers. This takes on a similar form to that of Equation A3:

$$SR(\omega) = \frac{SP(\omega)}{SE(\omega)} \quad (A14)$$

However, this basic ratio is incorrect because  $SP(\omega)$  and  $SE(\omega)$  are error terms.

The error propagation is properly:

$$SR^2(\omega) = SE^2(\omega) \left( \frac{\delta \left( \frac{P(\omega)}{E(\omega)} \right)}{\delta E(\omega)} \right)^2 + SP^2(\omega) \left( \frac{\delta \left( \frac{P(\omega)}{E(\omega)} \right)}{\delta P(\omega)} \right)^2 \quad (A15)$$

or:

$$SR(\omega) = \left[ \left( SE \frac{\bar{P}}{E^2} \right)^2 + \left( SP \frac{1}{E} \right)^2 \right]^{\frac{1}{2}}$$

Figure A19 illustrates a ratio spectrum,  $\bar{R}$ , along with its corresponding error bars  $R \pm SR$

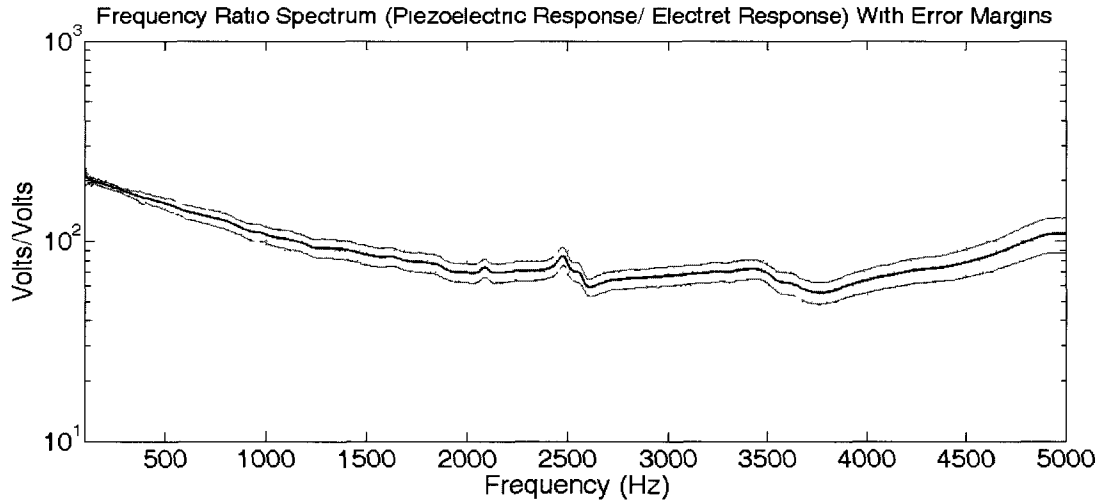


Figure A19: Amplitude Ratio Spectrum,  $\bar{R}$  With Error Bounds  $\bar{R} \pm SR$ .

The example given in Figure A19 shows the error spectrum propagated to a mean ratio spectrum  $\bar{R}$  for a single electret sensor. All 12 of the sensors in the population are processed by the same method.

Step 4. Error Propagation through the Calibration Correction

Similar to the ideal case (Equation A4), any electret accelerometer signal and its associated error band,  $E \pm SE$ , can be mapped to the equivalent response of the piezoelectric accelerometer. This relationship represents error propagation between the piezoelectric and electret accelerometer:

$$E'(\omega) \pm SE'(\omega) = \bar{R}(\omega) E(\omega) \pm [(E(\omega)SR(\omega))^2 + (\bar{R}(\omega)SE(\omega))^2]^{\frac{1}{2}} \quad (A16)$$

The second term in Equation A16 is the definition of error propagation for a product in which both terms contain an error term. The corrected error spectrum,  $E' \pm SE'$ , is generated for each individual sensor and contains the error over 32 electret sensor tests as well as the error from the piezoelectric accelerometer. There is a unique  $E \pm SE$  for each of the 12 sensors in the population.

After this calibration correction has been determined for each individual sensor, the corrected spectra can be compared between each other, over the population. This calibration step allows the population to be analyzed with a similar mean spectrum. The mean spectrum represents the mean of the piezoelectric signal to which the electret spectra were mapped. Figures A17-A19 are an example of this mapping, demonstrating the result of a corrected fit to the piezoelectric response. The frequency scale of this figure is reduced to show detail.

#### Steps 5 and 6. Calculating a Mean Corrected Spectrum for the Population of Electret Sensors

Once all 12 electret sensors are corrected by Equation A16, the equation can be shown as a single spectrum representative of the entire population. The first term in Equation A16 contains no deviation over the population since it is the ideal mapping of

each individual electret sensor to the mean piezoelectric response,  $\bar{P}$ . After this mapping has occurred by each individual sensor's  $\bar{R}$ , the first term of Equation A16 is nearly identical for all sensors. Recalling that the error present in this mapping is explained by the second term in Equation A16, these error spectra must be combined over all 12 sensors. Once again, this takes the form of error propagation over the population of sensors. Without considering uncertainty, this ideal relationship is given as:

$$\begin{aligned} \bar{E}'(\omega) \pm \bar{SE}'(\omega) = & \frac{1}{P} \sum_{p=1}^P [\bar{R}_p(\omega) E_p(\omega)] \\ & \pm \frac{1}{P} \sum_{p=1}^P [[(E_p(\omega) S R_p(\omega))^2 + (\bar{R}_p(\omega) S E_p(\omega))^2]^{\frac{1}{2}}] \end{aligned} \quad (\text{A17})$$

Where  $P=12$  representing the series of individual sensors tested.  $\bar{E}'(\omega) \pm \bar{SE}'(\omega)$  is the mean corrected response spectrum and corresponding error band for the population of sensors tested.

However this relationship is incorrect without applying proper error propagation to the second term. The second term in this equation considers error propagation over the population according to the definition of uncertainty in a sum:

$$A \pm B \pm C \dots = \sqrt{\Delta A^2 + \Delta B^2 + \Delta C^2 \dots} \quad (\text{A18})$$

Recalling that the error of the first term (ideal  $E'(\omega)$ ) is zero, the second term is now properly defined as:

$$\begin{aligned} E'(\omega) \pm SE'(\omega) = & \frac{1}{P} \sum_{p=1}^P [\bar{R}_p(\omega) E_p(\omega)] \\ & \pm \sqrt{\sum_{p=1}^P [(E_p(\omega) S \bar{R}_p(\omega))^2 + (\bar{R}_p(\omega) S E_p(\omega))^2]} \end{aligned} \quad (\text{A19})$$

### **Results of the Electret Accelerometer Statistical Analysis**

The outcome of studying the behavior of the response over a population of individual

sensors was insightful. As a result of performing repeated individual tests and propagating the error over a population of corrected sensor responses, a clear understanding of the sensor's performance characteristics are observed. Figure A20 shows  $\bar{E}'(\omega) \pm SE'(\omega)$ .

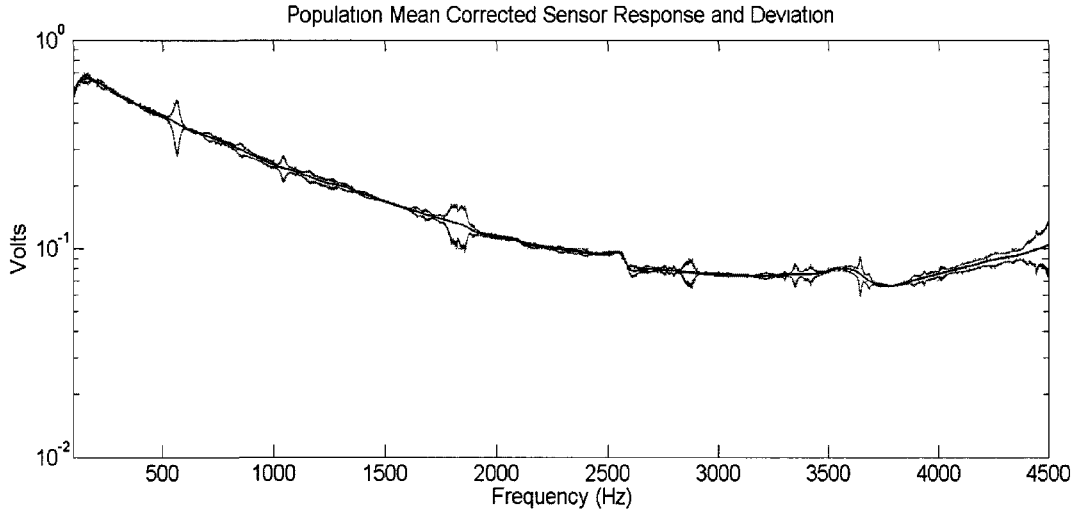


*Figure A20: Population Mean Response Spectrum Showing Error Bound*

It is observed that the error bounds for the sensor are higher in certain frequency ranges. The first natural frequency of the electret accelerometer diaphragm is known to be 6800 Hz. Therefore, the error peaks observed in Figure A20 may be the outcome of nonlinearities in the shaker table system. Without a statistical observation of the individual sensors and propagating the error results over the population, these instances would go unnoticed. The tolerance of the electret accelerometer is within  $\pm 6\%$ . Although some error was introduced by the piezoelectric sensor, this was unavoidable since the piezoelectric was used as the reference. These error bounds are for the population of electret sensors. Therefore, each individual sensor in the population falls within the error range of the calibration.



### **Temperature Effects on the Electret Accelerometer**

To test the temperature sensitivity, electret accelerometers (outside of a cutting tool body) are heated to a isothermal state. These sensors are embedded at the core of a thermal mass of 304 stainless steel and composite epoxy. The temperature is measured with a thermocouple and is considered accurate to  $\pm 1$  degree C. The heated electret sensors are removed from the heated environment, placed on a shaker, and a 0 to 10 kHz chirp is conducted (identical to the procedure for frequency response testing). Figure A21 details the frequency response at various temperatures

The spectrum response of the electret accelerometer is temperature dependent. Throughout the tests, increases in temperature lead to an increase in the amplitude over the stable region of the response. Throughout the three lower-temperature tests (21°C, 32°C, and 43°C), the responses remained relatively consistent, only posting changes in amplitude. When examining the responses from the 43°C to the 54°C temperature tests, an apparent change occurred. This spectrum response may have been caused by a physical change of the electret diaphragm, thus providing a different spectrum. As the temperature increased from 54°C to 77°C, the change in response became even more apparent. The electret used in this research utilizes a Teflon polymer diaphragm, which may have undergone a physical transformation at the elevated temperatures. Moreover, the threshold temperature dependence of the field effect transistor (FET) affects both frequency response and gain [39]. Overall, the spectrum response of the electret accelerometer was dependent on the temperature at which operation occurred. Therefore, the effects of

temperature will have to be considered and will play an important role in the calibration of the electret accelerometer if the operation is not at room temperature. However, this does not eliminate the electret sensor from consideration in flood coolant operations or for operations requiring destructive placement of the sensor (where other sensors may be cost prohibitive). Furthermore, as discussed in Section 3.7, the tool core temperature has a significant phase lag and time constant. This fact renders a tool-core accelerometer effective for laboratory tests even at dry cutting conditions.

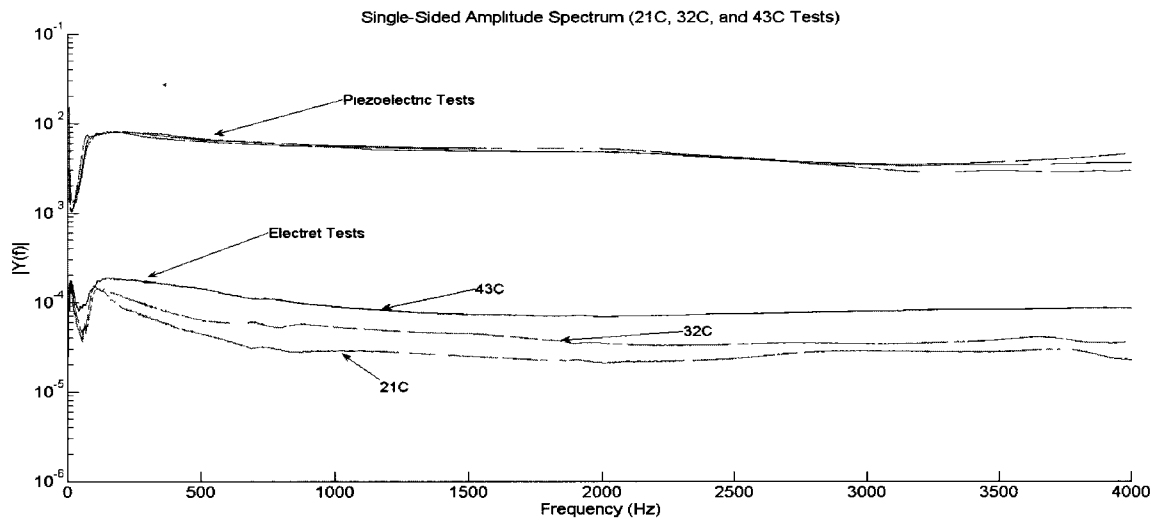


*Figure A21: Electret Temperature Response Spectra*

Given that the electret was shown to provide a repeatable and mappable signal, the next step towards developing an end milling condition monitoring systems involves installing these sensors within the tool holder. Development of a Smart Tool Holder will require the electret accelerometer to be located on a rotating tool. These sensors will directly record the tool response without the need for transfer through the spindle or workpiece. The sensor will be embedded into the tool holder in close proximity to the

cutting tool, and thus requires a means of data transmission that does not rely on a physical connection to the sensor.

### **Wireless Data Transmission from the Electret Accelerometer**

Although a wireless data transmission method solves the physical problems involved with the integration of a sensor within the tool holder, the end milling environment presents additional challenges from the perspective of electromagnetic interference. Electric motors operate the machine spindle as well as the x, y, and z translation of the bed. The proximity of these motors to the wireless transmitter presents a problem due to the wide spectrum of electromagnetic interference generated during the cutting process. Moreover, these motors do not remain at a constant speed during cutting, resulting in the interference spectrum continually changing throughout the cutting process.

An additional issue with using a wireless connection is that the bandwidth of the wireless interface must be able to capture a large frequency range from the electret accelerometer. As previously mentioned, the end milling system produces a wide spectrum of useful information and it must be captured with substantial resolution for analysis purposes.

Upon investigation of existing commercial methods of wireless data transmission, it becomes evident that the majority of existing commercial methods have significant drawbacks relating to the challenges expressed above. For instance, an FM or AM interface is immediately eliminated by the expected high level of radio frequency noise. Other methods such as the 802.XX standards require a substantial power source and are not commercially offered in a form that is small enough to practically position within a

typical end milling tool holder.

Although most existing wireless protocols are not ideal, the Bluetooth protocol was found to answer the demands of tool holder placement, bandwidth, and motor interference. The Bluetooth wireless standard has been designed for implementation in devices such as wireless headsets, cellular telephones, and data transmission over Personal Area Networks. As a result, Bluetooth transmitters and receivers have been designed with physical size as a primary constraint, often being smaller than several centimeters in size. Since Bluetooth was developed for data transmission, the 2.0 version of the protocol reaches transmission rates of 2.1 Mbps, which is sufficient bandwidth to capture high resolution end milling data. Additionally, the upcoming version 3.0 is anticipated to reach transmission rates of 480Mbps. Manufacturers identify transmission range between 10 to 30 meters depending on interference, which is adequate for transmission out of the end mill (~2 meters).

The Bluetooth standard was developed using spread-spectrum techniques [NTIA Manual] considering that the devices would be used in environments with a high level of electromagnetic interference across a broad spectrum. The standard uses the license-free ISM band at 2.4-2.4835 GHz and is divided into 79 channels. These channels can be changed at up to 1600 times per second to actively avoid interference. As a result, the quality and continuity of transmission is high, even in noisy radio environments.

The wireless response testing performed in this work was conducted on a shaker table with an electromagnetic motor. The field generated by this motor swept the test spectrum and did not appear to cause interruption of the Bluetooth transmitter.

Similar to the testing work performed with the electret accelerometer, the Bluetooth accelerometer interface was also assessed by contrasting its frequency response with that of the piezoelectric accelerometer sampled through a traditional DAQ system. Figure A22 details the shaker table and attached sensors and corresponding device under test (DUT) block diagram.

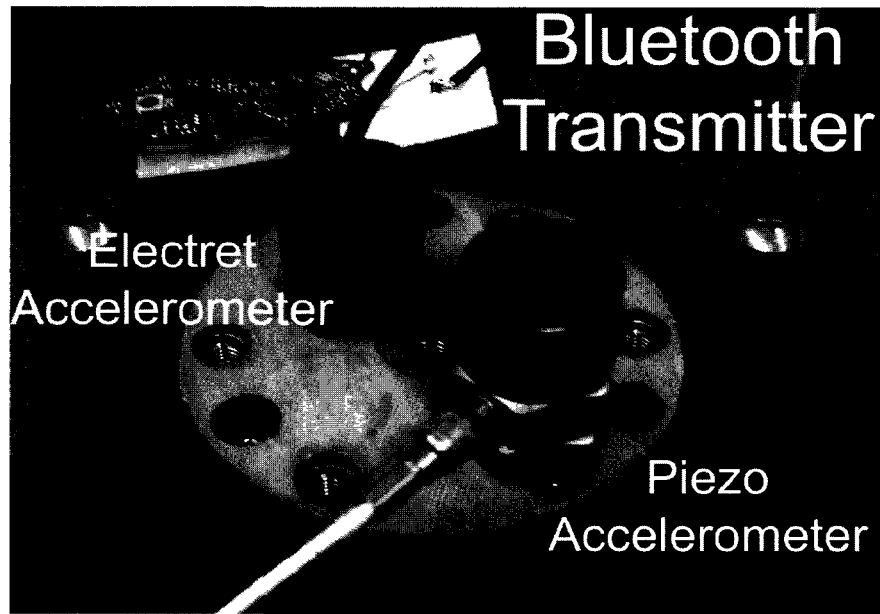


*Figure A22: Bluetooth Test Interface*

As with the wired electret accelerometer discussed above, a sinusoidal vibration input is generated using a shaker table. A single-axis PCB piezoelectric accelerometer (Model 320 C33, serial number 5901) is fixed to the table at the same reference point as the electret sensor. The output sensitivity of this piezoelectric accelerometer is 100mV/g with a maximum range of 50g's. This piezoelectric accelerometer is amplified through a PCB charge amplifier. The corresponding voltage signal is monitored through a traditional DAQ system. The electret sensor is sampled by the Bluetooth transmitter and sent as a 16 bit digital signal to the PC's Bluetooth wireless receiver. Both the piezoelectric

accelerometer and the Bluetooth electret accelerometer signals are sampled at 20 kHz.

Figure A23 shows the response curves for the electret accelerometer sampled via the Bluetooth interface and the baseline piezoelectric accelerometer.

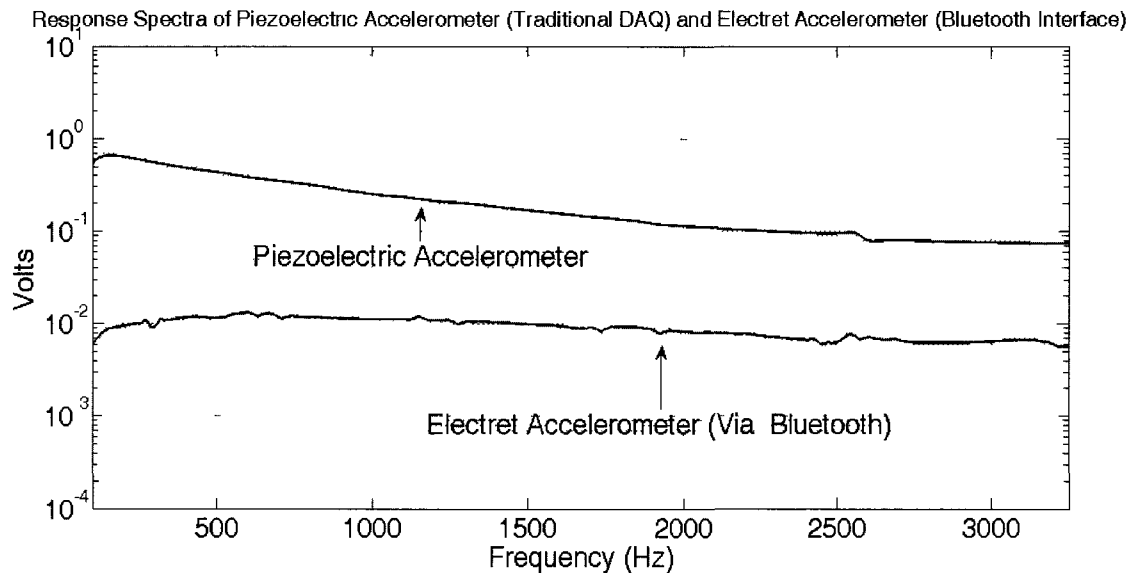


*Figure A23: Response Spectra for Piezoelectric and Wireless Electret Accelerometers*

As with the wired electret accelerometer, the response can be mapped to the desired (piezoelectric) frequency response through a gain ratio function. This procedure is described in detail in the section “Linear Response and Calibration of the Electret Accelerometer”. The Bluetooth wireless interface produced a stable response between 100 and 3500 Hz.

The results observed from the testing of the Bluetooth Wireless interface are promising and identify that the method is acceptable for transmitting high bandwidth acceleration data from the electret sensor. Due to the acceptable bandwidth, it is feasible to use the Bluetooth interface for application in a smart tool holder.

The electret accelerometer has demonstrated good robustness over a battery of tests including a population performance study. Based on the outcome of these tests, the electret accelerometer is a feasible alternative to a piezoelectric accelerometer for application in a Smart Tool Holder, under controlled temperatures. Performance is observed to be comparable to the piezoelectric device, through minimal signal processing.

The frequency response error throughout the population was estimated by propagating error observed in the individual sensors over the population. Although each individual sensor was tested for repeatability over 32 frequency response tests, the population exposed features of the response error spectrum that were not noticeable in the individual sensor repeatability tests. The outcome of the statistical population tests and error propagation is positive and identifies that the electret accelerometer has an acceptable expected error magnitude of  $\pm 6\%$  over a spectrum of 100 to 4000 Hz.

Furthermore, it is also shown that the Bluetooth wireless interface is capable of transmitting the acceleration signal from the electret accelerometer. The particular Bluetooth transmitter used with the electret accelerometers has a bandwidth comparable to the frequency response of the electret sensor, to approximately 4000Hz. The goal of identifying feasibility for this wireless method has been accomplished.

## APPENDIX B

### Tool Tip Temperature Measurement

A 12 bit thermocouple junction/sampler is used to capture temperature three times per second. The range of the temperature A/D is 0-1023.75 °C in steps of 0.25°C. The temperature sensor is embedded axially in the core of the 19.05 mm insert holder body. Therefore, it is necessary to determine how the sensor responds with respect to an applied temperature condition on the cutting edge of the tool. To do so, a temperature boundary condition is applied with a feedback controlled heating element. Figures B1 and B2 show torque and temperature integrated smart tools. The temperature sensor is embedded at the core of the tool holder.



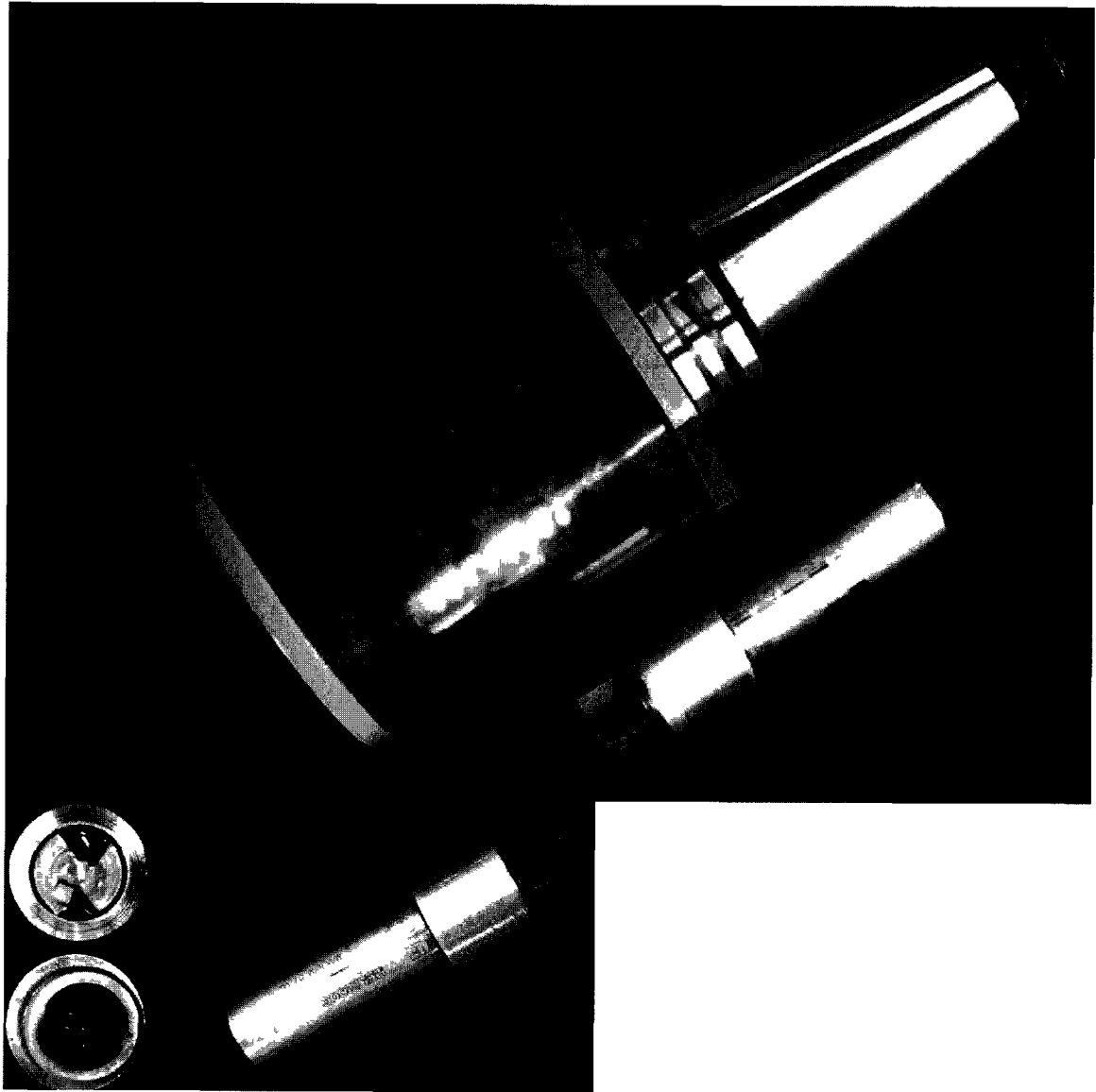


*Figure B1: Torque & Temperature Smart Tool*

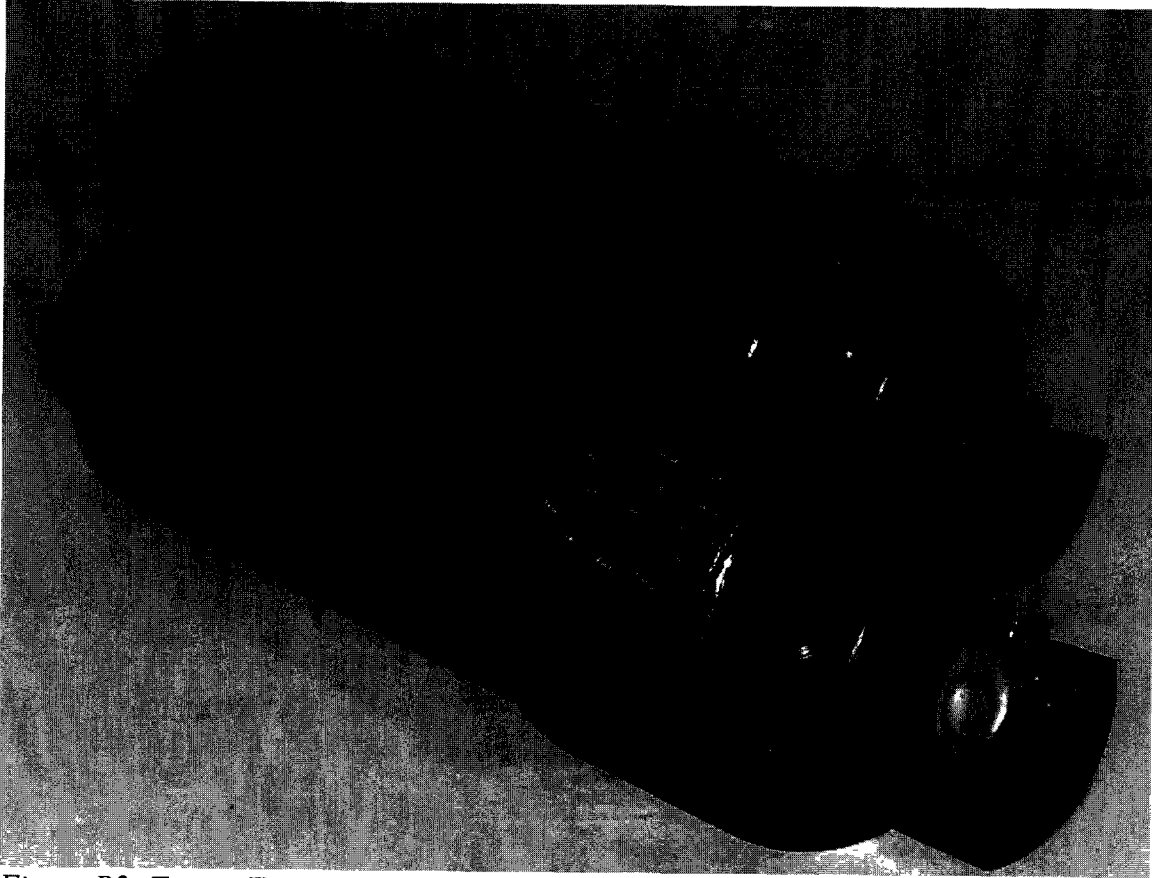


*Figure B2: Torque Temperature Integrated Tools*

The temperature condition is applied to simulate a 0.254 cm (0.1 inch) axial engagement. All of the tools tested are commercial carbide cutting tools. A second research goal of this experiment is to determine if the insert coating type has a significant effect on the time constant, phase, and gain of the temperature signal. Two different uncoated tools, TiCN, and TiAlN coatings were compared. It was hypothesized that the coating plays a minimal effect on the heat transfer observed by the embedded thermocouple. However, this hypothesis needed to be confirmed to ensure proper sensor calibration. The thermal conductivity of tungsten carbide is approximately 84 W/m/K whereas the conductivity of thin coatings such as TiN is less than 20 W/m/K [41]. Figure B3 shows a picture of the temperature control setup in the milling machine and a thermal

resistance network.

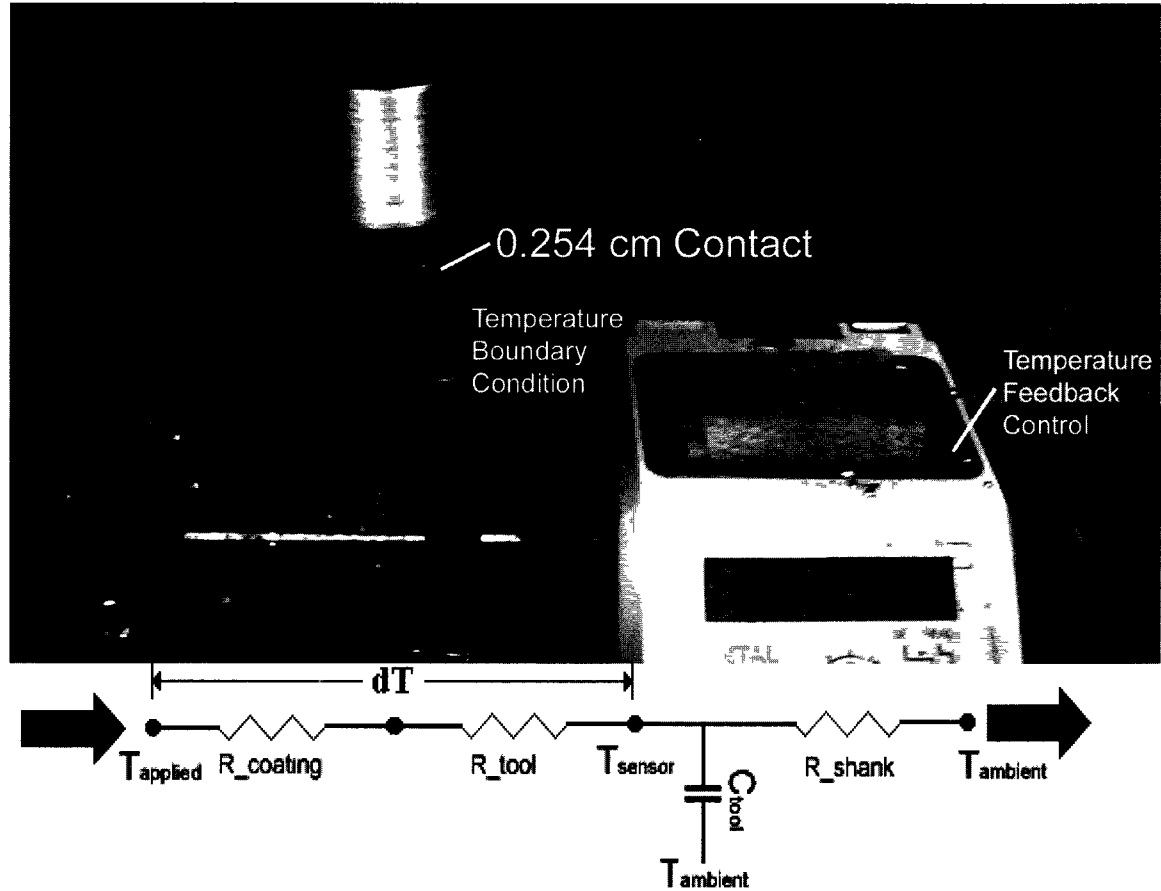


Figure B3: Experimental Temperature Setup

To test the performance of the temperature sensor and determine if insert coating has an effect on the sensor response, a Balanced Incomplete Block design was implemented. For each condition, the time constant and gain of the temperature signal was observed from the data. The coating materials inspected change their heat transfer coefficients as a function of temperature. For example, the thermal conductivity of TiN is 28.84 W/m/K at 25°C and changes to 16.72 W/m/K at 200°C [41]. Therefore, the block unit for this experiment is Temperature. The variation in the heat transfer due to the applied temperature is not of interest. The comparison made between the coating types is

separated from the effect of temperature. Table 17 details the experimental design.

Table B1: Block Design of Temperature Tests

Block Temperature °C	Treatments (Insert Coating)		
150	Uncoated 1	TiN	TiAlN
250	Uncoated 1	TiN	Uncoated 2
350	Uncoated 1	TiAlN	Uncoated 2
485	TiN	TiAlN	Uncoated 2

The observed temperature response shows an exponential approach to steady state. This agrees with the experimental setup of a RC thermal circuit. The data is fit with an exponential function to estimate the time constant. In addition to estimating the time constant, the gain between  $T_{applied}$  and  $T_{sensor}$  can be given as a ratio:

$$Gain = \frac{T_{sensor}}{T_{applied}} \quad (B1)$$

where  $T_{sensor}$  is the steady state thermocouple temperature and  $T_{applied}$  is the heating temperature. Figure B4 shows an example temperature response, estimated time constant, and gain.

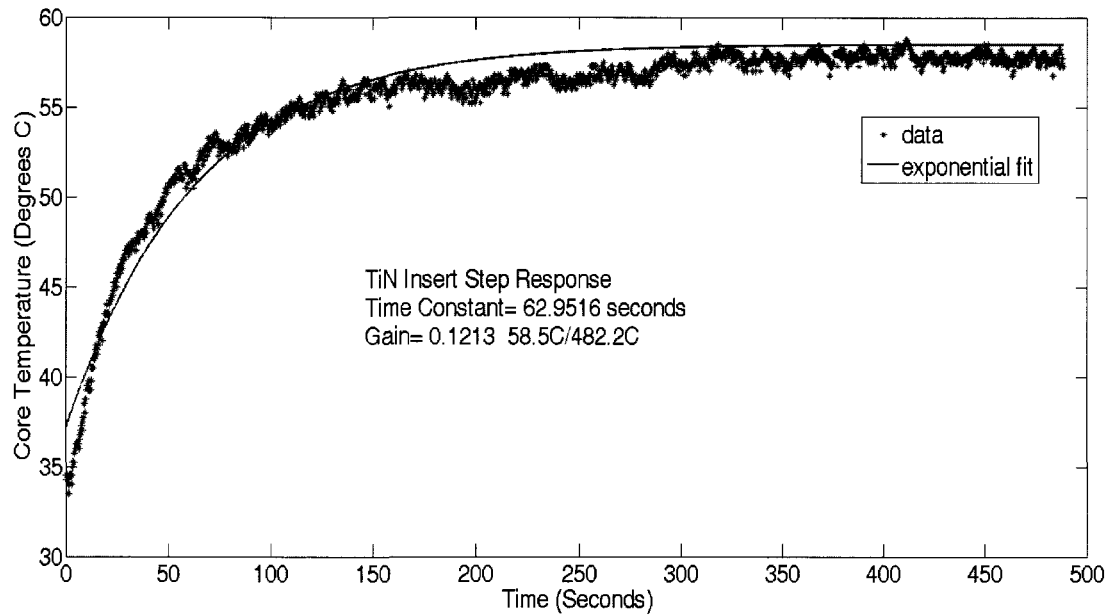


*Figure B4: Temperature Sensor Step Response*

To observe if the coating value has an effect on the time constant or gain, the time constants and gain values were collected for all of the cases in Table B1. These values were analyzed in the JMP statistical software package to determine if an effect existed as a function of temperature. A standard least squares model was used to estimate time constant as a function of coating. The temperature variable was modeled as a random effect nested with coating type. Figure B5 shows the least squares means for coating types with standard error.

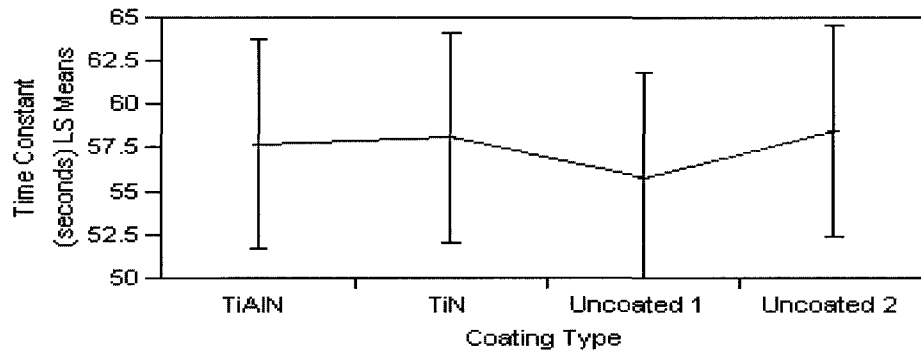


Figure B5: Temperature Sensor Time Constant LS Means

The overlapping standard errors shows that time constants have insignificant differences. Because the coatings are thin films and thermal resistance is a function of thickness, it is not surprising that the coating has a negligible effect on the time constant.

Unlike time constant, the gain value is influenced by the tool type. Figure B6 shows a least squares mean plot of gain values with corresponding standard error.

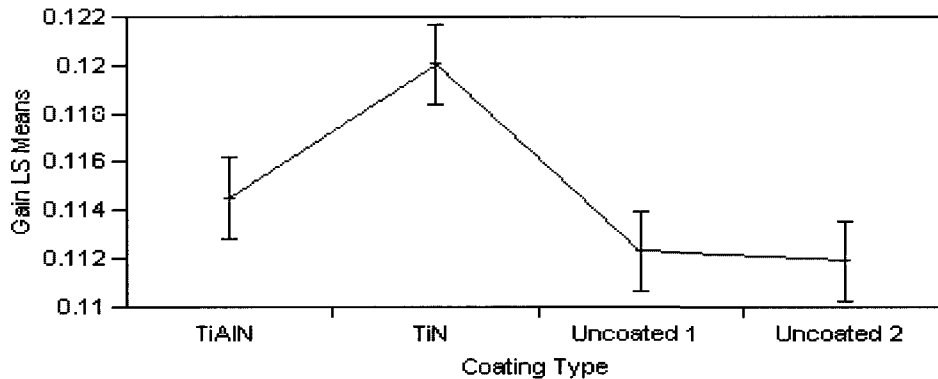


Figure B6 Temperature Sensor Gain LS Means

The TiN coated tool appears to have a slightly higher gain value compared to the other tools tested. Since the standard errors do not overlap, this difference is significant. This is insightful, since the gain value relates the the thermal resistance of the coating plus the tool substrate. If the gain increases, the thermal resistance (  $R_{coating} + R_{tool}$  ) between  $T_{applied}$  and  $T_{sensor}$  decreases. However, there is no observed effect in the

time constant for the TiN coated tool. Thus, for the time constant,  $\tau = (R_{coating} + R_{tool}) \times C$ , to remain the same, the value of  $C$  must increase.

This effect can be attributed to unknown substrate properties between the tool types tested. The experiment assumes that the carbide substrate is identical between tool types. It is likely that the substrate carbide for the different tools contains slightly different percentages of a binder material such as cobalt.

From the experiments, the accuracy of the temperature sensor is related to the error of the gain. From equation B1, the gain value is 0.115 with a standard deviation of  $0.0036^{\circ}\text{C}$ . Therefore, the resolution of the temperature sensor is  $\pm 3.64^{\circ}\text{C}$  at full scale of  $1023.75^{\circ}\text{C}$ . The time resolution can also be quantified from the experimental time constants and is  $57.496 \pm 4.040$  seconds. Changes of temperature less than  $0.0028^{\circ}\text{C}$  (changes in average temperature) can be resolved. For this sensor integrated tool, the expression for estimating mean temperature at the tool-workpiece interface is:

$$\bar{T}_{interface} \approx \frac{T_{core}}{0.115} \quad (\text{B2})$$

This expression is the fixed temperature sensor calibration for this tool geometry and sensor location. The temperature calibration experiment confirms that different tool coatings do not require recalibration of an embedded thermocouple sensor. This is useful in practice where different inserts may be deployed without modifying the sensor system. Furthermore, the time resolution of the sensor demonstrates that the tool-core location of the thermocouple is appropriate for estimating the mean temperature of the tool-workpiece interface.

Based on the calibration experiments for the embedded thermocouple, the

temperature sensor is limited to near steady state changes in cutting temperature. A cut is conducted at 2500 RPM in tool steel with 3.175 mm axial depth, 9.525 mm radial engagement (half immersion of a 19.05 mm tool), and a feed per tooth of 0.122 mm/tooth. This test is designed to last 120 seconds~ 2 time constants. Figure B7 shows the tool core temperature calibrated according to Equation B7. At one time constant, the sensor temperature is 63.2% of the steady state value. Therefore the cutting interface is estimated at 989°C during this experiment. The result is encouraging since it agrees with feasible tool-workpiece interface temperatures [42].

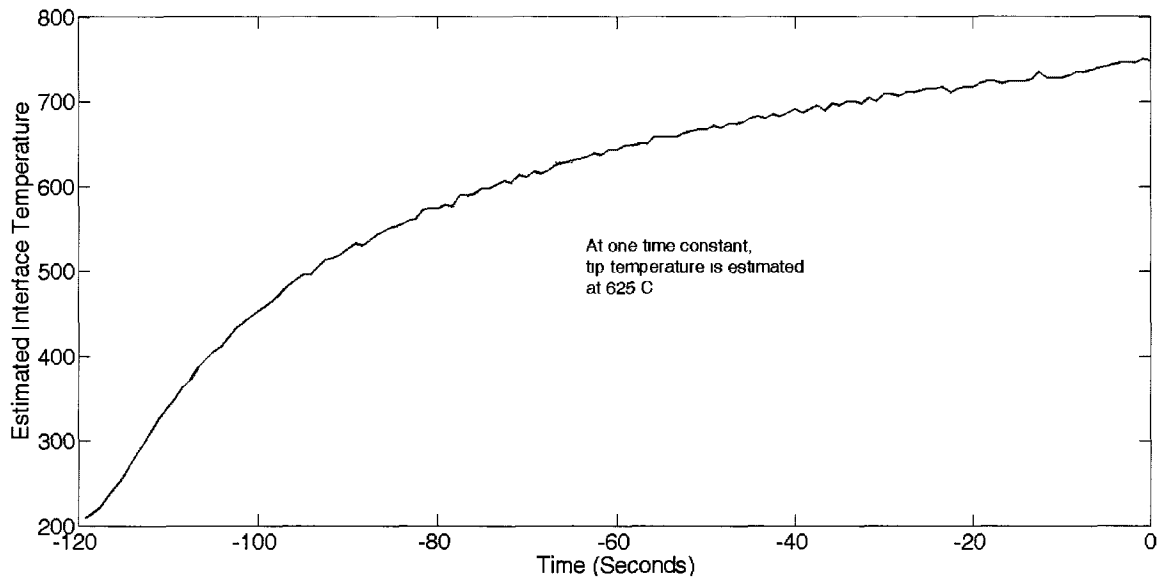


*Figure B7: Tool Tip Cutting Temperature Test*

On a number of smart tool versions, torque was measured simultaneously to temperature. This allowed interesting relationships to be observed between the sensors, specifically with time response and phase lag in the physical system.



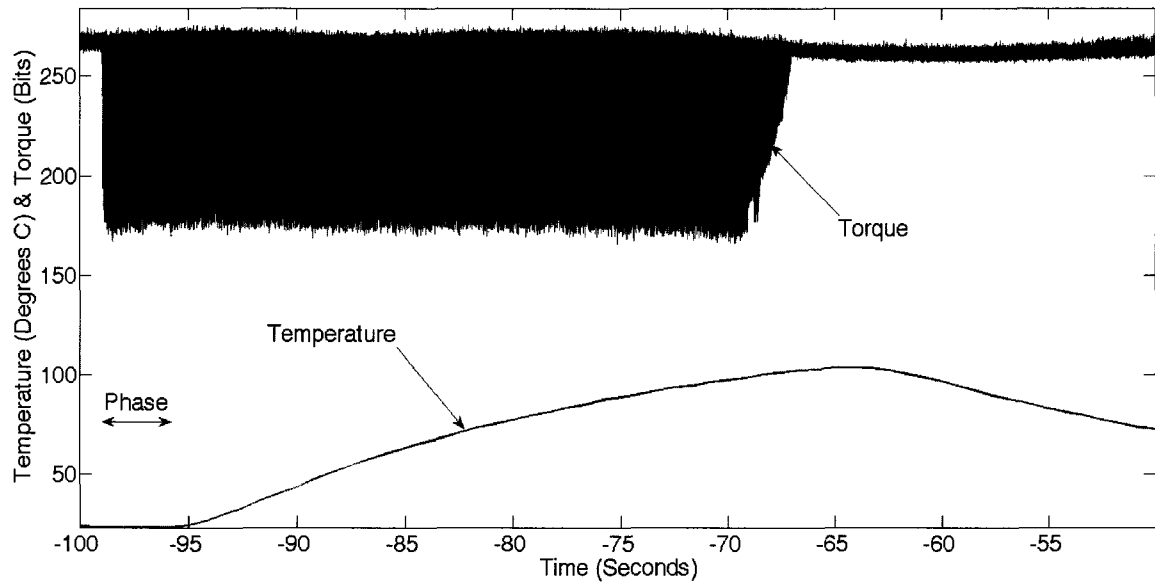


*Figure B8: Torque and Temperature Simultaneously Sampled*

Simultaneous sampling of both torque and temperature exposes the phase delay of the temperature sensor. This is expected since heat must transfer through the thermal mass of the tool body (Figure B8). To quantify this value, a cutting test is conducted and the high bandwidth torque signal is used as a reference. This is evident in the plot of a cutting test, showing temperature time-aligned with the torque signal.

Tool tip temperature measurement was shown successful in estimating the temperature at the tool-workpiece interface temperature. Although not directly related to dynamics, this information is helpful in evaluating the temperature conditions experienced by the dynamic sensors (i.e. electret accelerometer). The information is also useful for tool wear monitoring.

## APPENDIX C

### 2DOF Time Domain Model

**function [dRPM,x,y,Fx,Fy,t,sdt,hlhistorical]=millchatt(b,N1,N2,M,sweep,yesrand)**

```

mx=3.3787; kx=4728424; my=4.5049; ky=6304566; %physical constants
%rx=3.3787; kx=5.6355e+007; ry=4.5049; ky=7.5140e+007; %physical constants
Ks=400; %Ks=1500; 400 for aluminum 6061, 1500 for gray cast iron n/mm^2
cx=500; cy=450;
c=0.0254; %material removal rate mm/tooth (feed per tooth)
%example: [dRPM,x,y,Fx,Fy,t,sat,hlhistorical]=millchatt(2,500,7500,2000000,'up',0);
dx=0; dy=0; i=0;
dfi=pi/160; %timesteps per toothpass
%dt=60/(320*N);

if (N1==N2)
    dRPM=ones([1 M+1])*N1;
else
    dRPM=[N1:(N2-N1)/M:N2];
end

if length(sweep)==4
    dRPM=fliplr(dRPM); % run the sweep backwards
else
    %sweep is up
end

if yesrand==1
    rnddamping=rand([1,M])*10; %small random perturbations to z...
    rnddamping=rnddamping-mean(rnddamping); %mean subtract
    rndstiff=rand([1,M])*1e6; %small random perturbations to z...
    rndstiff=rndstiff-mean(rndstiff); %mean subtract
else
    rnddamping=zeros([1,M]);
    rndstiff=zeros([1,M]); %mean subtract
    %rnanur=zeros(1,M); %No random perturbations to z...
end

t=zeros([1 M]);
Fx=zeros([1 M]);
Fy=zeros([1 M]);
x=zeros([1 M+1]);
y=zeros([1 M+1]);
zold1=zeros([1 M]);
hlhistorical=zeros([1 M]);
sdt=t;
for n=1:M
    dt=60/(320*dRPM(n));
    t(n)=(n-1)*dt;
    fil=i*dfi;
    i=i+1;
    sdt(n)=dt;
    %after 160 steps the positions of the teeth repeat
    if (i>160)
        i=0;
    end
end

```

```

end
%radial displacement z on every tooth is obtained as the sum
%of the projections of the displacements in x and y on the tooth radius
%the factor 1000 is used to obtain z in mm while x and y are in m
z1=1000*(x(n)*sin(fil)+y(n)*cos(fil));

if(n<=160)
    %formulating chip thickness
    h1=c*sin(fil)-z1; zold1(n)=z1;
else
    h1=c*sin(fil)-(z1-zold1(n-160));
end
h1historical(n)=h1;
%see if the tooth is still in the workpiece
if(h1>0)
    F1=Ks*b*h1;
    zold1(n)=z1;
else
    F1=0;
    zold1(n)=z1+h1;
end

%Fx and Fy components
Fx(n)=F1*(cos(fil)+0.3*sin(fil));
Fy(n)=F1*(sin(fil)-0.3*cos(fil));

%the accelerations in ddx and ddy are produced by forces Fx and Fy and
%displacements x and y are obtained by double integration
ddx=(Fx(n)-(cx+rnddamping(n))*dx-(kx+rndstiff(n))*x(n))/mx;
dx=dx+ddx*dt;
x(n+1)=x(n)+dx*dt;
ddy=(Fy(n)-(cy+rnddamping(n))*dy-(ky+rndstiff(n))*y(n))/my;
dy=dy+ddy*dt;
y(n+1)=y(n)+dy*dt;

%
subplot(3,1,1)
%
plot(t,x(2:end))
%
subplot(3,1,2)
%
plot(t,y(2:end))
%
subplot(3,1,3)
%
plot(t,F_hyp)
%
pause(0.0001)
%
if(max(x)>2)
%
break
%
end
end

%there have been M-1 values of x and y generated and only M for t, Fx, Fy;
% Fx(M+1)=Fx(M);
% Fy(M+1)=Fy(M);
% t(M+1)=M*dt;
%x=x(1:end);
%y=y(1:end);
%subplot(2,1,1)
%plot(aRPM,x) %plot the displacement in x
%subplot(2,1,2)
%plot(aRPM,(x.^2+y.^2).^0.5) %plot resolved displacement

```

## APPENDIX D

### 4DOF TIME DOMAIN MODEL

```
function [x1,x2,y1,y2,dex,dely,Fs,dRPM]=mill_cant_RK_EU(b,N1,N2,M,sweep)

%stiffness, mass, damping matrices
mx1=3.3787; kx1=4728424;
mx2=0.1; kx2=7e6;
my1=4.5049; ky1=6304566;
my2=0.1; ky2=7e6;
cx1=450; cy1=450;
cx2=450; cy2=450;

%rx=3.3787; %x=5.6355e-007; %y=4.5049; %y=7.5140e-007; %physical constants
Ks=400; %Ks=1500; 400 for aluminum 6061, 1500 for gray cast iron n/mm^2

c=0.0254; %material removal rate rr/tooth (feed per tooth)
%example: [x1,x2,y1,y2,dex,dely,Fs,dRPM]=millcatt_cantilever(2,2501,2501,2000000,'up');
%initial condit_ons
dx1=0; dx2=0; dy1=0; dy2=0; i=0;

dfi=pi/(2*160); %timesteps per toothpass %%%ANGLE HALVED FROM ORIGINAL
%dt=60/(320*N);

if (N1==N2)
    dRPM=ones([1 M+1])*N1;
else
    dRPM=[N1:(N2-N1)/M:N2];
end

if length(sweep)==4
    dRPM=fliplr(dRPM); % run the sweep backwards
else
    %sweep is up
end

t=zeros([1 M]);
Fx=zeros([1 M]);
Fy=zeros([1 M]);
ddx1=zeros([1 M]);
dx1=zeros([1 M]);
ddx2=zeros([1 M]);
dx2=zeros([1 M]);
ddy1=zeros([1 M]);
dy1=zeros([1 M]);
ddy2=zeros([1 M]);
dy2=zeros([1 M]);
x1=zeros([1 M+1]);
x2=zeros([1 M+1]);
y1=zeros([1 M+1]);
```

```

y2=zeros([1 M+1]);
delx=zeros([1 M+1]);
dely=zeros([1 M+1]);
zold1=zeros([1 M]);
hlhistorical=zeros([1 M]);
sdt=t;
for n=1:M
    dt=60/(2*320*dRPM(n));    %?%? at HALVED FROM ORIGINAL
    t(n+1)=t(n)+dt;           % storing time steps. t(1)=0 is the starting time
    fil=i*dfi;
    i=i+1;
    sdt(n)=dt;
    %after 160 steps the positions of the teeth repeat
    if(i>160)
        i=0;
    end
    %radial displacemnt z on every tooth is obtained as the sum
    %of the projections of the displacements in x and y on the tooth radius
    %the factor 1000 is used to obtain z in mm while x and y are in m
    z1=1000*(delx(n)*sin(fil)+dely(n)*cos(fil));

    if(n<=160)
        %formulating chip thickness
        hl=c*sin(fil)-z1; zold1(n)=z1;
    else
        hl=c*sin(fil)-(z1-zold1(n-160));
    end
    hlhistorical(n)=hl;
    %see if the tooth is still in the workpiece
    if(hl>0)
        F1=Ks*b*hl;
        zold1(n)=z1;
    else
        F1=0;
        zold1(n)=z1+hl;
    end

    %Fx and Fy components
    Fx(n)=F1*(cos(fil)+0.3*sin(fil));
    Fy(n)=F1*(sin(fil)-0.3*cos(fil));

    %the accelerations in ddx and ddy are produced by forces Fx and Fy and
    %displacemnts x and y are obtained by double integration
    ddx1(n+1)=(-Fx(n)-cx1*dx1(n)-kx1*x1(n))/mx1;

    if mod(n,2)==1
        dx1(n+1)=dx1(n)+ddx1(n)*dt;
        x1(n+1)=x1(n)+dx1(n)*dt;
    else
        dx1(n+1)=dx1(n-1) + dt*(ddx1(n-1)+4*ddx1(n)+ddx1(n+1))/3;    %%%%Runge Kutta
        method here
        x1(n+1)=x1(n-1) + dt*(dx1(n-1)+4*dx1(n)+dx1(n+1))/3;          %%%%using current
        or as half the interval from t(n-1) to t(n+1)                  %%%%if nonuniform
        time steps, this may intro. slight error
    end

    ddx2(n+1)=(Fx(n)-cx2*dx2(n)-kx2*x2(n))/mx2;

    if mod(n,2)==1
        dx2(n+1)=dx2(n)+ddx2(n)*dt;
        x2(n+1)=x2(n)+dx2(n)*dt;

```

```

else
    dx2(n+1)=dx2(n-1) + dt*(ddx2(n-1)+4*ddx2(n)+ddx2(n+1))/3; %Runge Kutta
method here
    x2(n+1)=x2(n-1) + dt*(dx2(n-1)+4*dx2(n)+dx2(n+1))/3; %using current
dt as half the interval from t(n-1) to t(n+1) %if nonuniform
time steps, this may intro. slight error
end

delx(n+1)=x2(n+1)-x1(n+1);
%now y's turn
ddy1(n+1)=(-Fy(n)-cy1*dy1(n)-ky1*y1(n))/my1;

if mod(n,2)==1
    dy1(n+1)=dy1(n)+ddy1(n)*dt;
    y1(n+1)=y1(n)+dy1(n)*dt;
else
    dy1(n+1)=dy1(n-1) + dt*(ddy1(n-1)+4*ddy1(n)+ddy1(n+1))/3; %Runge Kutta
method here
    y1(n+1)=y1(n-1) + dt*(dy1(n-1)+4*dy1(n)+dy1(n+1))/3; %using current
dt as half the interval from t(n-1) to t(n+1) %if nonuniform
time steps, this may intro. slight error
end

ddy2(n+1)=(Fy(n)-cy2*dy2(n)-ky2*y2(n))/my2;

if mod(n,2)==1
    dy2(n+1)=dy2(n)+ddy2(n)*dt;
    y2(n+1)=y2(n)+dy2(n)*dt;
else
    dy2(n+1)=dy2(n-1) + dt*(ddy2(n-1)+4*ddy2(n)+ddy2(n+1))/3; %Runge Kutta
method here
    y2(n+1)=y2(n-1) + dt*(dy2(n-1)+4*dy2(n)+dy2(n+1))/3; %using current
dt as half the interval from t(n-1) to t(n+1) %if nonuniform
time steps, this may intro. slight error
end

dely(n+1)=y2(n+1)-y1(n+1);

end

Fs=0.5*1./(diff(t)); %Runge Kutta required half-time steps, this is generating the
sampling frequency

```

## APPENDIX E

### INTEGRATION TECHNIQUE

This function demonstrates the integration technique used on the 4<sup>th</sup> order time domain model. The integration starts through time with Euler (rectangular) integration until several time steps have elapsed, and sufficient points are available to begin integration based on Runge Kutta techniques. It is proven that this technique is highly accurate compared to a rectangular-only technique and this can be demonstrated by using input functions such as sine and cosine.

```
function x1=test_hybrid(ddx1,dt,initial_vel,initial_pos)

M=max(size(ddx1));
dx1=zeros([1 M]);
x1=zeros([1 M]);
dx1(1)=initial_vel;
x1(1)=initial_pos;
for n=1:M-1
    if mod(n,2)==1
        dx1(n+1)=dx1(n)+ddx1(n)*dt;
        x1(n+1)=x1(n)+dx1(n)*dt;
    else
        dx1(n+1)=dx1(n-1) + dt*(ddx1(n-1)+4*ddx1(n)+ddx1(n+1))/3; %Runge Kutta
        x1(n+1)=x1(n-1) + dt*(dx1(n-1)+4*dx1(n)+dx1(n+1))/3; %using current
        % as half the interval from t(n-1) to t(n+1) % if nonuniform
        time steps, this may intro. slight error
    end
end
end
```

## APPENDIX F

## FORMANT FREQUENCY TRACKING FUNCTION

```
function [formant, numerator, denominator] = formant_tracker(input, Fs, step, window_size, p, threshold)
% ex. [formant, numerator, denominator] = formant_tracker(' (vcd), (l i-1)), l=4, 'CDL', l=4, l=6, l=1);
% Formant Tracker Base on LPC Analysis
% Input [formants] Output [numerator(denominator), step, window_size, p, threshold]
while
    if input speech validort;
    dimension=input size, if number of samples;
    step=step size, if interval of samples;
    window_size=frame window size, if number of samples;
    p=number of LP coefficients;
    threshold: the threshold value for pole magnitude P less than or higher magnitude are candidate for formant extraction
end while;

%window = avfilter('FIRFs')

num=1;
dimension=length(input);
dimension=dimension-window_size;

for i=1:step:dimension-window_size
    if i<window_size/2+1
        frame=input(abs(i+window_size));
    else
        frame=input(round((num*step-window_size)/2:num*step+window_size/2));
    end

    for k=1:p+1
        autocorrelation(k)=0;
        for l=1>window_size-k
            autocorrelation(k)=autocorrelation(k)+frame(l)*frame(l+k-1);
        end
        autocorrelation(k)=autocorrelation(k)/window_size;
    end

    t=window_size/2;
    for k=2:(t+1)
        %if(t) ,
        for l=1>window_size-k
            f(k)=autocorrelation(k)+f(k-1)*exp(-alpha*(l-k));
        end
        %f(k)=autocorrelation(k)/window_size;
    end

    %1,1,1,-max(autocorrelation(t),
    % -p*10^(-1),

    alpha=zeros(p,p);
    a=zeros(p,1);
    E=zeros(p,1);
    E(1)=autocorrelation(1);
    for i=1:p
        sum=0;
        for j=1:i-1
            if i>j
                sum=sum+alpha(j,i-1)*autocorrelation(abs(i-j)+1);
            end
        end

        k(i)=(autocorrelation(i+1)-sum)/E(i);
        alpha(i,1)=k(i);
        if i>1
            for j=1:i-1
                alpha(j,i)=alpha(j,i-1)-k(i)*alpha(i-j,i-1);
            end
        end
        E(i+1)=(1-k(i)^2)*E(i);
    end
end
```



```

        var=E(i+1);
    end
    for j=1:p
        a(j)=alpha(j,p);
    end
    f=[1 -a'];
    gain=0;
    p;
    for i =1:p+1
        gain=gain+f(i)*autocorrelation(i);
    end
    gain;
    gain=gain^0.5;

root1=roots([1,-a']);

mag_root=abs(root1);
arg_root=angle(root1);
k=1;
for j=1:p
    if mag_root(j)>threshold
        if arg_root(j)>0 &&arg_root(j)<pi
            formant(num,k)=arg_root(j)/pi*(Fs/2);

            num;
            k;
            k=k+1;
        end
    end
end

% =====
f = 1000*(1 - (a') ), 'Fs', Fs, for is alias' rotated ffr
numerator=1;
denominator=[1 -(a')];
freqz(1,1-(a'),1, Fs)
subplot(2,1,1)
% pformant= sort(z roots'),
plot(pformant(1,:),),
hold
% pformant= sort(z roots'),
% root(pformant(3,:));
plot(pformant(3,:),),
% subplot(2,1,1)
plot((-length(frate)-Fs+1:Fs -Fs/2),frate)
% plot((-length(frate)-Fs+1:Fs -Fs/2),frate)
% F = detfrate('r(0, 'Juxx-rf'au(re)'),
%       = addtime(1,200),F),
% close

num=num+1;
end
s=size(formant);
for i=1:length(formant)
    for j=1:s(2)
        if formant(i,j)==0
            formant(i,j)=NaN;
        end
    end
end
end

formant=sort(formant');
time=[0:length(formant)-1]*step*1/Fs +2;
Wn=[2]/(Fs/step);
[b,a]=butter(2,Wn,'low');

% plot(time, filter(b,a,formant(1,:)));
% hold all
% plot(time,filter(b,a,formant(2,:)));
% plot(time,filter(b,a,formant(3,:)));
% plot(time,filter(b,a,formant(4,:)));
% plot(formant(4,:));
% % time limit

figure
plot(formant,'b'),
% format -g t(formant),
% -----
% plot(time, formant(1,:), 'b'),
% hold all;
% plot(time, formant(2,:), 'b');

```

```

% plot(tire, fpart(3,:),'.');
% plot(tire, fpart(4,:),'.');
% -----
% plot(fpart(5,:),
%
%     nr = 0.5;
%     figure
%     plot(20:100,fpart(1,:),[1 64], 'slidc ',30:30);
%
%     avobj = close(avobj);
%     return;
end

```

## APPENDIX G

### FUNCTION TO CALL FORMANT FREQUENCY TRACKING AND PASS FORMANT FREQUENCIES TO STABILITY LOBE FUNCTION

```
function [kx_hist]= formant2FRF(data, Fs)

[formant, numerator, denominator]=formant_tracker(data,Fs,1024,1024,10,0.01);
plot(formant(1,:),'.');
hold all
plot(formant(2,:),'.');
plot(formant(3,:),'.');
plot(formant(4,:),'.');
pause(1)
x=round(ginput(2));
formant=formant(:,x(1):x(2));
close
figure
hold
for (ndx=1:length(formant))
[kx ky]=lobe_generator(formant(1,ndx), formant(1,ndx), 0.4135, 0.413, 0.04, 0.04);
    %wnx = formant(1,ndx)*2*pi;           , rad/s
    % kx = wnx^2 * 0.4135;                % N/m
    %kx_hist(ndx)=kx;

    pause(0.001)
end
figure
plot(kx_hist)
```

## APPENDIX H

### STABILITY LOBE FUNCTION, BASED ON [48]

```
function [kx, ky] = lobe_generator(wnx, wny, mx, my, zetax, zetay)

% clear all
% close all
% cld

% Define parameters for x direction

wnx = wnx*2*pi;           % rad/s
kx = wnx^2 * mx           % N/m
% zetax = 0.02;

% Define parameters for y direction

wny = wny*2*pi;           % rad/s
% zetay = 0.02;
ky = wny^2 * my;         % N/m
% Define specific force and force angle
Ks = 750;                 % N/mm^2
beta = 68;                % deg

% Define FRFs for two directions
w = (0:0.5:2000*2*pi); % frequency, rad/s
rx = w/wnx;
FRF_real_x = 1/kx*(1-rx.^2)./((1-rx.^2).^2 + (2*zetax*rx).^2);
FRF_imag_x = 1/kx*(-2*zetax*rx)./((1-rx.^2).^2 + (2*zetax*rx).^2);
ry = w/wny;
FRF_real_y = 1/ky*(1-ry.^2)./((1-ry.^2).^2 + (2*zetay*ry).^2);
FRF_imag_y = 1/ky*(-2*zetay*ry)./((1-ry.^2).^2 + (2*zetay*ry).^2);

% Convert to mm/N
FRF_real_x = FRF_real_x*1e3;
FRF_imag_x = FRF_imag_x*1e3;
FRF_real_y = FRF_real_y*1e3;
FRF_imag_y = FRF_imag_y*1e3;

% Directional orientation factors for slotting
mux = cos(beta*pi/180);
muy = 0;

% Oriented FRF
FRF_real_orient = mux*FRF_real_x + muy*FRF_real_y;
FRF_imag_orient = mux*FRF_imag_x + muy*FRF_imag_y;

% figure(1)
% subplot(211)
% plot(w/2/pi, FRF_real_orient)
% axis([0 1000 -7e-4 7e-4])
% set(gca, 'FontSize', 14)
```

```

% ylabel('Real (mm/N)')
% subplot(212)
% plot(w/2/pi, FRF_imag_orient)
% axis([0 1000 -1.3e-3 1.3e-4])
% set(gca,'FontSize', 14)
% xlabel('f (Hz)')
% ylabel('Imag (mm/N)')

% Determine valid chatter frequency range
index = find(FRF_real_orient < 0);
FRF_real_orient = FRF_real_orient(index);
FRF_imag_orient = FRF_imag_orient(index);
w = w(index);

% Define average number of teeth in cut, Nt_star
Nt = 4;
phis = 0; % deg
phie = 180;
Nt_star = (phie - phis)*Nt/360;

% Calculate blim
blim = -1./(2*Ks*FRF_real_orient*Nt_star); % mm

% Calculate epsilon
for cnt = 1:length(FRF_imag_orient)
    if FRF_imag_orient(cnt) < 0
        epsilon(cnt) = 2*pi - 2*atan(abs(FRF_real_orient(cnt)/FRF_imag_orient(cnt)));
    else
        epsilon(cnt) = pi - 2*atan(abs(FRF_imag_orient(cnt)/FRF_real_orient(cnt)));
    end
end

% Calculate spindle speeds for N = 0 to 3
omega0 = w/(Nt*2*pi)./(0 + epsilon/2/pi); % rps
omega1 = w/(Nt*2*pi)./(1 + epsilon/2/pi);
omega2 = w/(Nt*2*pi)./(2 + epsilon/2/pi);
omega3 = w/(Nt*2*pi)./(3 + epsilon/2/pi);

% figure(2)
% subplot(211)
% plot(w/2/pi, FRF_real_orient)
% axis([0 1000 -7e-4 1e-4])
% set(gca,'FontSize', 14)
% xlabel('f (Hz)')
% ylabel('Real (mm/N)')
% subplot(212)
% plot(omega0, blim)
% axis([0 250 0 6])
% set(gca,'FontSize', 14)
% xlabel('\Omega (rps)')
% ylabel('b {lim} (mm)')

%figure
plot(omega0*60, blim, 'b-', omega1*60, blim, 'b-', omega2*60, blim, 'b-', omega3*60,
blim, 'b-')
axis([0 15000 0 6])
set(gca,'FontSize', 14)
xlabel('RPM')
ylabel('b {lim} (mm)')

%~logical(round(omega3-omega2);

```

## APPENDIX I

### Analytical Vibration Models to Explain Variation in Chatter Frequency During Tool-Workpiece Cutting Engagement

#### **Introduction**

This section has been included to prompt future work in exploring the tool-workpiece boundary conditions associated with different cutting conditions for the purpose of postulating about the cause of in-cut drift of the chatter frequency. Interest in the boundary conditions of the cutting system are also relevant to entrance effects, not discussed in this dissertation. Further, it is a suggestion that future work explores the inclusion of various boundary conditions into the modeling effort, specifically, in formulating the equations of motion for the time domain model. The differences in boundary condition are shown to be a factor in the following derivations and can significantly affect the natural frequencies (hence chatter frequency predictions) of the system. This is a physical argument for why tap tests are insufficient to correctly estimate the natural frequencies since the boundary conditions during cutting are influenced by engagement with the workpiece material.

The approach used in the time domain models is fixed-free assumption for the cutting tool with a complex forcing function between the workpiece and tool. While it is agreed that this approach captures behavior of the tool-workpiece interaction, it may be overlooking additional factors restricting the motion of the tool while it is engaged in the workpiece material. Although cutting force imposes a restriction on movement, the tool is in contact with the workpiece radially on both major and minor cutting faces, and the

rake face of the tool in contact with developing chips. It is the author's belief that this is a significant factor, particularly with the development of flank wear, which increases the non-cutting sliding material interface between the tool and workpiece material. It is possible that Columb damping effects become more pronounced as the interface friction increases.

### **Modeling the Tool Support Configurations at the Tool-Workpiece Interface**

Transverse vibration in a beam is a classic topic for analytical vibration analysis and can be adopted to model the vibration of a cutting tool system. The typical approach assumes that the shear deformation in the beam is much smaller than the deflection so that the angular displacement of a differential element along the axis of the beam can be neglected and a small angle assumption is valid. In the elastic region at small deflections, this approach is acceptable and yields accurate results. A model of bending vibration can be derived for a cutting tool given the boundary conditions the cutting tool is subject to while it is engaged within workpiece material.

The first step is to set up boundary conditions based on the tool fixation at both ends. A cutting tool is typically modeled as a Fixed-Free configuration so that the bending moment and shear force at the free end of the beam are zero. Based on the results of experimental and modeling evidence, the Fixed-Free boundary conditions may not accurately model the condition during cutting. The literature cites that a Fixed-Free supported cantilever has a first natural frequency of:

$$\omega = \frac{3.5156}{l^2} \sqrt{\frac{EI}{\rho}} \quad (I.1)$$

where  $\rho$  is the tool mass density (mass/length),  $E$  is the modulus of elasticity,  $I$  is the moment of inertia, and  $l$  is the overhang length. Given this equation, the point mass, denoted  $\hat{m}$ , of the tool can be estimated:

$$\hat{m} = \frac{k}{(2\pi f_n)^2}, \quad \hat{m} = \frac{3EI}{L^3 \left( \frac{3.5156}{L^2} \sqrt{\frac{EI}{\rho}} \right)^2}, \quad \hat{m} = 0.243 L \rho \quad (I.2)$$

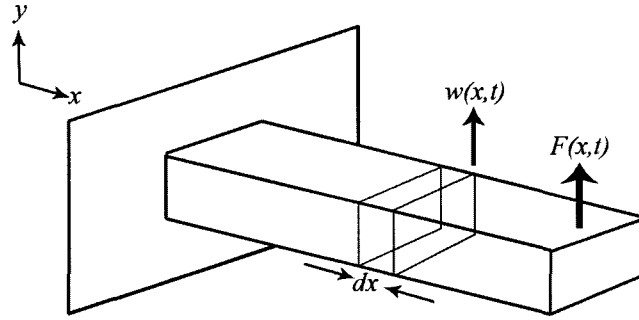


Figure II: Cantilever Coordinates

### **Modeling the Workpiece-Engagement as a Pinned Boundary Condition**

A Fixed-Pinned condition is explored to more accurately explain the engaged cutting tool system. The boundary conditions of the fixed end, where  $w$  is deflection and  $x$  is the position longitudinally along the tool are given as:

$$w=0 \quad \text{and} \quad \frac{\delta w}{\delta x}=0 \quad (I.3)$$

At the workpiece-engaged (cutting) end of the tool holder, the boundary conditions are not as obvious. The cutting supports the tool holder similar to a pin and there is no



impedance to bending at the tool-workpiece interface. Also like a pinned joint, the cutting interface imposes a deflection restriction. Note: the author is proposing that a restriction to deflection may exist that is independent of the restriction imposed by cutting forces alone. Therefore, the boundary conditions for the cutting interface are:

$$w=0 \quad \text{and} \quad EI \frac{\delta^2 w}{\delta x^2} = 0 \quad (I.4)$$

Where E and I are the material modulus and moment of inertia respectively. It is noted that the moment is zero at the cutting interface since there is no resistance to bending at this point.

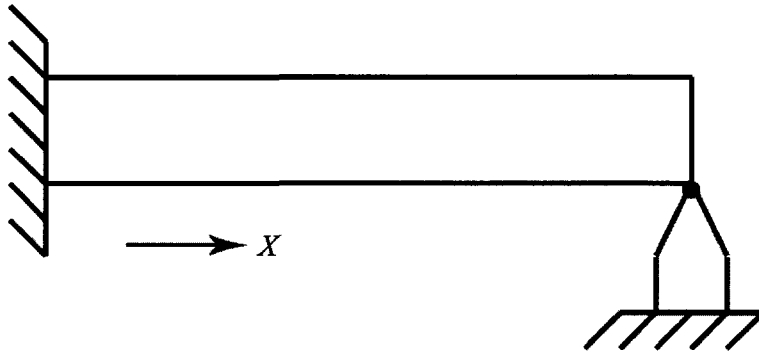


*Figure I2: Pinned Boundary Condition*

### **Application of Boundary Conditions into General Solution for Beam Vibration**

The boundary conditions can be adopted into the general form for vibration of a beam, to satisfy coefficient values and solve for system properties (i.e. mode shapes, natural frequencies, and displacement). According to Rao [55], the general solution for beam vibration takes the form:

$$X(x) = a_1 \sin \beta x + a_2 \cos \beta x + a_3 \sinh \beta x + a_4 \cosh \beta x \quad (I.5)$$

where  $a_1 \dots a_4$  are coefficients of integration and  $\beta^4 = \frac{\rho \omega^2}{EI}$ .  $\beta$  relates density, area, and elastic properties of the material. Substitution of the fixed end boundary conditions into the general solution for position gives:

$$X(l=0) = 0; a_2 + a_4 = 0 \quad (I.6)$$

and for the deflection, at  $l=0$ , the derivative of  $X$  is zero resulting in

$$\dot{X}(l=0) = 0; \beta(a_1 + a_3) = 0 \quad (I.7)$$

Evaluating  $X$  at the end of the cutting tool (where  $x=l$ ) and applying the position boundary condition results in :

$$X(x=l) = 0; a_1 \sin \beta l + a_2 \cos \beta l + a_3 \sinh \beta l + a_4 \cosh \beta l = 0 \quad (I.8)$$

Recalling the zero moment boundary condition at the tool-workpiece interface, the second derivative is taken to evaluate the moment boundary condition:

$$EI \ddot{X}(x=l) = 0; \beta^2(-a_1 \sin \beta l - a_2 \sin \beta l + a_3 \sinh \beta l + a_4 \cosh \beta l) = 0 \quad (I.9)$$

These four equations are sufficient to solve for the coefficients by solving the determinant of the coefficient matrix:

$$\begin{bmatrix} 0 & 1 & 0 & 1 \\ \beta & 0 & \beta & 0 \\ \sin \beta l & \cos \beta l & \sinh \beta l & \cosh \beta l \\ -\beta^2 \sin \beta l & -\beta^2 \cos \beta l & \beta^2 \sinh \beta l & \beta^2 \cosh \beta l \end{bmatrix} \begin{bmatrix} a_1 \\ a_2 \\ a_3 \\ a_4 \end{bmatrix} = \begin{bmatrix} 0 \\ 0 \\ 0 \\ 0 \end{bmatrix} \quad (I.10)$$

The determinant can be solved using a calculator or symbolic mathematics toolbox. Setting the determinant to zero gives the characteristic equation  $\tan \beta l = \tanh \beta l$ . This means that the solutions of  $\beta l$  that satisfy the characteristic equation relate to the modes of the system. With some additional algebra, the solutions for  $a_1 \dots a_4$  could be created, but this is not necessary unless mode shapes are of interest. For this discussion, the natural frequencies are interesting in that they show that the engaged cutting tool has different characteristics than the free ended cutting tool. Table 7.1 gives the solutions for  $\beta l$  in the Fixed-Pinned configuration.

*Table II: Values for Workpiece-Engaged Tool Holder Modeled as Fixed-Pinned*

$\beta_1 l$	3.926602
$\beta_2 l$	7.068582
$\beta_3 l$	10.21018
$\beta_4 l$	13.35177
$\beta_5 l$	16.49336

Based on the relationship of  $\beta$  to the physical parameters of the tool, the natural frequencies can be evaluated based on  $\beta l$ . The fundamental frequency is given as:

$$\left[ \frac{\rho \omega^2}{EI} \right] l^4 = 3.926602^4 \quad ; \quad \omega = \frac{3.926602^2}{l^2} \sqrt{\frac{EI}{\rho}} = \frac{15.41819}{l^2} \sqrt{\frac{EI}{\rho}} \quad (I.11)$$

The conclusions that are drawn from this are that the boundary conditions have a significant effect on the natural frequency of the system and they should be inspected in

higher detail.

### **Modeling the Workpiece-Engagement as a Sliding Boundary Condition**

Repeating a similar process to the Fixed-Pinned boundary condition, the Fixed-Sliding boundary condition can also be evaluated. The boundary conditions of the fixed end are the same as previously, where  $w$  is deflection and  $x$  is the position longitudinally along the tool are given as:

$$w=0 \quad \text{and} \quad \frac{\delta w}{\delta x}=0 \quad (\text{I.12})$$

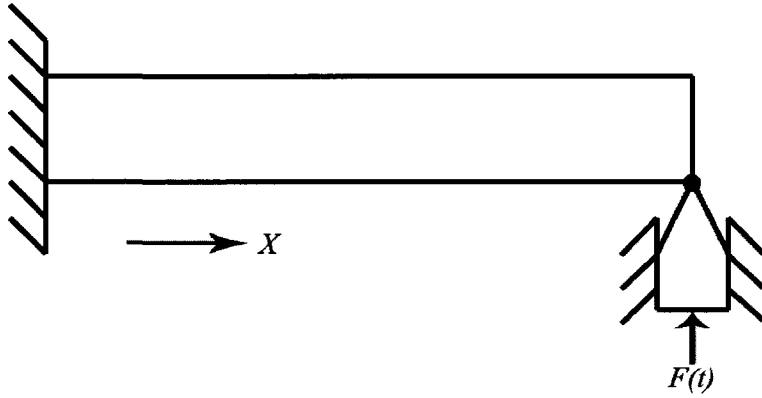


*Figure I3: Sliding Boundary Condition*

Unlike the Fixed-Pinned configuration, the end of the beam has a sliding condition instead of a pinned condition. The sliding boundary condition is restricted rotationally and no shear force exists since the tool is free to move linearly at the boundary. This results in boundary conditions of zero slope and zero shear force:

$$\frac{\delta w}{\delta x}=0 \quad \text{and} \quad \frac{\delta}{\delta x} \left( EI \frac{\delta^2 w}{\delta x^2} \right) = 0 \quad (\text{I.13})$$

Repeating the same process to above, gives a set of  $\beta l$  values that can be used to calculate the natural frequencies of the Fixed-Sliding condition. Table 7.2 gives the

solutions for  $\beta l$  for the Fixed-Sliding configuration:

*Table 12: Values for Workpiece-Engaged Tool Holder Modeled as Fixed- Sliding*

$\beta_1 l$	2.365020
$\beta_2 l$	5.497803
$\beta_3 l$	8.639379
$\beta_4 l$	11.78097
$\beta_5 l$	14.92256

Based on the relationship of  $\beta$  to the physical parameters of the tool, the natural frequencies can be evaluated based on  $\beta l$ . The fundamental frequency is given as:

$$\left[ \frac{\rho \omega^2}{EI} \right] l^4 = 2.365020^4 \quad ; \quad \omega = \frac{2.365020^2}{l^2} \sqrt{\frac{EI}{\rho}} = \frac{5.5933}{l^2} \sqrt{\frac{EI}{\rho}} \quad (I.14)$$

The sliding boundary condition may have more validity over the pinned boundary condition, since the bottom of the cutting tool is free to slide on the workpiece material, while the radial face of the tool is producing a forcing input from the cutting.

### **Insight to the Tool-Workpiece Boundary Condition**

The results of investigating different boundary conditions for the tool-workpiece interface intimates the need for more attention to this area in chatter model construction. Two possible additional boundary conditions were discussed briefly to highlight the substantial influence boundary conditions present to this system, independent of forcing input. It has been shown analytically that there is a strong influence in the dynamics for deviations from the Fixed-Free boundary assumption that is often made in chatter models. The Fixed-Sliding boundary condition is closest to the observed change in

chatter frequency that occurs during a cut. However, this analysis of boundary conditions is only part of the picture and does not capture many real variables that exist in the cutting system.

An important outcome of this analysis is the acknowledgment of these conditions and their potential effect on the system dynamics. The literature does not investigate these boundary conditions and they could be included in future work to provide a more comprehensive modeling approach that captures these effects. The author feels that it is important to investigate the boundary conditions and how they can be applied to any future modeling efforts.